AD-767 668

INTERACTION OF TWO PERPENDICULAR BOUNDED JETS

Y. S. Cha, et al

Lehigh University

LEHIGH UNIVERSITY

INTERACTION OF TWO PERPENDICULAR

BOUNDED JETS

D D C

OCT 12 1973

F

by
Y. S. Cha
and
J. A. Owczarek

August 1973

Appr... d re public rei...
tribution U...

Department of Mechanical Engineering
and Mechanics
Lehigh University
Bethlehem, Pennsylvania

Distribution of this document is unlimited.

Reproduction in whole or in part is permitted for any purpose of the United States Government.

DOCUMENT CONTROL DATA · R & D

Security classification of title, body of abstract and indexing annotation must be entered when the overall report is classified

1 ORIGINATING ACTIVITY (Corporate author)	2a. REPORT SECURITY CLASSIFICATION
Lehigh University, Bethlehem, Pa. 18015 Dept. of Mechanical Engr. and Mechanics	Unclassified
	2b. GROUP

3 REPORT TITLE

Interaction of Two Perpendicular Bounded Jets

4 DESCRIPTIVE NOTES (Type of report and inclusive dates)
Technical Report

5 AUTHOR(S) (First name, middle initial, last name)

Y. S. Cha and J. A. Owczarek

6 REPORT DATE	7a. TOTAL NO OF PAGES	7b. NO OF REFS
August 1973	180	23

8a. CONTRACT OR GRANT NO	9a. ORIGINATOR'S REPORT NUMBER(S)
N00014-69-A-0417	
b. PROJECT NO	1.7
c.	9b. OTHER REPORT NO(S) (Any other numbers that may be assigned this report)
d.	

10 DISTRIBUTION STATEMENT

Distribution of this report is unlimited.

11 SUPPLEMENTARY NOTES	12 SPONSORING MILITARY ACTIVITY

13 ABSTRACT

The interaction of two incompressible, turbulent bounded jets was investigated experimentally by using hot wire technique. Detailed measurements of velocity in the interaction zone and farther downstream were made for different values of setback, width of the control jet nozzle and control jet total pressure. Turbulence intensity profiles across the jet for various distances downstream from the stronger (power) jet nozzle exit are also reported. Angles of deflection of the power jet were determined experimentally. The aspect ratio at the power jet nozzle exit was 2, and the Reynolds numbers, based on the average power jet velocity and power nozzle width, in the tests were 12,800 and 20,000. It was found that the control jet separates from the setback wall before it reaches the power jet. Two analytical models, an ideal fluid model and a real fluid model, were used in predicting the angle of deflection. The ideal fluid model is only fairly successful in prediction of the angle of deflection of the power jet. The real fluid model, which utilizes some empirical information, allows accurate prediction of the angle of deflection of the power jet as a function of nozzle geometry and flow conditions. It also allows calculation of the velocity distribution of the combined jet at a location where the potential core disappears.

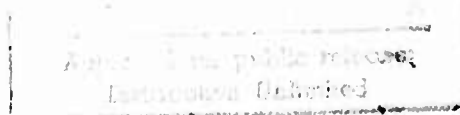| KEY WORDS	LINK A		LINK B		LINK C	
	ROLE	WT	ROLE	WT	ROLE	WT
Interaction of Two Jets						
Bounded Jets						

Technical Report No. 17

INTERACTION OF TWO PERPENDICULAR
BOUNDED JETS

by
Y. S. Cha
and
J. A. Owczarek

August 1973

Department of Mechanical Engineering and Mechanics
Lehigh University
Bethlehem, Pennsylvania

ib

ACKNOWLEDGEMENT

ii

TABLE OF CONTENTS

iv

LIST OF FIGURES

v

vi

ix

LIST OF TABLES

NOMENCLATURE

A	Area
A^*	Throat area
d	Coordinate axis shown in Figure 9
E	Volumetric entrainment rate
E_1	Volumetric entrainment rate on the free side of the combined jet
E_2	Volumetric entrainment rate on the control jet side of the combined jet
h	Location of separation of the control jet from the setback wall (see Figure 9)
J	Momentum flux of the power jet at the location where the potential core disappears
J_o	Momentum flux of the power jet at nozzle exit
k	A constant in equation (26)
K_1	Entrainment coefficient
M	A constant
N	Distance (see Figure 79)
P	Pressure
P_a	Atmospheric pressure
P_A	Pressure at point A in Figure 79
P_c	Constant pressure along the setback wall (see Figure 80)
P_t	Total pressure

P_{tc}	Control jet total pressure
P_{tR}	Pressure in the reservoir
P_{ts}	Power jet total pressure with control jet present
$(P_{ts})_0$	Power jet total pressure without control jet
Q	Volumetric flow rate
Q_0	Volumetric flow rate at nozzle exit
γ	Coordinate axis (see Figure 9)
R	Radius of curvature of the power jet in ideal fluid model (see Figure 79)
Re_w	Reynolds number based on the width of the power jet nozzle and the average velocity at the nozzle exit obtained from flow rate, $Re_w = \overline{U}W/\nu$
RMS	The magnitude of turbulence intensity defined by $\sqrt{\overline{u'^2} + \overline{v'^2} + \overline{w'^2}}$
s	Setback of the control jet nozzle
T	Distance from the pivot point where the pressure across the jet is everywhere uniform (see Figure 79)
u'	Turbulent fluctuation component in the x direction
u_{max}	Maximum velocity
U_0	Uniform velocity at the nozzle exit for a two-dimensional free jet
$\overline{U}$	Average velocity at the power jet nozzle exit, obtained from flow rate

xiv

v'	Turbulent fluctuation component in the y direction
V	Flow velocity
V_o	Maximum velocity of the combined jet
V_1, V_2	Velocities of the combined jet at the location where the potential core disappears (see Figure 80)
$V_{\mathcal{C}}$	Centerline velocity of the two-dimensional free jet
w'	Turbulent fluctuation component in the z direction
w	Width of the power jet nozzle at the nozzle exit
w_1	Width of the power jet at the location where the pressure is uniform across in the ideal fluid model (see Figure 79)
w_2	Width of the control jet at the location where the pressure is uniform across in the ideal fluid model (see Figure 79)
w_c	Width of the control jet nozzle at the nozzle exit
x	Coordinate axis (see Figure 9)
x_o	Distance from the nozzle exit where the potential core disappears for a two-dimensional free jet
x_p	Coordinate of the pivot point
y	Coordinate axis (see Figure 9)
y_e	Effective value of the coordinate y in Simson's profile for a two-dimensional free jet (see Figure 81)

ABSTRACT

The interaction of two incompressible, turbulent, bounded jets was investigated experimentally by using hot wire technique. Detailed measurements of velocity in the interaction zone and farther downstream were made for different values of setback, width of the control jet nozzle and control jet total pressure. Turbulence intensity profiles across the jet for various distances downstream from the stronger (power) jet nozzle exit are also reported. Angles of deflection of the power jet were determined experimentally. The aspect ratio at the power jet nozzle exit was 2, and the Reynolds numbers, based on the average power jet velocity and power nozzle width, in the tests were 12,800 and 20,000. It was found that the control jet separates from the setback wall before it reaches the power jet. Two analytical models, an ideal fluid model and a real fluid model, were used in predicting the angle of deflection. The ideal fluid model is only fairly successful in prediction of the angle of deflection of the power jet. The real fluid model, which utilizes some empirical information, allows accurate prediction of the angle of deflection of the power jet as a function of nozzle geometry and flow conditions. It also allows calculation of the velocity distribution of the combined jet at a location where the potential core disappears.

1

1. INTRODUCTION

A phenomenon basic to many classes of fluid amplifiers
is the interaction of a weak control jet with a power jet.
The information on the angle of deflection of the power jet
as well as the velocity distribution of the combined jet is
necessary in evaluating the gain of such amplifiers. In
view of the previous work that has been done in this area,
one finds that there is still a lack of understanding of
the process of interaction and that the analyses reported
by various investigators for prediction of the angle of
deflection of the power jet are not very satisfactory. (A
review of previous work is described in the next section.)

The specific aim of the present investigation was to
study the interaction of two incompressible, turbulent,
bounded jets. The aspect ratio of the power jet nozzle at
the exit was 2. The test Reynolds numbers based on the
average velocity of the power jet at the nozzle exit and on
the width of the power jet nozzle were 20,000 and 12,800.
The control jet supply pressure ranged from zero to forty
percent of the power jet supply pressure. Air was used as
the working fluid.

Two analytical models were employed to predict the
angle of deflection of the power jet. A comparison with
the experimentally determined values was made. Detailed

2

velocity measurements near the nozzle exits and far down-
stream are reported.

2. REVIEW OF PREVIOUS WORK

In 1962, Dexter [1]* employed a simple momentum balance
of the control and power jets to determine analytically the
angle of deflection of the combined jet. The effect of the
pressure distributions in the interaction region was neglected.
Also in 1962, Reilly and Moynihan [2] in their first publi-
cation on the subject used a similar momentum balance to
determine the angle of deflection. Later, in 1964, in an
investigation of the deflection of the power jet by two
unbalanced control jets, Moynihan and Reilly [3] extended
the control volume into the nozzles thus taking into account
the effects of the wall pressure and of the static pressure
near the nozzle exits. The aspect ratio of their power
nozzle at exit was 6, and the Reynolds number of the power
jet was 16,000. Experimental results of Moynihan and Reilly
showed that the static pressure varied across the flow at
the nozzle exits. However, the static pressure was uniform
approximately one nozzle width upstream of the nozzle exits.
The experimental results obtained by them showed that the
knowledge of the pressure acting on the walls as well as

---

*Numbers in brackets denote references listed on page 156

3

the static pressure in the interaction region were important
in determining the angle of deflection. They reported that
there was a pinching action of the control jets on the power
jet. The effective pivot point of the combined jet was
found to be approximately at the intersection of the center-
lines of the power and control jet nozzles.

Chiu and Man [4], in 1967, also studied the interaction
of three jets. Empirical formulae for the centerline veloc-
ity decay and static pressure distributions in the inter-
action region were reported. Power jet deflection angles
were calculated by considering the momentum and static pres-
sure forces. They used empirical formulae for the static
pressure distributions in the interaction region which are
valid for their test rig geometries. This approach was
similar to that of Moynihan and Reilly [3]. The aspect
ratio of the power jet nozzle used by Chiu and Man was 2.5,
and the power jet Reynolds number range was $5,000 < Re_w <$
20,000.

Also in 1967, Douglas and Neve [5] used flow visualiza-
tion on a water table to study the interaction of a power
jet with control jets. They observed that a triangular
stagnant region existed between the control jet, the power
jet and the setback wall. The fluid in the triangular
region was observed to be circulating. The control jet was
observed to turn along the edge of the triangular region

4

and thus retained its own identity as it approached the power jet. They explained that the power jet acted like a brick wall and caused an adverse pressure gradient along the setback wall and thereby caused the boundary layer associated with the control jet to separate from the wall. An enlarged scale pneumatic model was also used in their experimental study. The flow visualization study in the pneumatic model showed that the control jet retained its individuality until a distance of approximately 2.5 times the width of the power jet nozzle, after which it appeared to break up. The test results also showed that when two equal control jets were operating, they appeared to cause pinching of the power jet. The velocity profiles obtained by Douglas and Neve showed an increase in the maximum jet velocity to a distance of 2.5 times the width of the power jet nozzle and a subsequent decrease. They interpreted this as the pinching effect on the power jet by the control jets. This effect became more and more severe as the control jets strengths were increased. The acceleration of the power jet, when there was only one control jet, was far less than that when both control jets were present. Douglas and Neve were the first investigators to report the existence of the separated flow in the interaction region. The present investigation, in which this flow separation region was independently rediscovered, indicates that this flow separation must be included in a successful model of

5

interaction of perpendicular jets.

Zalmanzon, Ivanov and Limonova [6], in 1968, employed the complex variable theory for an ideal fluid to predict the angle of deflection of the power jet by one control jet. Their model was not able to calculate the deflection angle as a continuous function of the control and power jet velocities.

Vladimirov [7], in 1969, reported the results of a theoretical study of interaction of two gas jets emerging from channels having parallel walls, whose axes form an arbitrary angle. The problem was solved by the method of Chaplygin. The flow was assumed to be planar, subsonic, steady and potential. Both jets were assumed to have the same total pressure. This assumption makes their results inapplicable to fluid amplifier design.

Gungor [8], also in 1969, performed theoretical and experimental investigation of two plane, incompressible, turbulent, air jets impinging at right angle. The angle of deflection was calculated theoretically through the application of the free-streamline theory. Channels of parallel walls were used for both the power and the control jets in the experimental investigation. Channel widths were kept identical. The aspect ratio for the power jet nozzle used by Gungor was 8, and the power jet Reynolds number was

6

11,300. The main objectives of Gungor's study were to make
an analysis of the plane irrotational and incompressible
two-jet interaction and to determine experimentally the jet
deflection angle and the combined jet velocity distribu-
tions. The comparison of the analytical and experimental
jet deflection angle shows a reasonably good agreement even
for large deflection angles (up to approximately 35 degrees).
The main limitation of the analysis of Gungor lies in the
fact that it is valid only for the case when both the power
jet and the control jet have the same total pressures. This
case is of little interest in fluidic applications.

Weeks [9], also in 1969, made an experimental investi-
gation of the interaction of two perpendicular incompres-
sible jets. The test section used by Weeks was similar to
that used by Gungor except that the aspect ratio was 4.
The power jet Reynolds number in his tests was 11,140. In
Weeks' test, the flow rates of the power jet were maintained
constant and the flow rates of the control jet were varied.
Weeks observed that very near the nozzle exit, the two jets
essentially retained their separate identities. Two veloc-
ity peaks were observed. At a certain distance from the
power jet nozzle exit the two jets merged, and a single
symmetrical jet existed at a distance about 6 times the
width of the power jet nozzle. Two mixing regions caused
by the free shear layers at the outer edges of the combined

7

jet were observed. A third mixing region existed between the power and the control jets. The effective pivot point was found to be approximately at the intersection of the centerlines of the power and control jet nozzles. On the plot of maximum velocity of the combined jet versus distance, Weeks observed maxima occurring for all but the smallest control flows. This was explained as the effect of pinching of the power jet by the control jet. Weeks called this the vena contracta effect. One of the primary purposes of the investigation made by Weeks was to determine if any similarity existed in the jet interaction for similar geometries. To determine this, he compared his centerline flow velocity variation with distance, for the power jet nozzle width of 1/4 of an inch, with those of Gungor which were determined for the power jet nozzle width of 1/8 of an inch. Weeks concluded that the same general functional relationship exists between the centerline velocity and distance in both cases. The dimensionless centerline velocity was found to be a function of the dimensionless distance from the nozzle exits and of the control-to-power jet velocity ratio for similar geometries and comparable Reynolds numbers.

In 1970, Hiriart [10] investigated theoretically and experimentally the interaction of power jet with two control jets. In his test rig, the aspect ratio of the exit of the

power jet nozzle was 8. The setback and the widths of the
control nozzles were equal to the width of the power jet
nozzle. The angle of deflection,the flow velocity,and tur-
bulence intensity distributions were measured. The turbu-
lence intensity distribution exhibited four peaks near the
nozzle exits, two in the outer edges of the combined jet
where the jet mixed with surrounding fluid, and two in the
regions where the control jets mixed with the power jet.
As the distance increased from the pivot point, the turbu-
lence intensity exhibited a single minimum. Hiriart found
that the angle of deflection varied linearly with the nor-
malized differential control port pressures. In his analyt-
ical work, he applied the free-streamline theory to derive
equations for predicting the angle of deflection. The
results so obtained were found to be in good agreement with
those obtained experimentally. The analytical results of
Hiriart suffer from the same limitation as those of Vladi-
mirov [7] and Gungor [8] in that the total pressures of the
control port jets were the same as the total pressure of
the power jet.

In 1970, Sarpkaya, Weeks and Hiriart [11] reported the
results of theoretical and experimental investigation on
the interaction of a power jet with a single and with two
control jets. This report essentially combines the results
of the studies of Gungor [8], Weeks [9] and Hiriart [10]

9

made under the guidance of Dr. Sarpkaya.

Also in 1970, Bourque [12] studying the interaction
of two jets, proposed a control volume approach using only
one momentum equation to calculate the angle of deflection
of the power jet. The control volume suggested by him is
similar to that of Moynihan and Reilly [3]. This model
needs information from experimentally determined pressure
distributions inside the nozzles. Unfortunately, such a
model cannot be generalized to obtain the angle of deflec-
tion as a function of setback, and control nozzle width.
Some experimental results were also obtained by Bourque.
The aspect ratio of the exit of the power jet nozzle used
by him was 12 and the width of the control jet nozzle was
the same as the width of the power jet nozzle. It was found
that the angle of deflection was independent of setback.
The distance at which symmetry of the combined jet was ob-
served was found to be a function of the ratio of control to
power nozzle total pressure. It increased from zero for no
control flow to a maximum of about 16 nozzle widths at pre-
ssure ratio of 0.4 and subsequently decreased as the press-
ure ratio increased further. This finding is different from
that of Weeks [9] who observed at all pressure ratios the
symmetry of the combined jets at a distance of 6 nozzle
widths from the nozzle exit. The difference is probably due to
the effect of the power jet nozzle exit aspect ratio. (The

10

power jet nozzle exit aspect ratio in Weeks' study was 8.)

In 1971, Turken [13] reported the results of an experimental investigation on the interaction of three jets. The aspect ratio of the power jet nozzle exit was 2. The width of the control jet nozzle was 2.5 times the width of the power jet nozzle. The setback was equal to the width of the power jet nozzle. Turken observed that, in the range of the power jet Reynolds number (based on nozzle width) of 7,887 to 31,550, the effect of the power jet Reynolds number on the angle of deflection of the power jet was very small. The pressure along the setback walls was observed to be nearly constant. The turbulent fluctuation component $\sqrt{\overline{u'^2}}$ was found to be always highest and the component $\sqrt{\overline{w'^2}}$ was always lowest. Using the experimentally determined pressure distributions and the control volume analysis of Moynihan and Reilly [3], Turken calculated the angle of deflection and claimed good agreement with experiment.

In 1972, Sarpkaya [14] reported a momentum analysis of three-jet interaction by employing two control volumes. By assuming certain velocity distributions and by a free-streameline analysis for the contraction of the control jets, he obtained an iterative scheme allowing determination of the angle of deflection in terms of amplifier geometry and the supply pressures of the control and power jets. However, his calculated angle of deflection was compared with only one set of experimental data corresponding to one inter-action region geometry.

11

In summary, the experimental work just described shows lack of systematic investigation of the effect of amplifier geometry on the angle of deflection. Also, no detailed information about the velocity distribution very near the nozzle exits was reported. As far as analytical work aimed at prediction of the angle of deflection of the power jet is concerned, two approaches exist in the literature: one uses the theory of complex variables for an ideal fluid, and the other utilizes the control volume approach. The complex variable theory for ideal fluid requires that the point where the wall of the power jet nozzle meets the wall of the control jet nozzle be a stagnation point. This in turn requires that the total pressures of the power and control jets be the same (since the static pressure is assumed to be continuous in the flow field). This case is of little interest in fluidic applications. The control volume analysis is more useful than the analysis using the theory of complex variables since it does not require this limitation. However, it cannot predict all the pressure forces that are required in calculating the angle of deflection of the power jet, and empirical information is necessary. The reported models of the jet interaction zone are inadequate because they do not recognize the existence

12

of the separation zone along the setback wall between the control and power jets.

The objective of the present investigation was to make a systematic study of the effect of the control nozzle width and of the setback on the flow field in the interaction region of two perpendicular bounded jets tested in a rig having aspect ratio of two at the power nozzle exit. In addition, it was planned to develop an analytical method, based on the information obtained from the experimental part of this study, which would be capable of predicting the deflection angle of the power jet and the combined jet velocity distribution at the location where the potential core disappears,as a function of the control nozzle width and setback for power jet nozzle exit aspect ratio of two. This method was to be based on the control volume approach and was to utilize some empirical information related to the control port width and to the setback.

3. DESCRIPTION OF EXPERIMENTAL APPARATUS

3.1 Test Rig

Figure 1 shows a sketch of the experimental apparatus. Dry and clean air was pumped into a storage tank where the pressure was kept at 62 psig. Flexible plastic tubes were

13

used in connecting the test section to the storage tank. Flow rates were controlled by pressure regulators.

Two Fox Valve Co. venturi meters were used in determining the flow rates. One venturi meter was used for measuring the flow rate of the power jet. It had a throat diameter of 0.2260 of an inch and was expanding to a tube of 2 inches in diameter. The other venturi meter was used to measure the flow rate of the control jet. It had a throat diameter of 0.150 of an inch and was expanding to a tube one inch in diameter. The venturi meters were calibrated using an ASME long radius type nozzle shown in Figure 2a. The calibration procedure is described in reference [15]. As is common in fluidic applications, the power jet flow is described by a Reynolds number based on the average velocity calculated from flow rate and on the width of the power jet nozzle. Figure 3 shows a plot of the Reynolds number defined above versus the pressure drop through the venturi meters.

The stagnation tank for the power jet was 4 feet long and had a diameter of 13 inches. Two screens and one honeycomb were placed inside the tank as shown in Figure 4 in order to reduce the turbulence and to distribute the flow uniformly before it arrived at the test section. The stagnation tank of the control jet was one foot long and six inches in diameter. It also had a honeycomb inside.

14

3.2 Test Section

Figure 5 shows a sketch of the test section. The orig-
inal design included two control jets and the receivers.
However, the present investigation was limited to the inter-
action of a power jet with one control jet without the
presence of the receivers. The power and control jet noz-
zles were bounded by two side plates. All parts of the
test section were made of plexiglass. The thickness of the
sandwiched pieces was 0.8 inch. The width of the power jet
nozzle exit was 0.4 inch. Thus the aspect ratio of the
power jet nozzle exit in the present investigation was 2.
The detailed dimensions of the power jet nozzle and of the
control jet nozzle are shown in Figures 6 and 7 respectively.

The test section was so designed that by removing a
piece of the plexiglass between the power and the control
nozzles, the control nozzle could be made to be inclined at
an angle of 60 degrees with respect to the power nozzle
axis. The control nozzle setback could be varied by using
different plexiglass pieces that formed the control nozzle.
The width of the control jet nozzle could also be varied.

Three pressure taps were drilled near the exit of the
control jet as shown in Figure 8. One pressure tap was
also made in the power jet nozzle and one in the control
jet nozzle in order to measure the supply pressures of the
two jets.

15

3.3 Traversing Mechanism

Figure 2b shows a photograph of the traversing mechanism. This mechanism was designed for traversing hot wire or total pressure probes in three mutually perpendicular directions. The definitions of coordinates x, y, and z are given in Figure 9. Two micrometers were used to traverse the probes in the y and z directions respectively. The distances traveled by the micrometers were recorded by an X-Y recorder through a linear position potentiometer. The traversing mechanism could slide horizontally in the x direction on two 12-inch long arms. The two arms could also be made to slide on two circular slots and thus could make the probe aligned at right angle to the direction of the deflected jet. The traversing mechanism was placed on top of the test section.

3.4 Experimental Equipment

DISA 55D01 hot wire anemometer and 55D10 linearizer were used in measuring the velocity profiles. DISA 55D35 RMS unit was used in measuring the turbulent fluctuations. The detailed operation and calibration procedure can be found in the instruction and service manual supplied by DISA. Two types of miniature probes, shown in Figure 10, were supplied by DISA. One was the 55F31 straight general-purpose type and the other was the 55F35 right angle type.

16

The wire length was 1.25 mm and the wire diameter was 5 μm for both types.

Figure 11 shows a sketch of the total pressure probe used in preliminary testing. Model CD12 pressure transducer indicator and model DP15 pressure transducer supplied by Validyne Engineering Corp. were used in measuring the total pressure distributions.

Figure 12 shows a photograph of the test section, traversing mechanism and of the equipment used in the present investigation.

3.5 Experimental Procedures

Before running each test, the barometric pressure and the atmospheric temperature were recorded. (The temperature of the laboratory was always between 70 and 75 degrees Fahrenheit.) Also, the cold resistance of the hot wire probe was checked.

The velocity distributions measured by the hot wire equipment were recorded on an X-Y recorder in the following manner. The output from the hot wire anemometer after going through a linearizer was received by one of the inputs of the X-Y recorder. The other input of the X-Y recorder received signal from the linear position potentiometer. Thus, the output from the X-Y recorder gave a plot of the velocity

17

versus the distance traveled by the probe.

The total pressure distributions were determined in a similar way. The output from the transducer indicator rather than that of the linearizer went to the X-Y recorder. The X-Y recorder then gave a plot of the total pressure versus the distance traveled by the probe.

For each test, the pressure drop through the venturi meters was recorded. The upstream pressure in the power and the control jet nozzles as well as the pressure distributions along the setback wall of the control jet were measured by inclined manometers of different ranges. The finest increment on these manometers was 0.01 inch of water.

4.   EXPERIMENTAL RESULTS

4.1 Preliminary Test on Power Jet Alone

The coordinate system used in the present investigation is shown in Figure 9. The midplane was defined as the plane midway between the two bounding plates, that is, the plane corresponding to $z = 0$. The centerplane was defined as the plane midway between the two plexiglass pieces that formed the power jet nozzle, that is, the plane corresponding to $y = 0.5w$. Figures 13 to 18 show the total pressure variations with distance between the two bounding side plates.

18

Figure 19 shows the velocity profile obtained by using the hot wire. The results show that there is a big dip near the corner and a smaller dip near the midplane for all the profiles. This nonuniformity of total pressure and velocity was observed previously in an investigation of rectangular nozzles described in references [16], [17] and [18]. In order to reduce this nonuniformity, a flow straightener was inserted in the power jet nozzle as shown in Figure 5. Figure 20 shows the velocity distribution with flow straightener in the power jet nozzle. As expected in view of the previous studies on the planar nozzles, the dip near the midplane was eliminated by the flow straightener but the corner dip still existed. This is so because the corner dip is caused by the contraction of nozzle after the flow straightener while the dip near the midplane is caused by the transition from a circular to a rectangular duct at the nozzle inlet. A detailed explanation of this effect is described in references [16] to [18]. In the present investigation of the two-jet interaction process, flow straighteners were placed inside both the power and the control jet nozzles.

Velocity distributions across the power jet at midplane for different distances downstream from the nozzle exit are shown in Figure 21. A plot of the maximum jet velocity versus distance downstream from the nozzle exit is shown in

19

Figure 22. The location where the potential core disappears is at a distance of approximately 4.5w downstream from the nozzle exit. This is in agreement with the results obtained by Trapani [19] in an investigation of bounded jets of low aspect ratios.

The experimental results which follow are for the two jet interaction. The velocity profiles were measured at midplane. Only absolute velocities were measured and no effort was made to determine the components of the flow velocities. The definition of the coordinate system used in the present investigation was shown in Figure 9.

4.2 Angles of Deflection and the Pivot Points

The angles of deflection of the power jet, α, were determined from velocity profiles by connecting the points of maximum velocity at different locations downstream from the nozzle exit. Figures 23 to 26 show some typical examples of how angle α was determined. The pivot point was defined as the point of intersection of the centerline of the power jet nozzle with the line connecting the locations of the maximum jet velocities. It was found that for $w_c/w = 1$, the pivot points were at the intersection of the centerline of the power jet nozzle with that of the control jet nozzle. This is in agreement with the findings of Moynihan and Reilly [3] and Weeks [9]. However, this is not

20

so for $w_c/w = 1/2$. For example, it was found that for the case of $s/w = 1/2$ and $w_c/w = 1/2$, $x_p/w = w_c/w = 1/2$ gives the best fit of experimental points. For the case of $s/w = 1$ and $w_c/w = 1/2$, the values of x_p/w were found to be scattered between 1.5 and 3. Table 1 summarizes the experimental values of the dimensionless pivot point coordinate x_p/w.

Table 1. Experimental values of the dimensionless pivot point coordinate x_p/w

s/w w_c/w	1	$\frac{1}{2}$
1	0.5	0.5
$\frac{1}{2}$	1.5-3.0	0.5

Figure 27 shows the experimentally determined values of the angle of deflection of the power jet α for various values of the setback, width of the control jet nozzle, and dimensionless pressure $\pi_2 = (P_{tc}-P_a)/(P_{ts}-P_a)$ at power jet Reynolds number $Re_w = 20,000$. It shows that, in the range tested, the angle of deflection α varies very slightly with

21

the setback (which confirms the results of Bourque [12]) and
increases with the width of the control jet nozzle. The
angle of deflection also increases linearly with the dimen-
sionless pressure π_2. Figure 28 shows that the angle of
deflection is independent of the power jet Reynolds numbers
in the range between 12,800 and 20,000. Figure 29 shows a
comparison of the angle of deflection α for the control jet
inclined at angle of 60 degrees with respect to the power
jet with that for the control jet inclined at angle of 90
degrees to the power jet. It shows that the control jet
deflects the power jet less when the angle between the two
jets is decreased.

4.3 Velocity Distributions and Turbulence Intensities

Figures 30 to 39 show the velocity distributions and
turbulence intensities across the deflected jets in the direc-
tion perpendicular to the direction of flow, that is, at
angle α to the power jet nozzle axis, at various distances
downstream from the pivot point. These traverses correspond
to the dimensionless control nozzle width $w_c/w = 1$, and the
dimensionless setback $s/w = 1$ and to the power jet Reynolds
number $Re_w = 20,000$. Similar velocity plots for $w_c/w = 1/2$,
$s/w = 1$, for $w_c/w = 1$, $s/w = 1/2$, and for $w_c/w = 1/2$,
$s/w = 1/2$ were also obtained but are not included in this
report. The velocity and the RMS values of the turbulent

22

velocity fluctuations were normalized with respect to the maximum velocity at r/w = 1. The definition of the coordinates r and d are shown in Figure 9. At r/w = 1, the two jets are still distinguishable on the velocity distribution plots. The RMS profile shows three peaks which represent three mixing regions, two of them on the outer edges of the combined jet where the surrounding fluid is being entrained and the third one between the two jets. Qualitatively, turbulence intensity increases with increasing velocity gradient. The two peaks on the control jet side in the RMS profile begin to merge into one as the combined jet moves farther downstream and become undistinguishable at r/w = 4. Symmetry of the RMS profile is not reached until r/w ≈ 9. The magnitude of the RMS value does not exceed 15 percent of the maximum velocity at r/w = 1. The values of the RMS in the valleys between the peaks gradually approach this limiting value as r/w increases.

The traverses show that the power jet absorbs the control jet in a relatively short distance and that the velocity profiles become more and more symmetrical as the combined jet moves away from the pivot point.

The above description corresponds to one particular geometry ($w_c/w = 1$, $s/w = 1$) and to one value of dimensionless pressure π_2. The location where the two peaks in the RMS profile near the control jet become one and the location

23

where the velocity profile becomes symmetrical depend on the values of the dimensionless parameters w_c/w, s/w and π_2. Figures 40 to 49 show the results for a different value of the dimensionless pressure π_2 and a different power jet Reynolds number, Re_w = 12,800. These results are qualitatively similar to those shown in Figures 30 to 39 which correspond to Re_w = 20,000.

4.4 Velocity Distributions Near Nozzle Exits

Figures 50 to 53 show the velocity distributions close to the exit of the power jet nozzle. These profiles were obtained by traversing across the power jet nozzle and into the control jet nozzle. The power jet is located approximately between $0 \leq y/w \leq 1$. The velocity across the power jet nozzle is not uniform, being lower on the control jet side. This means that the static pressure across the power jet is not uniform since the total pressure upstream in the nozzle is uniform. Since the power jet deflects only through a small angle (in the present investigation, the maximum angle of deflection obtained was about 16 degrees), the pressure at the nozzle exit on the side where the power jet is free to entrain the surrounding fluid should be nearly equal to the atmospheric pressure. Therefore the pressure must be higher than atmospheric pressure on the control jet side at the exit of the power jet nozzle. This

24

pressure difference increases with increasing dimensionless control supply pressure π_2. That this is so can be seen by comparing Figure 50 with Figure 54.

In Figure 50, the velocity drops suddenly from a level of the power jet velocity to nearly zero as the probe passes through the edge of the power jet nozzle and begins to enter into the region in the vicinity of the setback wall of the control jet nozzle. The zone of low velocity continues for some distance. Then the flow velocity starts to increase sharply until a constant velocity is reached. The length of the low velocity zone decreases as the value of the coordinate x/w increases. The above description indicates that the control jet separates from the setback wall as shown in Figure 9. A plot of constant velocity lines in the jet interaction region is shown in Figure 55. It shows that the control jet begins to turn before it comes into contact with the power jet. The power jet and the control jet do not meet each other until the power jet has traveled a certain distance from the exit of the power jet nozzle. Before this distance, the deflection of the power jet is due entirely to the pressure difference existing across the power jet. After the two jets meet, the pressure difference across the power jet as well as the momentum of the rapidly turning control jet contribute to the deflection of the power jet.

Figures 50 to 53 also show that the flow is more

turbulent in the separated flow zone than in either the power jet or in the control jet.

Another important observation which follows from this study is that the velocity distribution across the control jet nozzle is very nonuniform. Figure 55 shows that the velocity is low near the inner wall (setback wall) and it increases towards the outer wall of the control jet nozzle. This implies that there is a pressure difference across the control jet at the nozzle exit.

4.5 Location of Separation Point and Pressure Distribution in the Separated Flow Zone

The distance h that specifies the location of the separation point of the control jet from the setback wall (see Figure 9) depends on the width of the control jet nozzle w_c, the setback s ,and the supply pressure of the control jet. The values of h could not be determined very accurately in the present investigation because the hot wire probe could not be brought to the immediate vicinity of the wall. The closest distance from the wall at which the hot wire could be located was 0.05 of an inch. The distance h was estimated from the plots of constant velocity lines such as the one shown in Figure 55.

The experimental results show that the distance h depends on the width of the control jet nozzle w_c and the

26

setback s. They also show that the distance h has a tend-
ency to decrease only very slightly with increase of the
supply pressure of the control jet π_2. Within the accuracy
of the present test, the values of the separation distance
h were obtained as a function of w_c and s only, and the
slight dependence on π_2 was ignored. Table 2 gives the
estimated values of the separation distance h made dimen-
sionless by division by the power nozzle width w for vari-
ous values of the dimensionless width of the control jet
nozzle w_c/w and setback s/w.

Table 2. Experimentally-determined values
of the dimensionless separation distance h/w

w_c/w \ s/w	1	1/2
1	0.3	0.6
1/2	-0.1	0

The results are also plotted in Figure 56.

The pressure variation along the setback wall in the
separated flow zone is shown in Figures 57 to 60. For

27

$w_c/w = 1$, the pressure remains nearly constant along the setback wall for all values of the dimensionless pressure π_2. For $w_c/w = 1/2$, the pressure also remains essentially constant along the setback wall except for large values of π_2 at which it varies slightly because the lower pressure tap or taps measure then the control jet pressure and not the pressure in the separation region. The finding that the pressure is uniform along the setback wall of the control jet nozzle is not surprising in view of the fact that a separated flow zone exists along that wall. Similar results (constant pressure along the setback wall) were reported by Moynihan and Reilly [3] and Turken [13]. However, they were not aware of the existence of the separated flow zone there.

4.6 Effect of the Control Flow on the Power Jet Nozzle Flow

Figures 61 to 64 show the plots of the maximum jet velocity versus the distance from the pivot point. The maximum velocities are normalized with respect to the velocity U_0 at the exit of the power jet nozzle when the control jet is absent. They show that the maximum velocity increases with the dimensionless pressure π_2. The pressure in the power jet nozzle also increases with π_2 as shown in Figure 65 while the flow rate of the power jet remains unchanged as indicated by the reading of the venturi meter. To explain this phenomenon, let us go back to Figure 54

28

which shows the velocity distribution across the power jet
nozzle. The velocity on the free side of the power jet is
higher than U_0 and the velocity on the control jet side is
lower than U_0. The loss of the mass flow in the lower
velocity zone is compensated by the extra mass flow in the
higher velocity zone and thus the flow rate of the power jet
is constant, that is, it is the same as the flow rate of the
power jet without the presence of the control jet. As ex-
plained before, since the pressure on the free side of the
power jet is nearly atmospheric, the higher power jet veloc-
ity must result from an increase in the total pressure up-
stream in the nozzle. That is, the total pressure of the
power jet with the presence of the control jet is higher
than that of the power jet alone for a constant flow rate
of the power jet. Figures 66 to 69 show comparisons between
the measured increase in the total pressure in the power jet
nozzle and the increase in the maximum velocity near the
exit of the power jet. The dimensionless pressure π_1
matches the maximum jet velocity very well and thus indi-
cates the correspondence between the increase in the maximum
combined jet velocity u_{max} shown in Figures 61 to 64 and
that of the total pressure in the power jet nozzle.

The reason why the flow rate of the power jet remains
constant while the downstream condition at the exit of the
power jet nozzle is changed by the control jet flow is as

29

follows. The flow rate of the power jet is measured by a venturi meter which has a form of a convergent-divergent nozzle. Figure 70 shows the performance curves of a convergent-divergent nozzle for a one-dimensional steady flow. The area ratio A/A^* of the venturi meter for the power jet is close to 80. With this area ratio, it follows from the tables of reference [20] that

$$\left(\frac{P}{P_{tR}}\right)_3 = 0.9999 \quad \text{and} \quad \left(\frac{P}{P_{tR}}\right)_8 = 0.0003503$$

for a gas having specific heat ratio $\gamma = 1.4$. In view of the above values and Figure 70, one can see that the venturi meter is operating between point 3 and point 8 because $(P/P_{tR})_3$ is very close to unity and $(P/P_{tR})_8$ is very close to zero. One can also calculate $(P/P_{tR})_5$ corresponding to a normal shock wave at nozzle exit which in the present case is equal to 0.0177 and is also very small. One can conclude that in the tests run in this investigation, the venturi was operating between point 3 and point 5 in Figure 70. From the mass flow diagram, one can see that the mass flow rate is constant from point 3 on. Therefore, in the tests the flow in the venturi meter was choked with a shock wave in the divergent part of the venturi meter. The location of the shock wave depends on the back pressure at nozzle exit of the venturi meter which in turn depends on the conditions downstream at the exit of the power jet nozzle. And so in

30

the tests performed the flow rate of the power jet was con-
stant and was independent of the conditions at the exit of
the power jet nozzle as long as the conditions upstream of
the venturi meter were not changed.

4.7   Decay of the Maximum Combined Jet Velocity

From Figures 61 to 64, it is clear that the dimension-
less parameter u_{max}/U_0 depends on π_2. If u_{max} is normalized
by the maximum velocity V_0 of the potential core of the com-
bined jet (which varies with π_2), then the relationship
becomes independent of π_2 as shown in Figures 71 to 74.

Figures 71 to 74 show the decay of the maximum combined
jet velocity at various distances from the pivot point.
From these figures one can conclude that the potential core
of the combined jet disappears at $r/w \approx 4$ for $0 < \pi_2 < 0.4$.
The same result was obtained in the test of the power jet
alone where it was found that the potential core disappears
at $x/w = 4.5$.

In Figures 61 to 64, the dimensionless parameter
u_{max}/U_0 shows a slight variation from $r/w = 0$ to $r/w = 4$.
To explain this, one must look at the velocity distributions
across the power jet at small values of the coordinate r/w,
like those shown in Figures 75 to 78. Very close to the
nozzle exit, say at $r/w = 0$, the maximum velocity is near

31

the edge of the power jet where it expands to atmospheric pressure (free side of the power jet). The velocity decreases across the power jet towards the control jet while the nozzle exit pressure increases towards the control jet. As the jet moves downstream, the part of the power jet whose pressure is higher than atmospheric continues to expand; therefore the velocity in that region increases. The velocity on the free side of the power jet decreases slightly due to the mixing with the surrounding fluid. At some distance downstream, say $r/w = 1$, the maximum velocity still occurs on the free side of the power jet, but there is a slight decrease in the magnitude of the velocity due to entrainment. The power jet velocity at locations away from the free side has not yet reached its maximum value because the pressure there is still higher than atmospheric. This situation corresponds to the small dip at $r/w \approx 1$ visible in Figures 61 to 64. As the power jet moves farther downstream, the velocity of its core tends to become uniform due to pressure equalization while at the same time it continues to entrain surrounding fluid from the free side and to mix with the control jet on the other side. For all geometries and all values of π_2 in the present tests, the value of r/w where the velocity of the core of the power jet becomes uniform was found to lie between 2 and 2.25. There the pressure distribution across the jet should be everywhere uniform and equal to the atmospheric pressure.

32

The local increase in the maximum power jet velocity
due to the increase in the control jet flow was also re-
ported by Weeks [9] and Sarpkaya et al [11]. In their
investigations, the flow rate of the power jet was also
constant while the flow rate of the control jet was varied.
The increase in the total pressure in the power jet nozzle
was not reported in their investigations. Weeks, and Sarp-
kaya et al, interpreted the increase in the maximum power
jet velocity by the effect of pinching (or vena-contracta)
on the power jet caused by the momentum of the control jet
in its initial direction.

The location of the vena-contracta reported by Weeks
[9] and Sarpkaya et al [11] coincides with the location
where, in the present tests, the flow velocity in the core
equalizes thus indicating that the pressure across the jet
is uniform and equal to the atmospheric pressure.

4.8   Summary of the Experimental Results

A.   Secondary flows were observed to exist in the power jet
      nozzle tested without a flow straightener and the flow
      was highly nonuniform at the nozzle exit. With the
      flow straightener inside the power jet nozzle, the
      velocity and total pressure profiles were uniform
      everywhere at the nozzle exit except near the corners.

33

B.   The angle of deflection of the power jet by a control
     jet was determined. The values of the angle of deflec-
     tion were obtained by connecting the point of maximum
     combined jet velocity at different distances from the
     pivot point. The location of the pivot point was found
     to depend on the setback and on the width of the con-
     trol jet nozzle.

C.   The angle of deflectio: was found to vary only slightly
     with setback and to increase with the width of the con-
     trol jet nozzle. It was found that the angle of de-
     flection increases linearly with the dimensionless
     control jet supply pressure π_2 and is independent of
     the power jet Reynolds number Re_w in the range between
     12,800 and 20,000. It was also found that the angle of
     deflection decreases with decrease of the angle between
     the power jet and the control jet.

D.   Three mixing regions were observed, one on the free
     side of the power jet, one on the free side of the con-
     trol jet and one between the two jets.

E.   The velocity profile of the combined jet was observed
     to become progressively more symmetrical with distance
     from the exit of the power jet nozzle.

F.   The velocity profile, and therefore also the pressure
     distribution, were not uniform at the exits of both

the power jet nozzle and the control jet nozzle.

G. Control jet was observed to separate from the setback
    wall of the control jet nozzle. Therefore,the two jets
    do not meet until a certain distance downstream from
    the exit of the power jet nozzle.

H. The location of separation on the setback wall was
    found to depend on the setback and width of the control
    jet nozzle and only very slightly on the dimensionless
    pressure π_2.

I. The pressure in the separated flow zone was observed to
    be nearly constant and was found to depend on the set-
    back, the width of the control jet nozzle,and on the
    dimensionless pressure π_2.

J. The maximum velocity of the combined jet and the total
    pressure of the power jet were found to increase with
    increasing dimensionless pressure π_2 in tests in which
    the mass flow rate of the power jet was kept constant.
    As expected, the dimensionless quantity π_1 is very
    nearly equal to the dimensionless maximum jet
    velocity u_{max}/U_0.

K. The flow rate of the power jet was independent of the
    conditions downstream at the nozzle exit because the
    flow was choked in the venturi meter.

35

L. For the power jet nozzle exit aspect ratio of 2, the potential cores of the combined jet and of the single power jet were found to disappear at a distance from the exit of the power jet of approximately 4.5 widths of the power jet nozzle for all values of setback, width of control jet nozzle, and the dimensionless pressure π_2.

M. For the power jet nozzle exit aspect ratio of 2, the core velocity (and therefore also the pressure) of the combined jet was found to become uniform across the jet at a distance of 2 to 2.25 power jet nozzle widths downstream from the exit of the power jet nozzle.

Table 3 gives the experimental variables covered in the present investigation.

Table 3. Variables studied in the present investigation for $Re_w = 20,000$, $\beta = 90°$ and $0 < \pi_2 < 0.4$

s/w ＼ w_c/w	1		$\frac{1}{2}$	
1	$\alpha, h,$	pressure distributions along setback wall	$\alpha, h,$	pressure distributions along setback wall
$\frac{1}{2}$	$\alpha, h,$	pressure distributions along setback wall	$\alpha, h,$	pressure distributions along setback wall

The power jet deflection angles α were also measured for $w_c/w = 1$, $s/w = 1$, $\beta = 90°$ and $Re_w = 12,800$ and for $w_c/w = 1$, $s/w = 1$, $\beta = 60°$ and $Re_w = 20,000$. Velocity distributions were measured at locations corresponding to $0 < x/w \leq 14$.

5.   CONTROL VOLUME ANALYSIS

The analysis described in this section is based on the assumptions that the flow is two-dimensional and incompressible. The main objective was to obtain the angle of deflection of the power jet as a function of amplifier geometry and supply pressures of the control and the power jets.

5.1 Ideal Fluid Model

Figure 79 shows the definitions of the symbols used in this model. Two control volumes are used in this model. One is the volume ABCDEFGA shown in Figure 79 which includes both the power and the control jets. The line CDE is perpendicular to the coordinate axis r and is located at a position where pressure across the jets is uniform and equal to the atmospheric pressure. The following additional assumptions are made:

A.   The flow is inviscid; as a result, the entrainment of fluid on the outer edges of the combined jet and the

37

mixing between the power and the control jets are
neglected.

B. Atmospheric pressure, P_a, acts on the free sides of the
jets and at section CDE. That is,

$$P_{BC} = P_{CD} = P_{DE} = P_{EF} = P_a \; .$$

C. Pressure distributions across the power jet (along AB),
along the setback wall AG and across the control jet
(along GF) are assumed to be linear, and given by
equations

$$P_{AB} - P_a = (P_A - P_a)(1 - \frac{y}{w}) \tag{1}$$

$$P_{AG} - P_a = (P_{tc} - P_a) + (P_A - P_{tc})(1 + \frac{y}{s+h}) \tag{2}$$

$$P_{GF} - P_a = (P_{tc} - P_a)(1 - \frac{x}{w_c}) \tag{3}$$

where P_A is the unknown pressure at point A. Since the
total pressure losses are neglected, the following
relations hold:

$$\begin{aligned}
V_{AB} &= [\frac{2}{\rho}(P_{ts} - P_{AB})]^{1/2} \\
&= \{\frac{2}{\rho}[(P_{ts} - P_a) - (P_A - P_a)(1 - \frac{y}{w})]\}^{1/2} \tag{4}
\end{aligned}$$

$$\begin{aligned}
V_{GF} &= [\frac{2}{\rho}(P_{tc} - P_{GF})]^{1/2} \\
&= \{\frac{2}{\rho}[(P_{tc} - P_a) - (P_{tc} - P_a)(1 - \frac{x}{w_c})]\}^{1/2} \\
&= [\frac{2}{\rho}(P_{tc} - P_a)\frac{x}{w_c}]^{1/2} \tag{5}
\end{aligned}$$

38

$$V_{CD} = [\frac{2}{\rho} (P_{ts} - P_a)]^{1/2} \tag{6}$$

$$V_{DE} = [\frac{2}{\rho} (P_{tc} - P_a)]^{1/2} \tag{7}$$

The velocities V_{AB} and V_{GF} are assumed to be in the x and y direction respectively. The velocities V_{CD} and V_{DE} are assumed to be inclined at angle α with respect to the horizontal axis.

The continuity equations for the power jet and the control jet are:

$$\rho \int_0^W V_{AB}dy = \rho \int_0^{W_1} V_{CD}d\xi \tag{8}$$

and

$$\rho \int_0^{W_c} V_{GF}dx = \rho \int_0^{W_2} V_{DE}d\eta \tag{9}$$

where ξ and η are dummy variables. Momentum equations for the control volume ABCDEFGA in the x-direction and in the y-direction can be written as

$$- \rho \int_0^W V_{AB}^2 dy + \rho \int_0^{W_1} V_{CD}^2 \cos\alpha d\xi + \rho \int_0^{W_2} V_{DE}^2 \cos\alpha d\eta$$

$$= \int_0^W (P_{AB} - P_a)dy + \int_{-(s+h)}^0 (P_{AG} - P_a)dy - \int_0^{W_c} (P_{GF} - P_a)\frac{h}{W_c} dx$$

$$\tag{10}$$

39

and

$$\rho \int_0^{W_1} V_{CD}^2 \sin\alpha\, d\xi + \rho \int_0^{W_2} V_{DE}^2 \sin\alpha\, d\eta - \rho \int_0^{W_c} V_{GF}^2\, dx$$

$$= \int_0^{W_c} (P_{GF} - P_a)\, dx \qquad (11)$$

Substituting equations (1) through (7) into equations (8) to (11) gives

$$\frac{W_1}{W} = \frac{2}{3} \frac{[1 - (1 - \pi_3)^{3/2}]}{\pi_3} \qquad (12)$$

$$\frac{W_2}{W} = \frac{2}{3} \frac{W_c}{W} \qquad (13)$$

$$-2 + 2\frac{W_1}{W} \cos\alpha + [1 - (\frac{s+h}{W})]\frac{\pi_3}{2} = \pi_2(-2\frac{W_2}{W} \cos\alpha + \frac{1}{2}\frac{s}{W}) \qquad (14)$$

and

$$2\frac{W_1}{W} \cos\alpha = (-2\frac{W_2}{W} \sin\alpha + \frac{3}{2}\frac{W_c}{W})\, \pi_2 \qquad (15)$$

where

$$\pi_2 = \frac{P_{tc} - P_a}{P_{ts} - P_a} \qquad (16)$$

$$\pi_3 = \frac{P_A - P_a}{P_{ts} - P_a} \qquad (17)$$

The second control volume chosen is volume ABCDJA

40

which involves only the power jet. The following additional assumptions are made for this second control volume:

D. The power jet begins to turn at point A with a constant radius R until it reaches point J (see Figure 79). From point J on, the power jet does not change its direction and moves along a straight line (line JD in Figure 79).

E. The static pressure varies linearly along AJD from P_A to P_a, and therefore

$$P_{AJ} - P_a = (P_A - P_a)(1 - \frac{R\theta}{R\alpha + N})$$ (18)

$$P_{JD} - P_a = (P_A - P_a)(1 - \frac{R\alpha + \zeta}{R\alpha + N})$$ (19)

where α is the angle of deflection of the power jet at any point between A and J and ζ is the dummy variable along JD.

The momentum equations in the x and y directions for the control volume ABCDJA are:

$$-\rho \int_0^W V_{AB}^2 dy + \rho \int_0^{W_1} V_{CD}^2 \cos\alpha d\xi$$

$$= \int_0^W (P_{AB} - P_a) dy - \int_0^\alpha (P_{AJ} - P_a)\sin\theta(Rd\theta) - \int_0^N (P_{JD} - P_a)\sin\alpha d\zeta$$

(20)

41

and

$$\rho \int_0^{W_1} V_{CD}^2 \sin\alpha \, d\xi = \int_0^\alpha (P_{AJ} - P_a) \cos\theta (Rd\theta) - \int_0^N (P_{JD} - P_a) \cos\alpha \, d\zeta$$

(21)

Substituting equations (1), (4), (6), (18) and (19) into equation (20) and equations (6), (18) and (19) into equation (21) gives

$$-2 + 2 \frac{W_1}{W} \cos\alpha = -\frac{\pi_3}{2} - \frac{R}{W} \pi_3 \left[1 - \cos\alpha - \frac{\frac{R}{W}(\sin\alpha - \alpha\cos\alpha)}{\frac{R}{W}\alpha + \frac{N}{W}} \right]$$
$$- \frac{\pi_3 \sin\alpha (\frac{N}{W})^2}{2(\frac{R}{W}\alpha + \frac{N}{W})}$$

(22)

and

$$2 \frac{W_1}{W} \sin\alpha = \pi_3 \frac{R}{W} \left[\sin\alpha - \frac{\frac{R}{W}(\cos\alpha + \alpha\sin\alpha - 1)}{\frac{R}{W}\alpha + \frac{N}{W}} \right]$$
$$+ \frac{\pi_3 \cos\alpha (\frac{N}{W})^2}{2(\frac{R}{W}\alpha + \frac{N}{W})}$$

(23)

Two geometrical relations can be obtained from Figure 79

$$\frac{1}{2} + \frac{T}{W} \sin\alpha = \frac{1}{2} \frac{W_1}{W} \cos\alpha + \frac{N}{W} \sin\alpha + \frac{R}{W}(1 - \cos\alpha) \quad (24)$$

$$\frac{x_p}{W} + \frac{T}{W} \cos\alpha + \frac{1}{2} \frac{W_1}{W} \sin\alpha = \frac{N}{W} \cos\alpha + \frac{R}{W} \sin\alpha \quad (25)$$

42

Equations (12) through (15) and equations (22) through (25) form a system of eight equations for the nine unknowns α, π_3, h/w, w_1/w, w_2/w, x_p/w, R/w, T/w and N/w. The additional equation used in solving this system of equations is $x_p/w = 0.5$. (The reason for choosing this value is given in Appendix A.) The nine equations were solved on the computer by using a program called LOPER [21] supplied by the library of the Lehigh University Computer Center. The results and comparisons with experimental results are described in Section 6.

5.2 Real Fluid Model

In this model only one control volume, which includes both the power and the control jets, is used. Referring to Figure 80, volume ABCEFGA is employed as the control volume. The section CE is at a location where the potential core of the combined jet disappears. According to the results described in Sections 3.1 and 3.7, the distance from the power nozzle exit to the location where the potential cores of the power jet with and without the control jet disappear is approximately 4.5w for the power jet Reynolds numbers (Re_w) equal to 20,000 and 12,800 and for the aspect ratio of the power jet nozzle exit of 2. The velocity distribution of the combined jet has a maximum at section CE. On the free side of the power jet the velocity distribution

43

is expected to be approximately like that of a free jet provided that the angle of deflection of the power jet is small. Simson [22] developed an empirical relation for the velocity profile of a two-dimensional free jet that can be used both in the transition region and in the fully developed region. A sketch of Simson's notation is shown in Figure 81 and the empirical relation for the velocity profile is

$$\frac{V}{V_{\ell}} = \left[1 - \left(\frac{y_e}{kx} \right)^M \right]^2 \tag{26}$$

with $k = 1.378 \ w/x_0$ and $M = 1.75$. In equation (26), V_{ℓ} is the centerline velocity, y_e is the effective value of the coordinate y for the transition zone and the actual value of y in the fully developed zone, and x is the distance downstream from the nozzle exit.

Simson's profile of a two-dimensional free jet requires that the half-width of the jet at the location where the potential core disappears be equal to 1.378 w. The experimental result of the present investigation with an aspect ratio of the power jet nozzle exit of 2 and the power jet Reynolds number of 20,000 shows that the half-width of the power jet is approximately equal to 1.75 w at the location where the potential core disappears. If 1.75 w is used as the half-width of the free jet at x_0, then the constant M

44

in equation (26) has to change to another value. Since the momentum is conserved, then

$$\frac{J}{J_0} = \frac{\int_0^{1.75\,w/x_0} V^2 dy}{U_0^2 w} = 1 \qquad (27)$$

where J is the momentum of the jet at x_0 and J_0 is the momentum of the free jet at the exit of the nozzle. Equation (27) gives M = 1.3615 (the numerical calculations are given in Appendix B). If V_1 denotes the jet velocity corresponding to the free-side portion of the power jet, then

$$\frac{V_1}{V_0} = \left[1 - \left(\frac{z'}{Y} \right)^{1.3615} \right]^2 \qquad (28)$$

where V_0 is the maximum potential core velocity of the combined jet, z' is a dummy variable and Y = 1.75 w is the part-width of the combined jet on the free side as shown in Figure 80.

The velocity at section CE on the control jet side of the combined jet is denoted by V_2. Its variation across the jet is assumed to be in the same form as that of velocity V_1. That is

$$\frac{V_2}{V_0} = \left[1 - \left(\frac{z''}{Z} \right)^{1.3615} \right]^2 \qquad (29)$$

where z" is a dummy variable and Z is the unknown part-width

45

of the combined jet as shown in Figure 80.

The following expressions for the pressure distribution and flow speeds are used:

$$P_{AB} - P_a = (P_c - P_a)(1 - \frac{y}{w}) \tag{30}$$

$$P_{AG} - P_a = P_c - P_a \tag{31}$$

$$P_{GF} - P_a = (P_c - P_a)(1 - \frac{x}{w_c}) \tag{32}$$

$$V_{AB} = [\frac{2}{\rho}(P_{ts} - P_{AB})]^{1/2}$$

$$= \{\frac{2}{\rho}[(P_{ts} - P_a) - (P_c - P_a)(1 - \frac{y}{w})]\}^{1/2} \tag{33}$$

$$V_{GF} = [\frac{2}{\rho}(P_{tc} - P_{GF})]^{1/2}$$

$$= \{\frac{2}{\rho}[(P_{tc} - P_a) - (P_c - P_a)(1 - \frac{x}{w_c})]\}^{1/2} \tag{34}$$

where P_c is the constant pressure along the setback wall in the separated flow zone.

The maximum velocity of the potential core of the combined jet, V_o, is related to the supply pressure of the power jet by the following equation,

$$V_o = [\frac{2}{\rho}(P_{ts} - P_a)]^{1/2} \tag{35}$$

Equation (35) is employed here in view of the finding that the maximum velocity of the combined jet increases with

46

increasing control jet supply pressure due to the corresponding increase of the supply pressure of the power jet. This effect was described in Section 4.6.

The momentum equations in the x and y directions for the control volume ABCEFGA are,

$$- \rho \int_0^W V_{AB}^2 dy + \rho \cos\alpha \int_0^Y V_1^2 dz' + \rho \cos\alpha \int_0^Z V_2^2 dz''$$

$$= \int_0^W (P_{AB} - P_a) dy + \int_{-(s+h)}^0 (P_{AG} - P_a) dy - \int_0^{W_c} (P_{GF} - P_a) \frac{h}{W_c} dx$$

$$(36)$$

and

$$\rho \sin\alpha \int_0^Y V_1^2 dz' + \rho \sin\alpha \int_0^Z V_2^2 dz'' - \rho \int_0^{W_c} V_{GF}^2 dx$$

$$= \int_0^{W_c} (P_{GF} - P_a) dx \qquad (37)$$

The continuity equation is

$$\rho \int_0^W V_{AB} dy + \rho \int_0^{W_c} V_{GF} dx + \rho(E_1 + E_2)$$

$$= \rho \int_0^Y V_1 dz' + \rho \int_0^Z V_2 dz'' \qquad (38)$$

47

where E_1 and E_2 are the volumetric entrainment rates on the free side and control jet side of the combined jet.

The volumetric flow for a free jet using equation (26) with M = 1.3615 is given by

$$\frac{Q}{Q_0} = 1 + 0.47588 \frac{x}{x_0} \tag{39}$$

(Detailed calculations are given in Appendix B.) The volumetric entrainment rate is therefore given by

$$E = Q - Q_0 = 0.47588 \frac{x}{x_0} Q_0 \tag{40}$$

At $x = x_0$,

$$E = 0.47588 \, Q_0 \tag{41}$$

where Q_0 is the volumetric flow rate of the jet leaving the nozzle and Q is that of the jet at any location x in the transition zone. In the present model, the following relation is assumed for the entrainment rate on the free power jet side of the combined jet at the location where the potential core disappears,

$$E_1 = (\frac{1}{2})(0.47588) \int_0^W V_{AB} dy \tag{42}$$

The expression for the entrainment rate on the control jet side of the combined jet at the location where the potential core disappears is assumed to be in the following form:

48

$$E_2 = \left(\frac{1}{2}\right)(0.47588)\left(\frac{4.5w - w_c}{4.5w}\right) K_1 \left(\int_0^w V_{AB} dy + \int_0^{w_c} V_{GF} dx\right)$$

(43)

where K_1 is an entrainment coefficient to be calculated using experimental data.

Substituting equations (28) through (35) into equations (36) and (37) gives

$$-2 + \frac{\pi_4}{2} + 2\cos\alpha\left(\frac{Y}{w} + \frac{Z}{w}\right)(0.28619) = \pi_4\left(\frac{S}{w} + \frac{1}{2}\frac{h}{w}\right)$$

(44)

and

$$2\sin\alpha\left(\frac{Y}{w} + \frac{Z}{w}\right)(0.28619) = 2\pi_2 \frac{w_c}{w} - \frac{1}{2}\frac{w_c}{w}\pi_4$$

(45)

where

$$\pi_4 = \frac{P_c - P_a}{P_{ts} - P_a}$$

Substituting equations (28), (29), (33), (34), (42) and (43) into equation (38) gives

$$1.2379 \pi_5 + \pi_6 + 0.05287\left(4.5 - \frac{w_c}{w}\right) K_1 (\pi_5 + \pi_6)$$

$$= \left(\frac{Y}{w} + \frac{Z}{w}\right)(0.42168)$$

(46)

where

$$\pi_5 = \frac{2}{3}\frac{[1 - (1 - \pi_4)^{3/2}]}{\pi_4}$$

(47)

$$\pi_6 = \frac{2}{3}\frac{w_c}{w}\pi_2^{3/2}\frac{[1 - (1 - \pi_4/\pi_2)^{3/2}]}{\pi_4}$$

(48)

and

$$Y = 1.75 \, w$$

(49)

49

Equations (44), (45) and (46) express the variables
α, π_4, h/w, Z/w and K_1 as functions of w_c/w, s/w and π_2.
Thus there are five unknowns and only three equations. Two
of the five unknowns must be determined empirically. It has
been decided to use the experimentally-determined values of
the dimensionless separation distance h/w and the dimension-
less pressure in the separated-flow zone π_4/π_2 and to cal-
culate from equations (44), (45) and (46) the angle of
deflection α, the dimensionless combined jet part-width Z/w,
and the control jet side entrainment coefficient K_1. The
values of the dimensionless separation distance h/w are
taken from Table 2 of Section 4.5.

The reason why the ratio $(\pi_4/\pi_2) = (P_c - P_a)/(P_{tc} - P_a)$
rather than the ratio $\pi_4 = (P_c - P_a)/(P_{ts} - P_a)$ was chosen
to be used as an empirical relation in the calculations is
because, for the relatively weak control flows, the ratio
π_4/π_2 is independent of the pressure ratio π_2 and is only a
function of geometry (setback and control nozzle width).
This is so because the power jet acts almost like a vertical
wall as far as the separation region is concerned. Figure
82 verifies the fact that, in the range of the power and
control jet supply pressures used, the ratio π_4/π_2 depends
only on the geometry.

Table 4 gives the empirical values of the dimensionless
pressure π_4/π_2 for various values of dimensionless setback

50

s/w and dimensionless control nozzle width w_c/w.

Table 4.   Empirically-determined values
of the dimensionless pressure ratio π_4/π_2

$\begin{matrix} & s/w \\ w_c/w & \end{matrix}$	1	$\frac{1}{2}$
1	0.692	0.85
$\frac{1}{2}$	0.41	0.61

The results of Table 4 are plotted in Figure 83.

The results of the calculations and a comparison with
the experiments are presented in the next section.

6.   RESULTS OF CONTROL VOLUME ANALYSIS AND COMPARISON
     WITH EXPERIMENTS

In this section, the results of the control volume
analysis are presented and compared with the experimental
results.

6.1 Angles of Deflection

Figures 84 to 87 show comparisons of the results obtained from the ideal fluid model and from the real fluid model with the experimental results obtained in the present investigation. Also shown in those figures are the results obtained by using a simple momentum balance. The experimental results obtained by Gungor [8] and Weeks [9] for two jets interaction were expressed in terms of the velocity ratio of the control and power jets obtained from flow rate measurements. Since the pressures at the power and control nozzle exits are not atmospheric and are not known, their experimentally-determined values of the angle of deflection cannot be compared with the results obtained in the present investigation. The only experimental results that are comparable with the present investigation are those obtained by Bourque [12]. His results were obtained for $w_c/w = 1$ and various values of setback and showed that the angles of deflection were independent of the values of setback. Therefore only one set of data for $w_c/w = 1$ and $s/w = 1$ from Bourque's results is plotted in Figure 84. The difference between the results obtained by Bourque and those of the present investigation is most likely due to the effect of the aspect ratio. Bourque used an aspect ratio of the power nozzle exit of 12 in his test while the corresponding aspect ratio in the present investigation was 2. The effect of

52

resistance (shearing stress) caused by the bounding walls is relatively smaller for a large aspect ratio jet than for a small aspect ratio jet. This explains why the angle of deflection obtained by Bourque is always higher than that obtained in the present investigation.

From an inspection of Figures 84 to 87, one can tell that, in general, the real fluid model gives the best agreement with experiments. The ideal fluid model agrees with the experiments fairly well at small values of the dimensionless pressure π_2 and deviates from the experimental values at higher values of π_2. The angles of deflection calculated from the ideal fluid model are always smaller than the experimentally determined values. The calculated results by using simple momentum balance deviate most from the experiments and are always substantially higher than the experimentally determined values. As described in Section 4.4, simple momentum analysis neglects the effect of the pressure difference across the power jet before it meets the control jet and it also neglects the fact that the control jet does not meet the power jet until the control jet has already turned through a large angle at the separation zone near the setback wall. The errors introduced by neglecting these two factors partially compensate each other. However, the fact that the angles of deflection calculated by using simple momentum balance are always higher than the

53

experimentally-determined values indicates that the effect
of neglecting the separation of the control jet is more
severe than the effect of neglecting the pressure difference
across the power jet. In other words, one overestimates the
angle of deflection a great deal by using the momentum of
the control jet in its initial direction.

Since the other variables used in the ideal fluid model
differ from those of the real fluid model, they are pre-
sented separately.

6.2 Results Obtained from the Ideal Fluid Model

Figure 88 shows the calculated dimensionless width w_1/w
of the power jet at the section where the pressure is uni-
form across and equal to the atmospheric pressure. It shows
that this dimensionless width is always less than unity.
This can be considered to represent the pinching effect on
the power jet caused by the control jet reported by Moynihan
and Reilly [3], Douglas and Neve [5], Weeks [9] and Sarpkaya
et al [11]. This pinching effect becomes more and more
severe as the control flow is increased. Figure 88 also
shows that the ideal fluid model predicts that the ratio
w_1/w depends on the control nozzle width ratio w_c/w only and
is independent of the value of dimensionless setback s/w.

Figure 89 shows the calculated width of the control jet

54

at the section where the pressure is uniform across the combined jet and equal to the atmospheric pressure. The result follows directly from equation (13) in Section 5.1, which shows that w_2/w increases with w_c/w and is independent of s/w and π_2.

Figure 90 shows the calculated radius of curvature of the power jet. The values of the dimensionless radius R/w are independent of the setback and decrease with increasing dimensionless pressure π_2. This means that, as expected, the power jet is deflected more rapidly when the control jet flow is increased.

Figure 91 shows the variation of the calculated dimensionless separation distance h/w with π_2 for different values of setback and width of the control jet nozzle. It shows that for fixed control nozzle width ratio w_c/w and fixed setback ratio s/w, the dimensionless separation distance h/w varies only slightly with dimensionless pressure π_2. However, a comparison of the results shown in Figure 91 with those of Table 2 in Section 4.5 shows that the agreement is not satisfactory.

Figure 92 shows the plot of the calculated dimensionless distance T/w versus dimensionless pressure π_2 for different values of setback and width of the control jet nozzle. It shows that the dimensionless distance T/w varies

only slightly with dimensionless setback, width of the con-
trol jet nozzle, and dimensionless pressure π_2. As Figure
79 shows, the value of $(x_p + T)$ represents approximately the
distance downstream from the exit of the power jet nozzle
at which the pressure becomes uniform across the combined
jet and equal to the atmospheric pressure (section CE). If
one chooses 1.2w as an average value for T and adds 0.5w,
which represents an approximate value of the x-coordinate
of the pivot point, then $(x_p + T)$ equals 1.7w. As stated in
Section 4.7 the value of the distance downstream from the
power jet nozzle exit where the pressure becomes uniform
across the combined jet is estimated from experiments to be
approximately 2.5w. Hence we may conclude that the agree-
ment with the ideal fluid model is not very good.

Figure 93 shows two comparisons of the calculated and
experimentally-determined pressure distribution in the
vicinity of the setback wall. The agreement again is poor.

6.3 Results Obtained from the Real Fluid Model

As was mentioned in Section 5.2, the real fluid model
makes use of the experimentally-determined variation of the
dimensionless separation distance h/w and dimensionless
pressure ratio π_4/π_2 and allows calculation of the entrain-
ment coefficient K_1, of the dimensionless part-width of the
combined jet at the location where the potential core

56

disappears, Z/w, and of the velocity distribution at that location in addition to the angle of deflection.

Figure 94 shows the calculated variation of the entrainment coefficient on the control jet side of the combined jet with dimensionless pressure π_2 for various values of dimensionless setback and width of the control jet nozzle. It shows that the coefficient K_1 depends only slightly on the values of setback for a fixed value of the width of control jet nozzle. For a fixed value of setback, the coefficient K_1 is less for larger values of the control jet nozzle width than for small values. Qualitatively speaking, entrainment depends on the velocity gradient in such a way that larger velocity gradient entrains more surrounding fluid. The width of the control jet before it mixes with the power jet depends strongly on the width of the control jet nozzle. If the width of the control jet nozzle is fixed, then the width of the control jet before it mixes with the power jet for $s/w = 1$ does not differ very much from that of the control jet for $s/w = 1/2$ and the intensity of the entrainment process does not differ much in these two cases. If the value of the setback is fixed and the width of the control jet nozzle varies, then a large control jet nozzle width produces thicker control jet than a narrow control jet nozzle. The thinner control jet merges with the power jet faster and therefore the combined jet

57

begins to entrain the surrounding fluid earlier than in the case when the control jet is thick. If in both cases the combined jets travel the same distance, then in the case of a wide control jet nozzle less fluid is entrained than in the case of a narrow control jet nozzle because the control jet velocity is much smaller than the velocity of the power jet.

Figure 95 shows the calculated variations of the dimensionless combined jet part-width at the location where the potential core disappears, Z/w, for various values of the dimensionless setback, width of the control jet nozzle, and dimensionless pressure π_2. It shows that the ratio Z/w increases with increasing value of π_2 (it therefore also increases with increasing control flow for a given power jet flow) and with increasing values of the setback and width of the control jet nozzle.

Figures 96 to 99 show several comparisons of the measured velocity distribution with that obtained from equations (28) and (29) described in Section 5.2 together with the values of the combined jet part-width Z calculated in this section. It shows that the calculated velocity profile predicts lower flow speeds than measured near the center and higher flow speeds than measured near the outer region of the combined jet. This means that while with the assumed velocity profile we are estimating correctly the flow rate,

58

we underestimate the linear momentum of the combined jet because we underestimate the velocity in the high velocity region. Also shown in Figures 96 to 99 is the Simson's profile for a two-dimensional free jet. Simson's profile underestimates the velocity in the outer region of the jet.

6.4   Summary of the Control Volume Analysis

A.   The ideal fluid model predicts fairly well the measured angle of deflection. However, other parameters are not predicted satisfactorily.

B.   The real fluid model, which makes use of empirical information concerning the location of the separation point of the control jet from the setback wall and of the pressure in the separated flow zone, predicts very well the measured angle of deflection of the power jet. It also allows calculation of the entrainment coefficient of the combined jet on the control jet side and of the velocity profile of the combined jet at the location where the potential core disappears.

7.   CONCLUSIONS AND SUGGESTIONS FOR FUTURE RESEARCH

The results of the present investigation are summarized in Sections 4.8 and 6.4. They show that an understanding of

59

the process of jet interaction is necessary before an
attempt can be made to analytically predict the angle of
deflection of the power jet. The control volume employed
in the present investigation proved to be very successful
in predicting the angles of deflection as a function of
setback, control port width and the ratio of the supply
pressure of the control jet to that of the power jet.

Suggestions for possible areas of research in the
future are described below.

(A) Flow visualization study of the process of separation
     of the control jet should be made to determine more
     accurately the location of the separation point on the
     setback wall. This information is needed to improve
     the real fluid model employed in the present investi-
     gation.

(B) An analytical model that is able to predict the sepa-
     ration of the control jet and to determine the pressure
     in the separated flow zone is essential to predict the
     angles of deflection of the power jet and should be
     developed. A model employing the frozen vorticity
     theory to predict the general nature of the flow sepa-
     ration of a turbulent boundary layer ahead of a normal
     step reported by Taulbee and Robertson [23] may repre-
     sent a proper approach to this problem.

60

(C) An experimental study should be made of the entrainment process and of the effect of curvature of the control jet on entrainment rate.

(D) An experimental study should be made of the effect of aspect ratio on the interaction process and on the development of the combined jet.

(E) The present analysis should be extended to the case of interaction of two jets with arbitrary angle between them.

(F) Experimental investigation should be extended to the case of interaction of three jets.
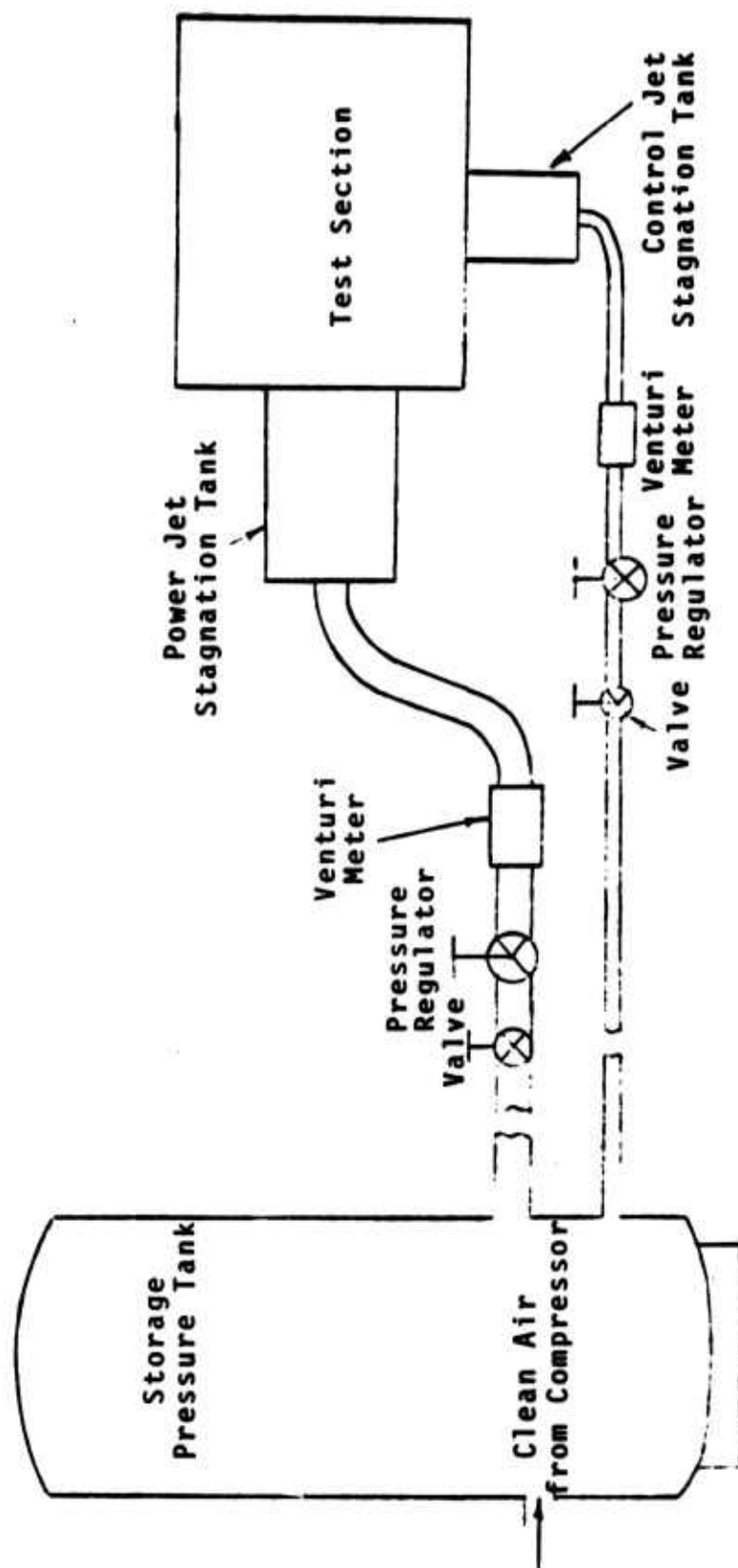
Figure 1 - A Sketch of Test Rig.
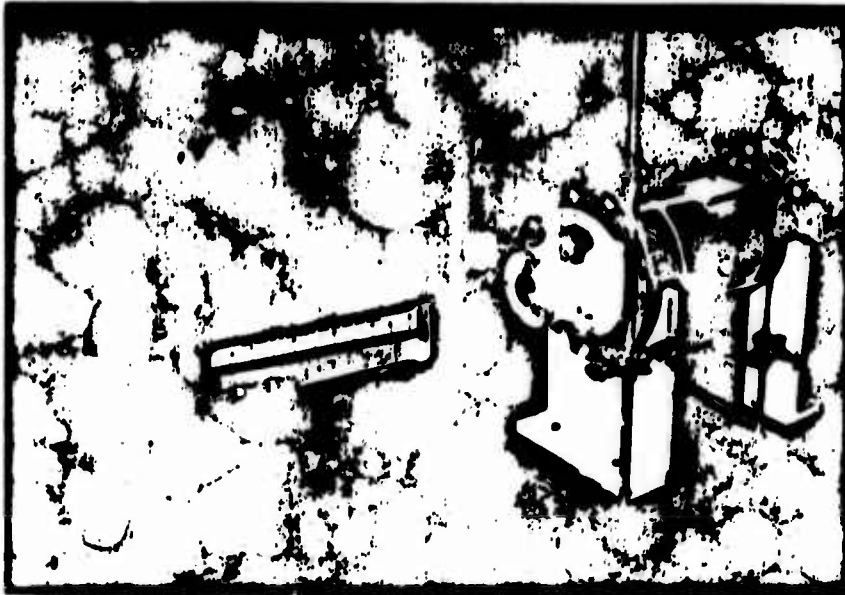
Figure 2a - Photograph of the Nozzle and the Manometer Used in Calibration.
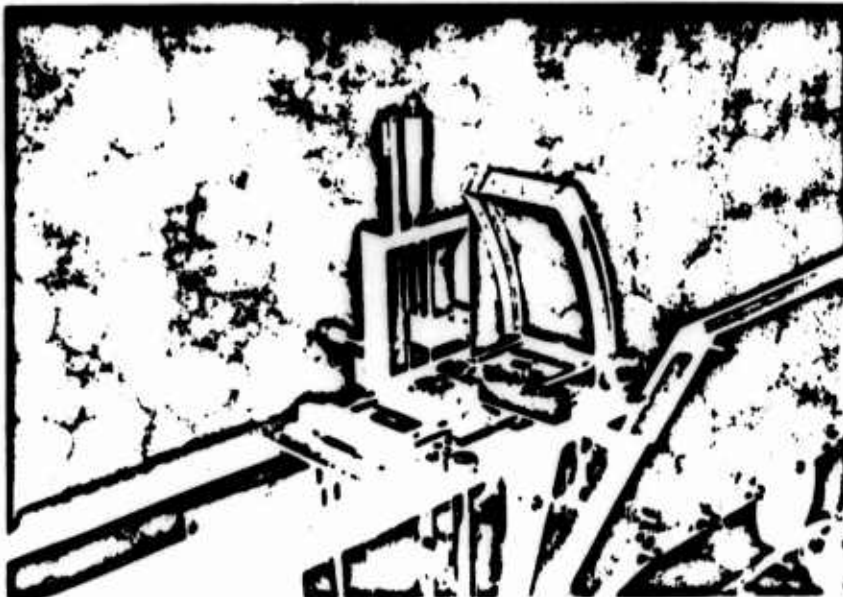
Figure 2b - Photograph of the Traversing Mechanism.

63

Re_w

2×10^4

10^4
8×10^3

6×10^3

4×10^3

2×10^3

10^3

0   5   10   15   20 ΔP,in.Hg

Venturi Meter for the
Power Jet Nozzle

Venturi Meter for the
Control Jet Nozzle
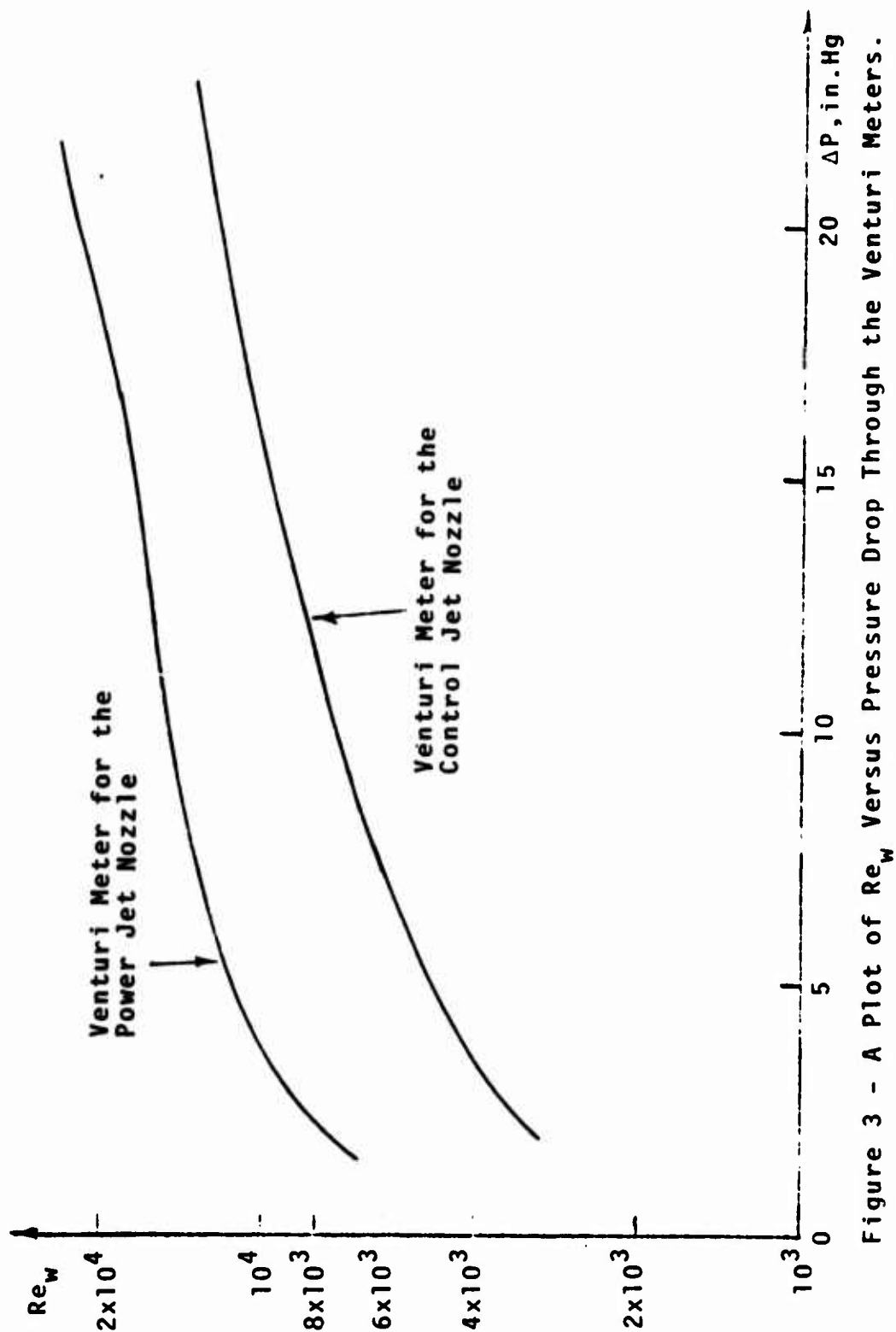
Figure 3 - A Plot of Re_w Versus Pressure Drop Through the Venturi Meters.
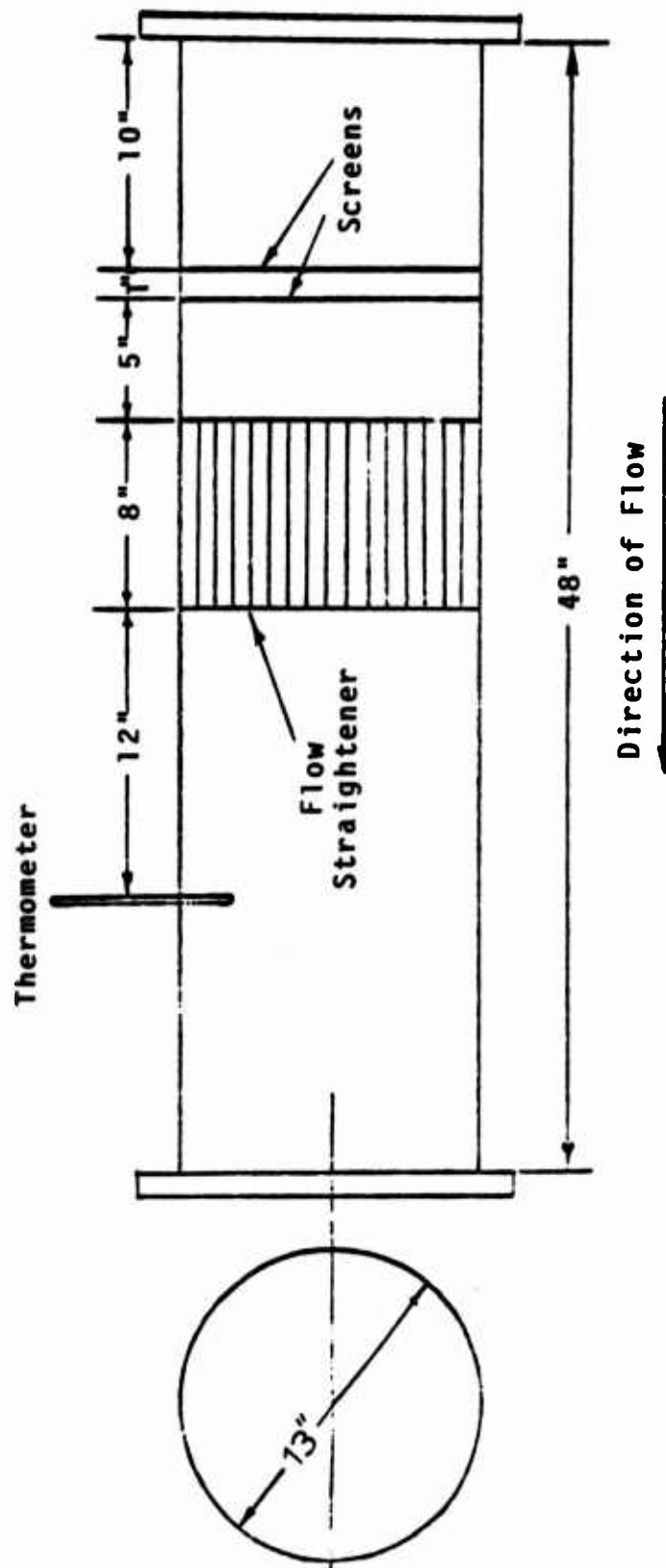
Figure 4 - A Sketch of the Dimensions of the Power Jet Stagnation Tank.
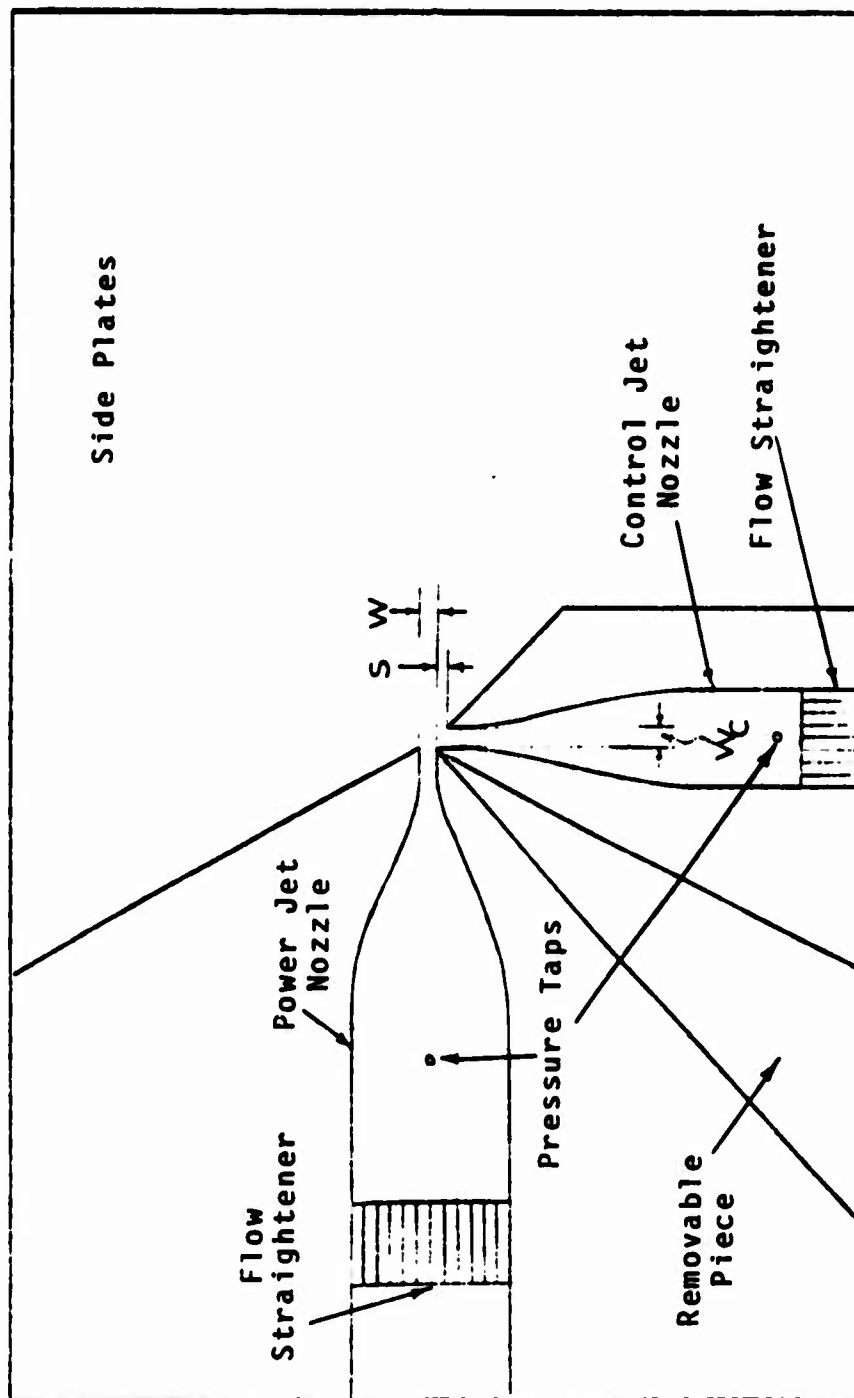
Figure 5 - A Sketch of the Test Section.

66
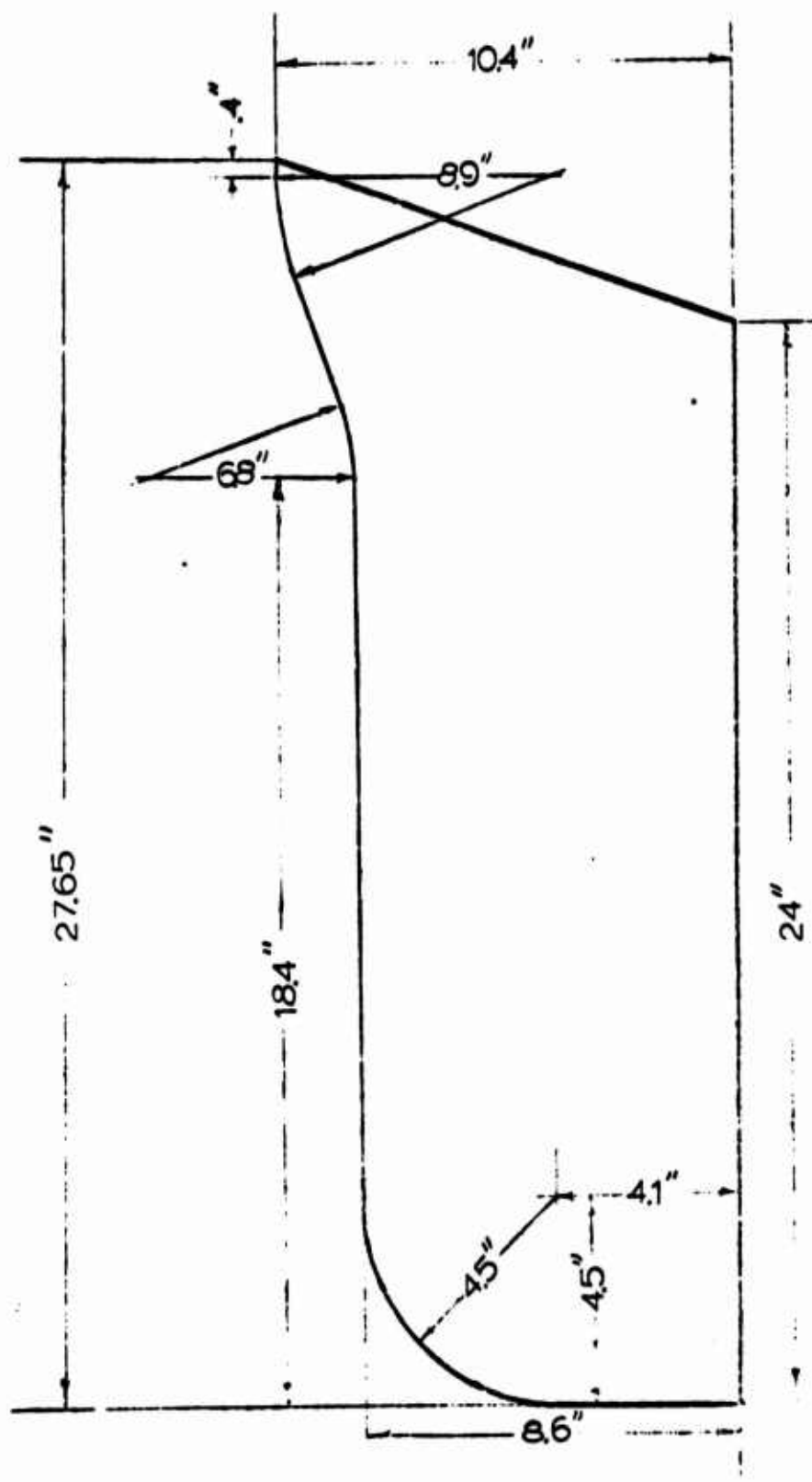
Figure 6 - A Sketch of the Dimensions of the Power Jet Nozzle Piece.
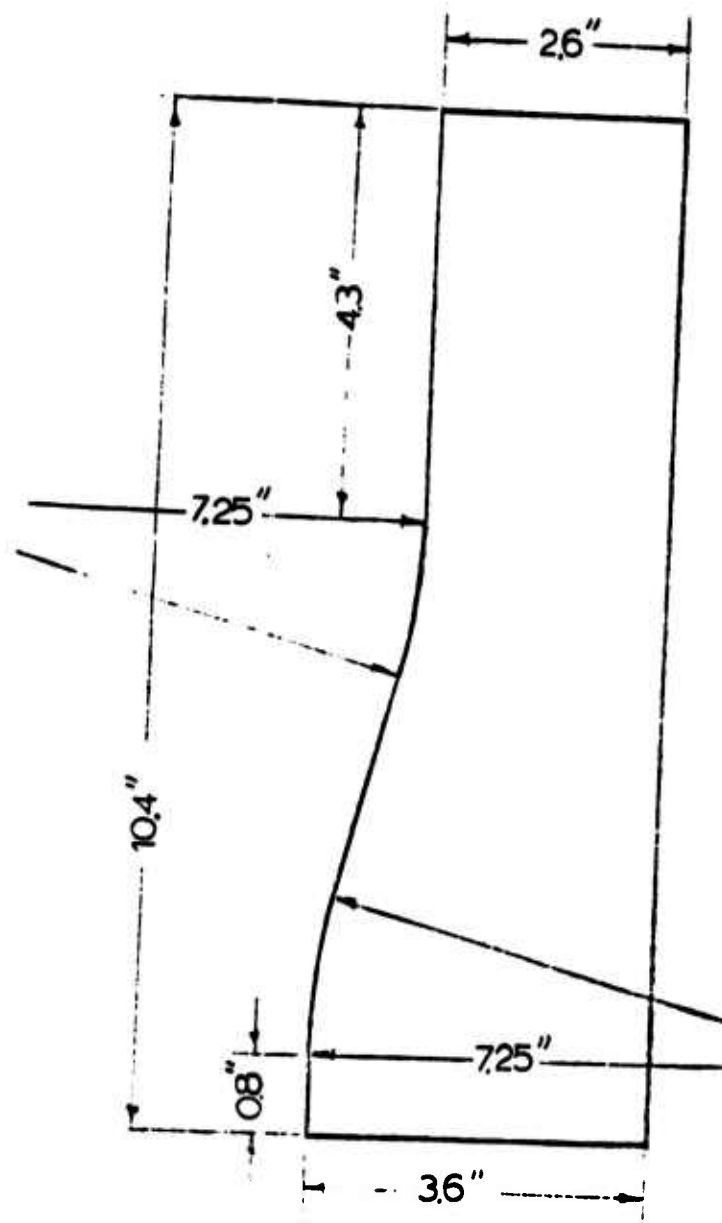
Figure 7 - A Sketch of the Dimensions of the Control Jet Nozzle Piece.
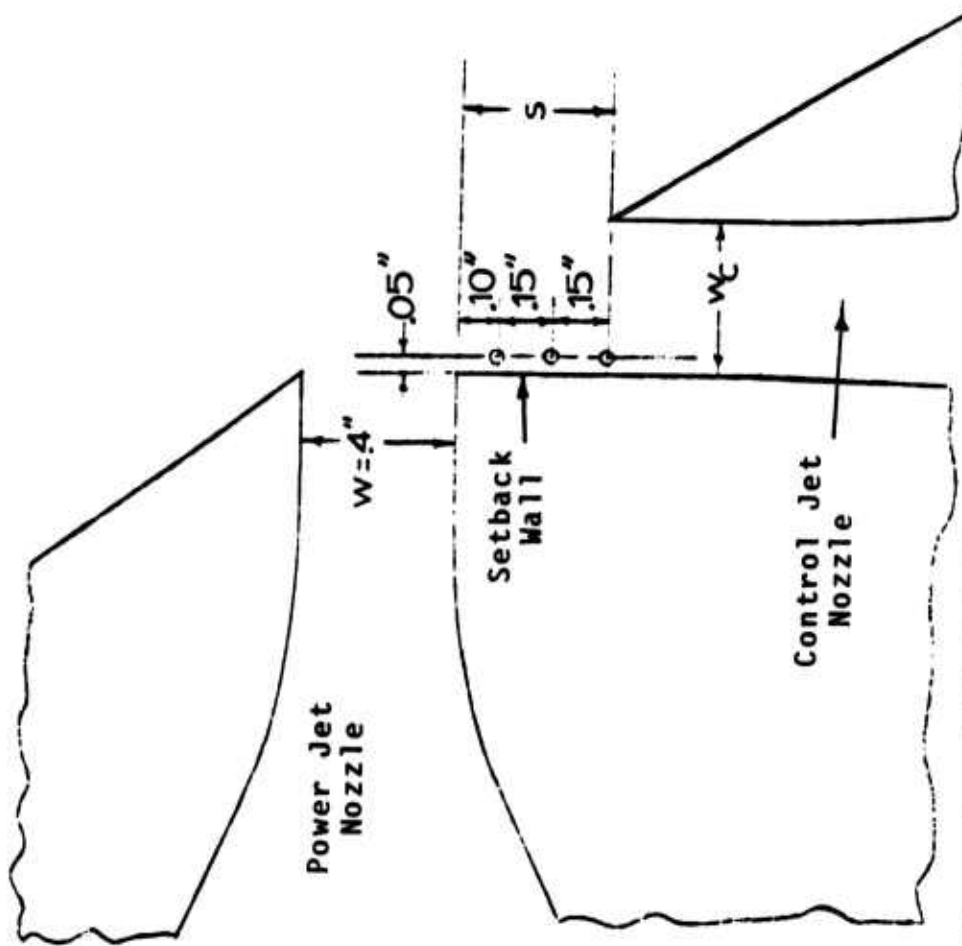
Figure 8 - A Sketch Showing the Locations of the Pressure Taps Near the Setback Wall.
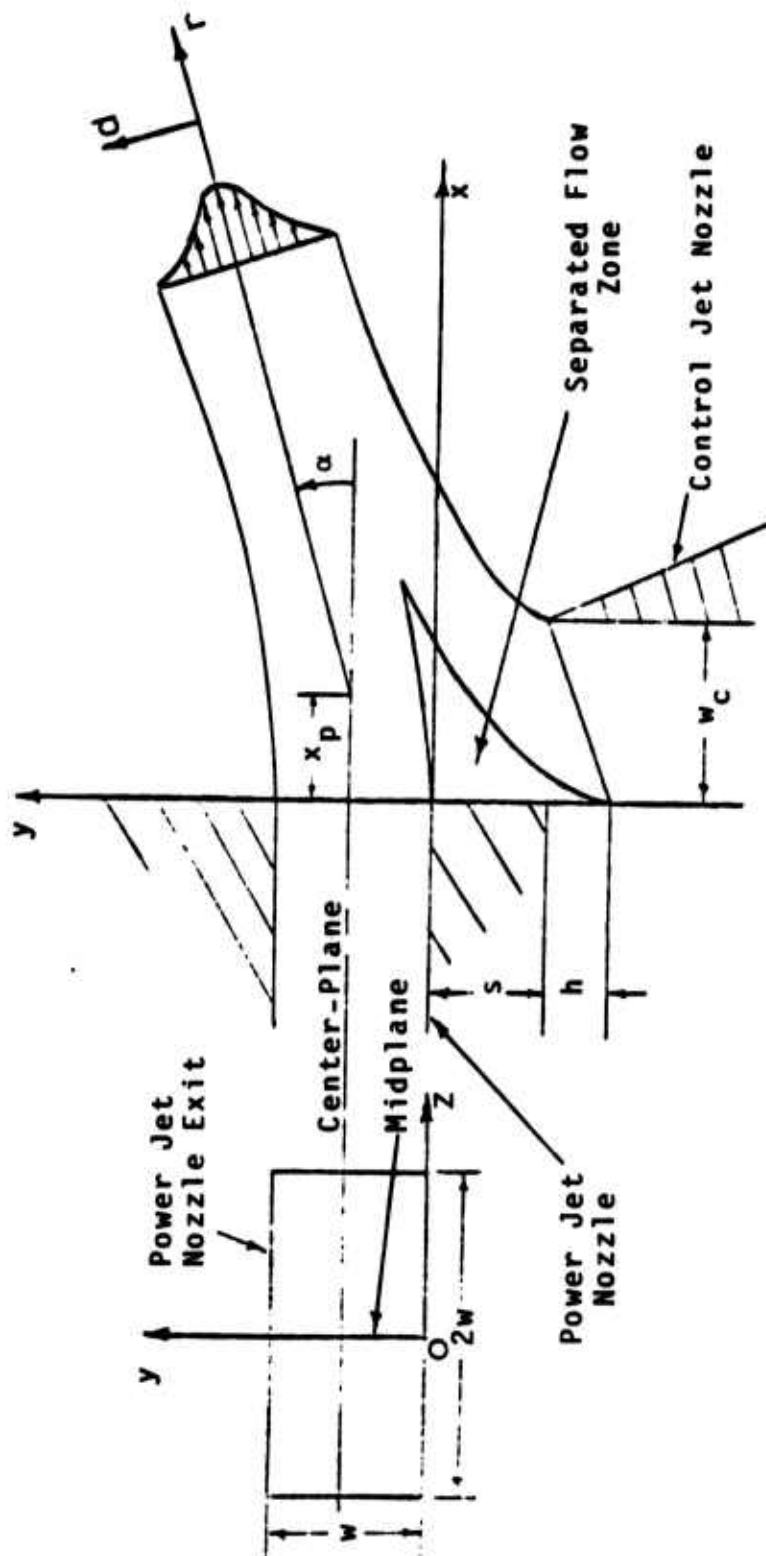
Figure 9 - A Sketch of the Coordinate Systems Used in the Present Study.

70
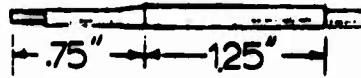
DISA 55F31 General-Purpose
Type Probe with Wire Length
of 1.25 mm and Wire Diameter
of 5 µm.

(a)

DISA 55F35 Right-Angle Type
Probe with Wire Length of
1.25 mm and Wire Diameter
of 5 µm.

(b)

Figure 10 - A Sketch of the
Two Hot Wire Probes Used in
the Velocity and Turbulence
Intensity Measurements.

71

17"

0.25"

0.1875"

1.0"

0.125"

10"

0.8"

0.0625"

0.5"

0.10"
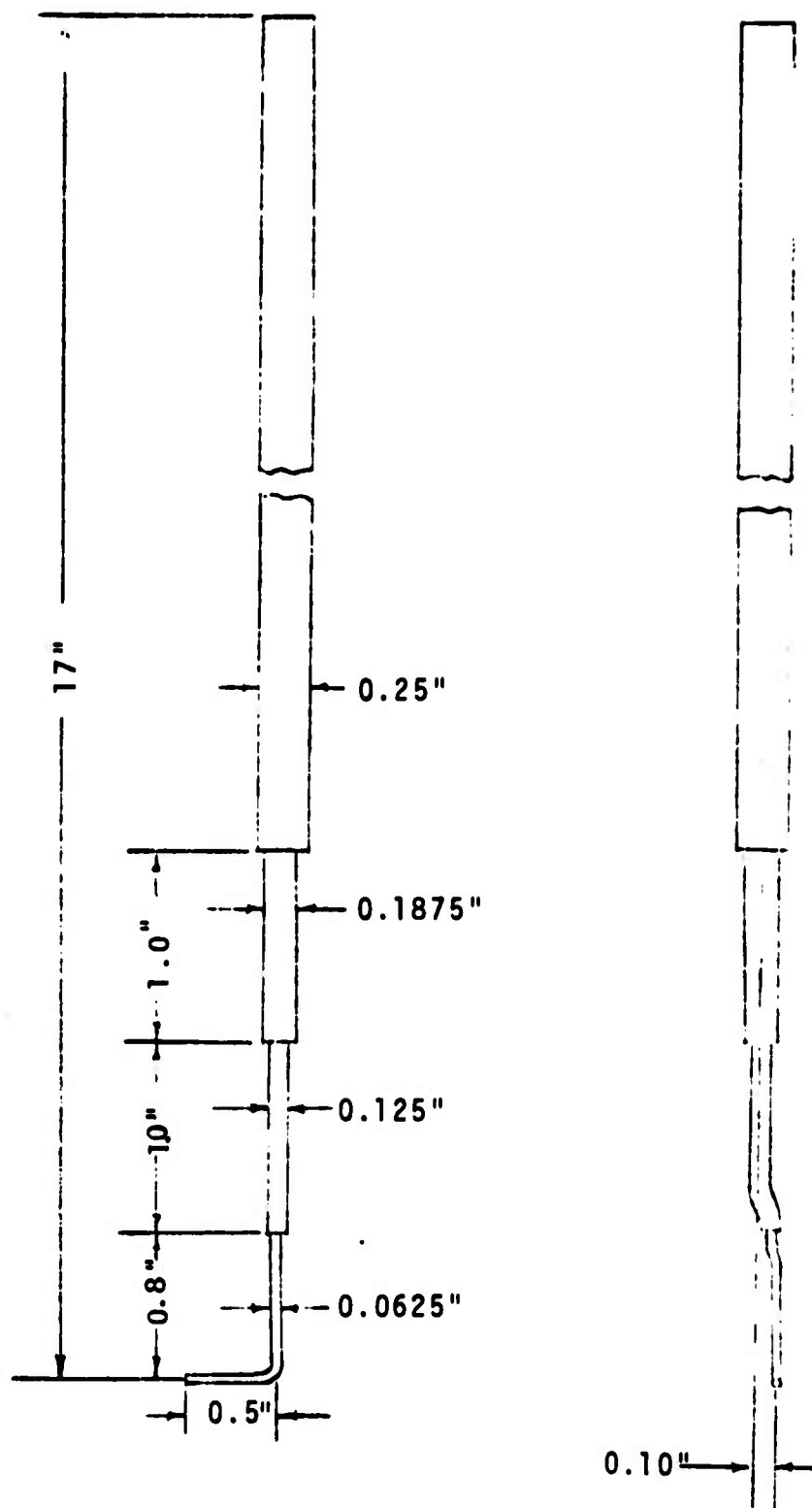
Figure 11 - A Sketch of the Total Pressure Probe.

72
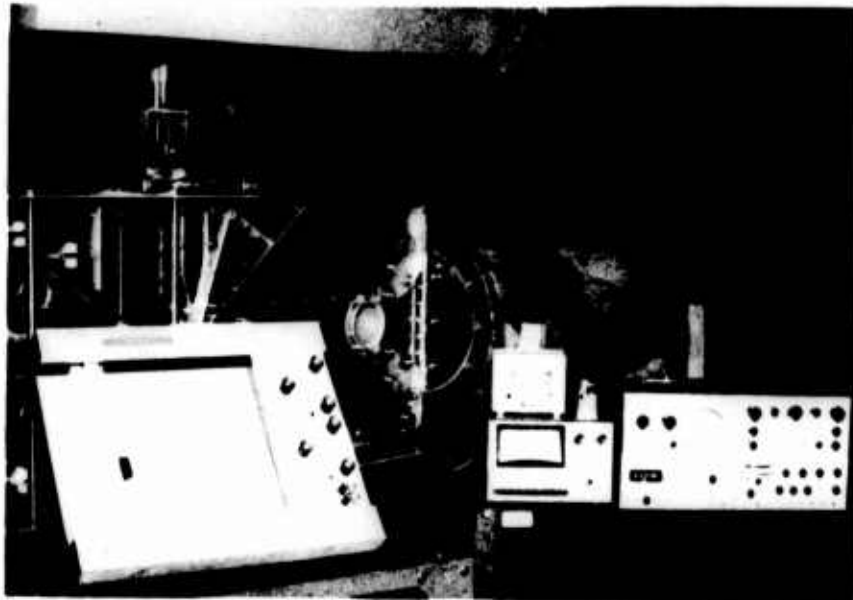
Figure 12 - A Photograph Showing the Test
Rig, the Experimental Equipment and the
Traversing Mechanism.
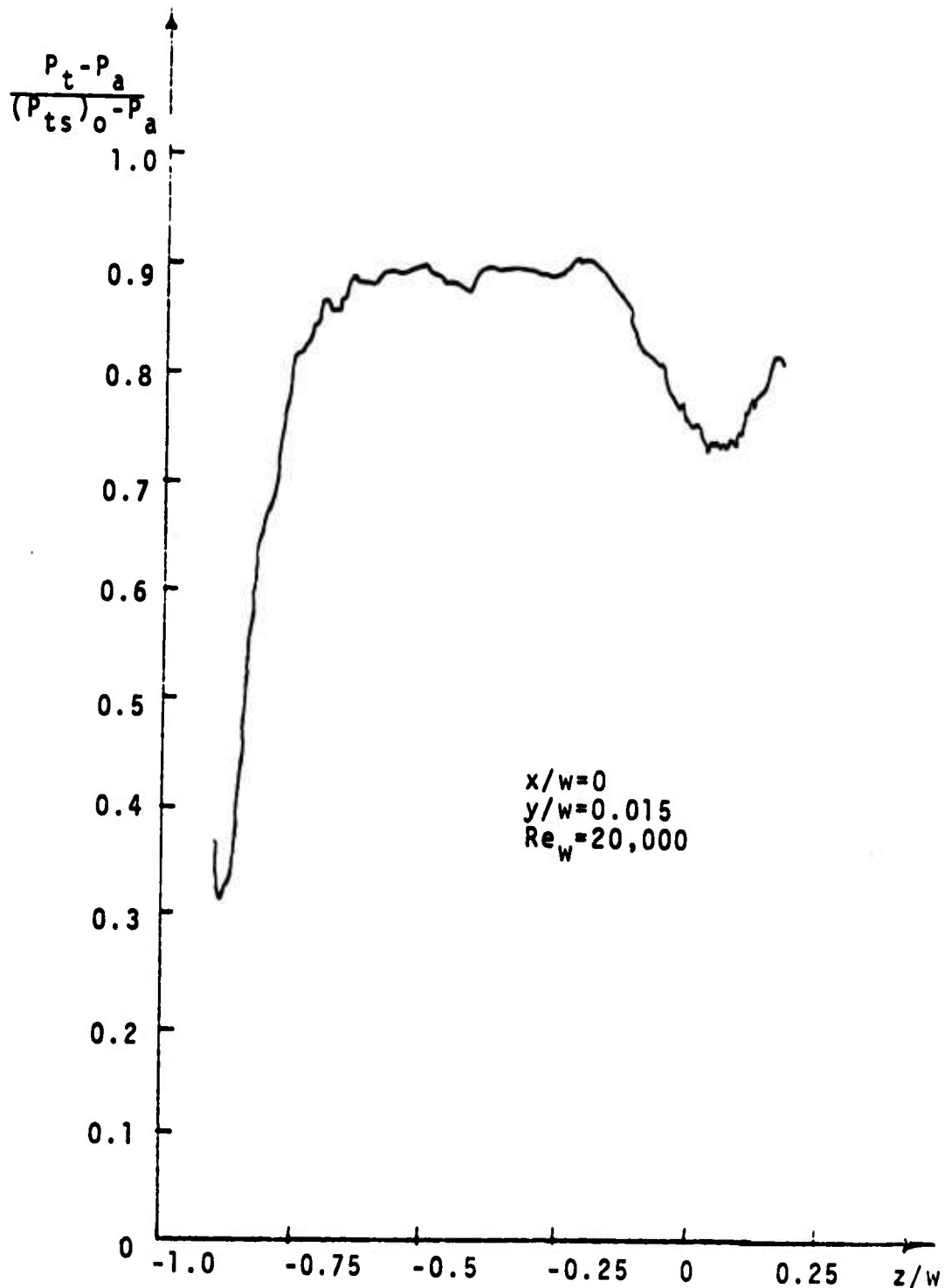
Figure 13 - Total Pressure Variation in the
Direction Normal to the Bounding Side Plates
for Power Jet without Flow Straightener.

74
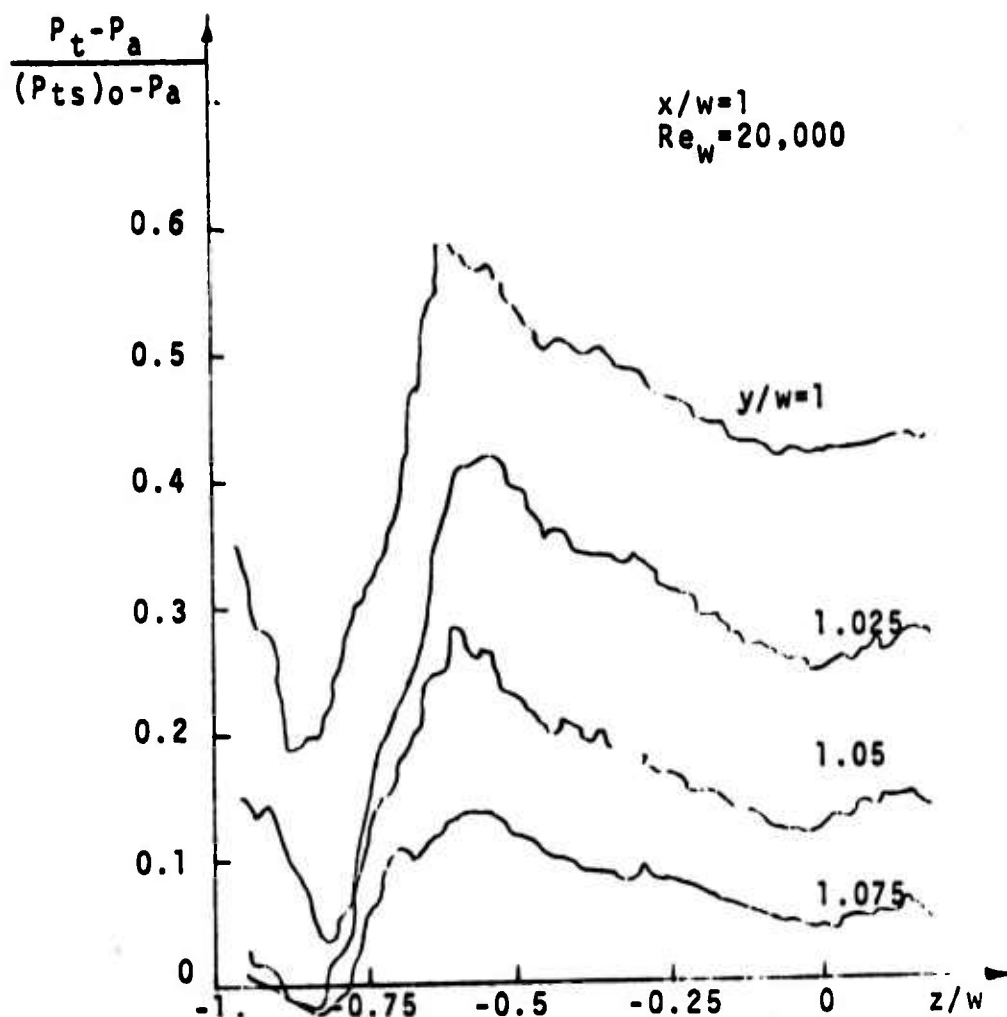
Figure 14 - Total Pressure Variation in the
Direction Normal to the Bounding Side Plates
for Power Jet Without Flow Straightener.

75
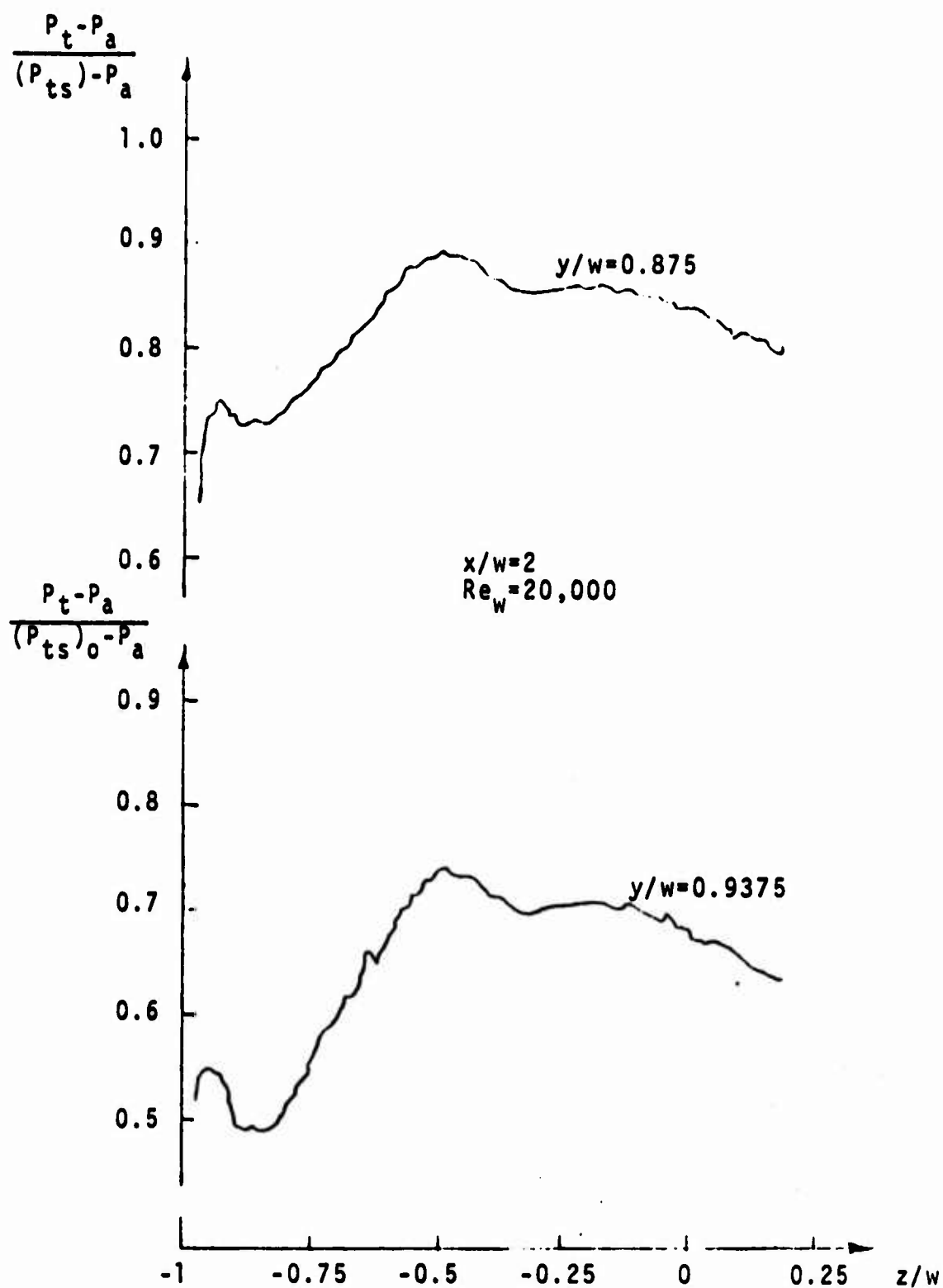
Figure 15 - Total Pressure Variation in the
Direction Normal to the Bounding Side Plates
for Power Jet Without Flow Straightener.

76
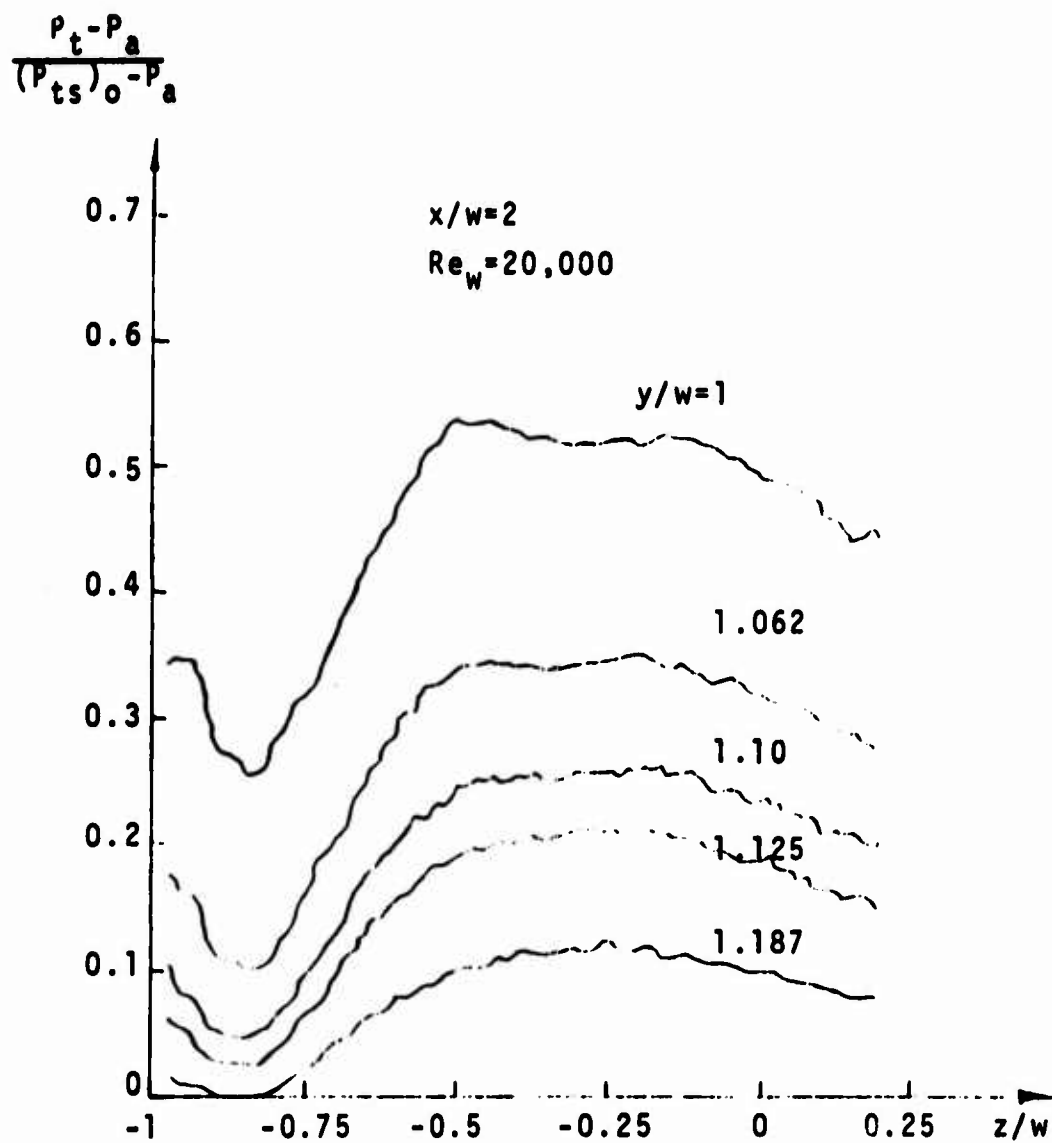
Figure 16 - Total Pressure Variation in the
Direction Normal to the Bounding Side Plates
for Power Jet Without Flow Straightener.
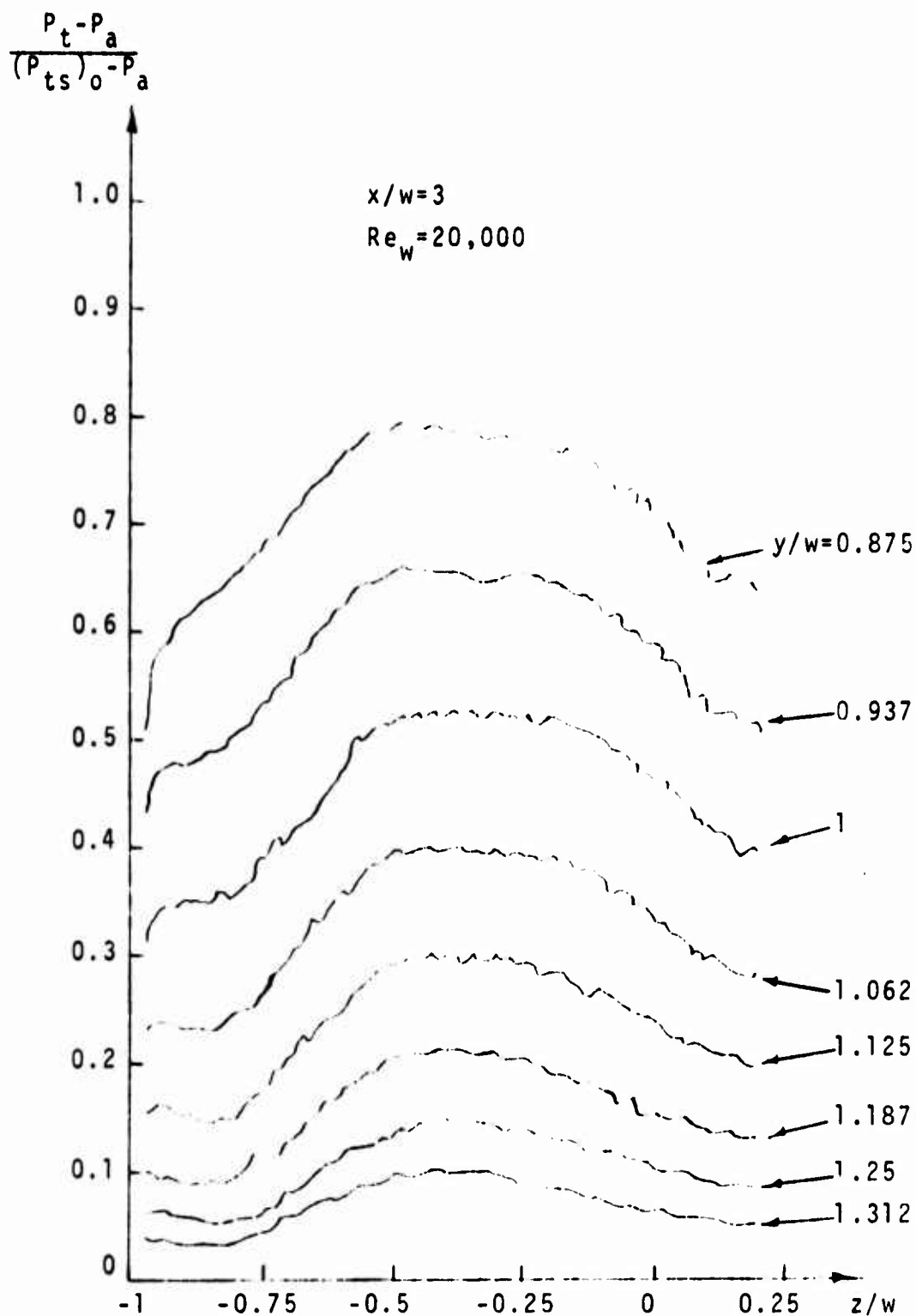
Figure 17 - Total Pressure Variation in the Direction Normal to the Bounding Side Plates for Power Jet Without Flow Straightener.

78
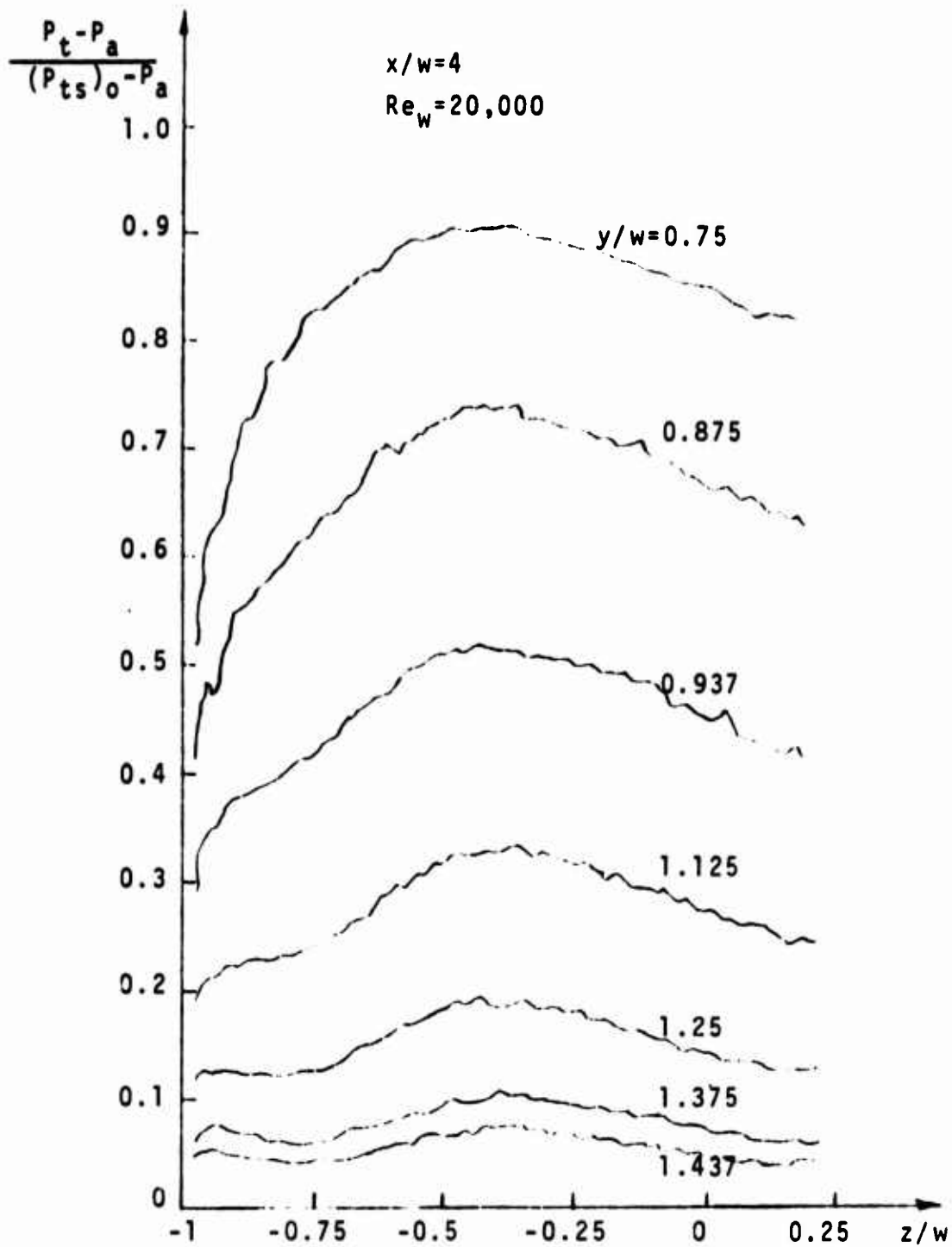
Figure 18 - Total Pressure Variation in the Direction Normal to the Bounding Side Plates for Power Jet Without Flow Straightener.
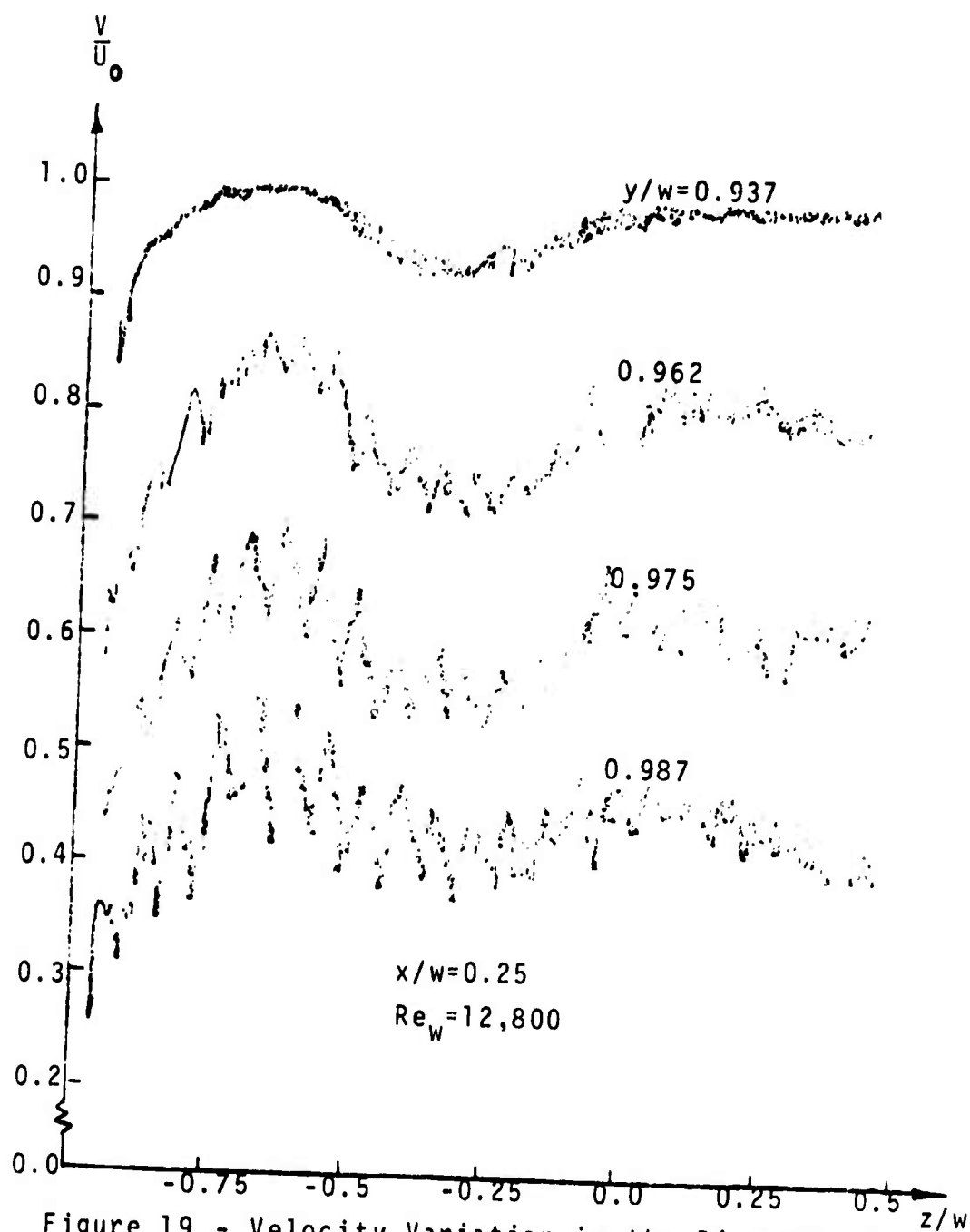
Figure 19 - Velocity Variation in the Direction Normal to the Bounding Side Plates for Power Jet Without Flow Straightener.
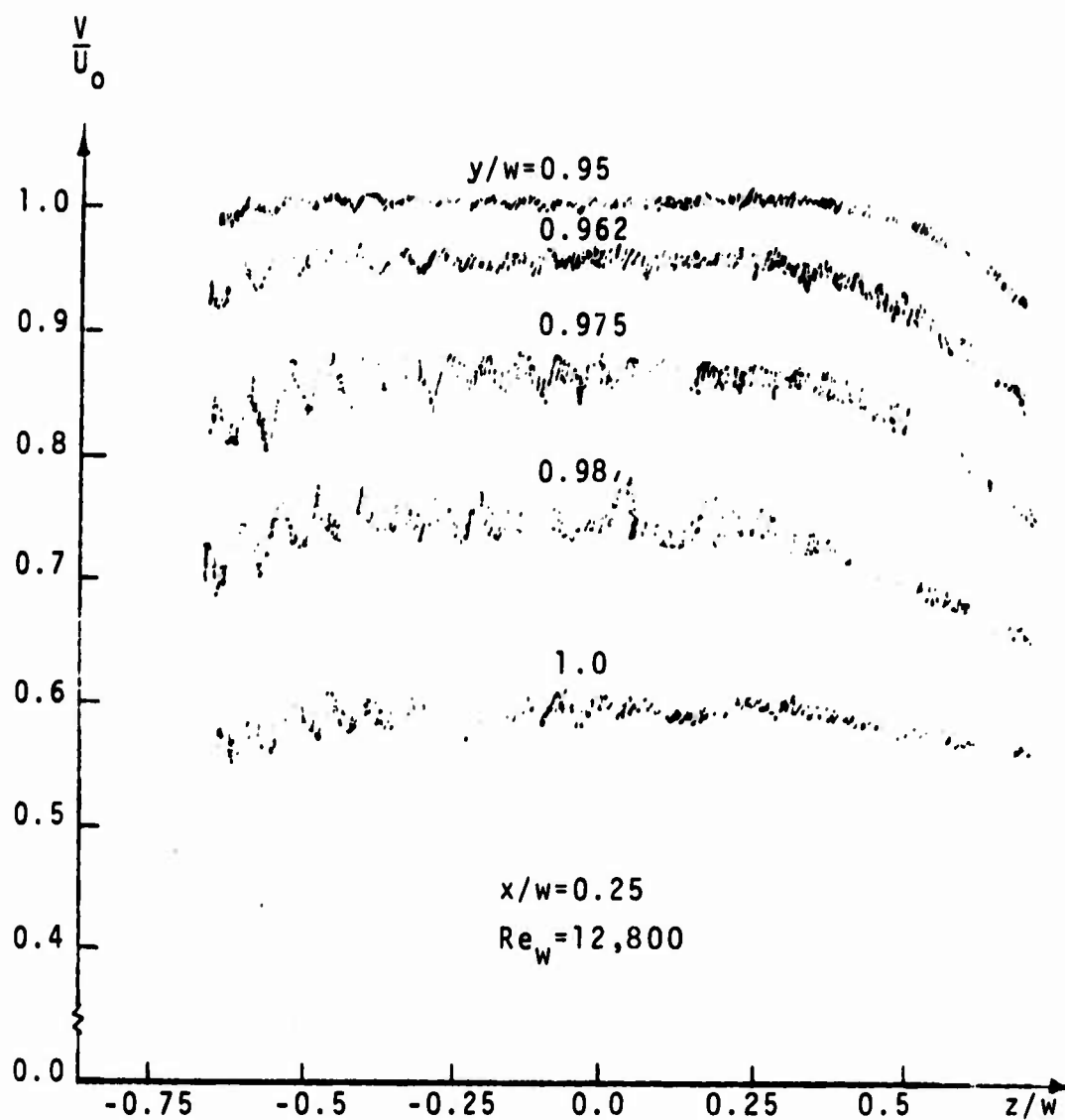
Figure 20 - Velocity Variation in the Direction
Normal to the Bounding Side Plates for Power Jet
With Flow Straightener.

81
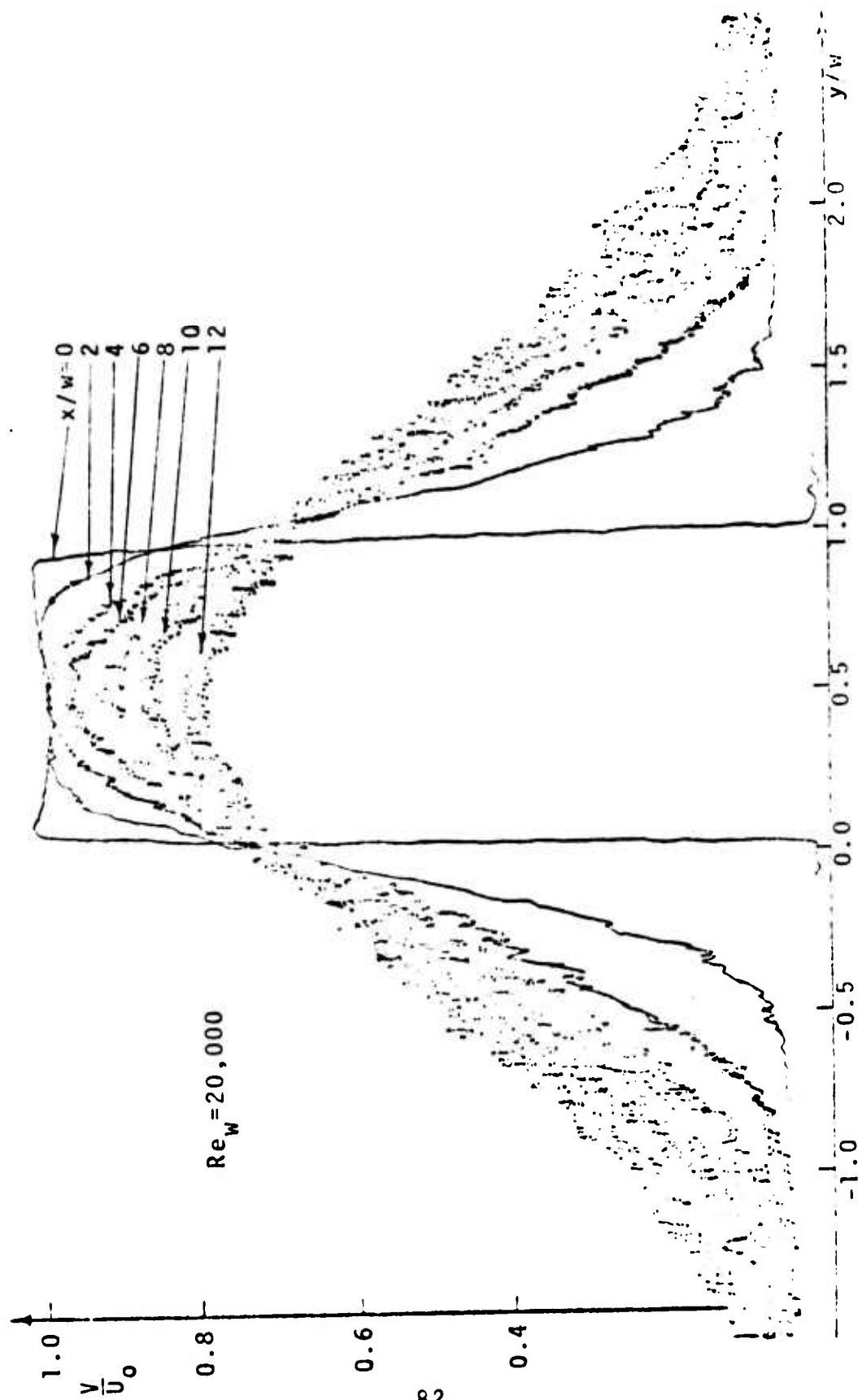
Figure 21 - Velocity Distribution Across the Power Jet at Various Locations Downstream from the Nozzle Exit.
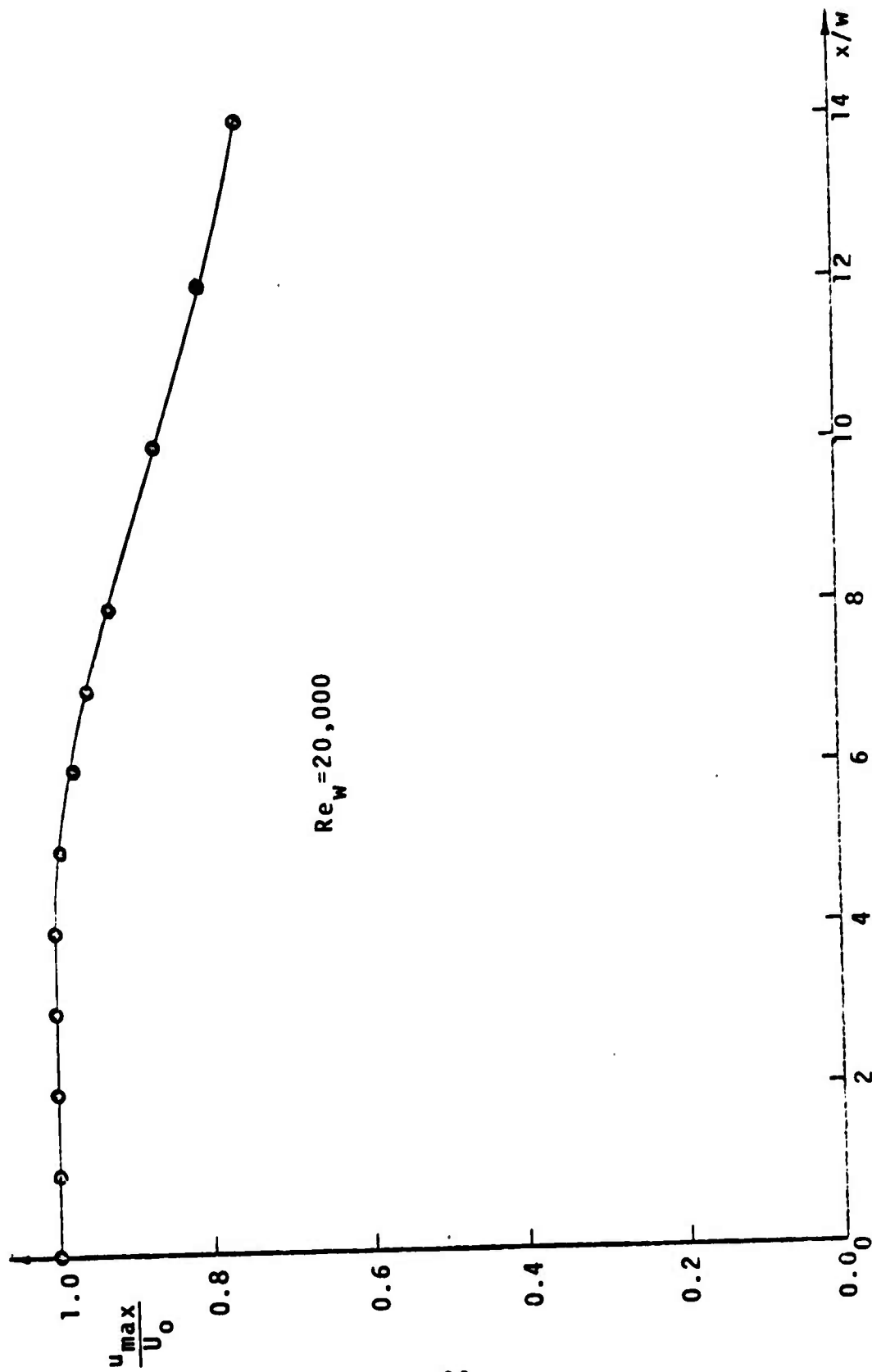
Figure 22 - Decay of Maximum Jet Velocity at Various Distances Downstream from the Nozzle Exit for Power Jet Alone.

$Re_w = 20,000$
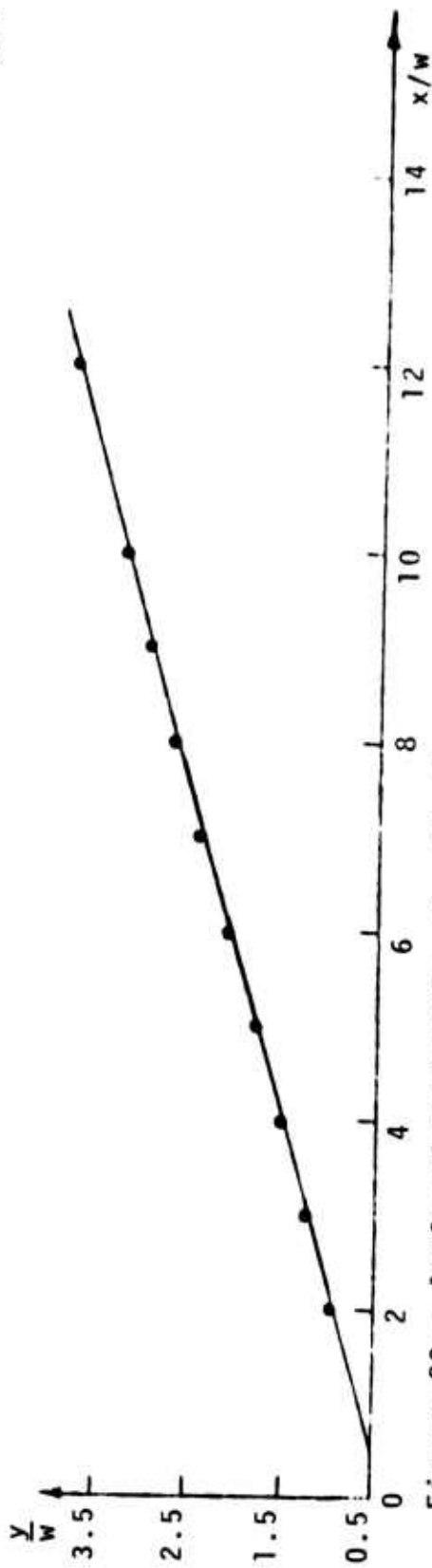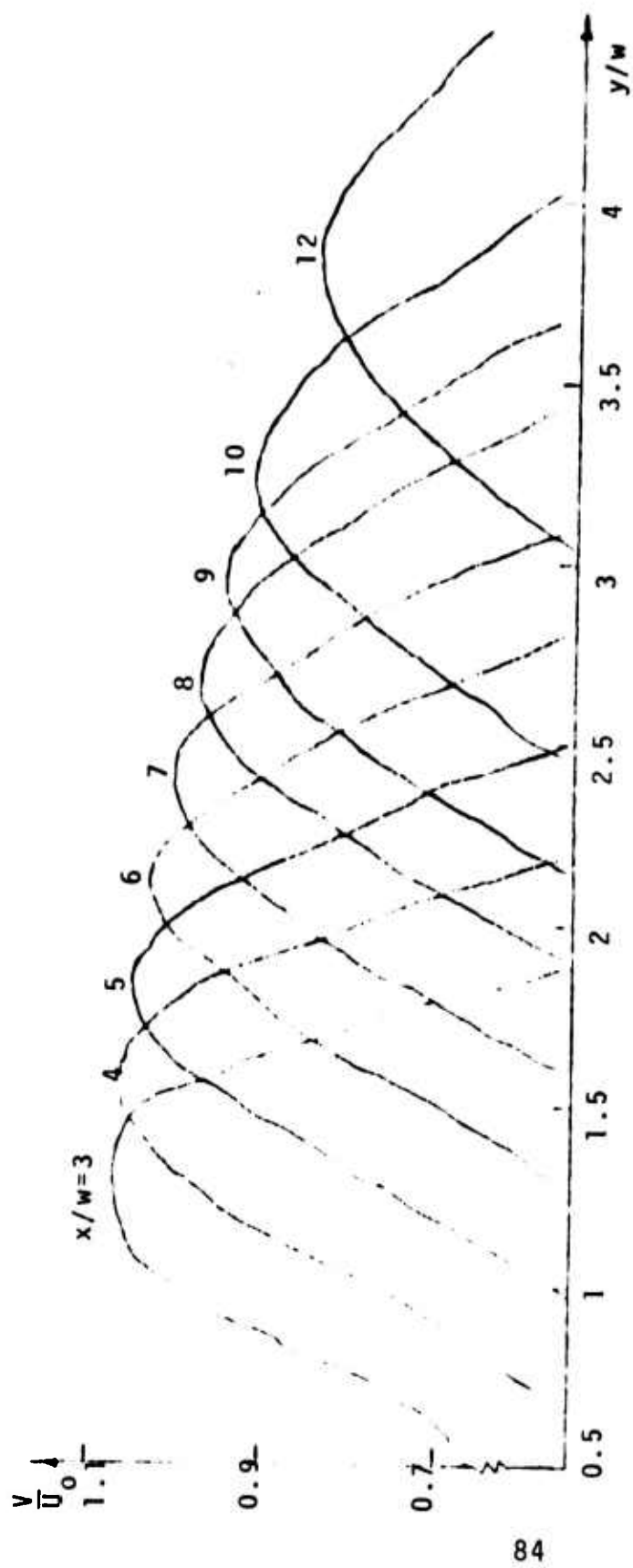
Figure 23 - Angle of Deflection for the Case of $w_c/w=1$, $s/w=1$ and $\pi_2 = 0.387$.

y/w

3.5

3

2.5

2

1.5

1

0.5

x/w=3   4   5   6   8   10   12

$\dfrac{V}{U_o}$

1.0

0.8

x/w

12

10

8

6

4

2

0

y/w

3.5

2.5

1.5

0.5
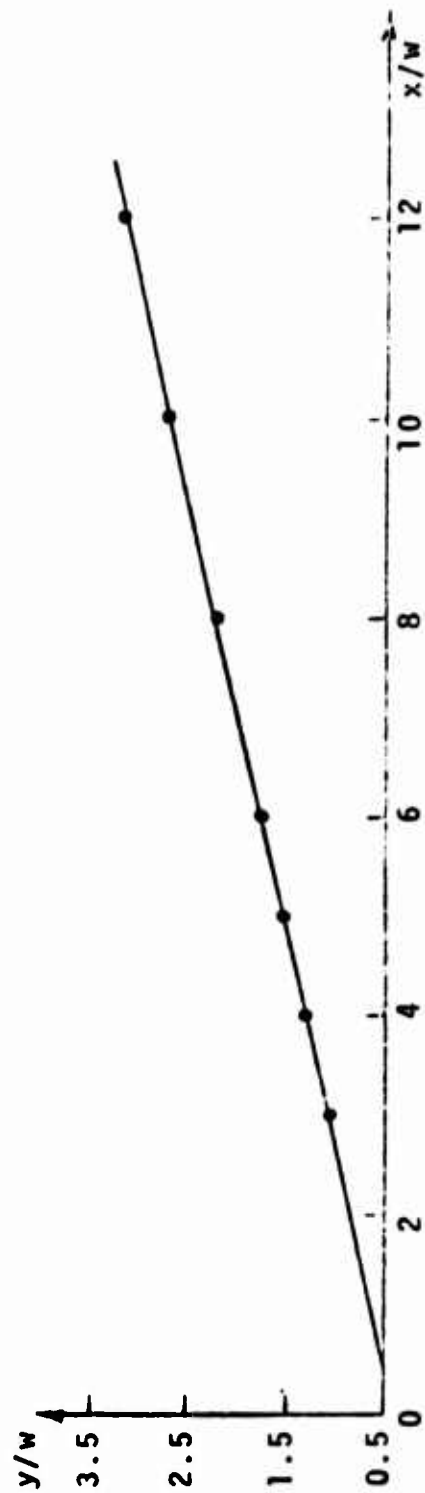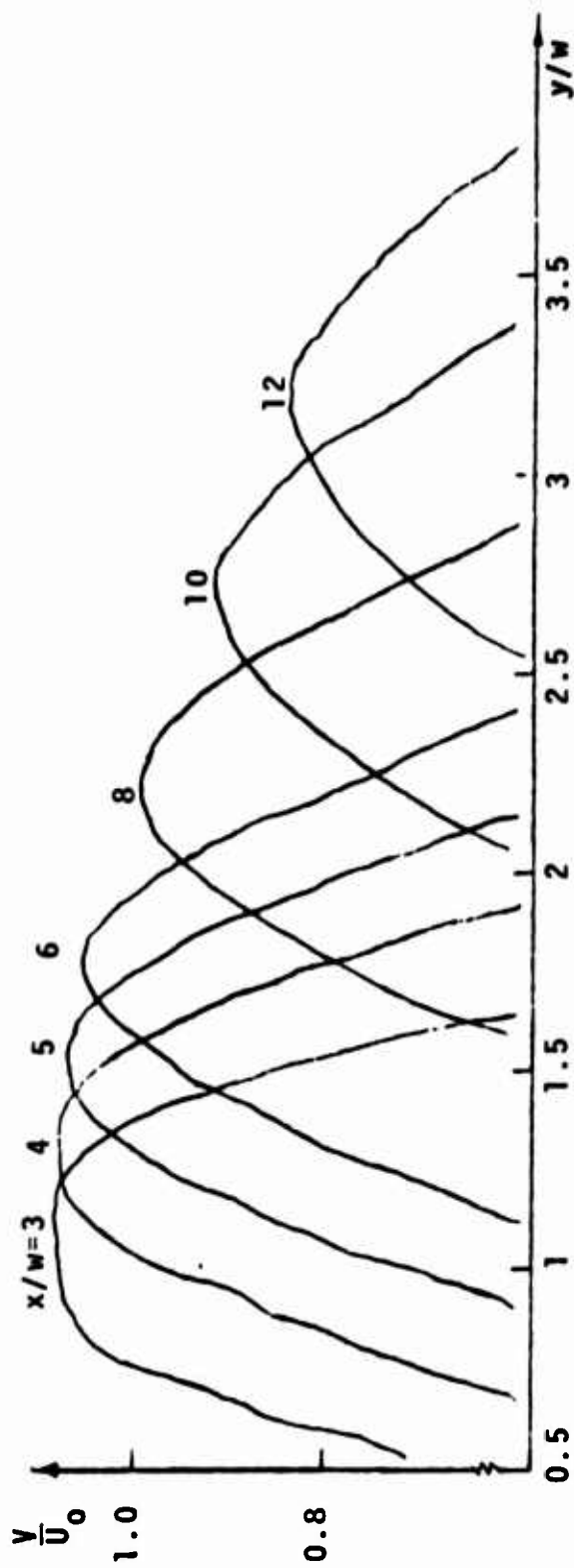
Figure 24 - Angle of Deflection for the Case of $w_c/w=1$, $s/w=1/2$ and $\pi_2=0.307$.
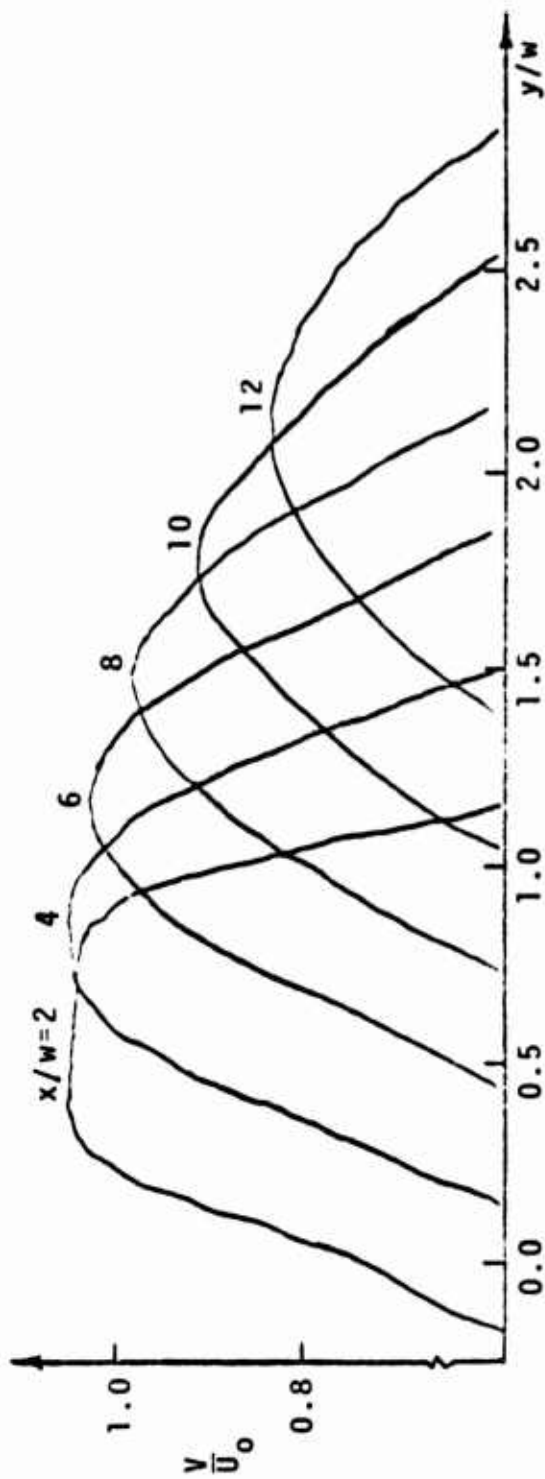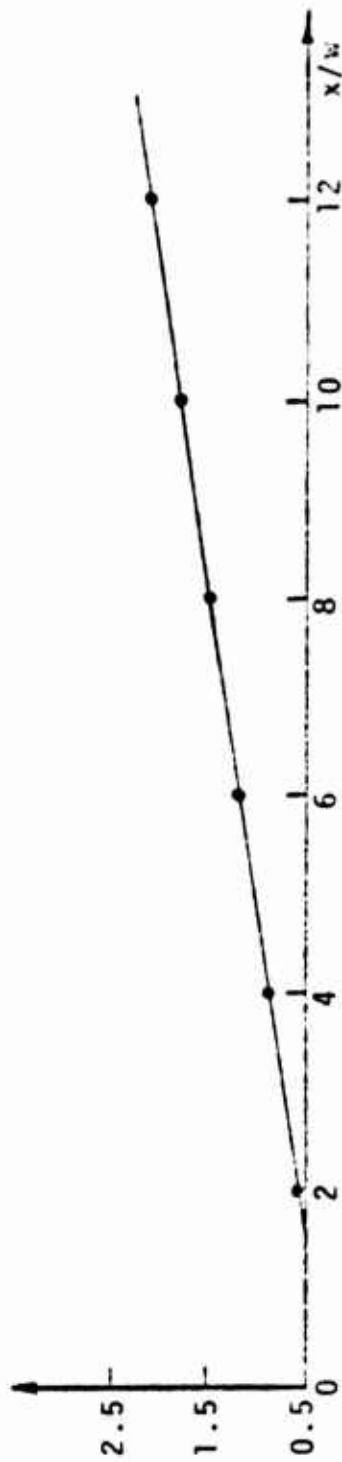
Figure 25 - Angle of Deflection for the Case of $w_c/w=1/2$, $s/w=1$ and $\pi_2=0.368$
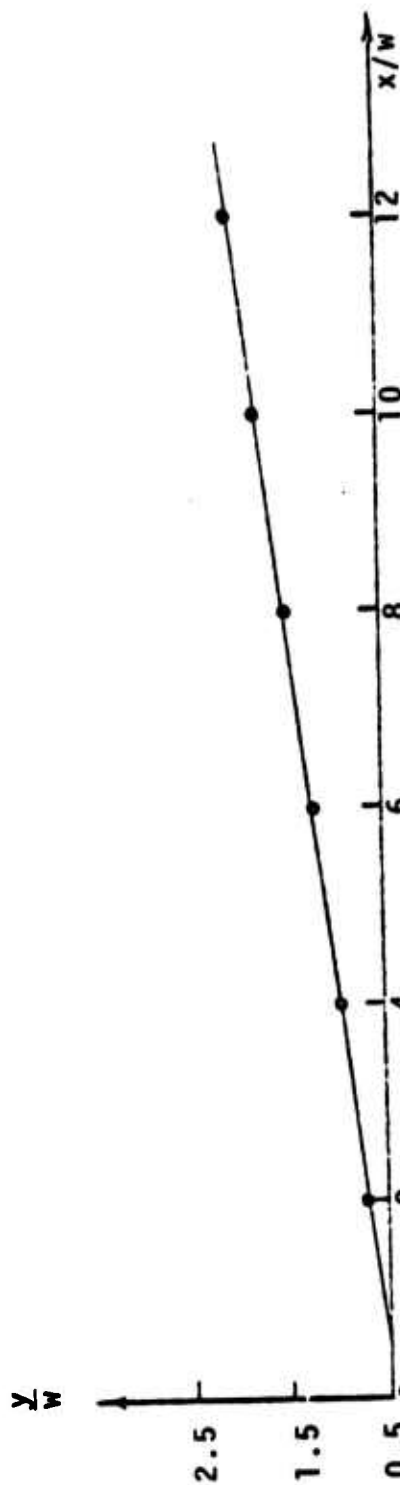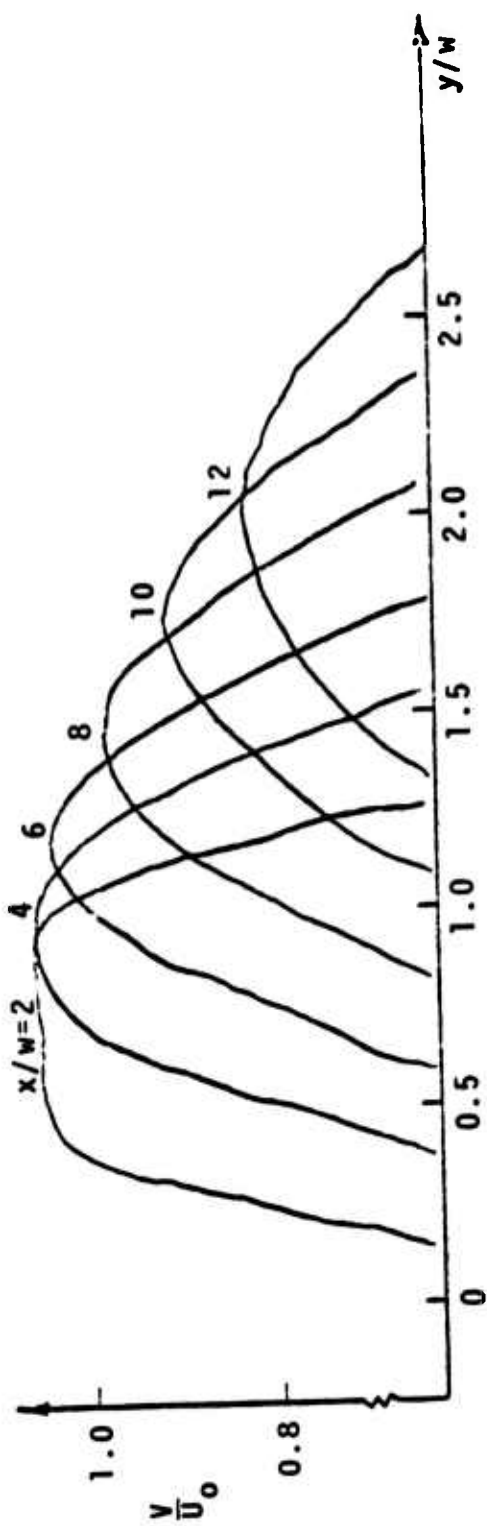
Figure 26 - Angle of Deflection for the case of $w_c/w=1/2$, $s/w=1/2$ and $\pi_2=0.30$.
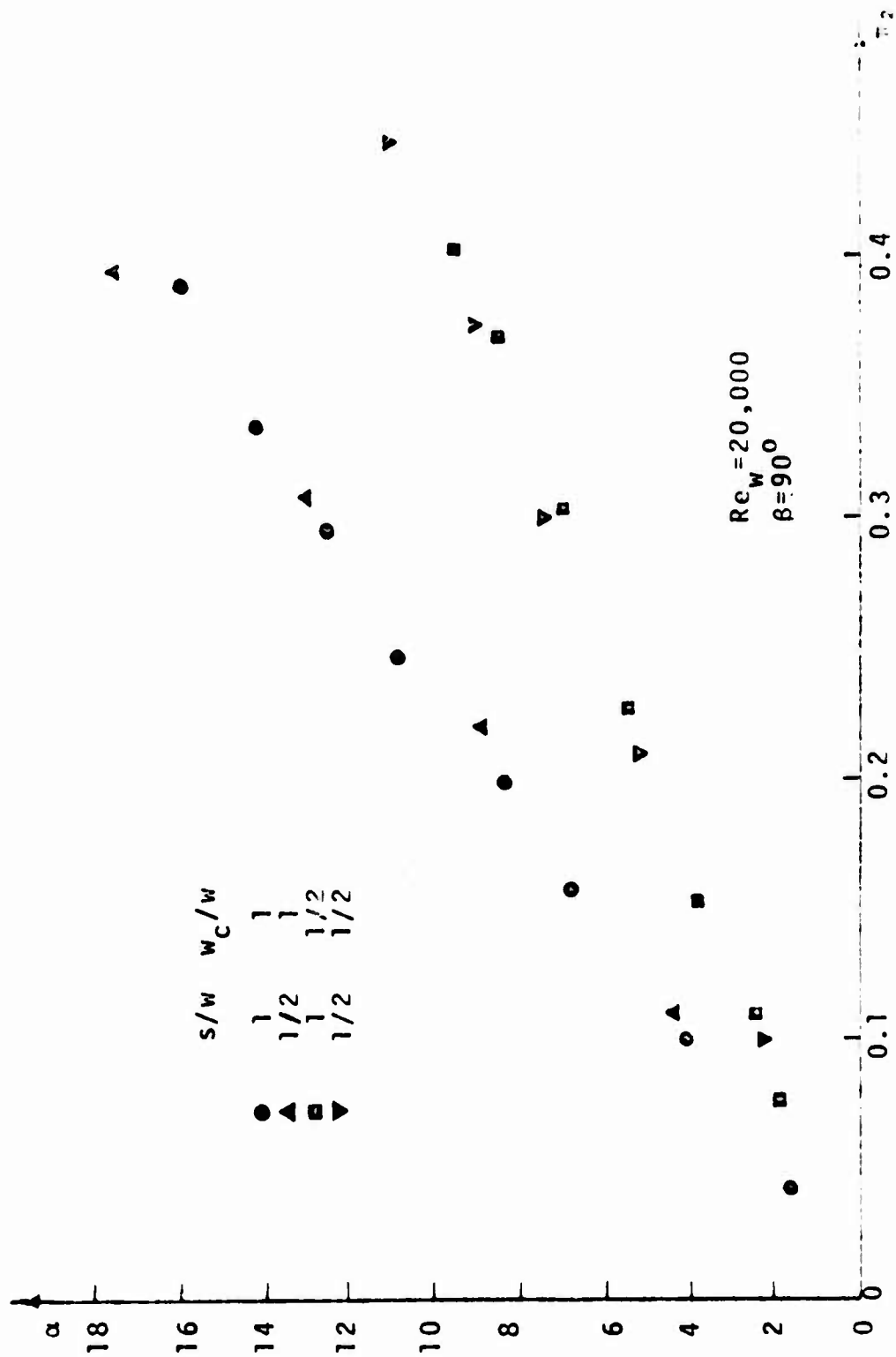
Figure 27- Variation of Angle of Deflection with Dimensionless Control Jet Pressure for Different Values of Setback and Width of Control Jet Nozzle.
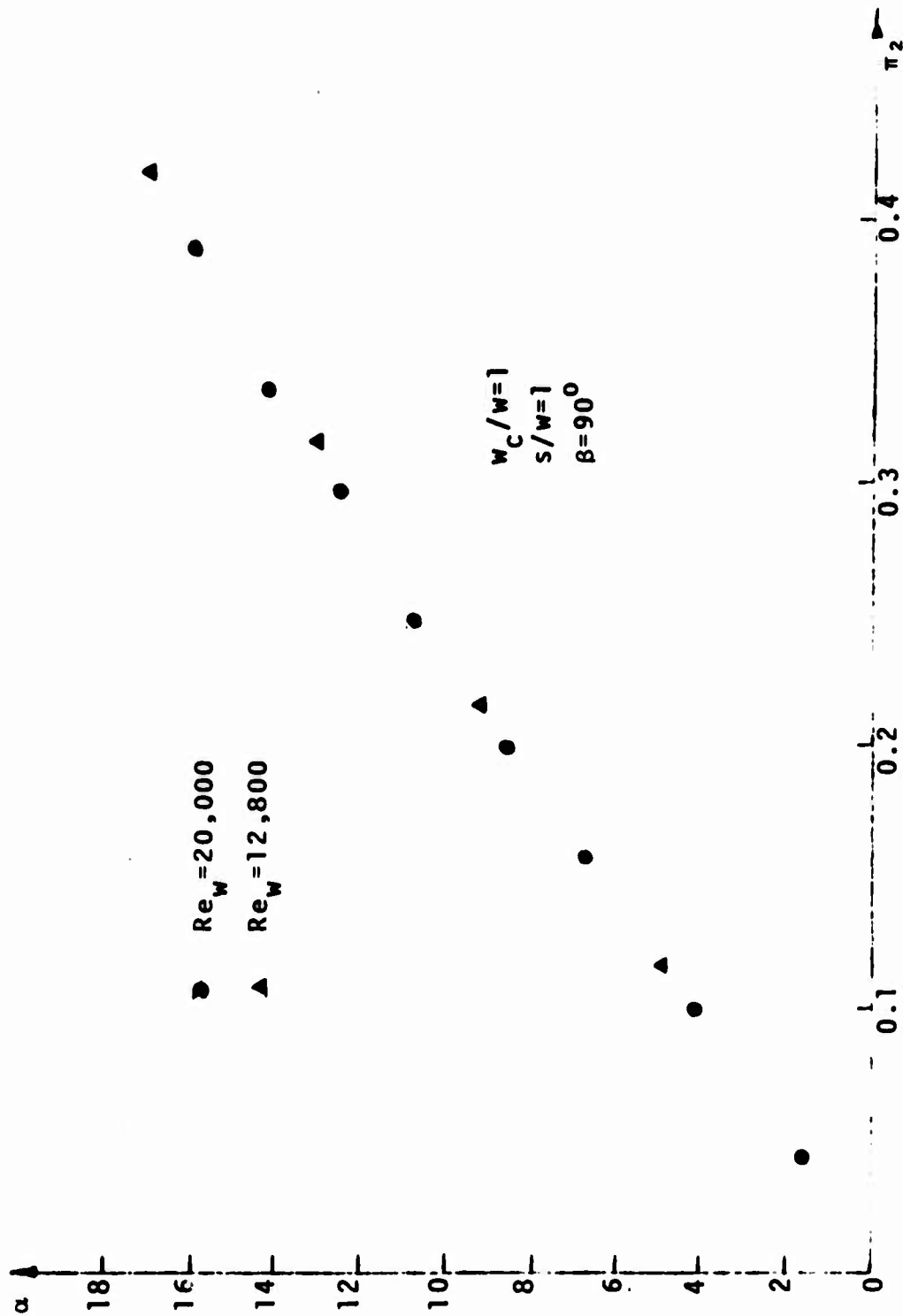
Figure 28 - Variation of Angle of Deflection with Dimensionless Control Jet Pressure for Two Different Reynolds Numbers.

89
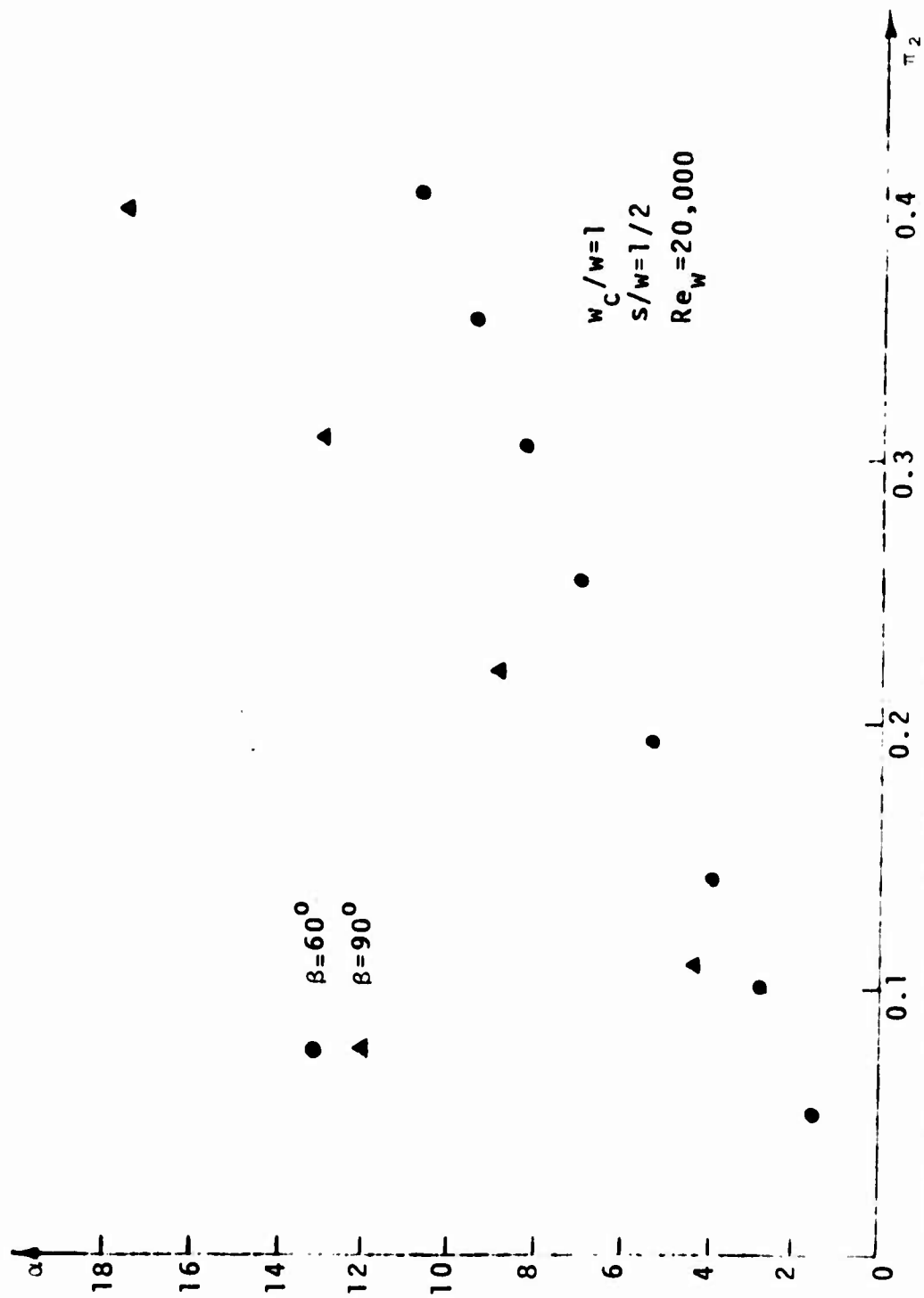
Figure 29 - Variation Of Angle Of Deflection with Dimensionless Control
Jet Pressure for Two Different Angles Between the Power and the Control Jets.
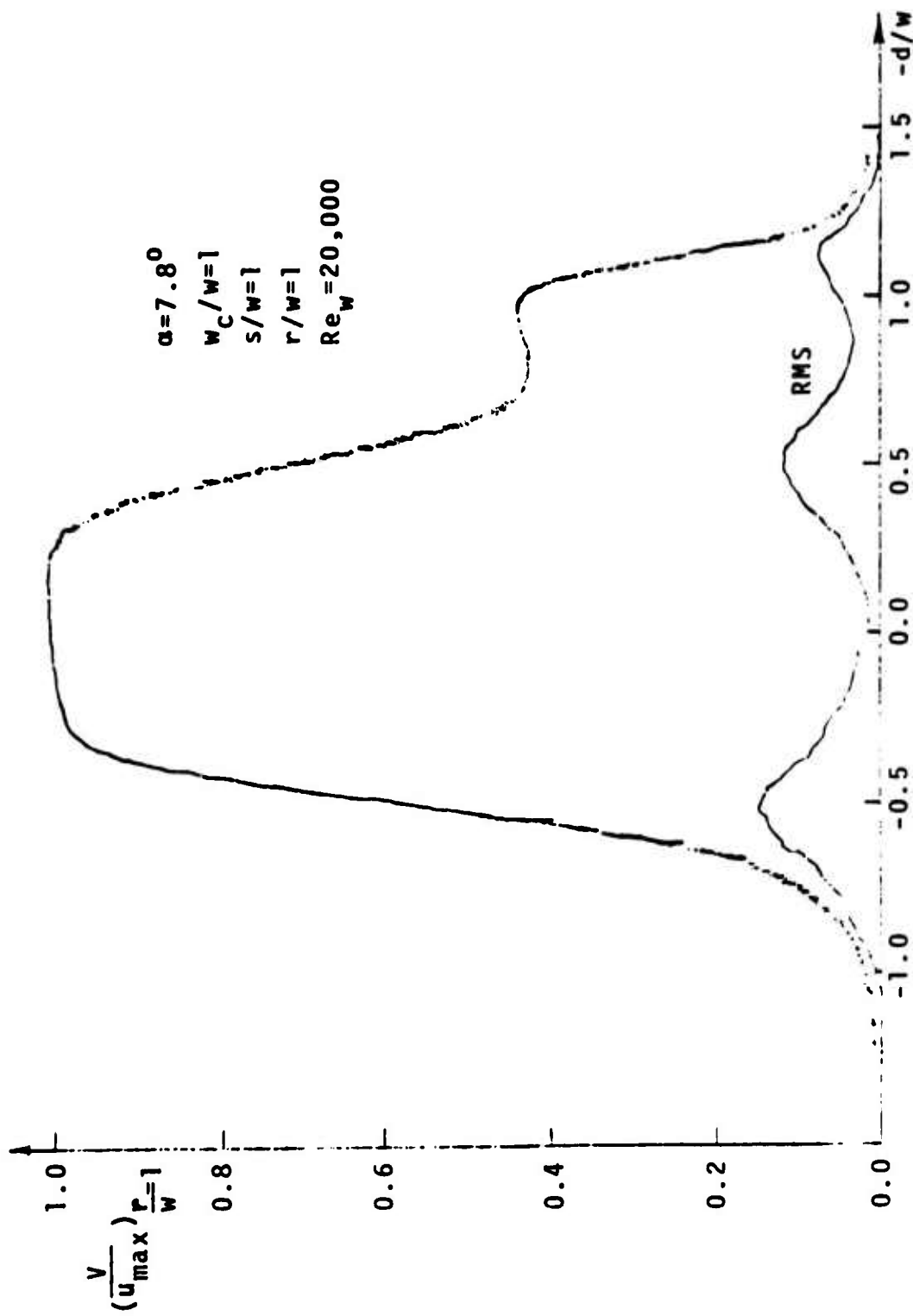
Figure 30 - Velocity and Turbulence Intensity Profiles Across the Jet at r/w=1.
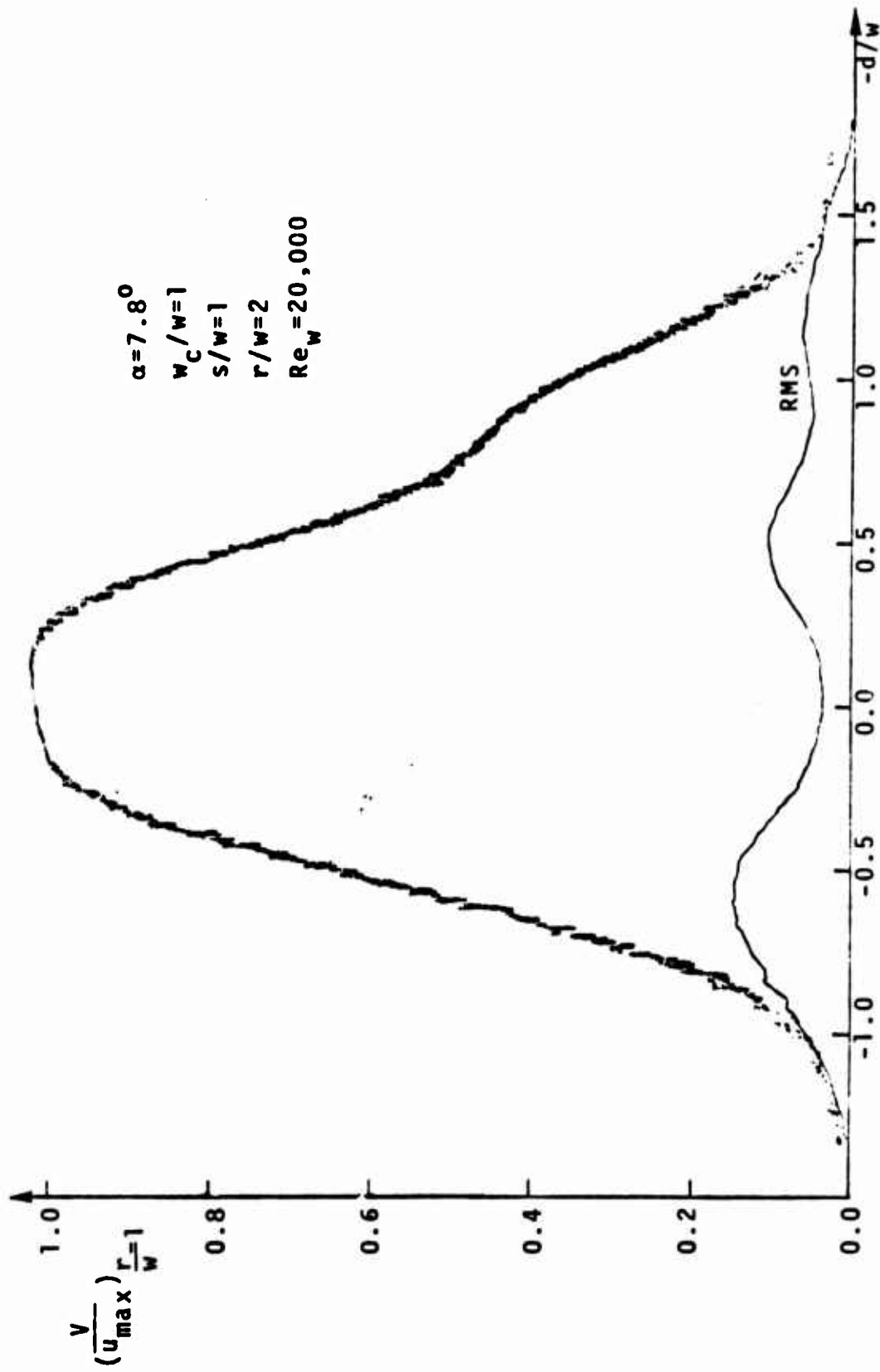
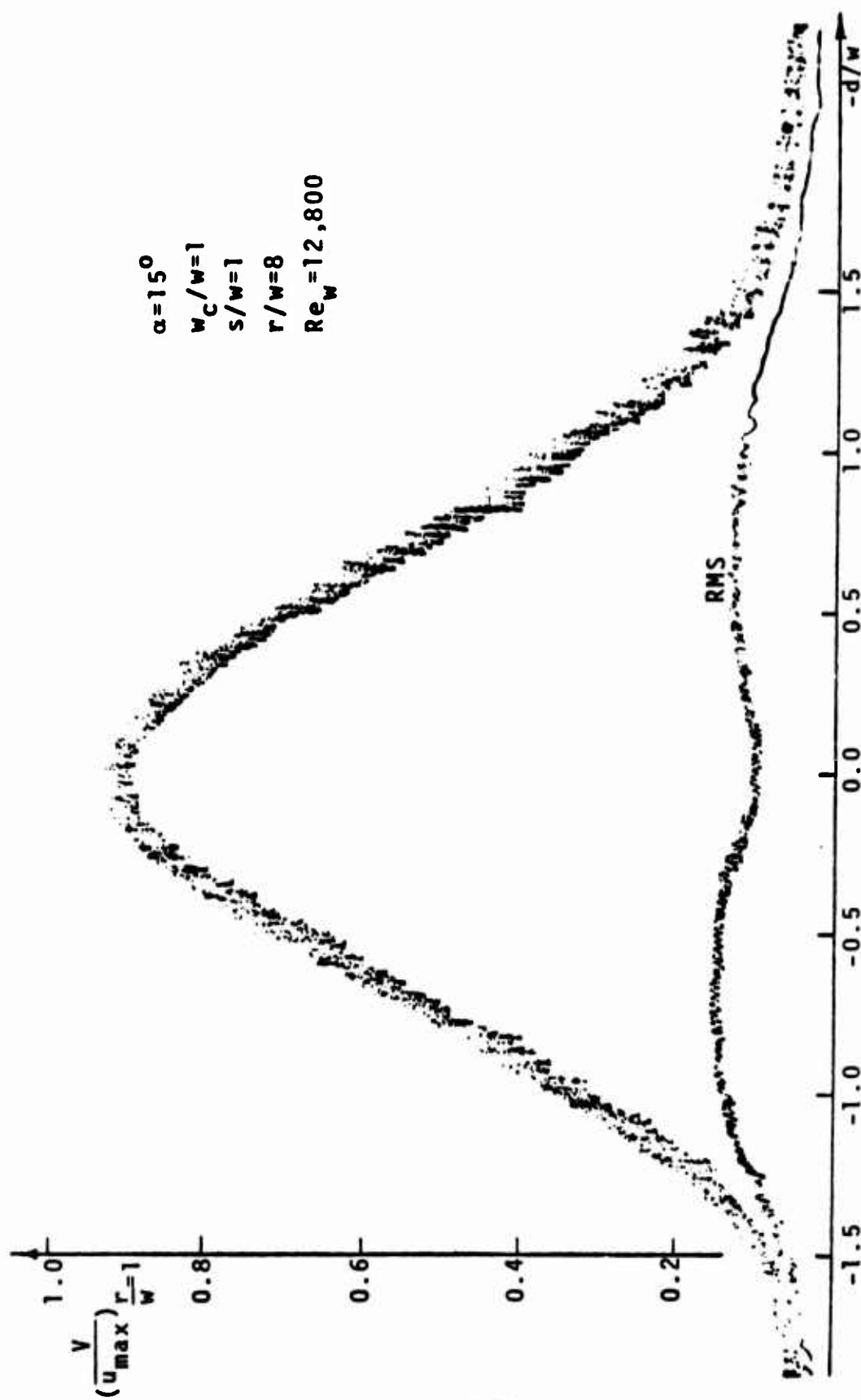Figure 31 - Velocity and Turbulence Intensity Profiles Across the Jet at r/w=2.

$\alpha=7.8^\circ$
$w_c/w=1$
$s/w=1$
$r/w=2$
$Re_w=20,000$

RMS

$\left(\dfrac{v}{u_{max}}\right)\dfrac{r}{w}=1$

1.0

0.8

0.6

0.4

0.2

0.0

-1.0   -0.5   0.0   0.5   1.0   1.5   -d/w
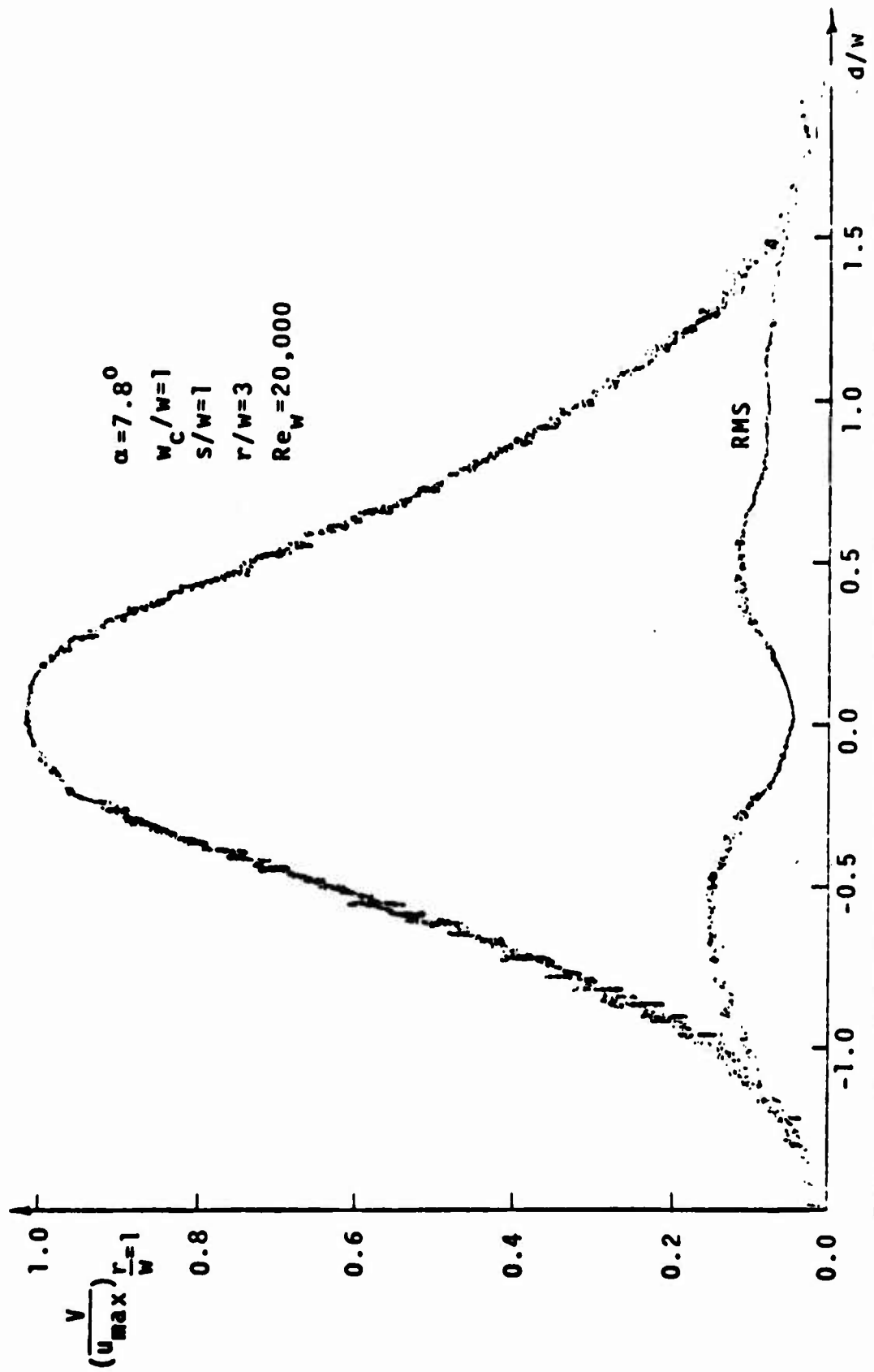
Figure 32 - Velocity and Turbulence Intensity Profiles Across the Jet at r/w=3.

$\alpha = 7.8^0$
$w_c/w = 1$
$s/w = 1$
$r/w = 3$
$Re_w = 20,000$

RMS

d/w

$\frac{V}{(u_{max})} \frac{r}{w} = 1$
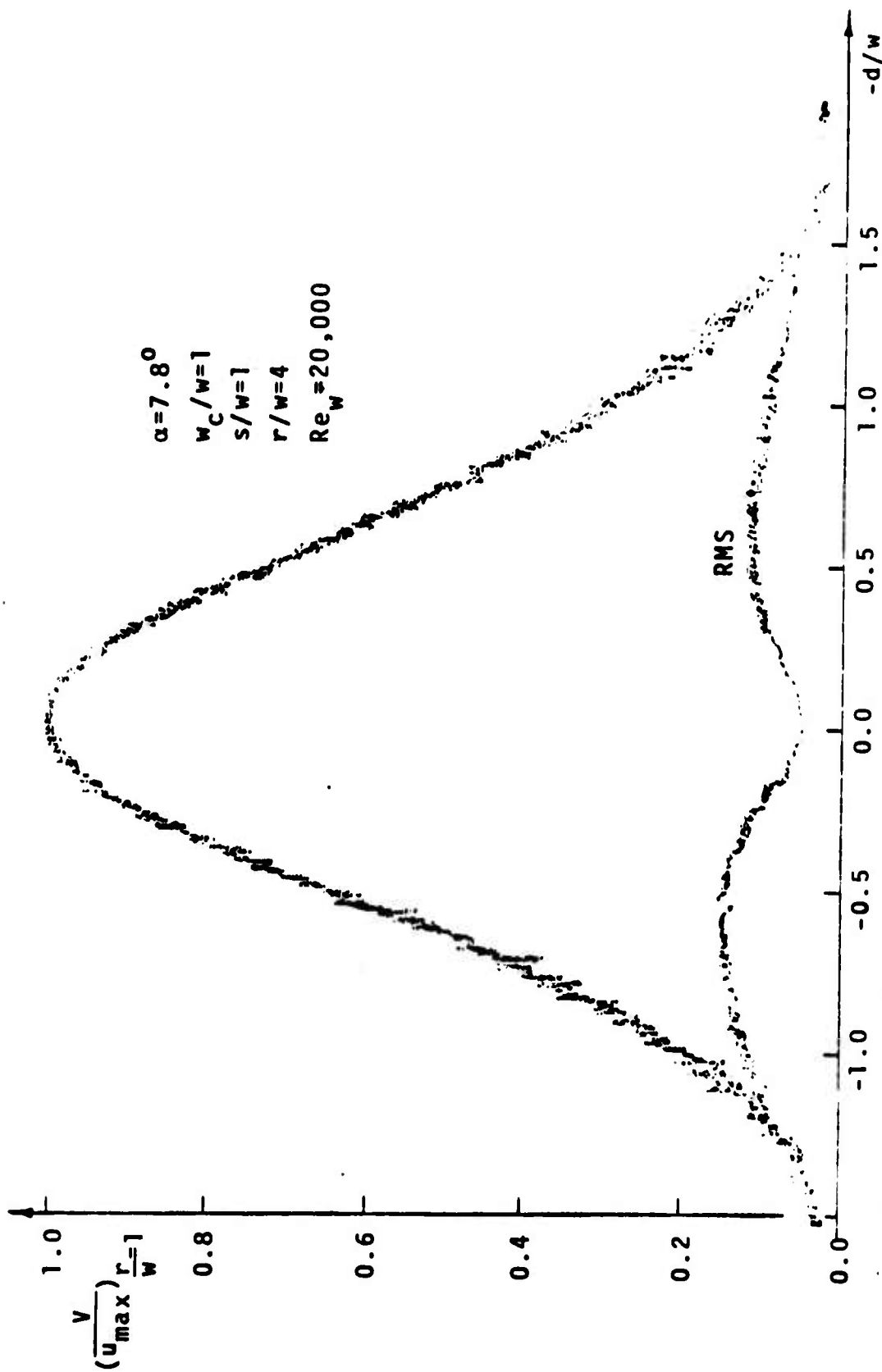
Figure 33 – Velocity and Turbulence Intensity Profiles Across the Jet at r/w=4.

Plot parameters:
$\alpha = 7.8^{\circ}$
$w_c/w = 1$
$s/w = 1$
$r/w = 4$
$Re_w = 20{,}000$

Vertical axis: $\dfrac{v}{(u_{max})} \dfrac{r}{w} = 1$

Horizontal axis: $-d/w$

RMS
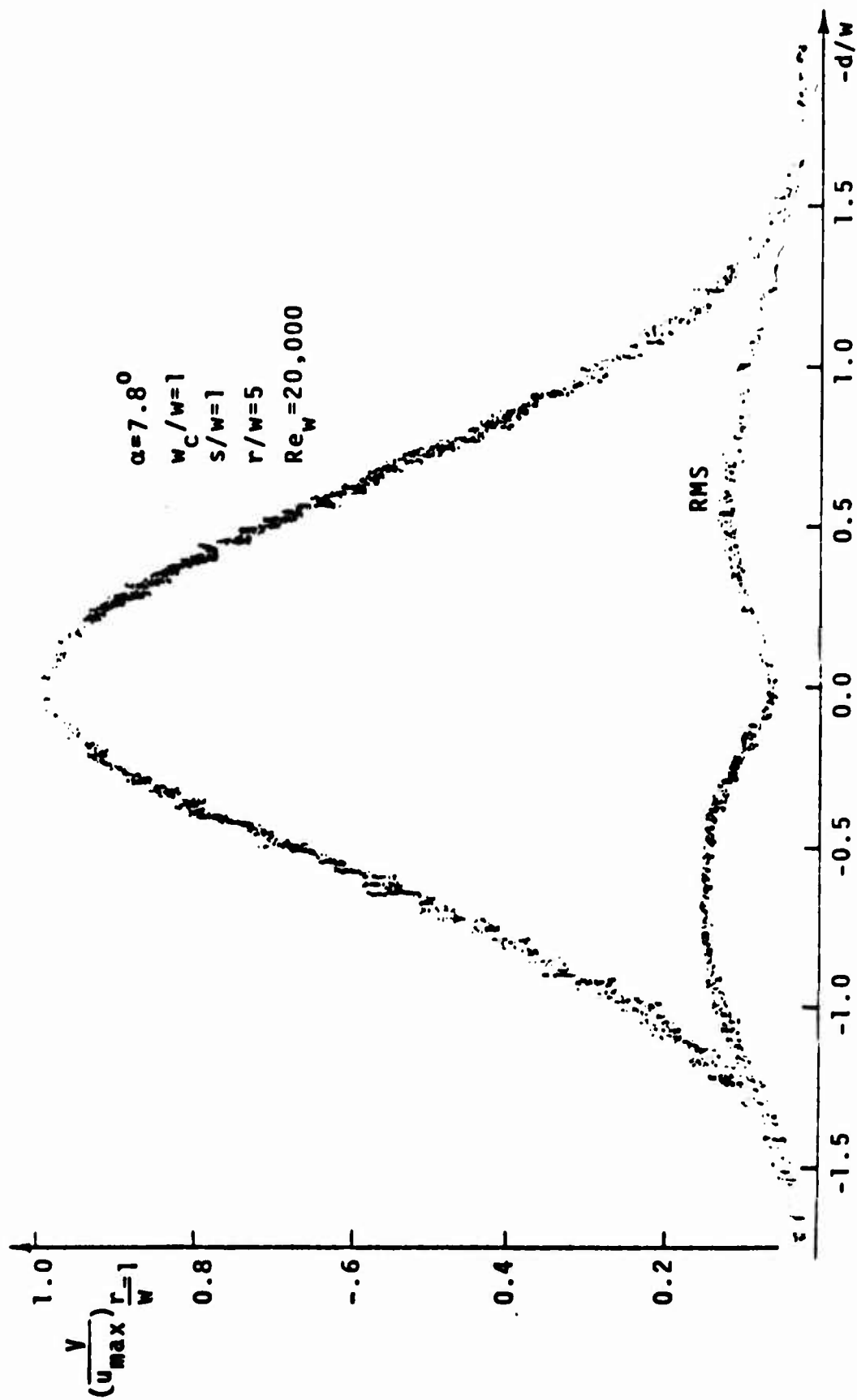
Figure 34 - Velocity and Turbulence Intensity Profiles Across the Jet at r/w=5.

The plot is labeled with:
- $\alpha = 7.8^\circ$
- $w_c/w = 1$
- $s/w = 1$
- $r/w = 5$
- $Re_w = 20,000$

Vertical axis: $\frac{v}{(u_{max})} \frac{r}{w} = 1$ with gridlines at 1.0, 0.8, .6, 0.4, 0.2

Horizontal axis: -d/w with values -1.5, -1.0, -0.5, 0.0, 0.5, 1.0, 1.5

RMS

95
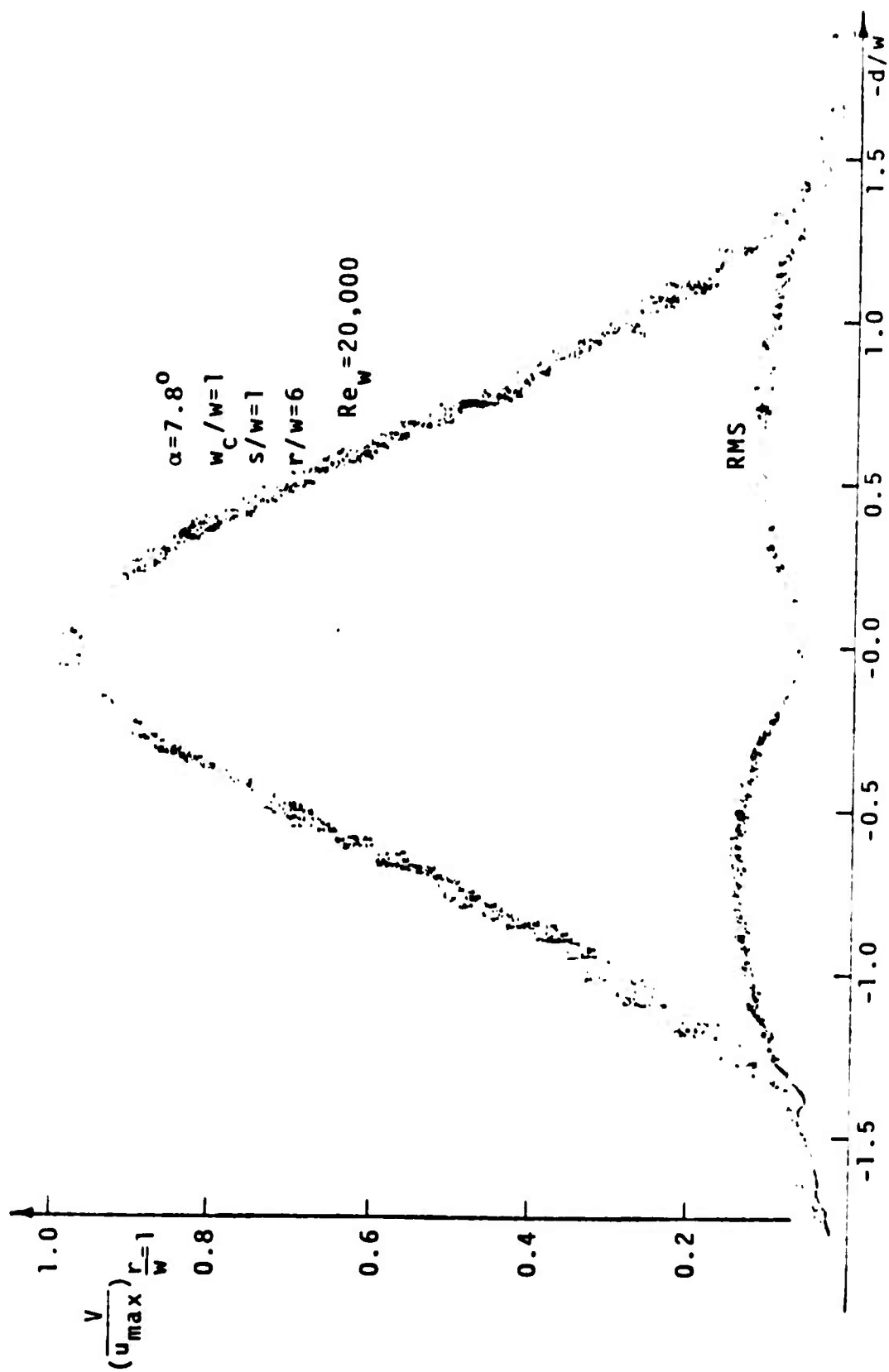
Figure 35 - Velocity and Turbulence Intensity Profiles Across the Jet at r/w=6.

$\alpha=7.8^{\circ}$
$w_c/w=1$
$s/w=1$
$r/w=6$
$Re_w=20,000$

RMS

$\left(\dfrac{V}{u_{max}}\right)\dfrac{r}{w}=1$
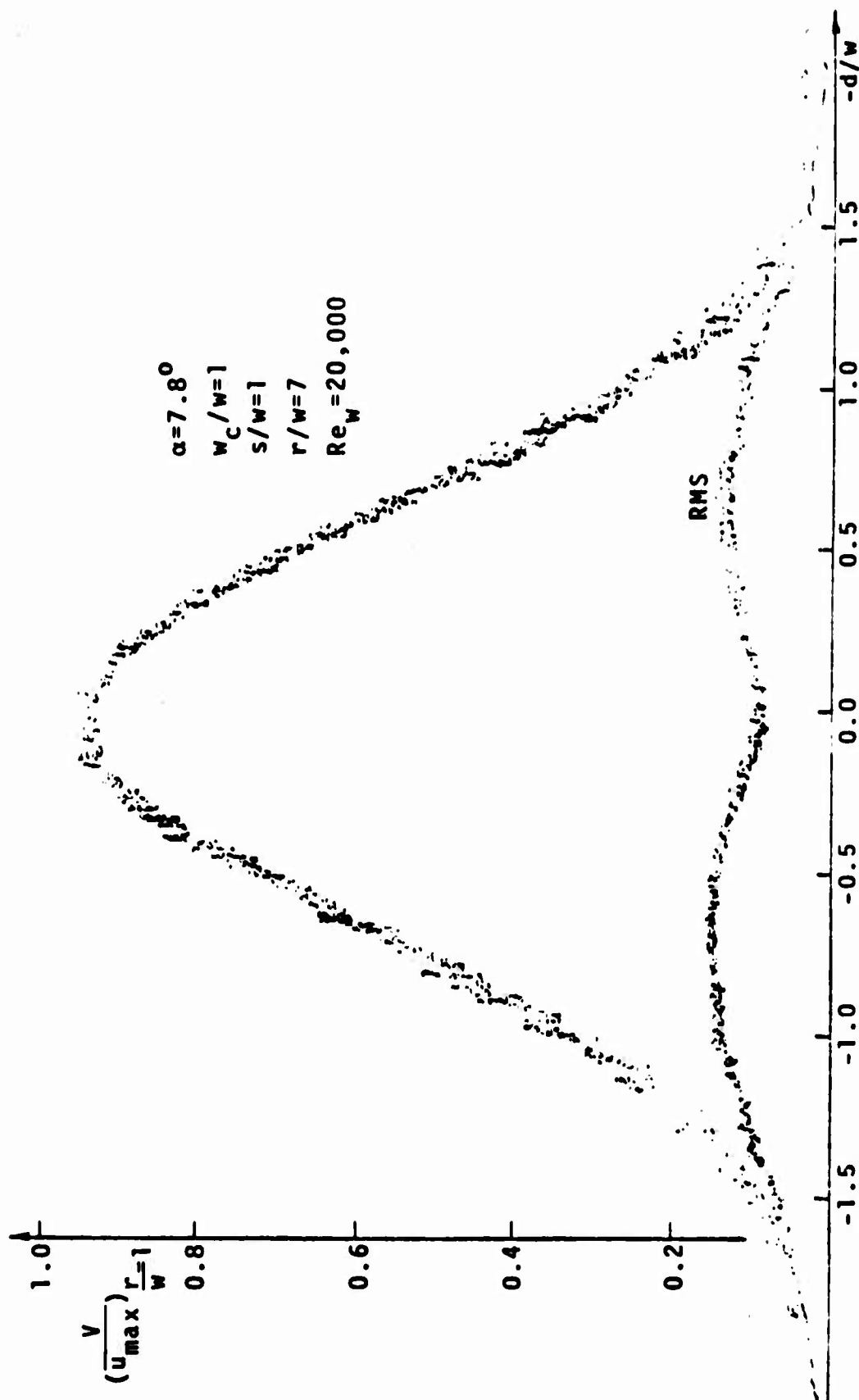
Figure 36 - Velocity and Turbulence Intensity Profiles Across the Jet at r/w=7.

$\alpha = 7.8^\circ$
$w_c/w = 1$
$s/w = 1$
$r/w = 7$
$Re_w = 20,000$

RMS

$\left(\dfrac{V}{u_{max}}\right)\dfrac{r}{w} = 1$

-d/w
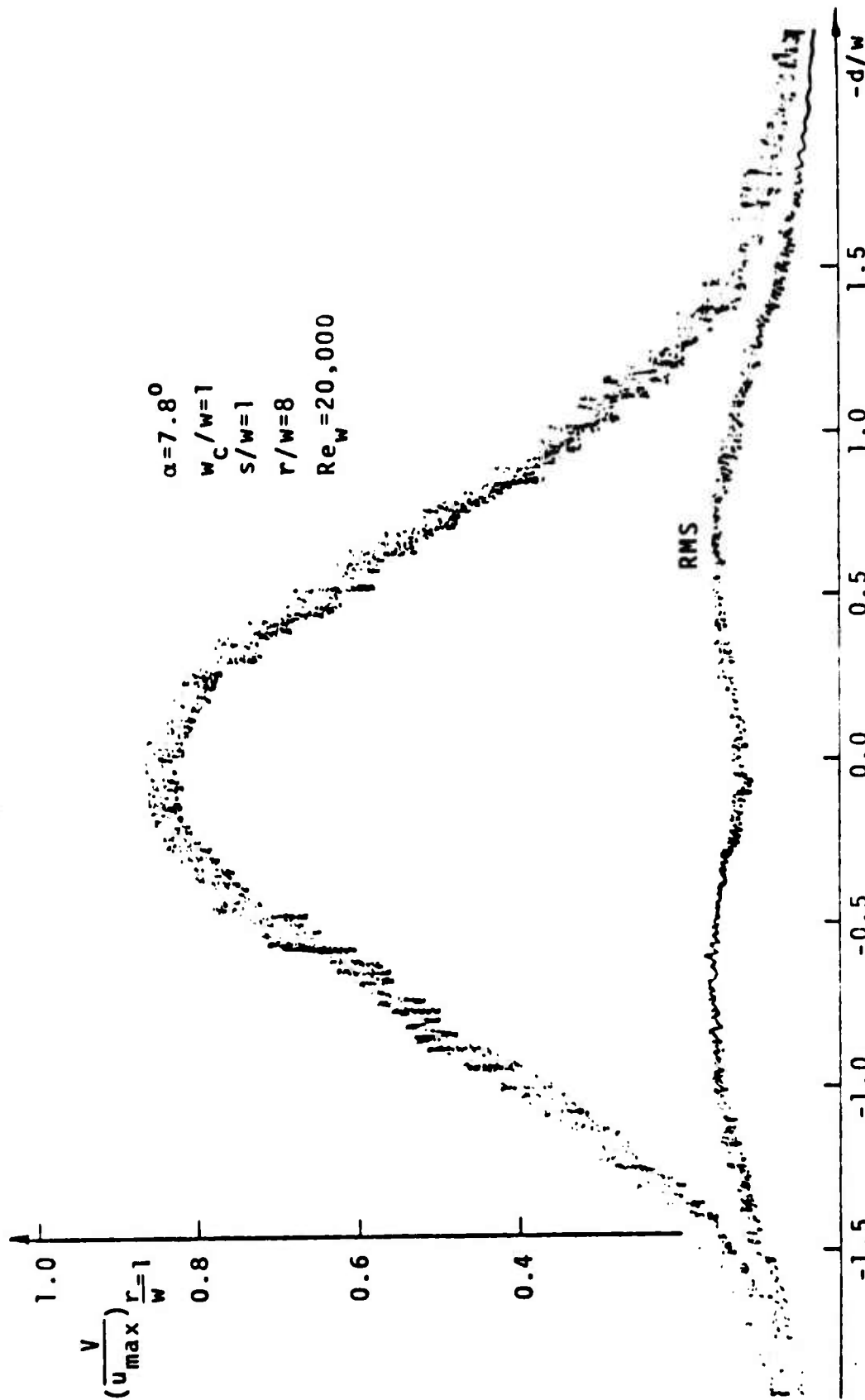
Figure 37 - Velocity and Turbulence Intensity Profiles Across the Jet at r/w=8.

$\alpha=7.8^{\circ}$
$w_c/w=1$
$s/w=1$
$r/w=8$
$Re_w=20,000$

RMS

$\left(\dfrac{V}{u_{max}}\right)\dfrac{r}{w}=1$
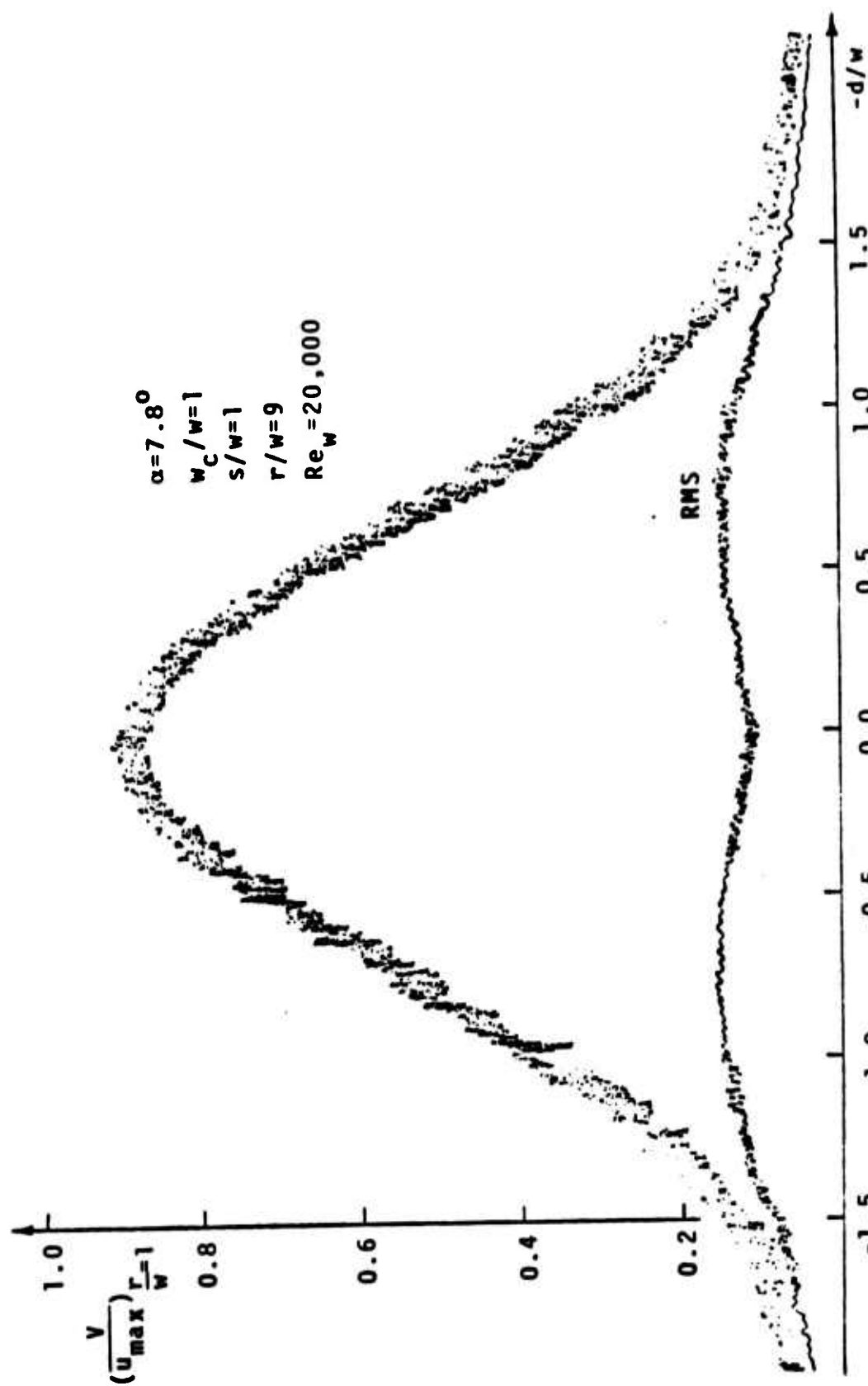
Figure 38 - Velocity and Turbulence Intensity Profiles Across the Jet at r/w=9.

$\alpha = 7.8°$
$w_c/w = 1$
$s/w = 1$
$r/w = 9$
$Re_w = 20,000$

RMS

$\left(\dfrac{v}{u_{max}}\right)\dfrac{r}{w} = 1$

99
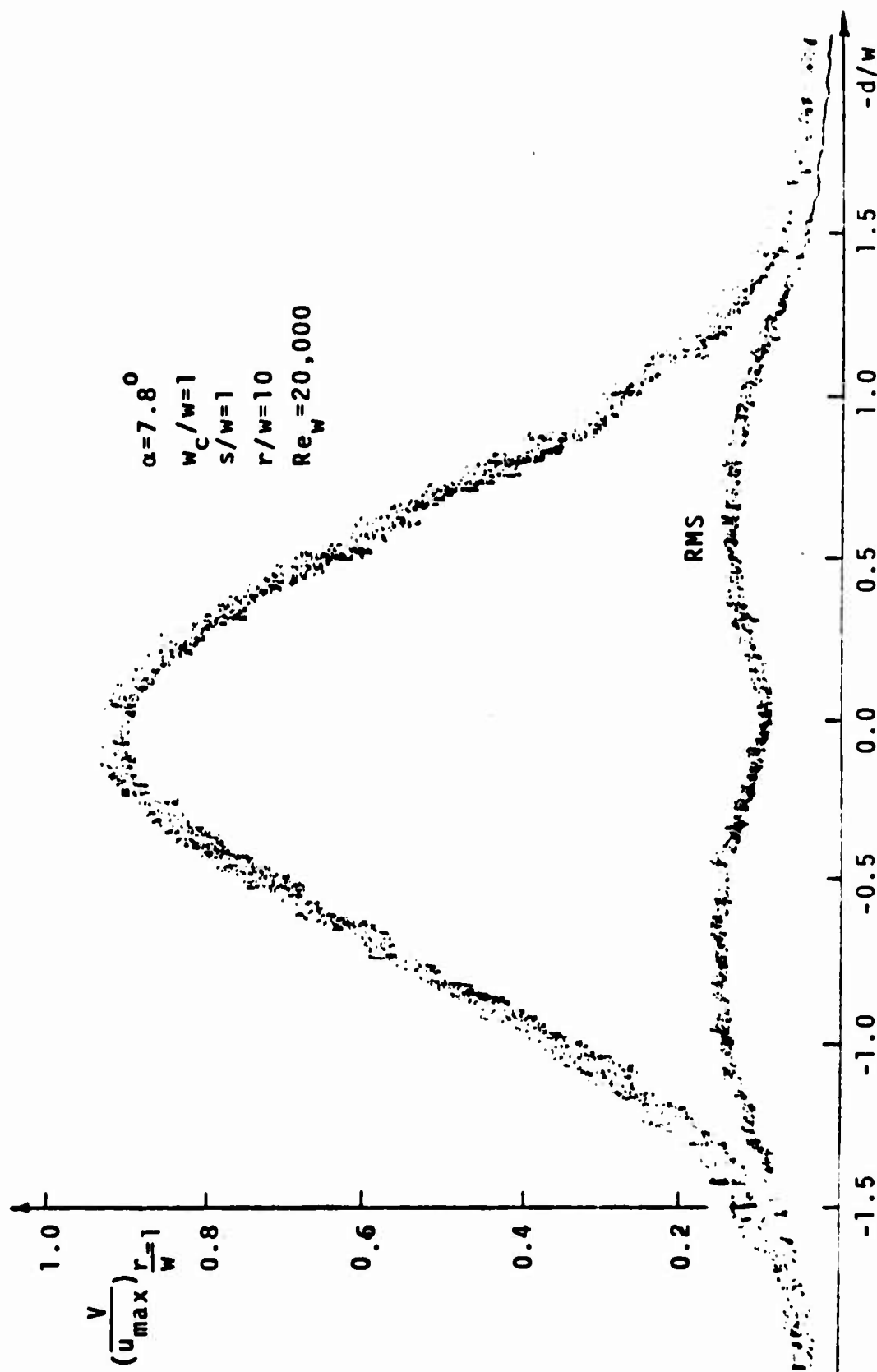
Figure 39 - Velocity and Turbulence Intensity Profiles Across the Jet at r/w=10.

$\alpha=7.8^{0}$
$w_c/w=1$
$s/w=1$
$r/w=10$
$Re_w=20,000$

RMS

$\left(\frac{V}{u_{max}}\right)\frac{r}{w}=1$

100

Figure 40 - Velocity and Turbulence Intensity Profiles Across the Jet at r/w=1.

$\alpha = 15^o$
$w_c/w = 1$
$s/w = 1$
$r/w = 1$

$Re_w = 12,800$

RMS

$-d/w$

$\left(\dfrac{v}{u_{max}}\right)\dfrac{r}{w} = 1$

101
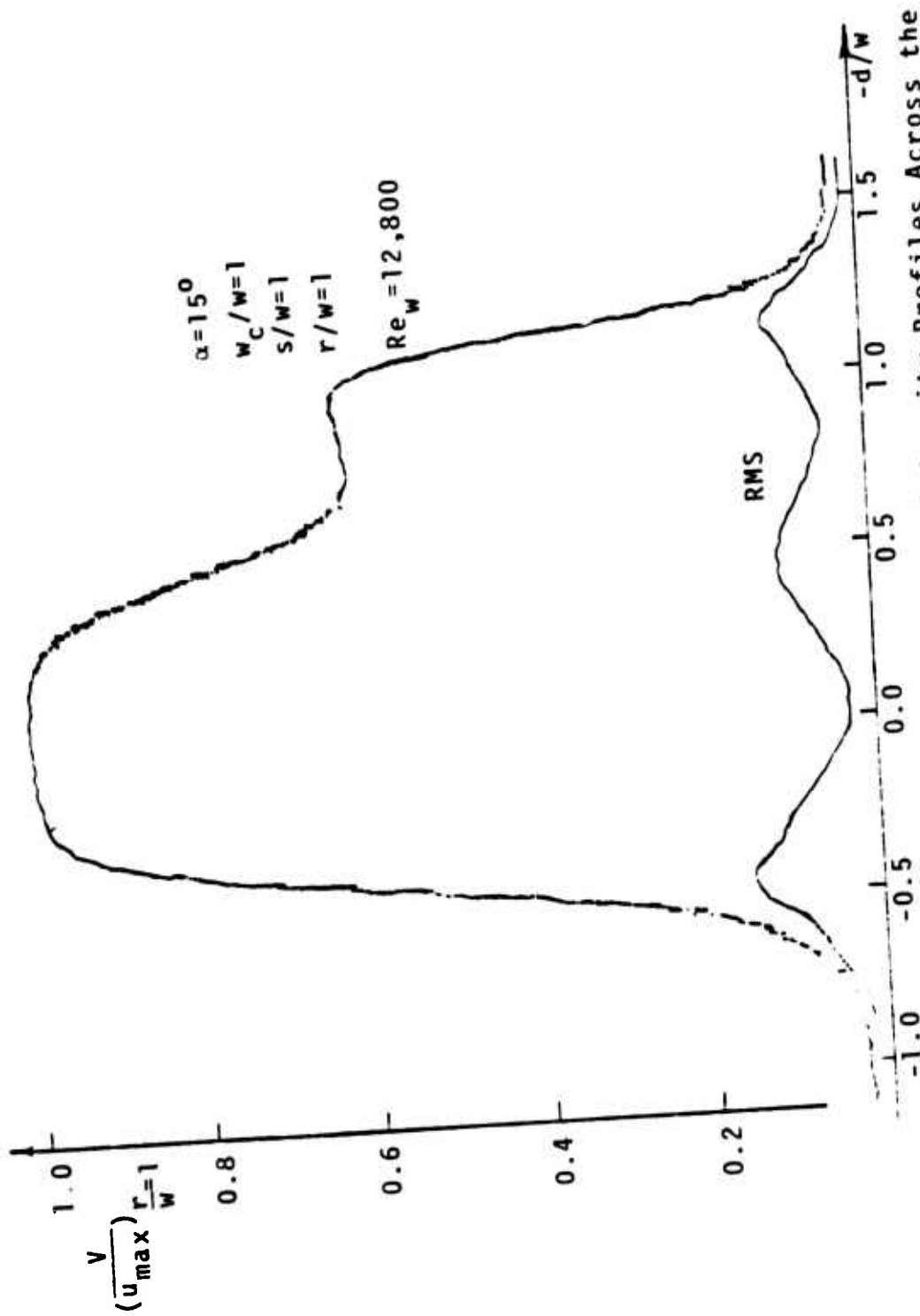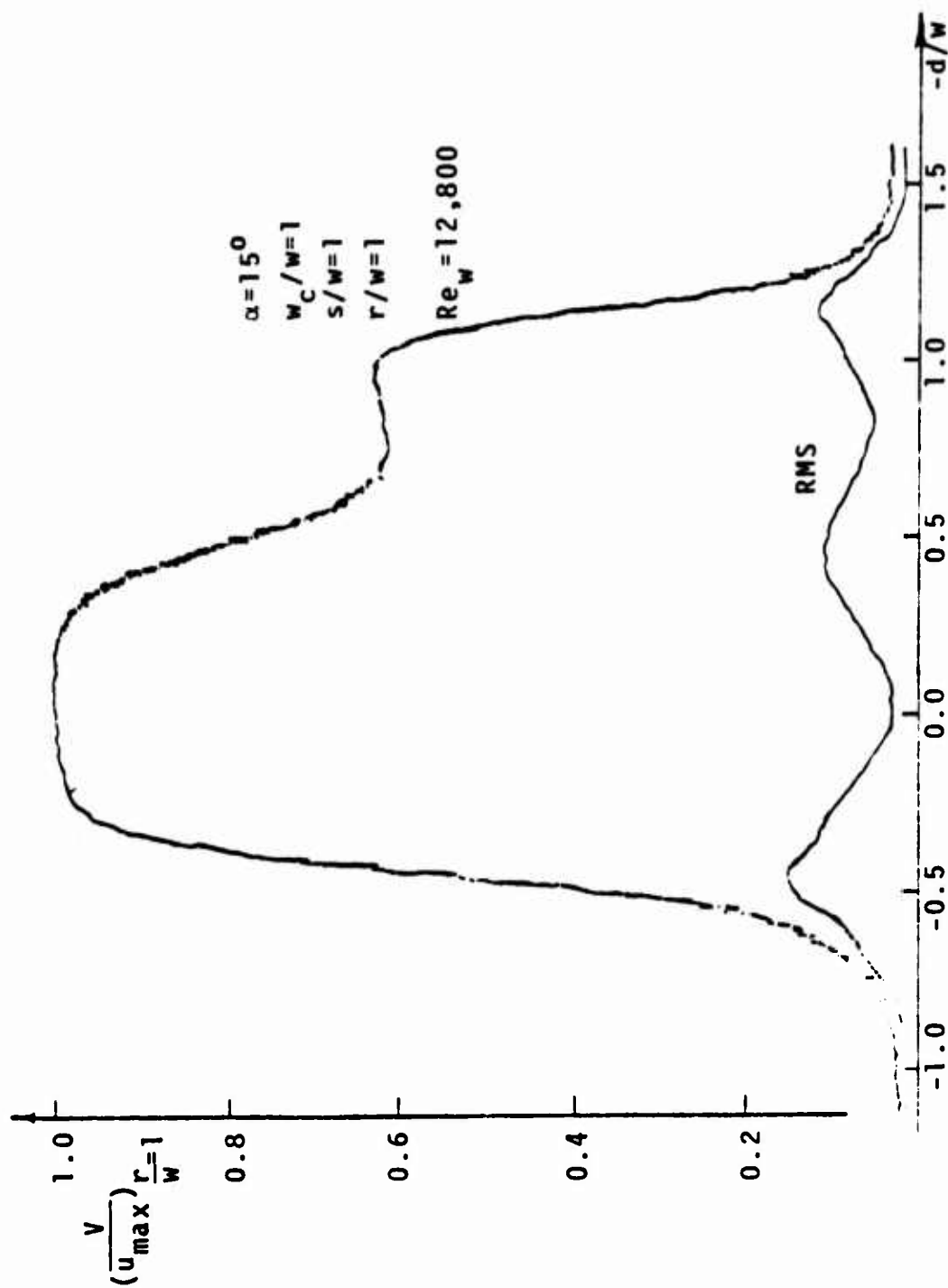
Figure 40 - Velocity and Turbulence Intensity Profiles Across the Jet at r/w=1.
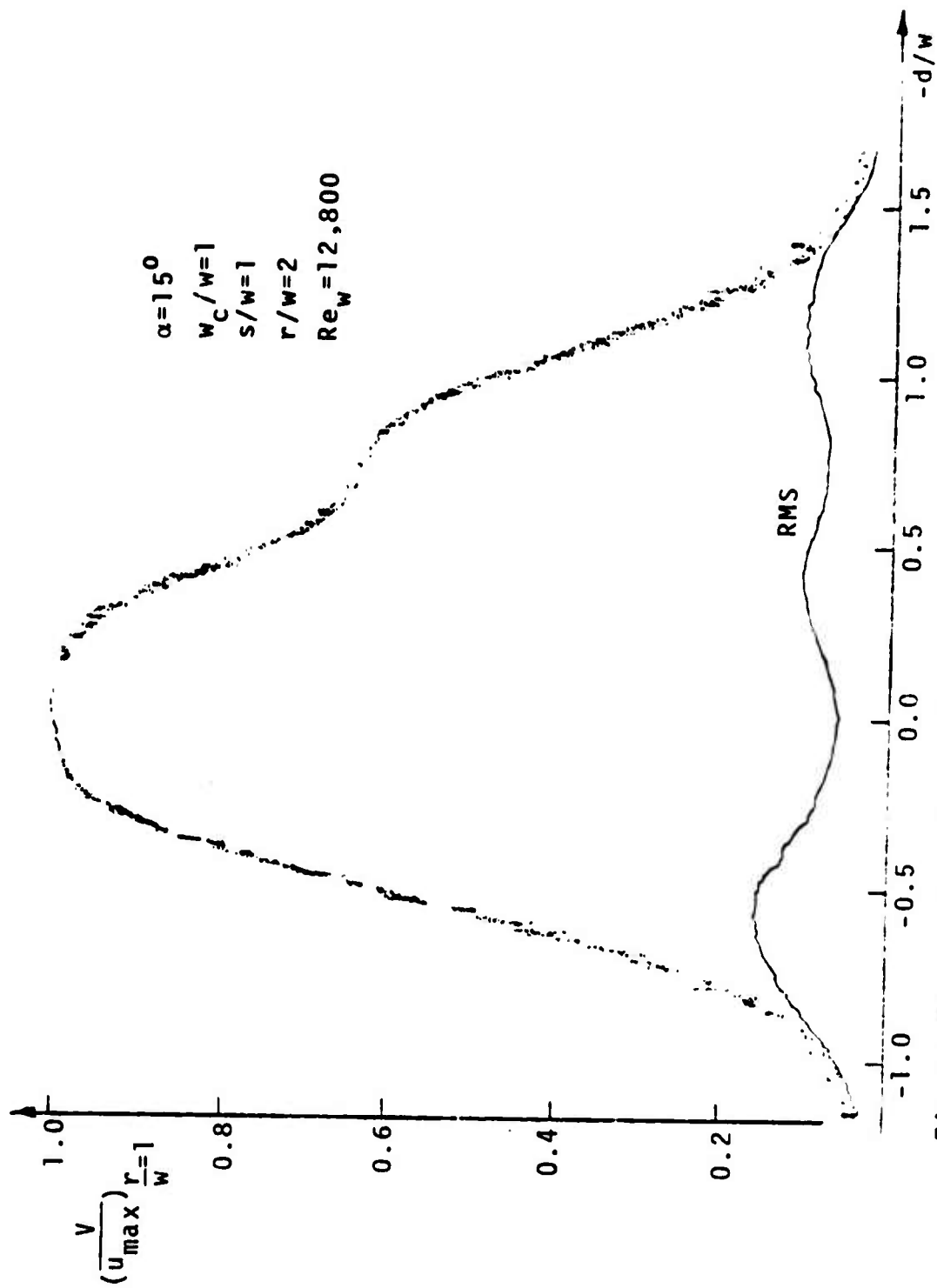
Figure 41 - Velocity and Turbulence Intensity Profiles Across the Jet at r/w=2.

α=15°
$w_c/w=1$
$s/w=1$
$r/w=2$
$Re_w=12,800$

RMS

-d/w

$\left(\frac{V}{u_{max}}\right)\frac{r}{w}=1$

102
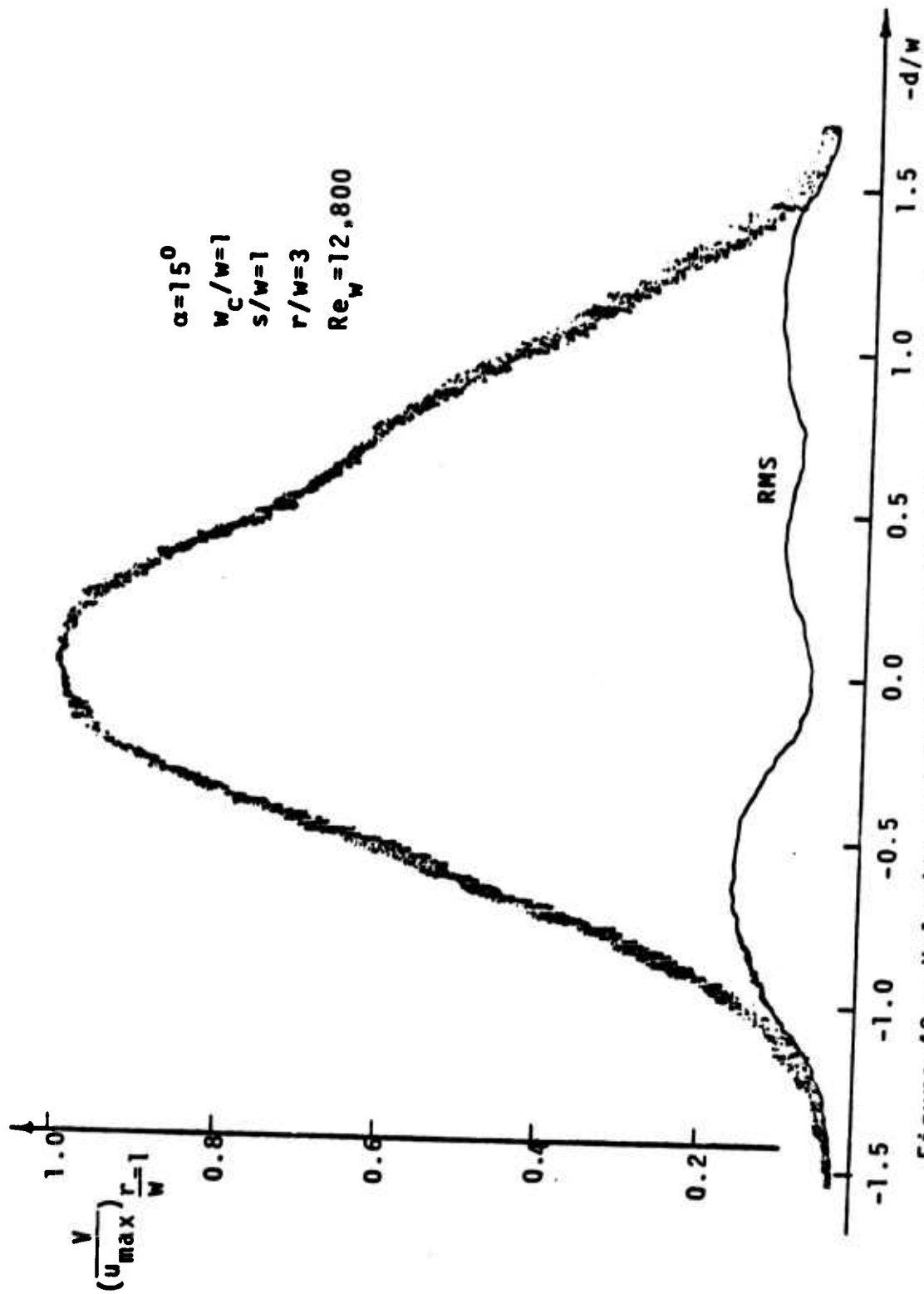
Figure 42 - Velocity and Turbulence Intensity Profiles Across the Jet at r/w=3.

$\alpha = 15^0$
$w_c/w = 1$
$s/w = 1$
$r/w = 3$
$Re_w = 12,800$
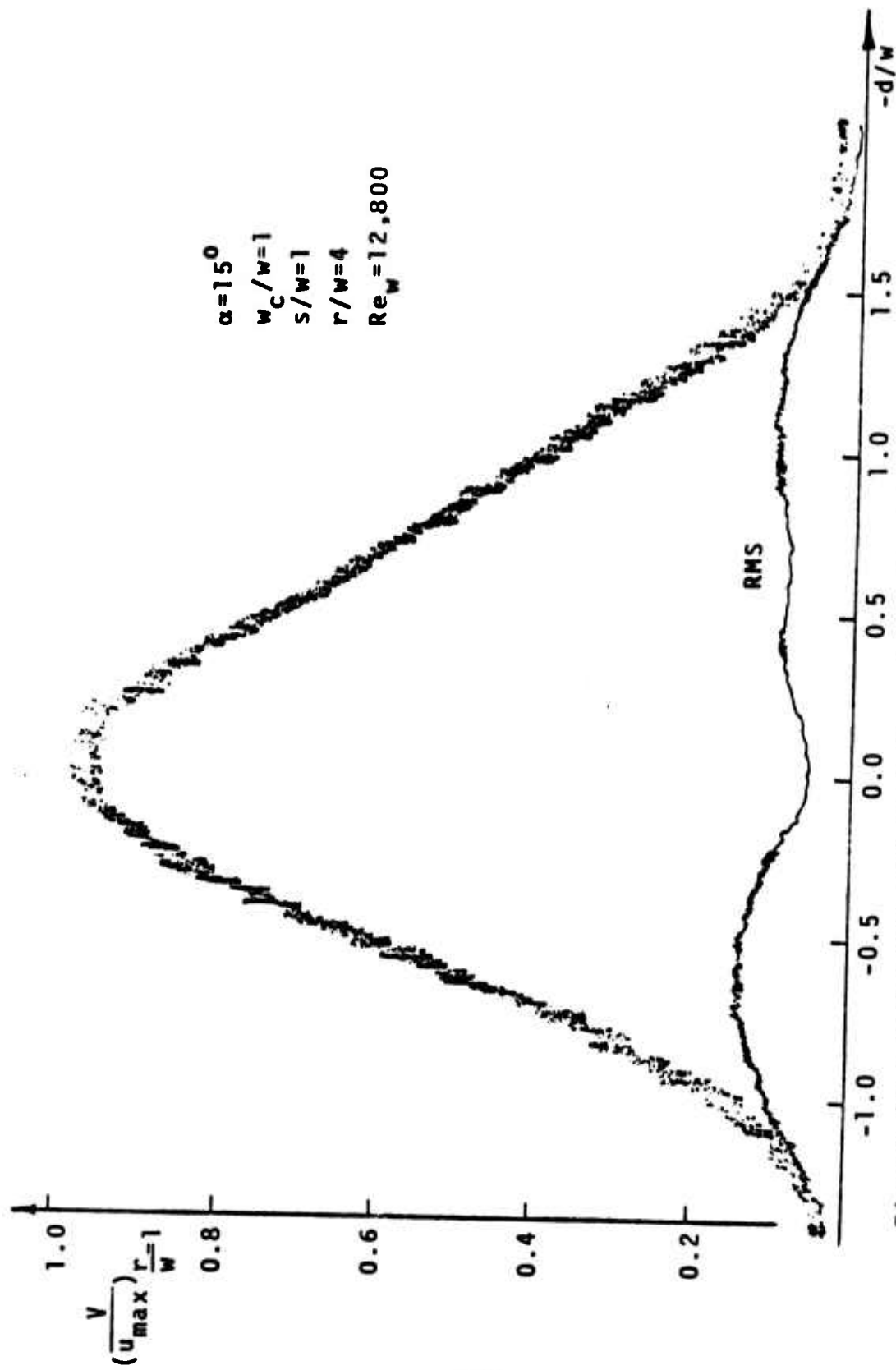
Figure 43 - Velocity and Turbulence Intensity Profiles Across the Jet at r/w=4.

104
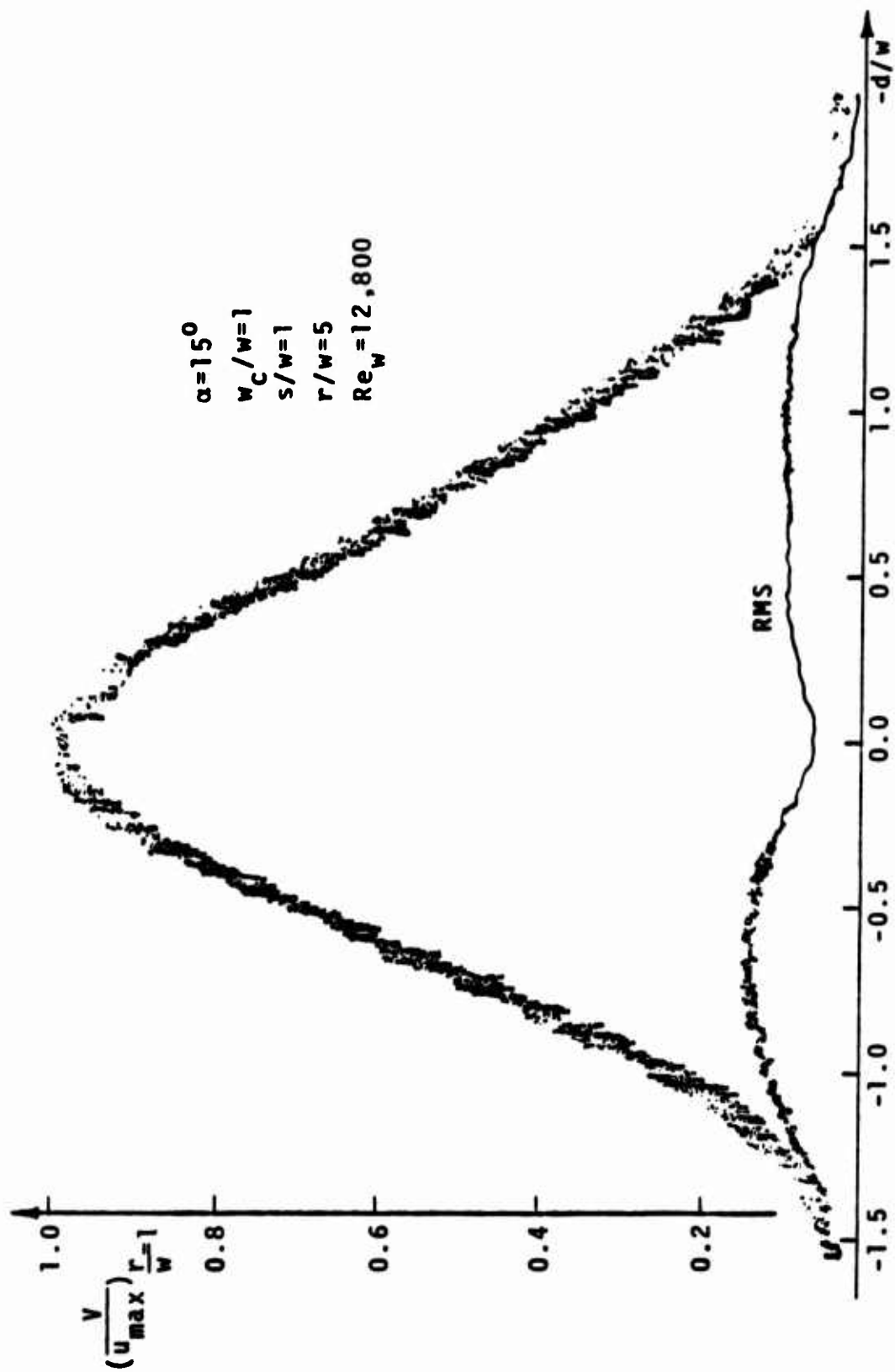
Figure 44 - Velocity and Turbulence Intensity Profiles Across the Jet at r/w=5.

$\alpha=15^{\circ}$
$w_c/w=1$
$s/w=1$
$r/w=5$
$Re_w=12,800$

$\left(\dfrac{V}{u_{max}}\right)\dfrac{r}{w}=1$

$-d/w$
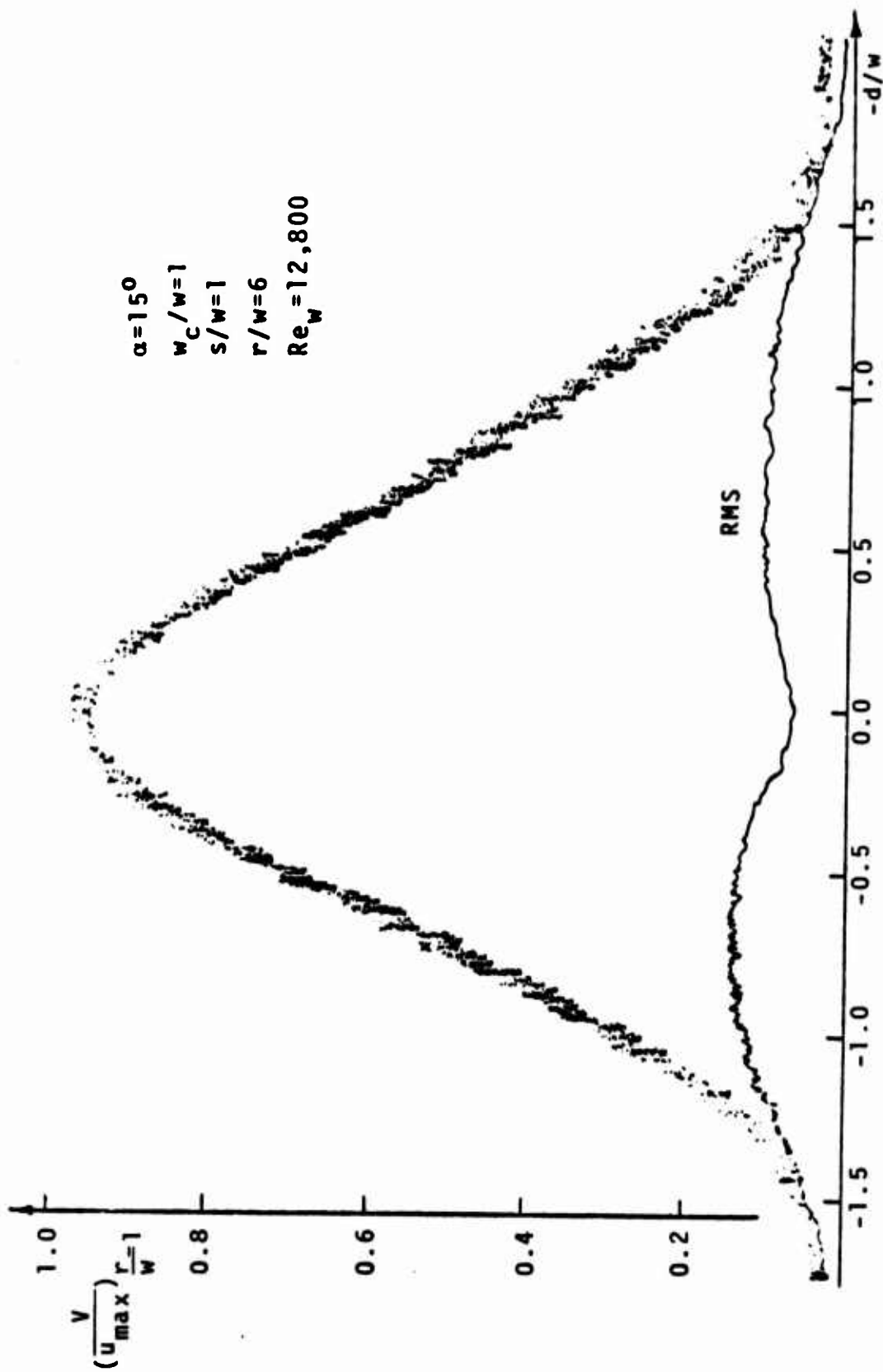
Figure 45 – Velocity and Turbulence Intensity Profiles Across the Jet at r/w=6.
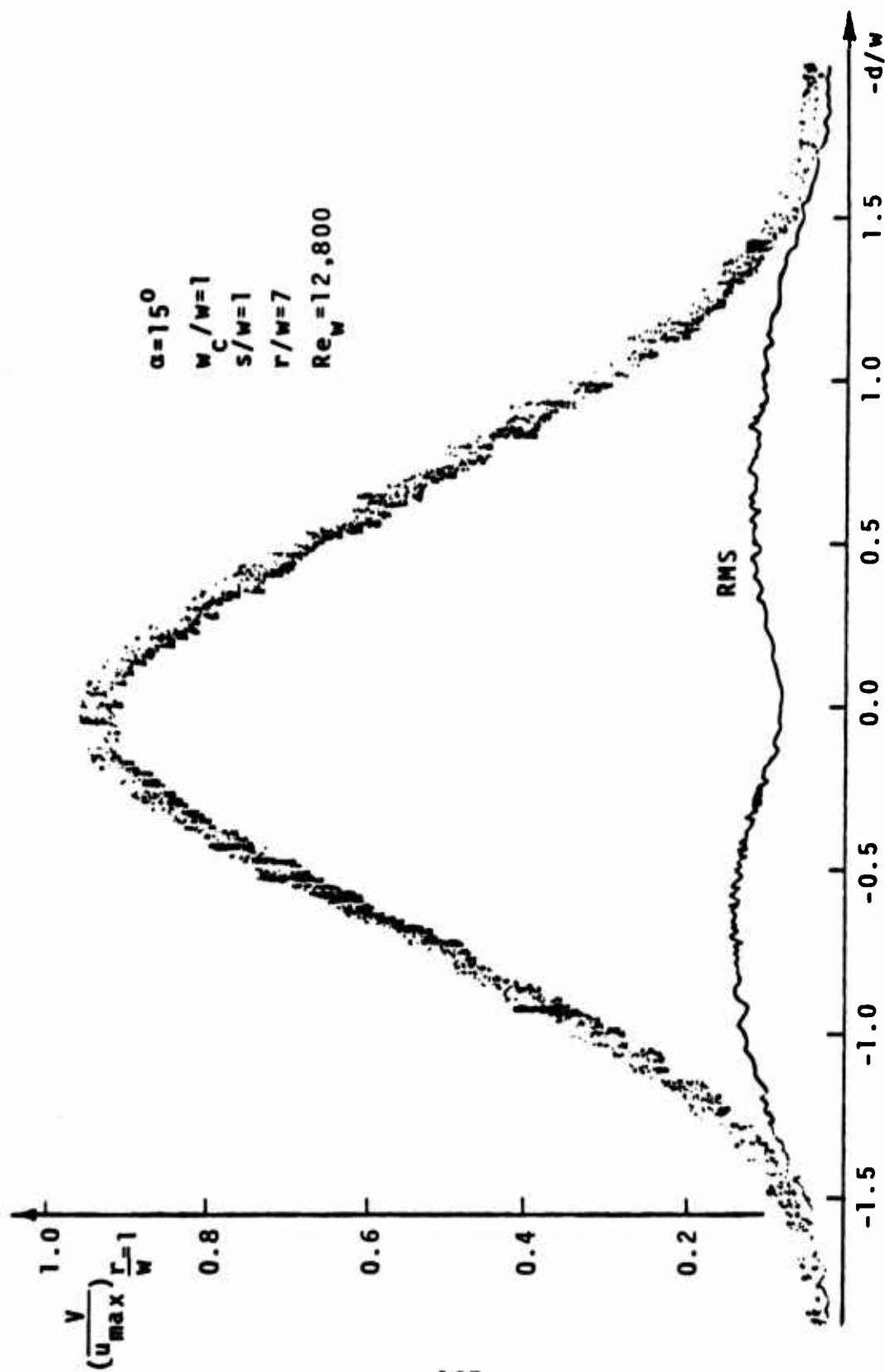
Figure 46 - Velocity and Turbulence Intensity Profiles Across the Jet at r/w=7.

$\alpha=15^{\circ}$
$w_c/w=1$
$s/w=1$
$r/w=7$
$Re_w=12,800$

RMS

$\left(\dfrac{V}{u_{max}}\right)\dfrac{r}{w}=1$

-d/w

107

Figure 47 - Velocity and Turbulence Intensity Profiles Across the Jet at r/w=8.

$\alpha = 15^{\circ}$
$w_c/w = 1$
$s/w = 1$
$r/w = 8$
$Re_w = 12,800$

RMS

$\left(\dfrac{v}{u_{max}}\right)\dfrac{r}{w} = 1$

108
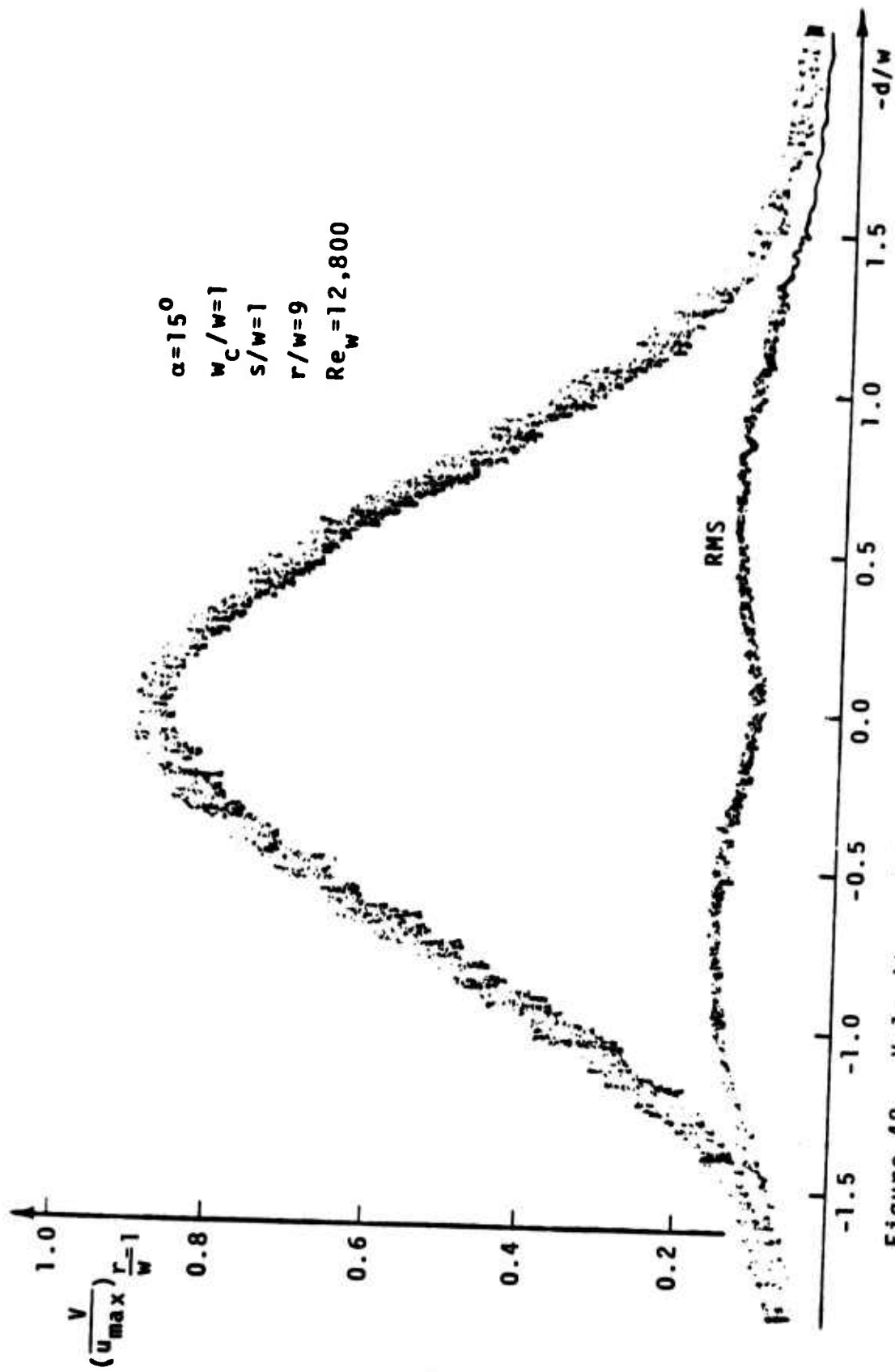
Figure 48 - Velocity and Turbulence Intensity Profiles Across the Jet at r/w=9.

$\alpha=15^0$
$w_c/w=1$
$s/w=1$
$r/w=9$
$Re_w=12,800$
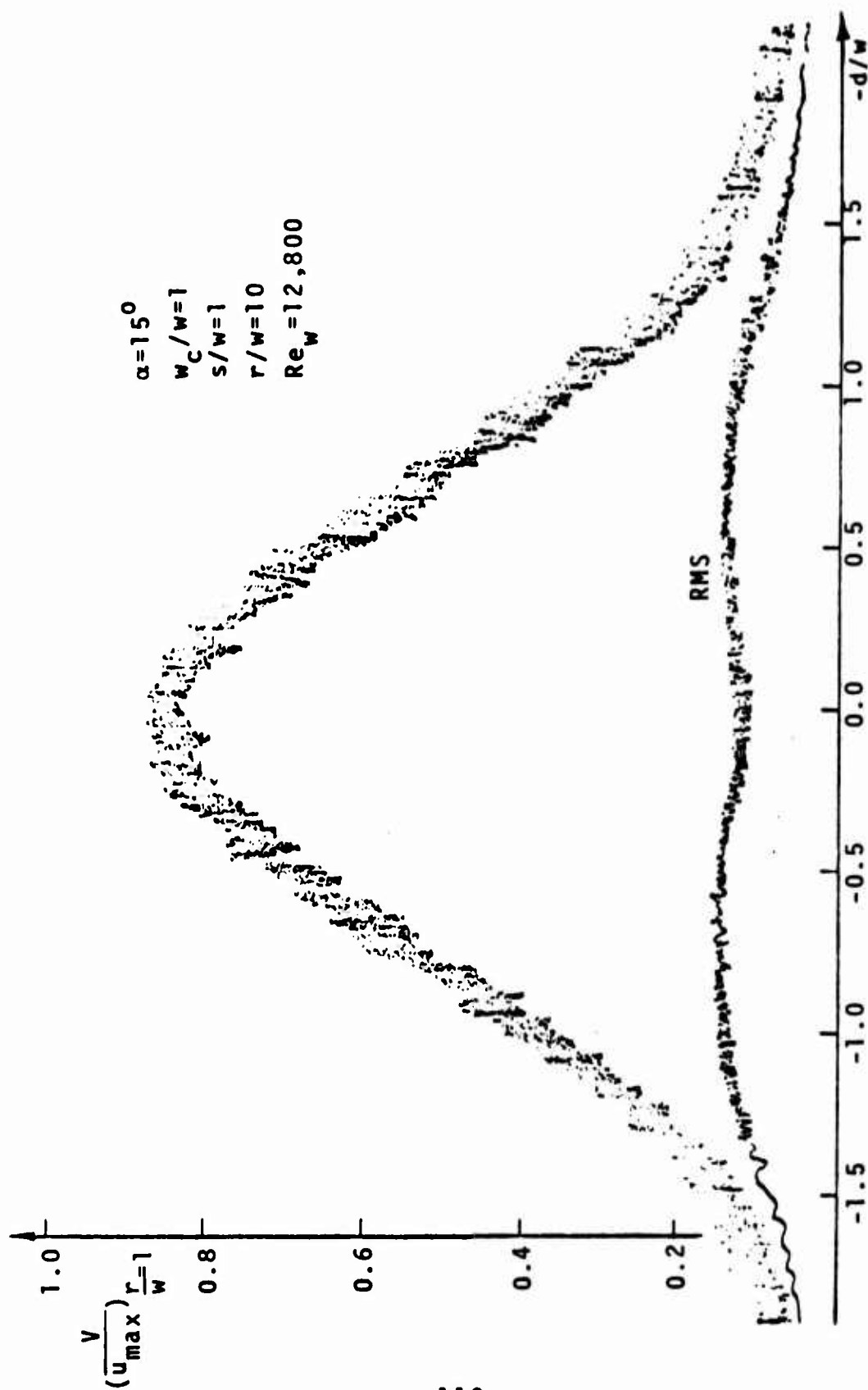
Figure 49 - Velocity and Turbulence Intensity Profiles Across the Jet at r/w=10.

$\alpha=15^{\circ}$
$w_c/w=1$
$s/w=1$
$r/w=10$
$Re_w=12,800$

RMS

$\left(\dfrac{V}{u_{max}}\right)\dfrac{r}{w}=1$
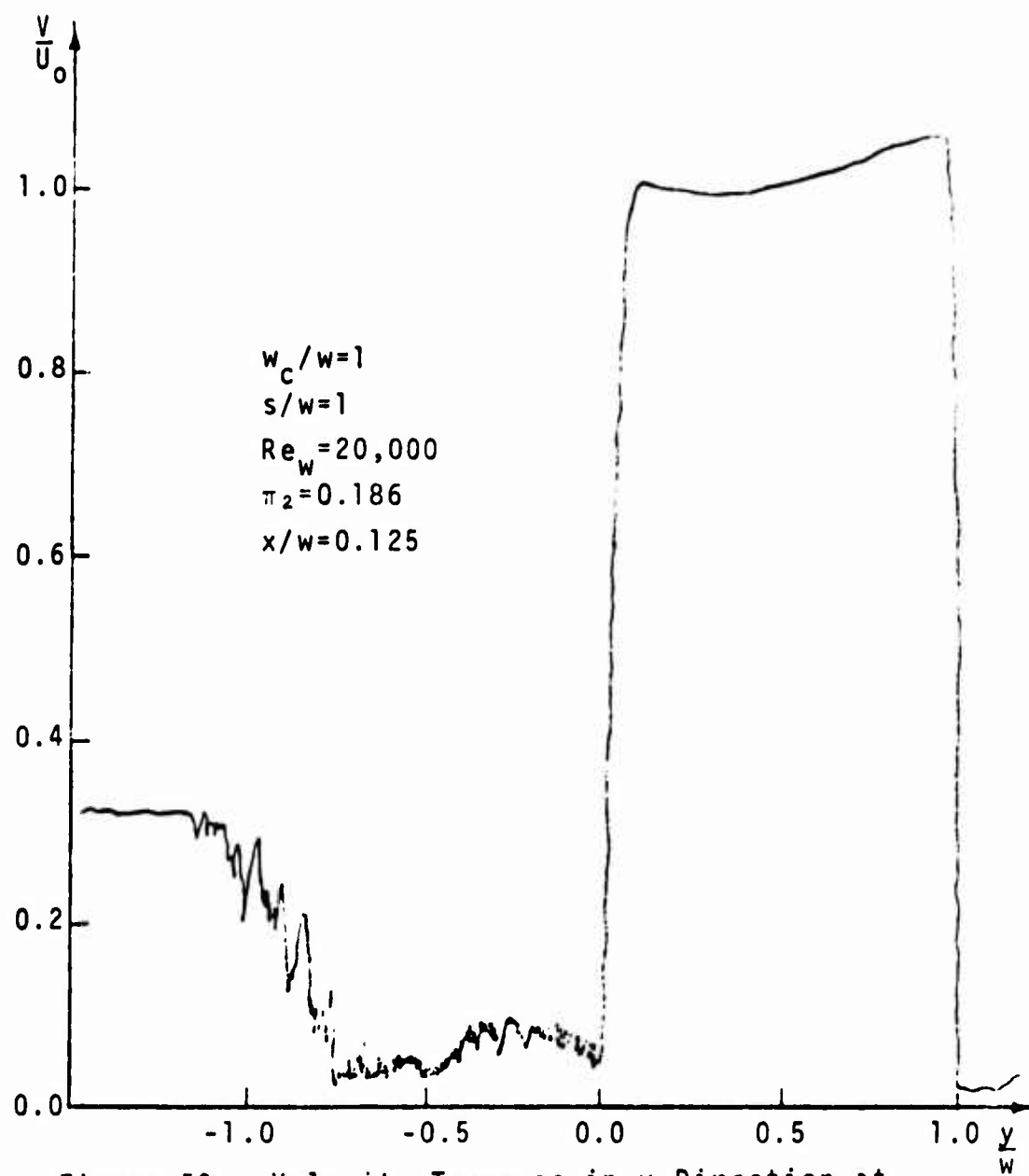
Figure 50 - Velocity Traverse in y-Direction at x/w=0.125.

111
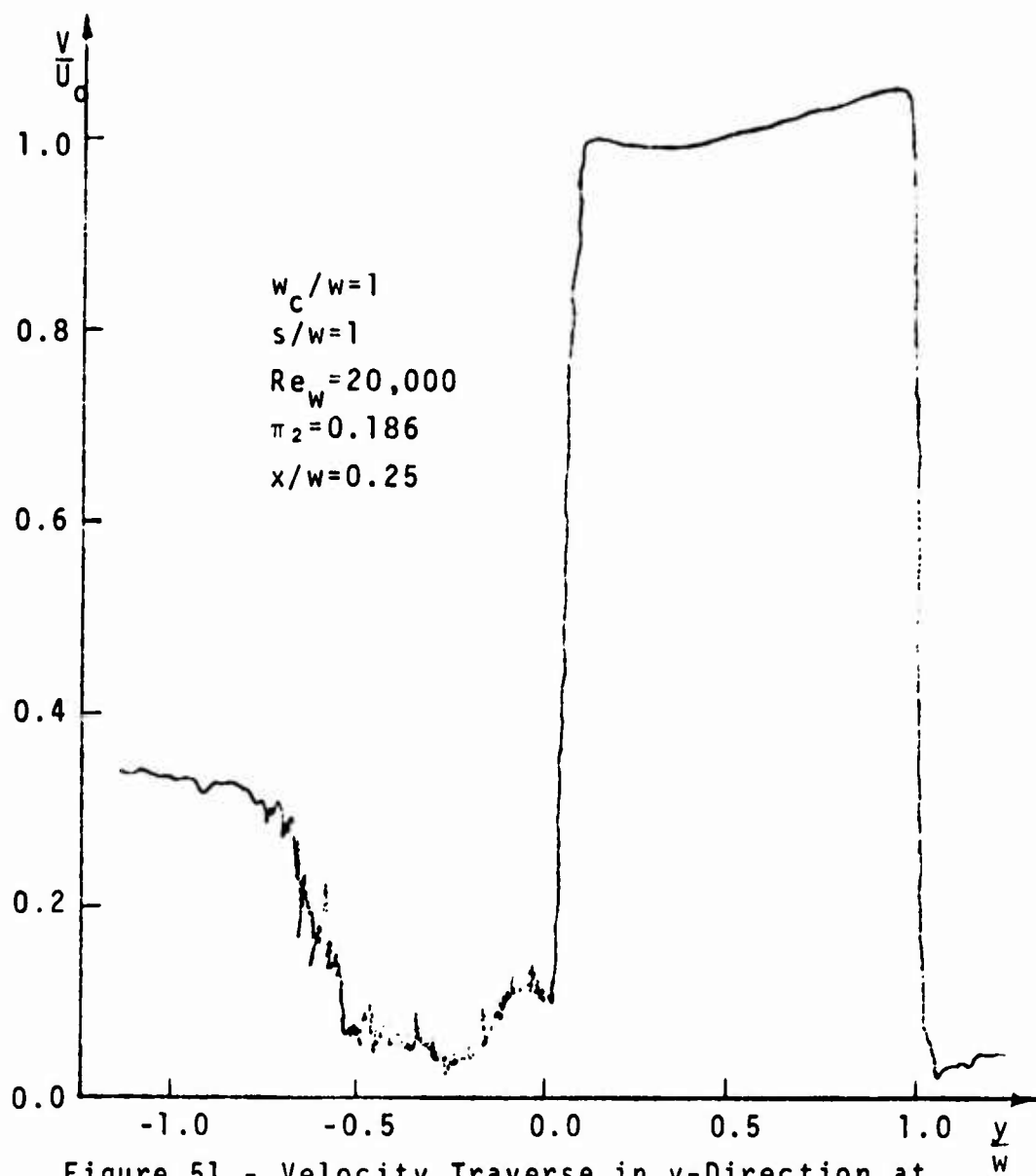
Figure 51 - Velocity Traverse in y-Direction at x/w=0.25.

112
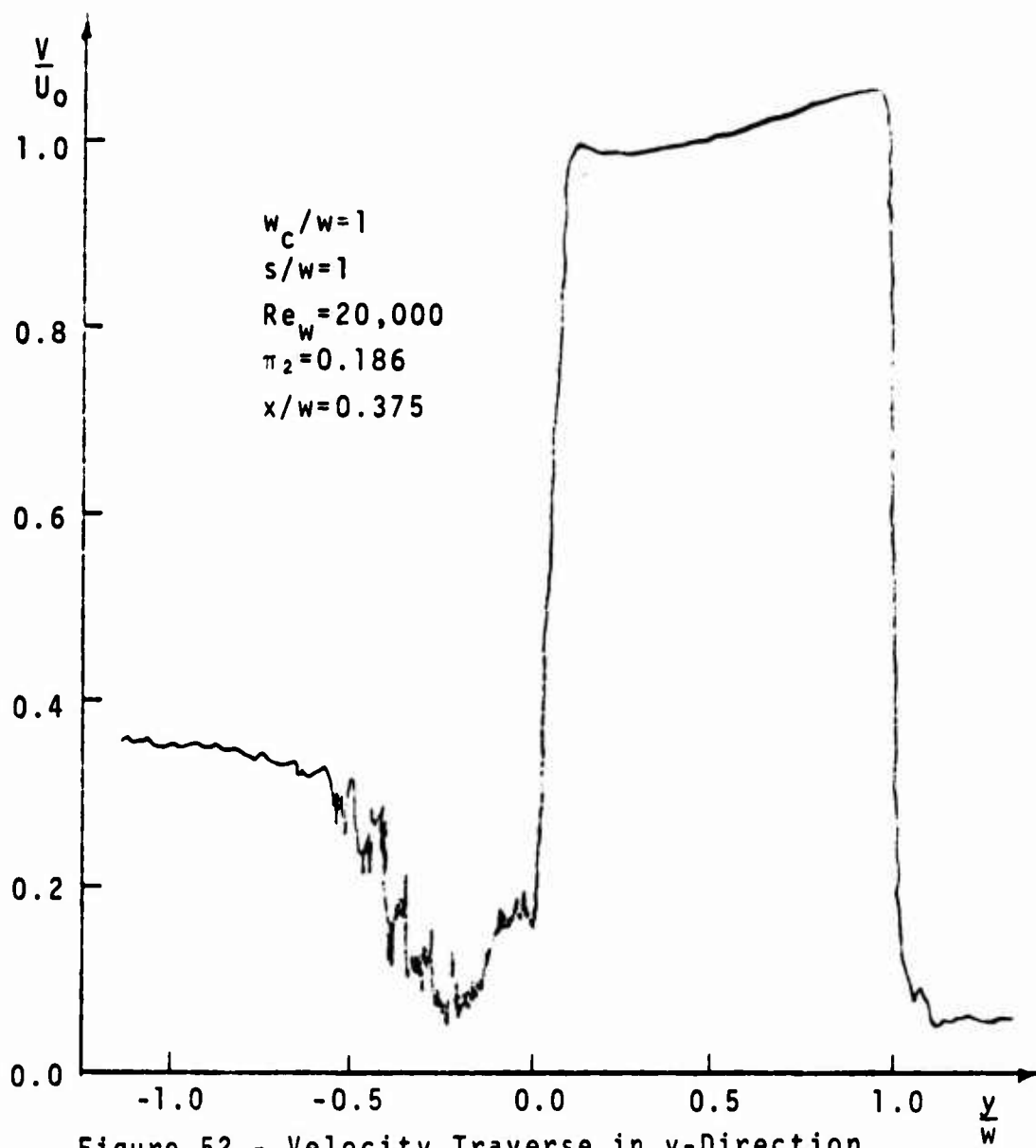
Figure 52 - Velocity Traverse in y-Direction at x/w=0.375.

113
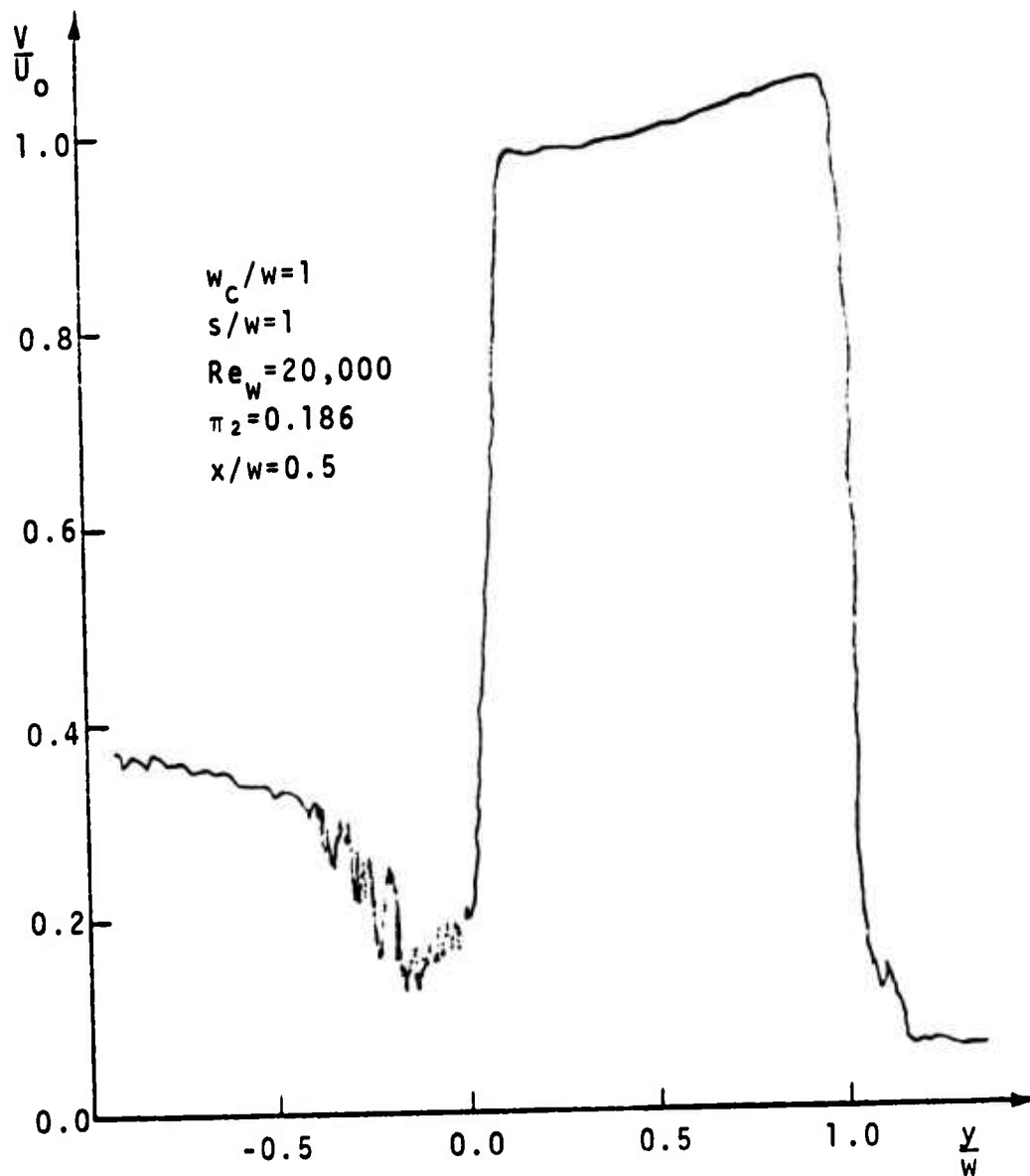
Figure 53 - Velocity Traverse in the y-Direction
at x/w=0.5.

114
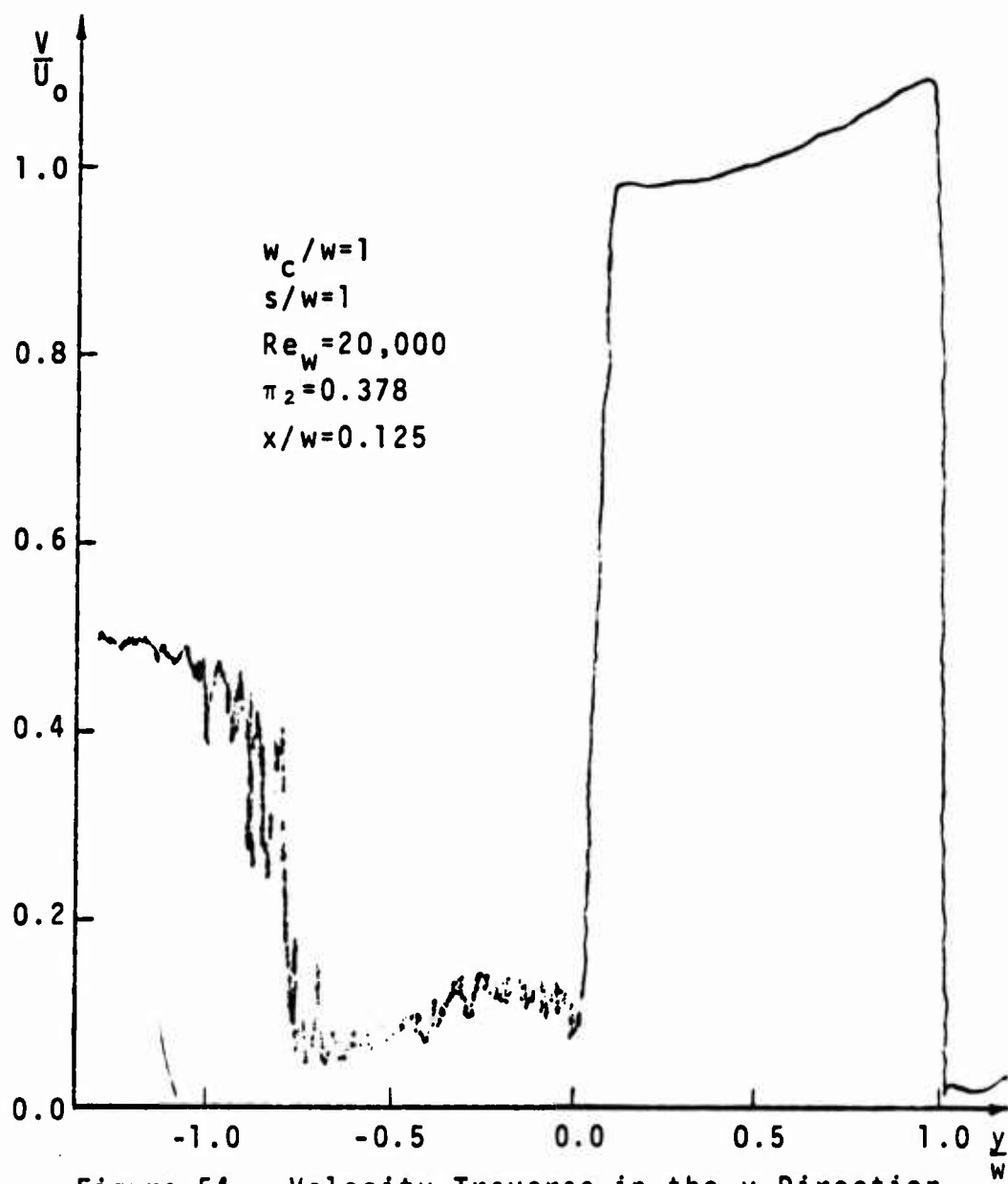
Figure 54 - Velocity Traverse in the y-Direction at x/w=0.125.

Plot axes: vertical axis labeled $\frac{V}{U_o}$ with values 0.0, 0.2, 0.4, 0.6, 0.8, 1.0; horizontal axis labeled $\frac{y}{w}$ with values -1.0, -0.5, 0.0, 0.5, 1.0.

Annotations on plot:
$w_c/w=1$
$s/w=1$
$Re_w=20{,}000$
$\pi_2=0.378$
$x/w=0.125$

Power Jet Nozzle

96 ft/sec

$w_c/w=1$
$s/w=1$
$Re_w=20,000$
$\pi_2=0.186$

18
28
32
35
36
39
43
48
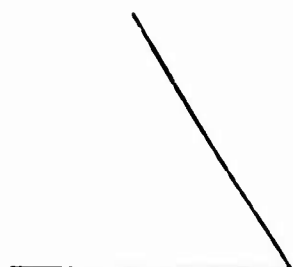
Control Jet
Nozzle
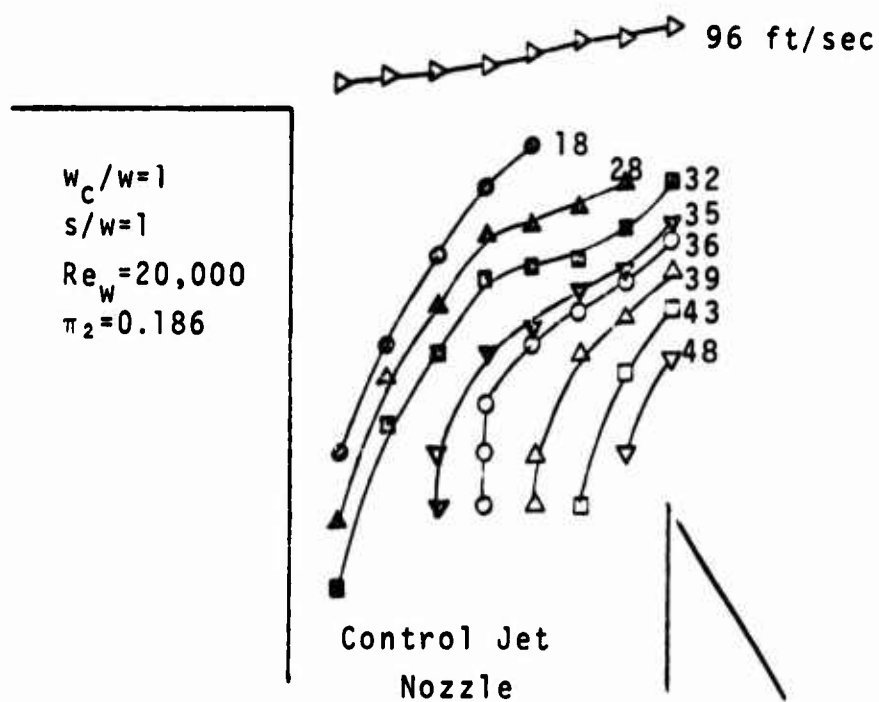
Figure 55 - A Plot of Lines of Constant Speed in
Feet Per Second in the Interaction Zone.

116
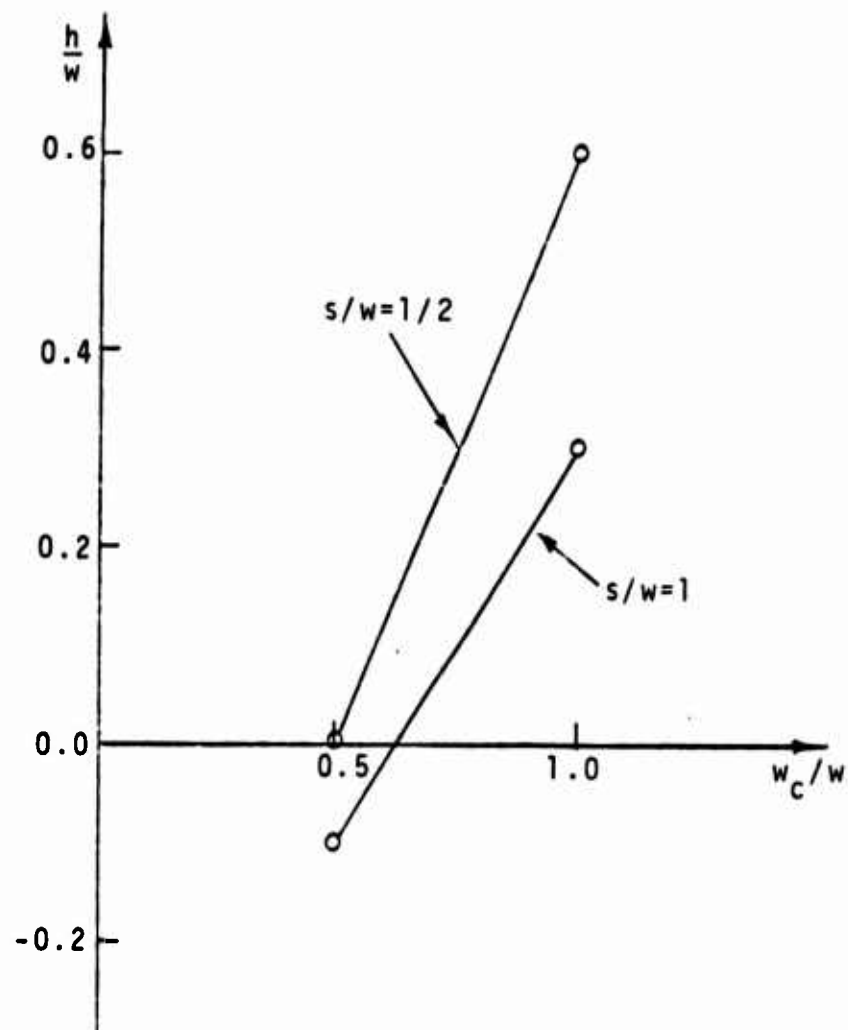
Figure 56 - A Plot of the Experimentally-
 Determined Values of the Dimensionless
Separation Distance Versus w_c/w for
Different Values of s/w.

117
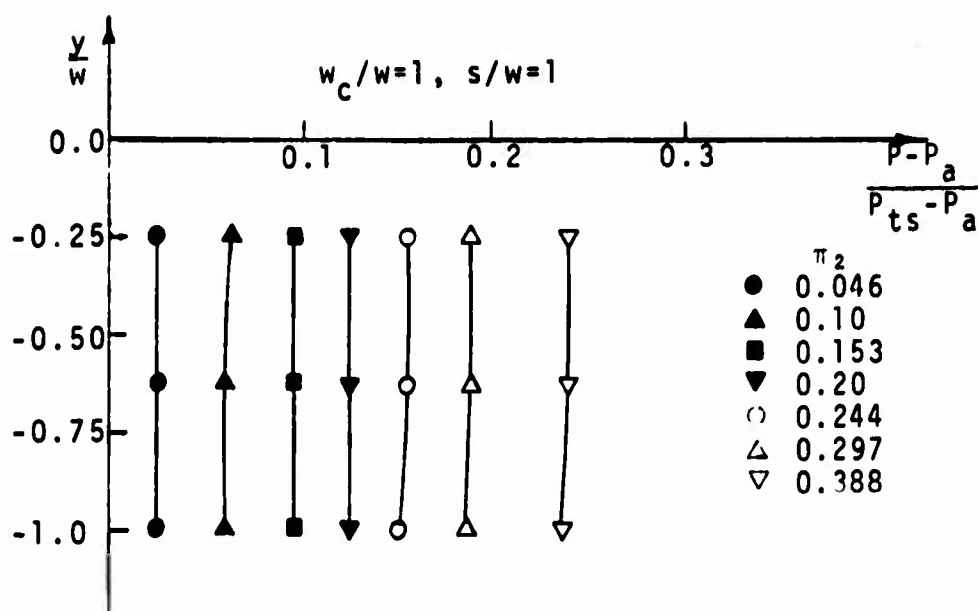
Figure 57 - Pressure Variation Along the Setback
Wall for Different Values of the Dimensionless
Pressure π_2.
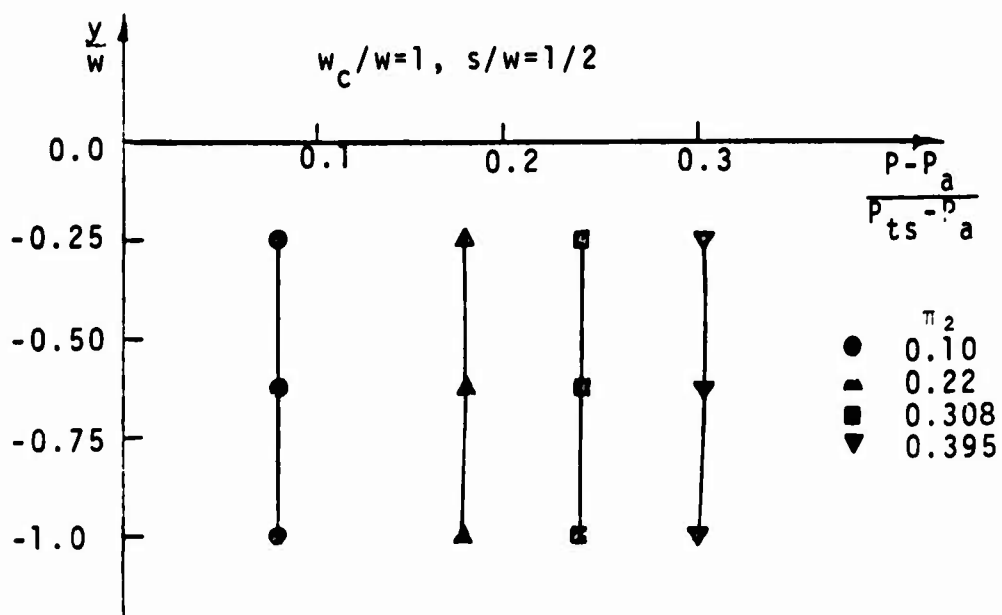
Figure 58 - Pressure Variation Along the Setback
Wall for Different Values of the Dimensionless
Pressure π_2.

118
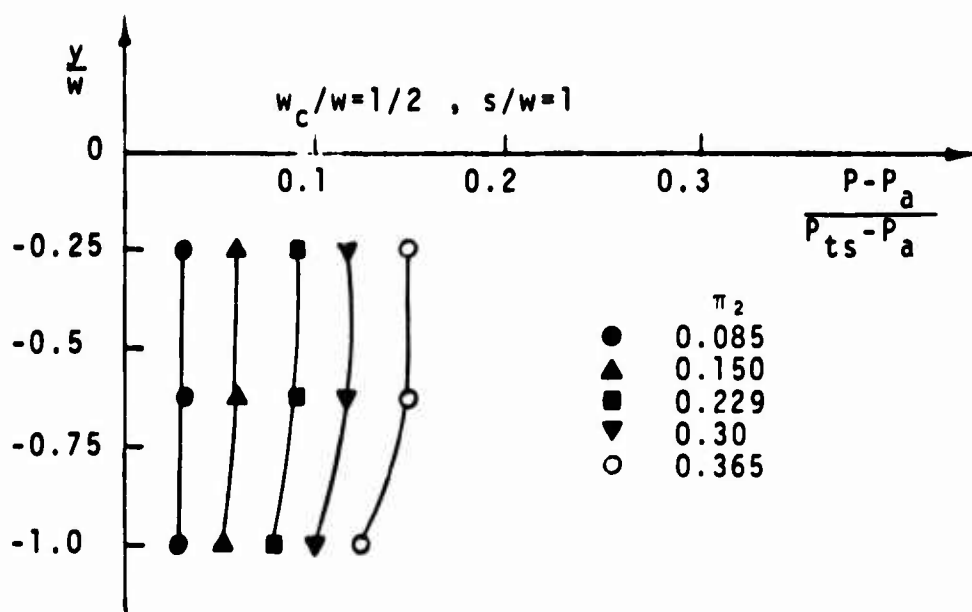
Figure 59 - Pressure Variation Along the Setback Wall for Different Values of the Dimensionless Pressure π_2.
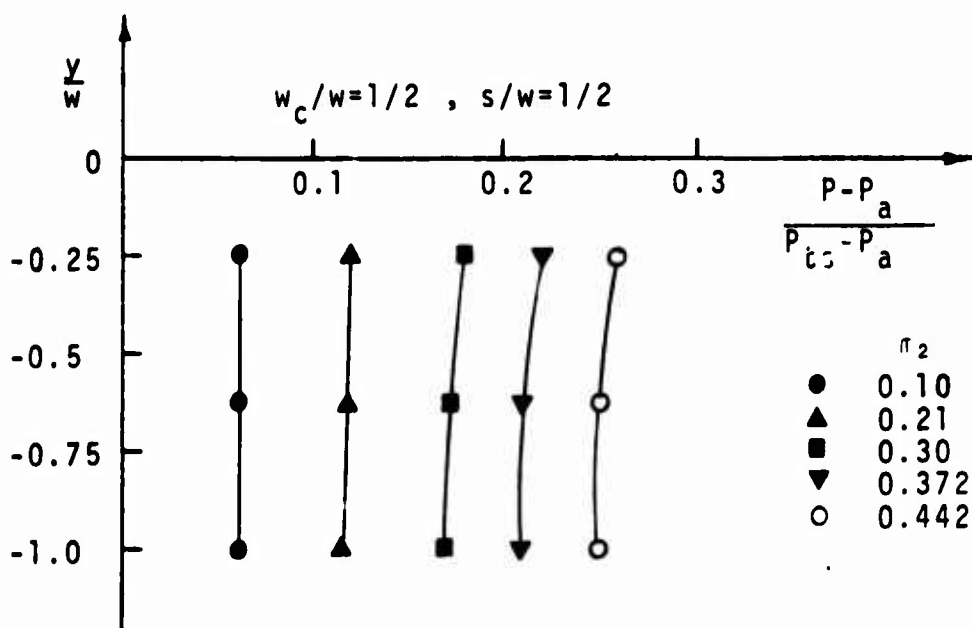
Figure 60 - Pressure Variation Along the Setback Wall for Different Values of the Dimensionless Pressure π_2.
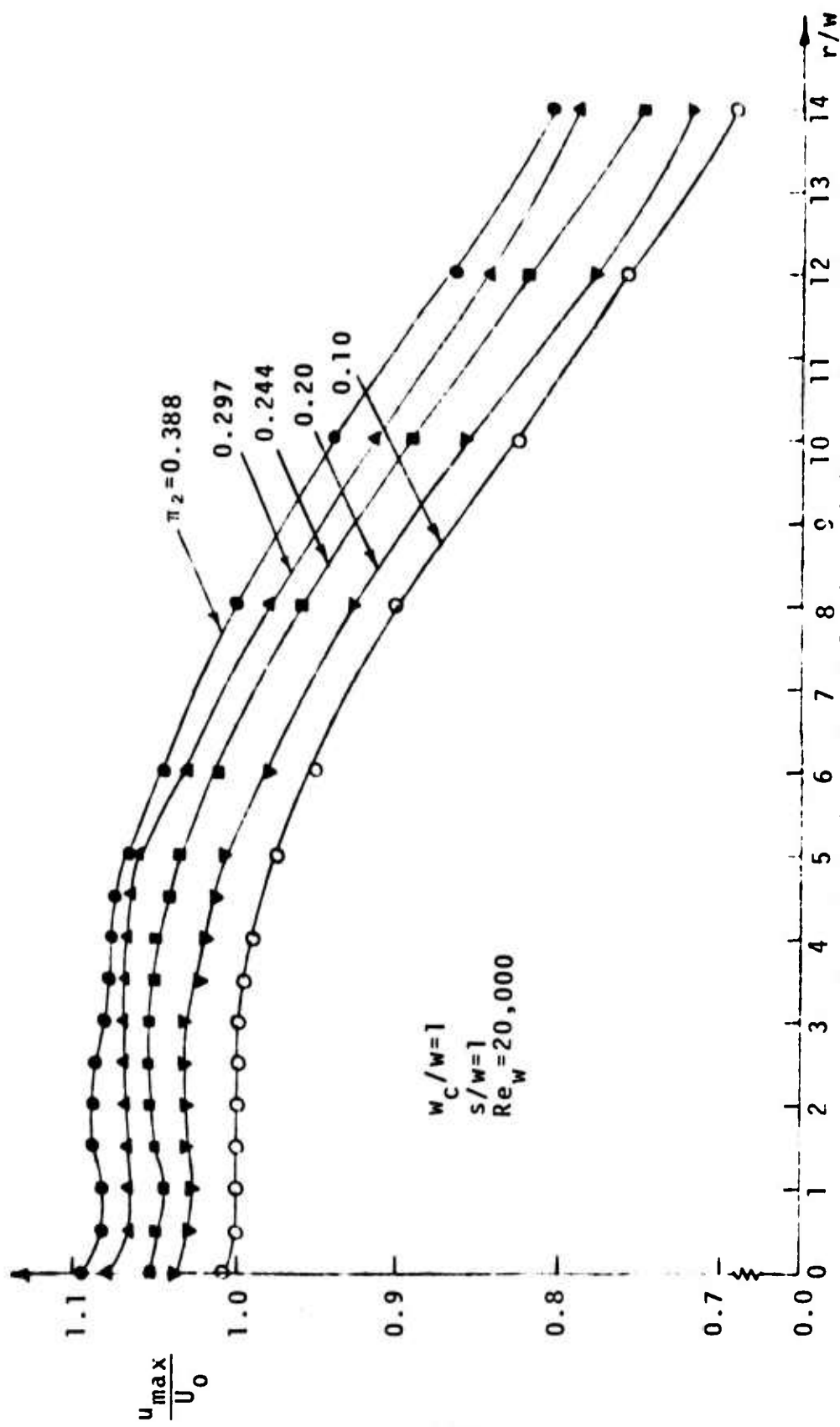
Figure 61 - Variation of Maximum Jet Velocity with r/w for Different Values of the Dimensionless Control Jet Pressure π_2.
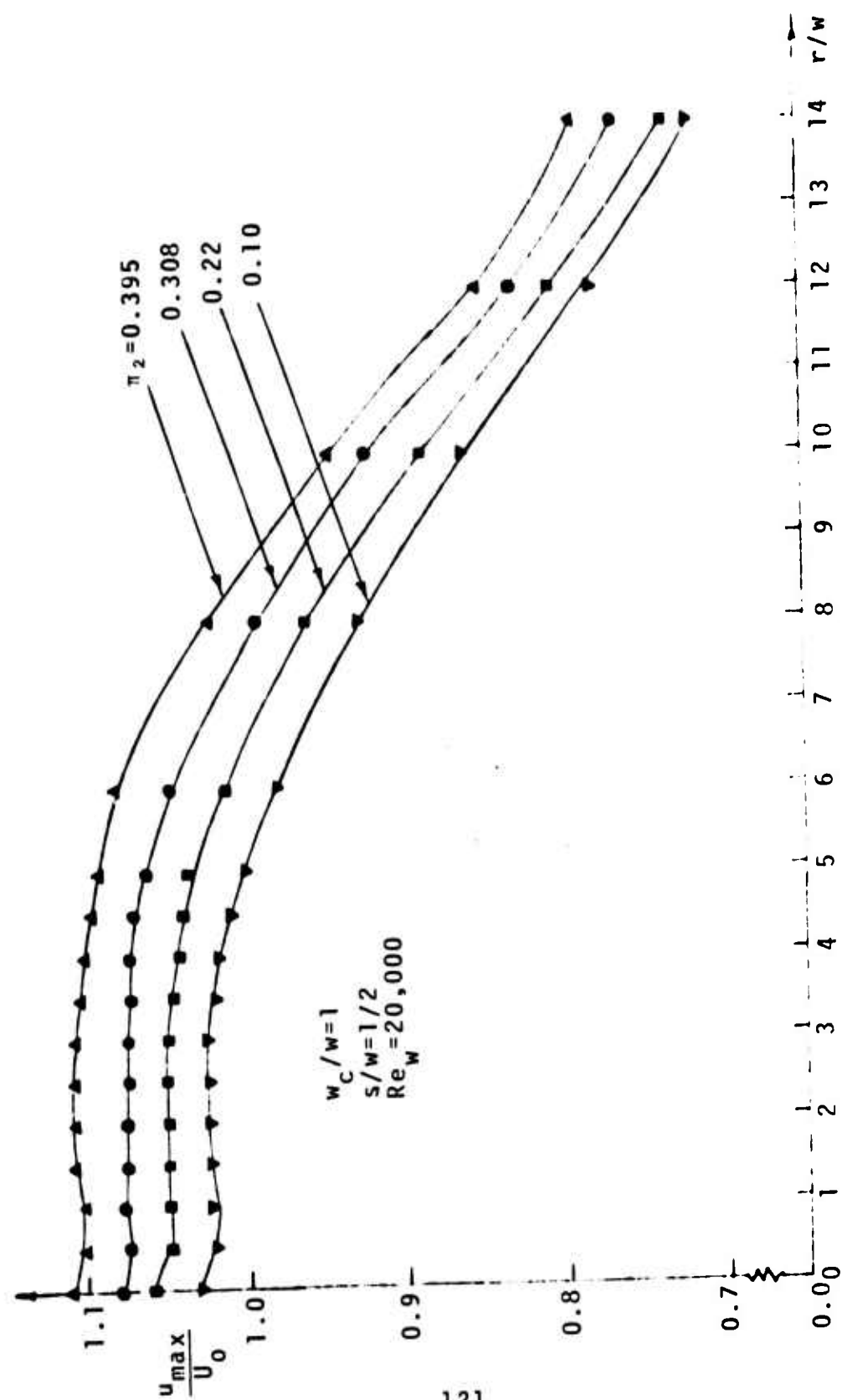
Figure 62 - Variation of Maximum Jet Velocity with r/w for Different Values of the Dimensionless Control Jet Pressure π_2.

121
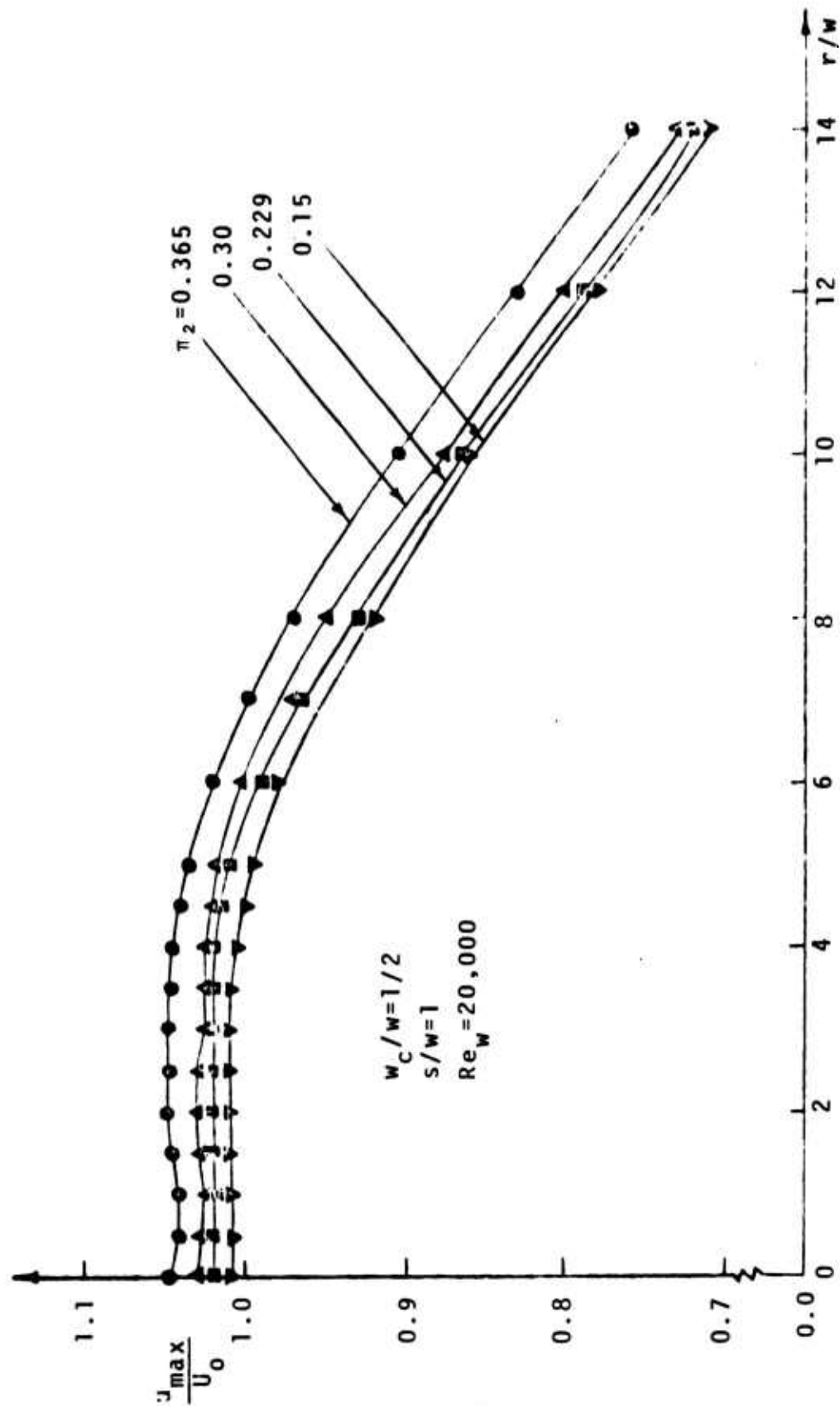
Figure 63 - Variation of Maximum Jet Velocity with r/w for Different
Values of the Dimensionless Control Jet Pressure π_2.

122
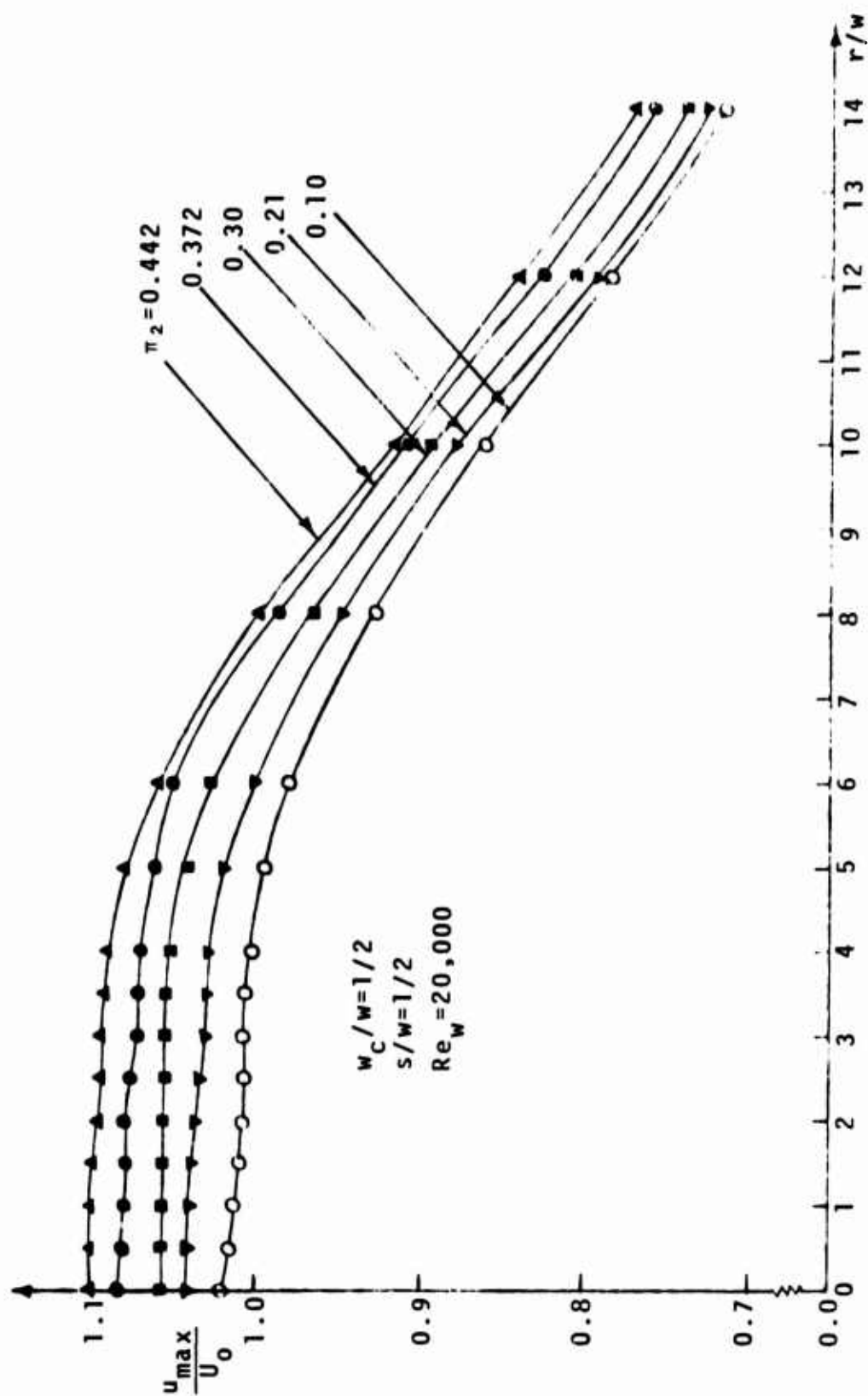
Figure 64 - Variation of Maximum Jet Velocity with r/w for Different Values of the Dimensionless Control Jet Pressure π_2.

123
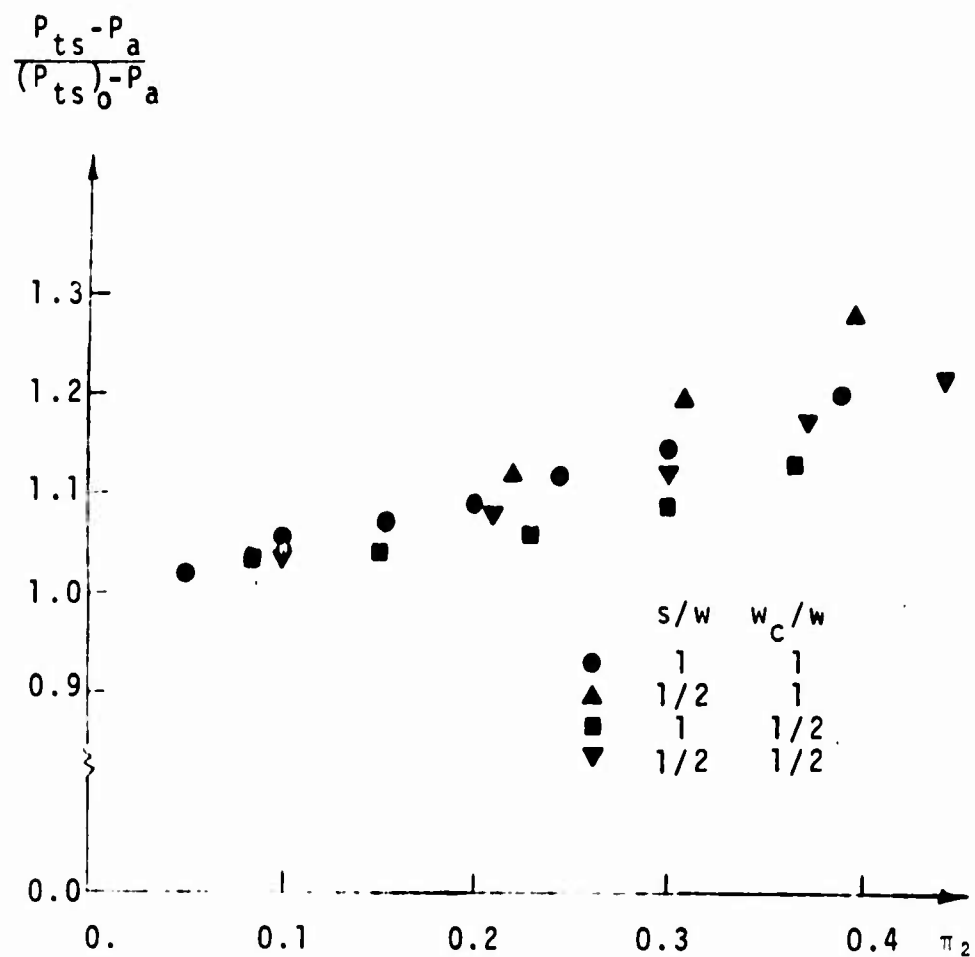
Figure 65 - Variation of the Dimensionless Power Jet Total Pressure with the Dimensionless Control Jet Total Pressure for Different Values of Setback and Width of the Control Jet Nozzle.

124
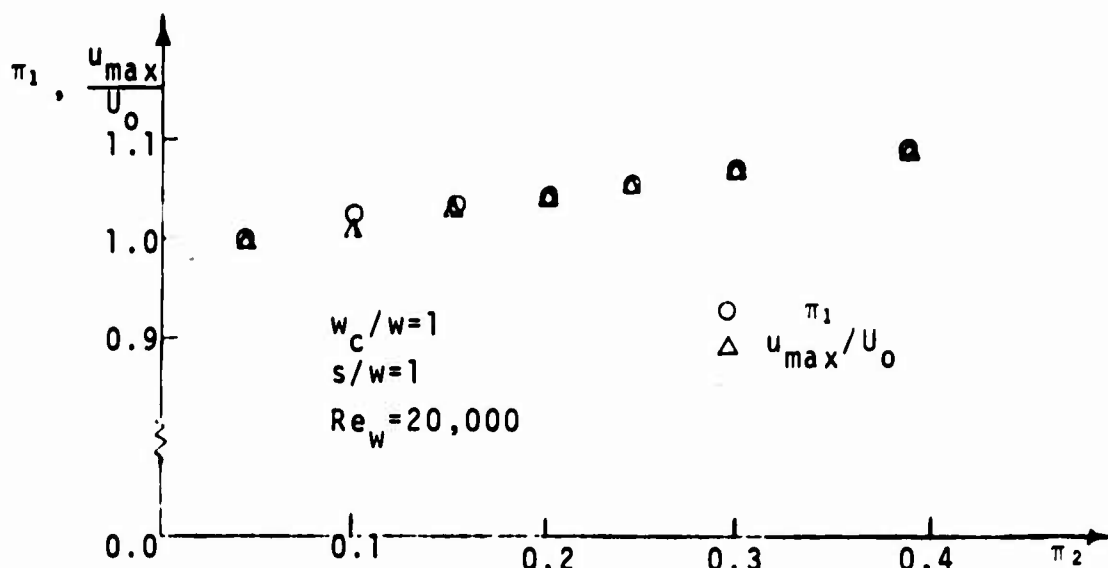
Figure 66 - Comparison Between the Dimensionless
Power Jet Total Pressure π_1 and the Dimensionless
Maximum Jet Velocity for Various Values of the
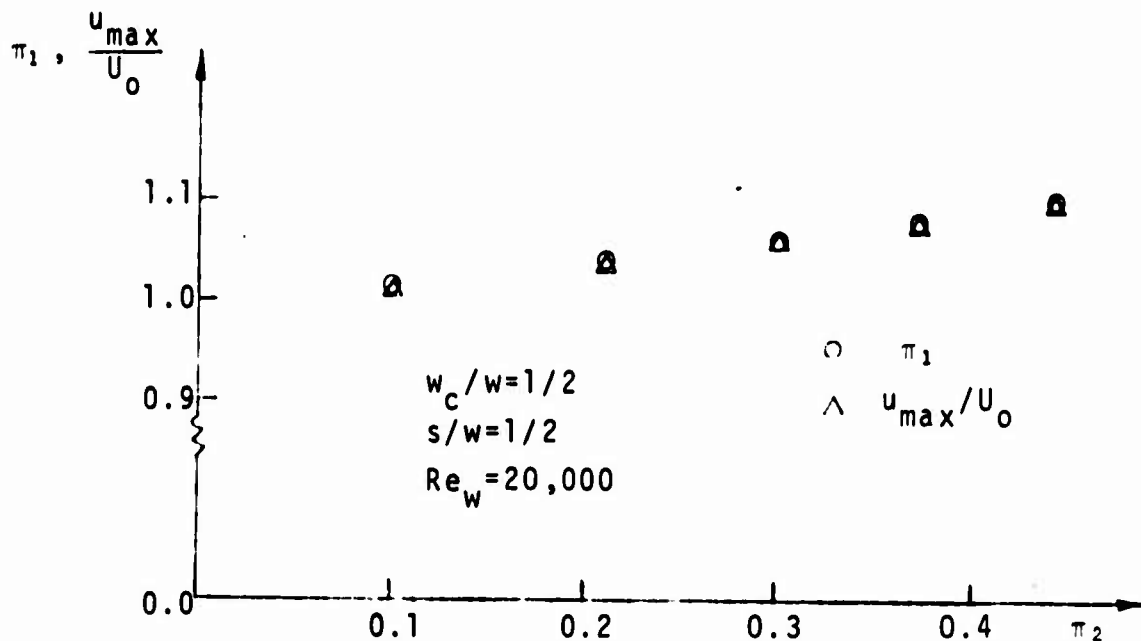Dimensionless Control Jet Total Pressure π_2.
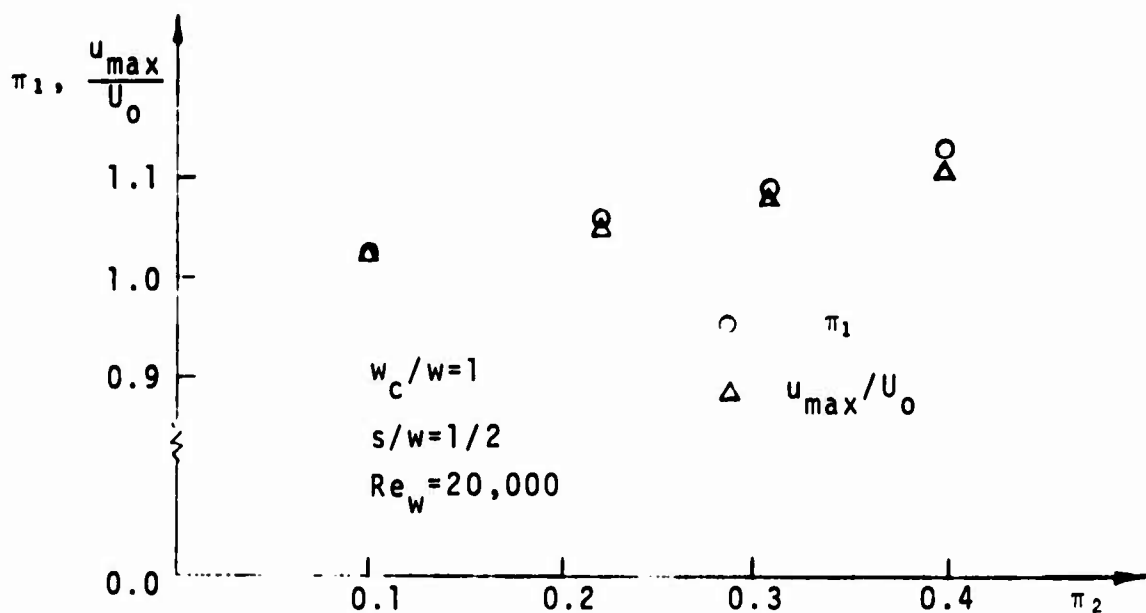
Figure 67 - Comparison Between the Dimensionless
Power Jet Total Pressure π_1 and the Dimensionless
Maximum Jet Velocity for Various Values of the
Dimensionless Control Jet Total Pressure π_2.

125
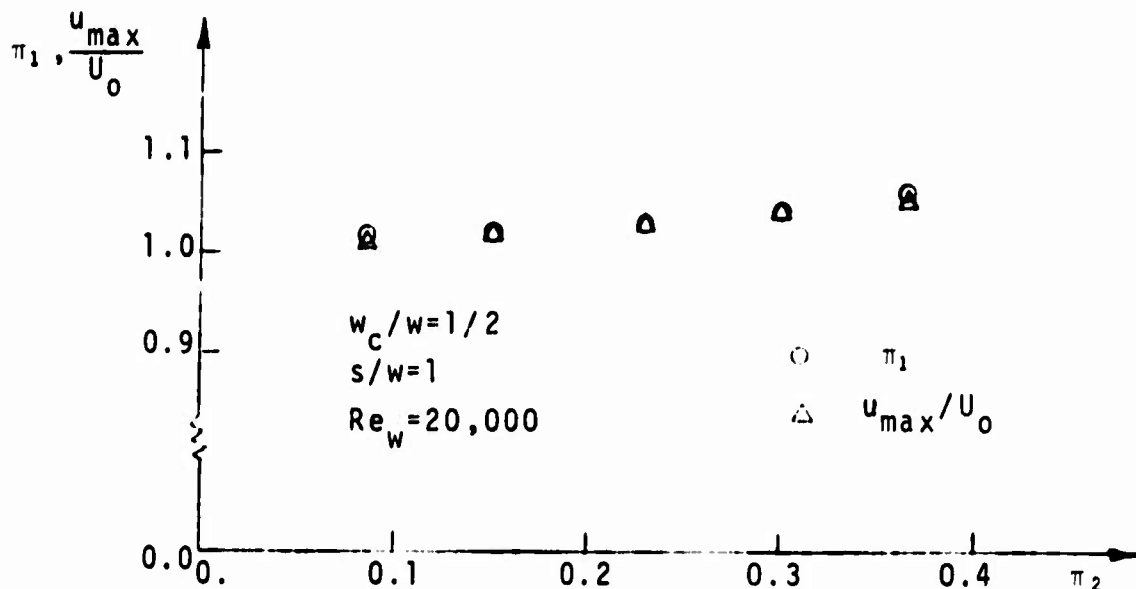
Figure 68 - Comparison Between the Dimensionless
Power Jet Total Pressure π_1 and the Dimensionless
Maximum Jet Velocity for Various Values of the
Dimensionless Control Jet Total Pressure π_2.

Figure 69 - Comparison Between the Dimensionless
Power Jet Total Pressure π_1 and the Dimensionless
Maximum Jet Velocity for Various Values of the D
Dimensionless Control Jet Total Pressure π_2.

126
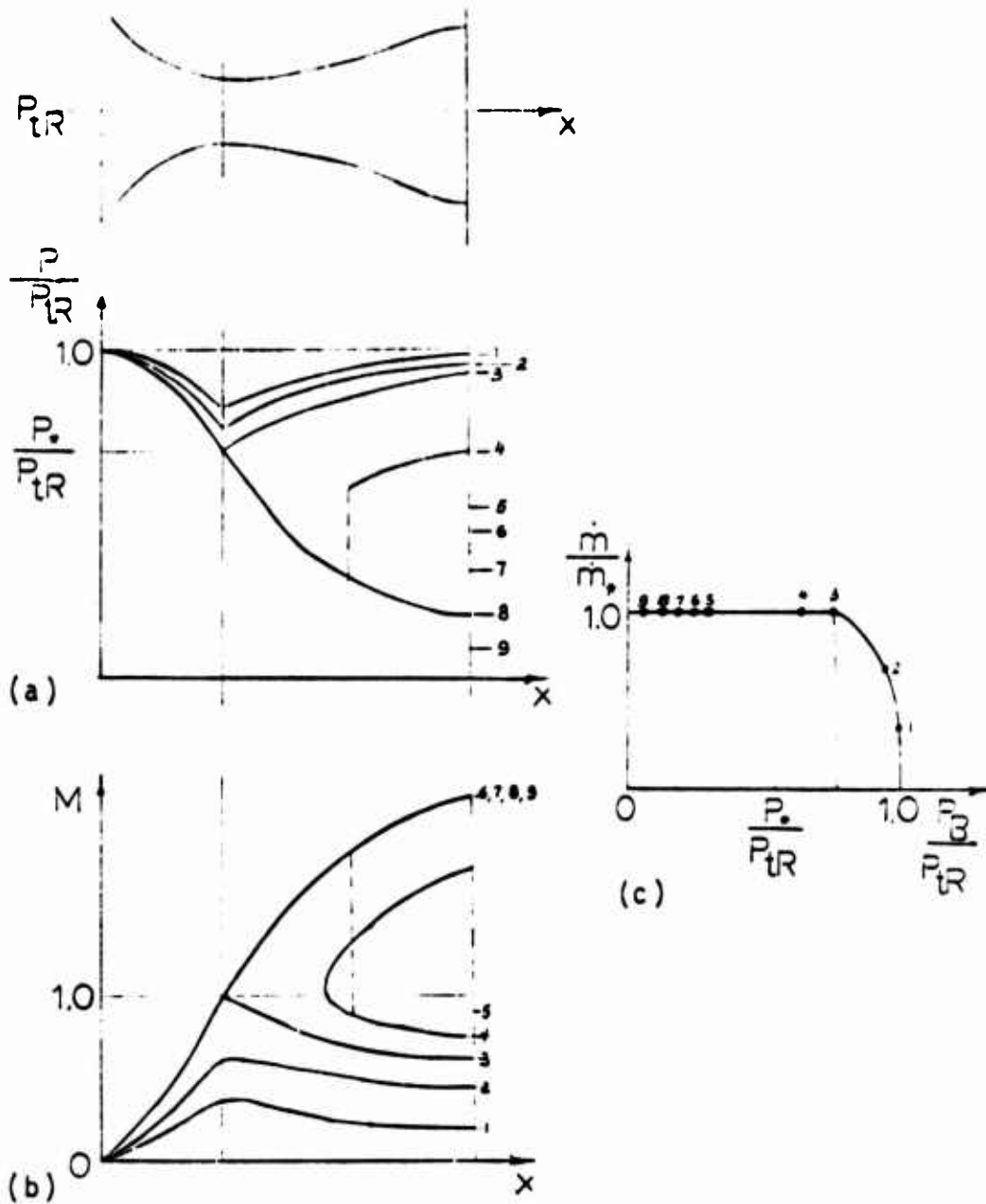
Figure 70 - Performance Curves for a Convergent-Divergent Nozzle with Varying Ratio of the Back Pressure to the Total Pressure at the Inlet. The Broken Lines Denotes Shock Waves. a) Variation of Pressure in the Nozzle. b) Variation of the Mach Number in the Nozzle. c) Relationship Between the Rate of Mass Flow and the Ratio of the Back Pressure to the Total Pressure in the Reservoir (from Reference [20]).
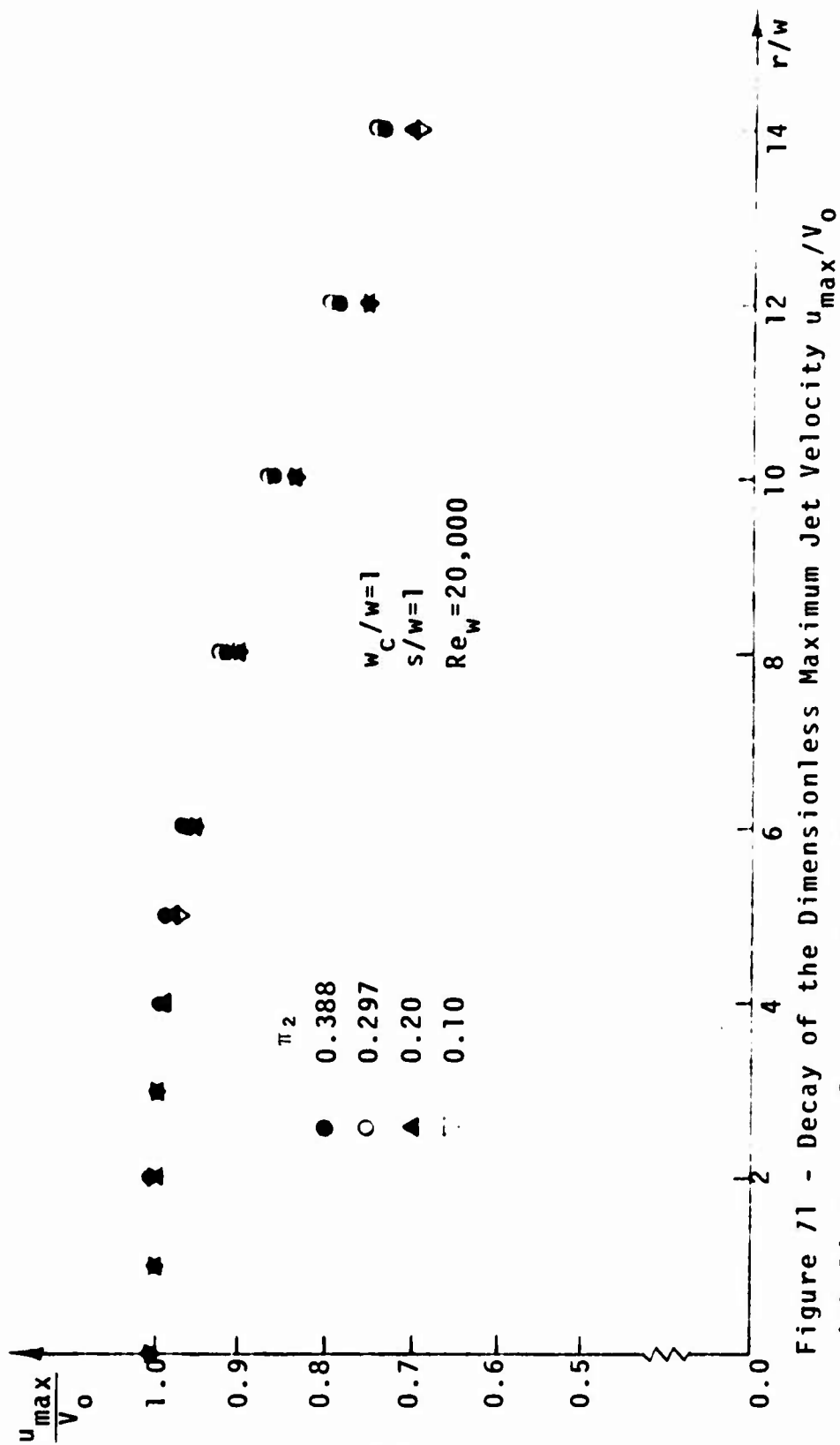
127

Figure 71 - Decay of the Dimensionless Maximum Jet Velocity u_{max}/V_o with Distance from the Pivot Point.

128
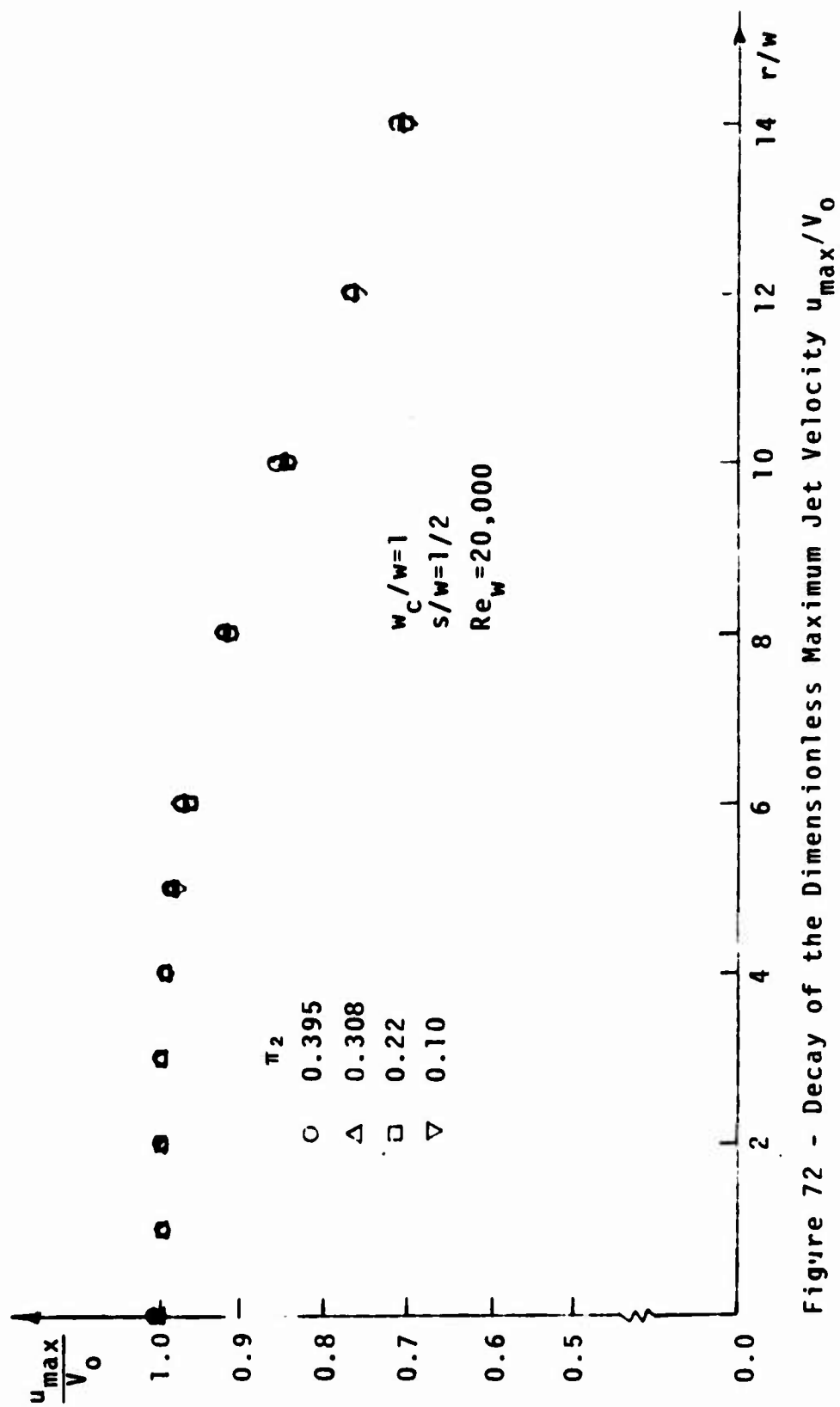
Figure 72 - Decay of the Dimensionless Maximum Jet Velocity u_{max}/V_o with Distance from the Pivot Point.
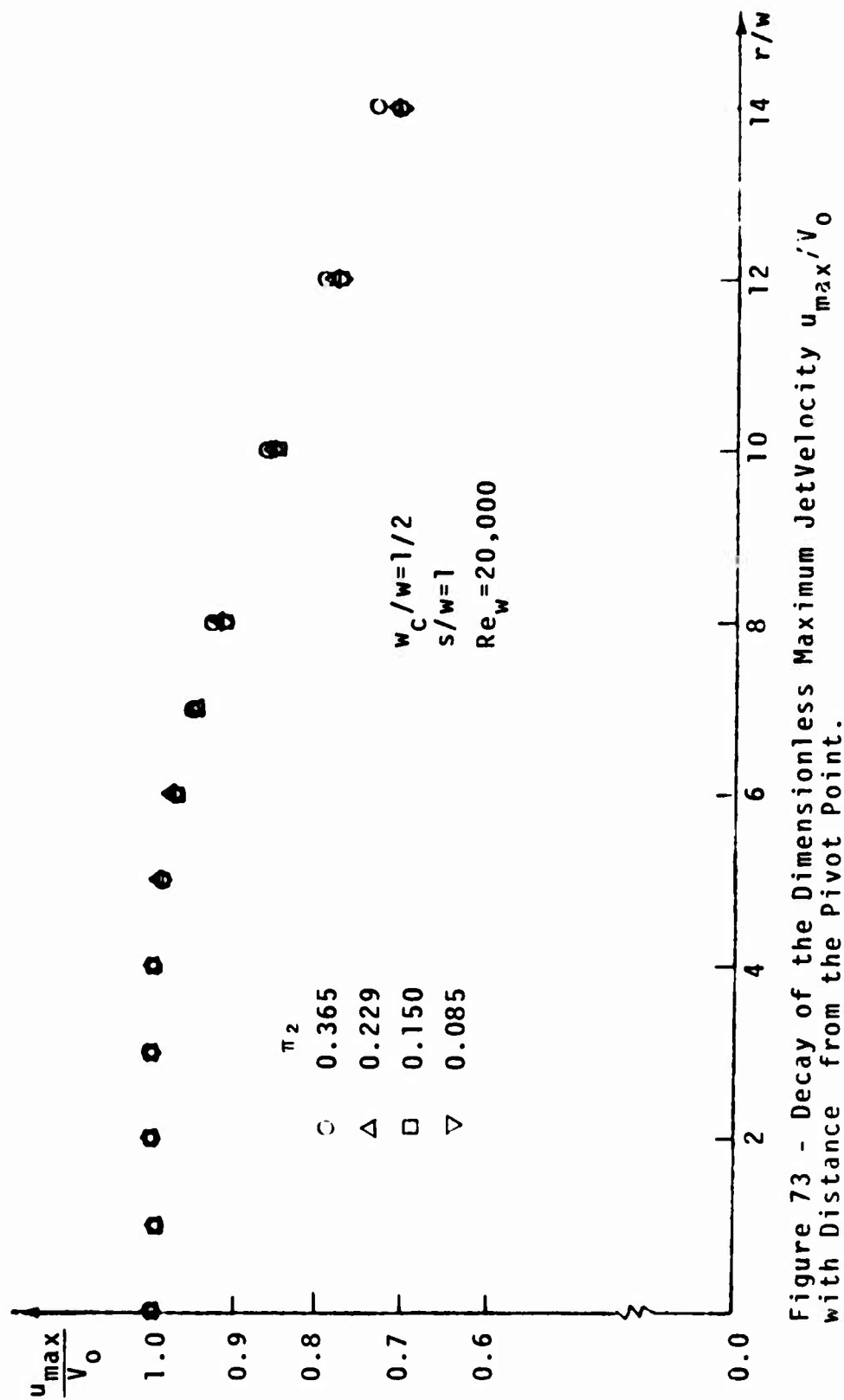
129

Figure 73 - Decay of the Dimensionless Maximum Jet Velocity u_{max}/V_o with Distance from the Pivot Point.
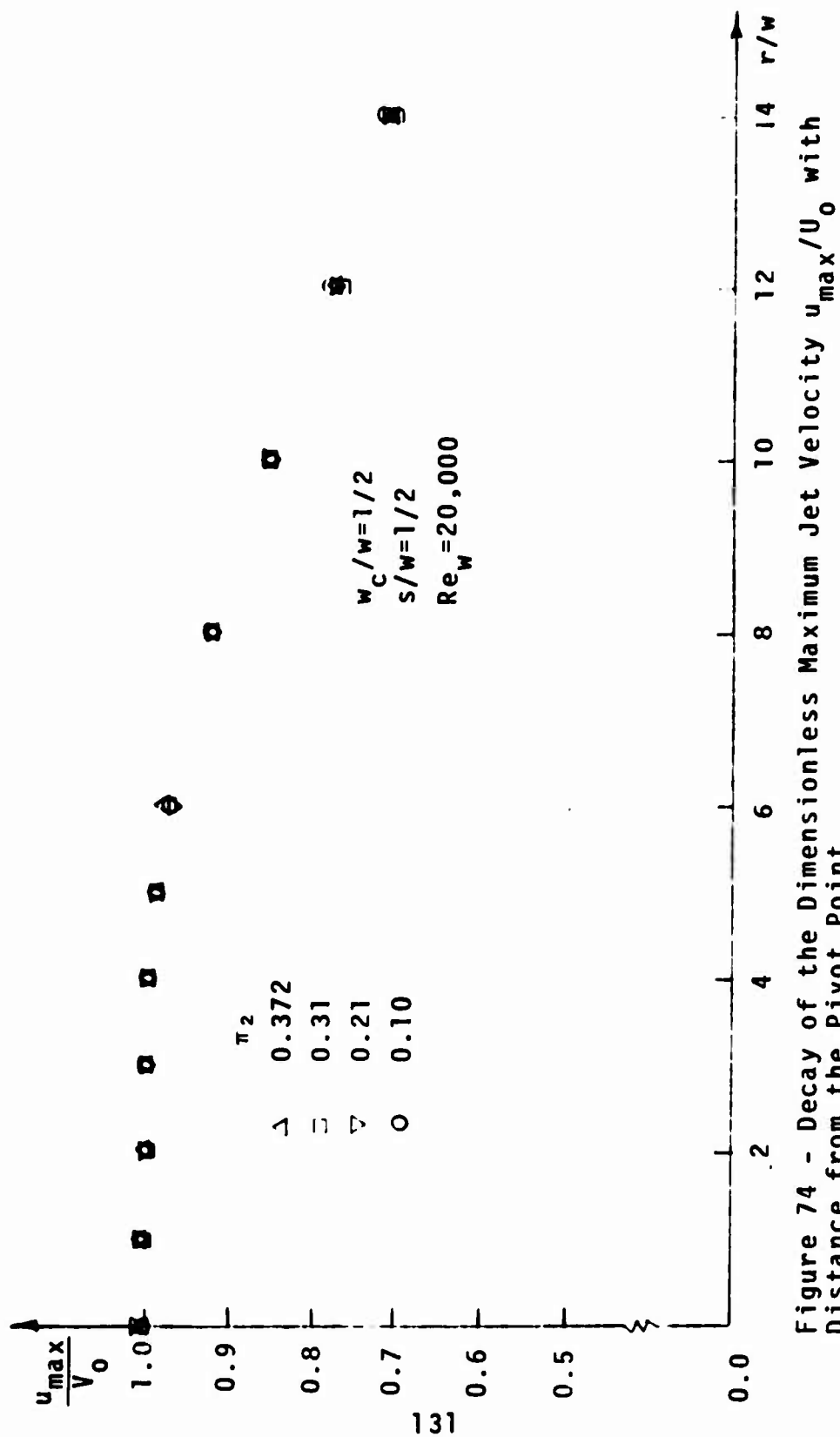
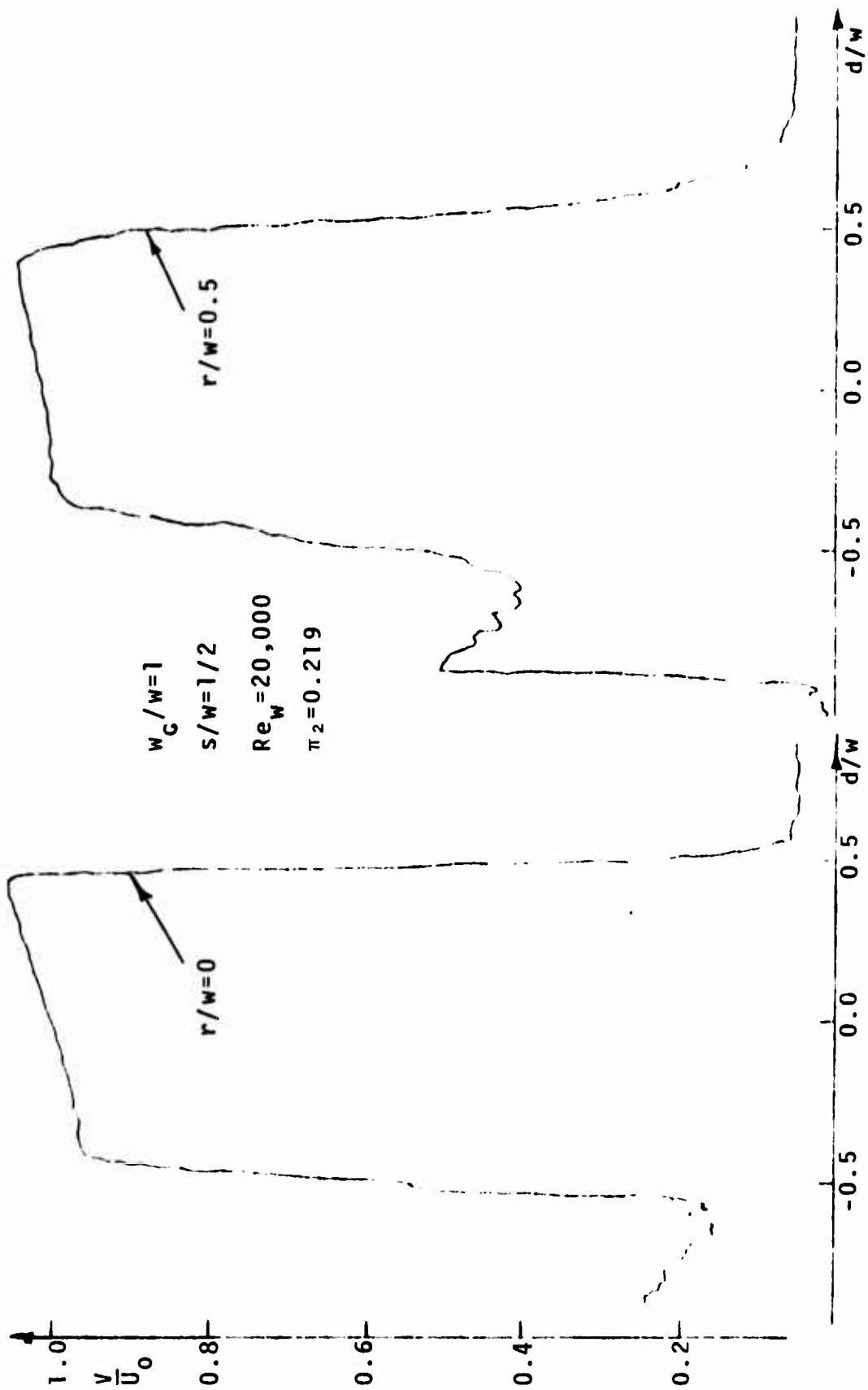Figure 74 - Decay of the Dimensionless Maximum Jet Velocity u_{max}/U_o with Distance from the Pivot Point.

131

Figure 75 - Velocity Distributions Across the Jet at Different Distances from the Pivot Point.
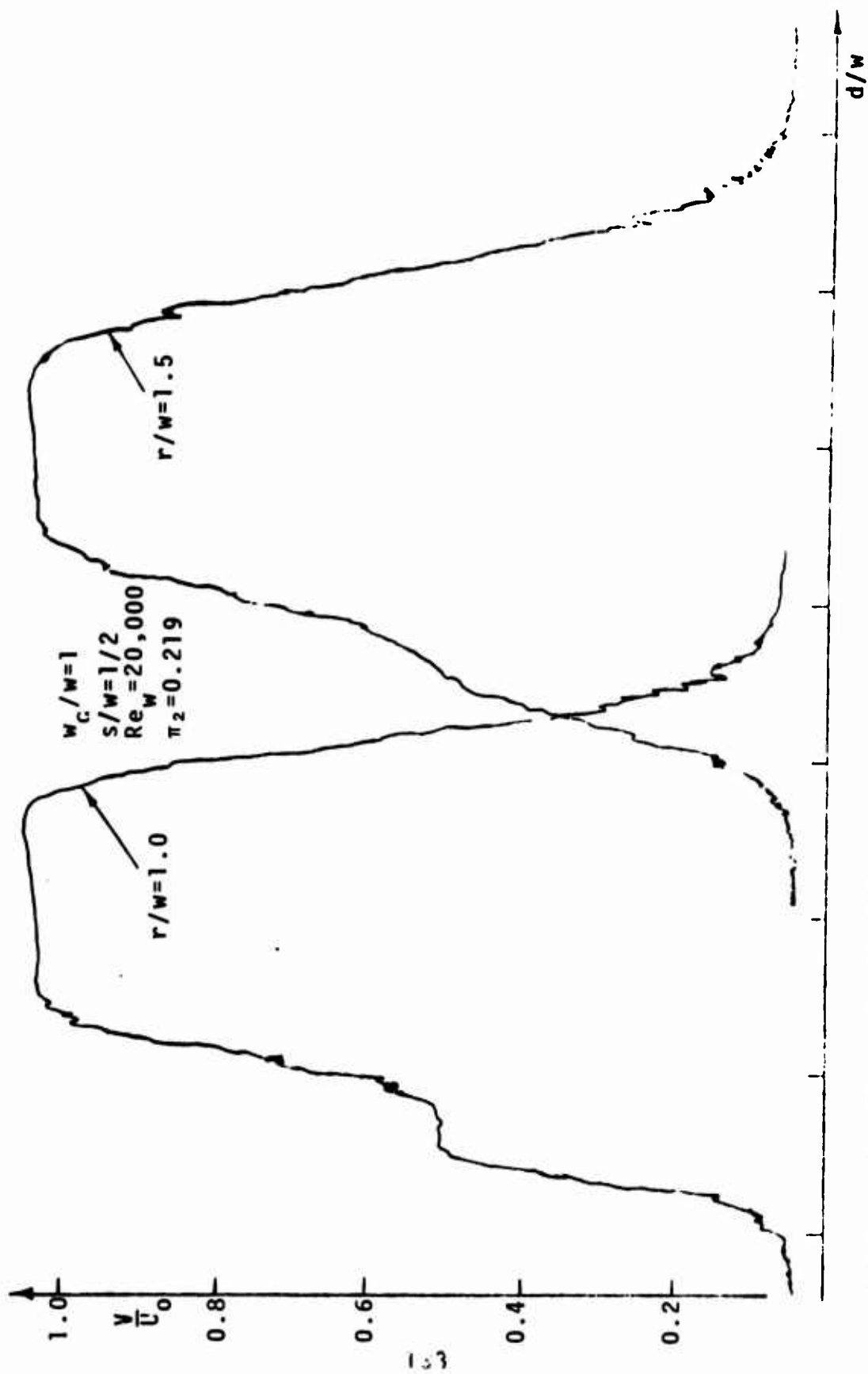
132

Figure 76 - Velocity Distribution Across the Jet at Different Distances from the Pivot Point.

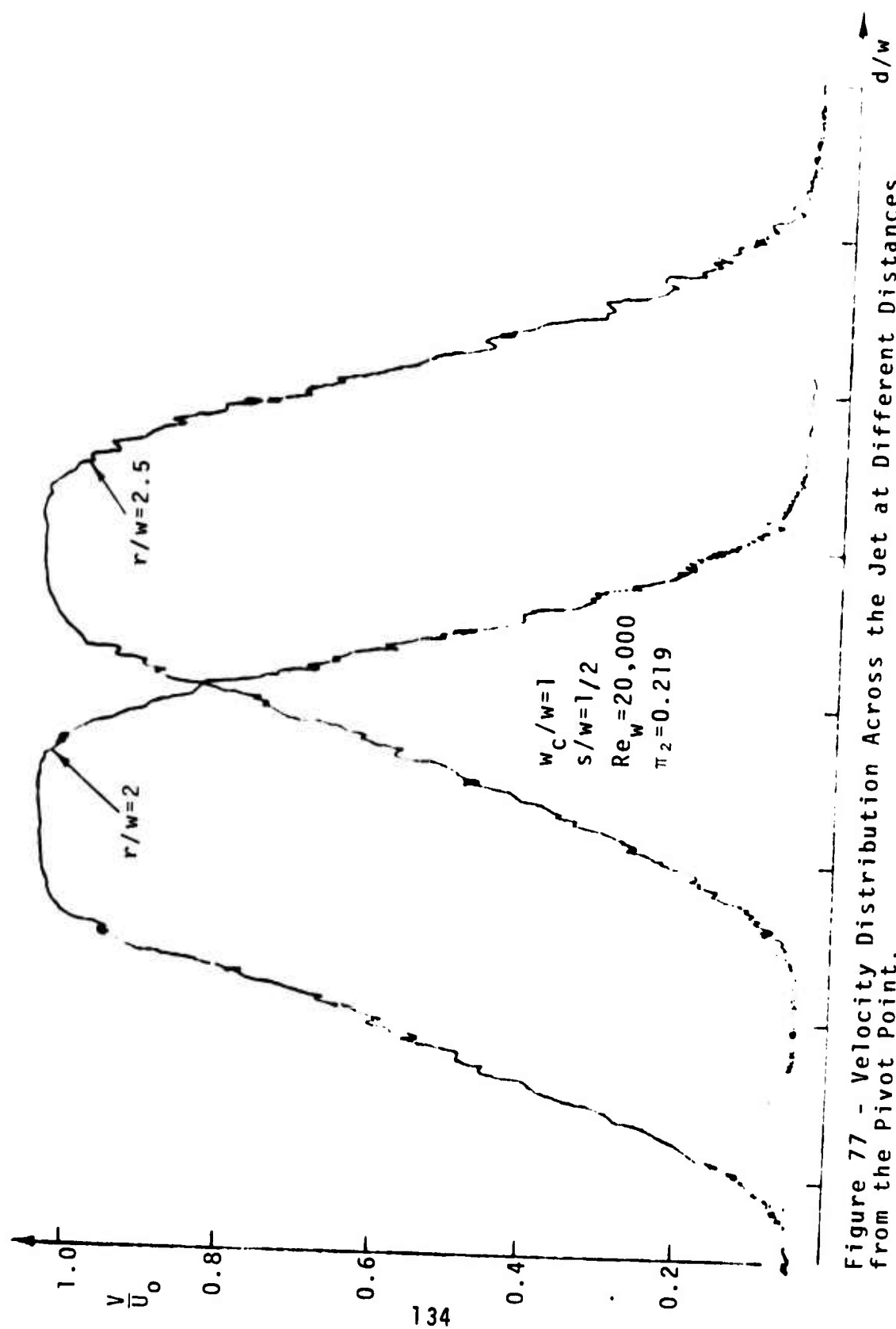Figure 77 - Velocity Distribution Across the Jet at Different Distances from the Pivot Point.
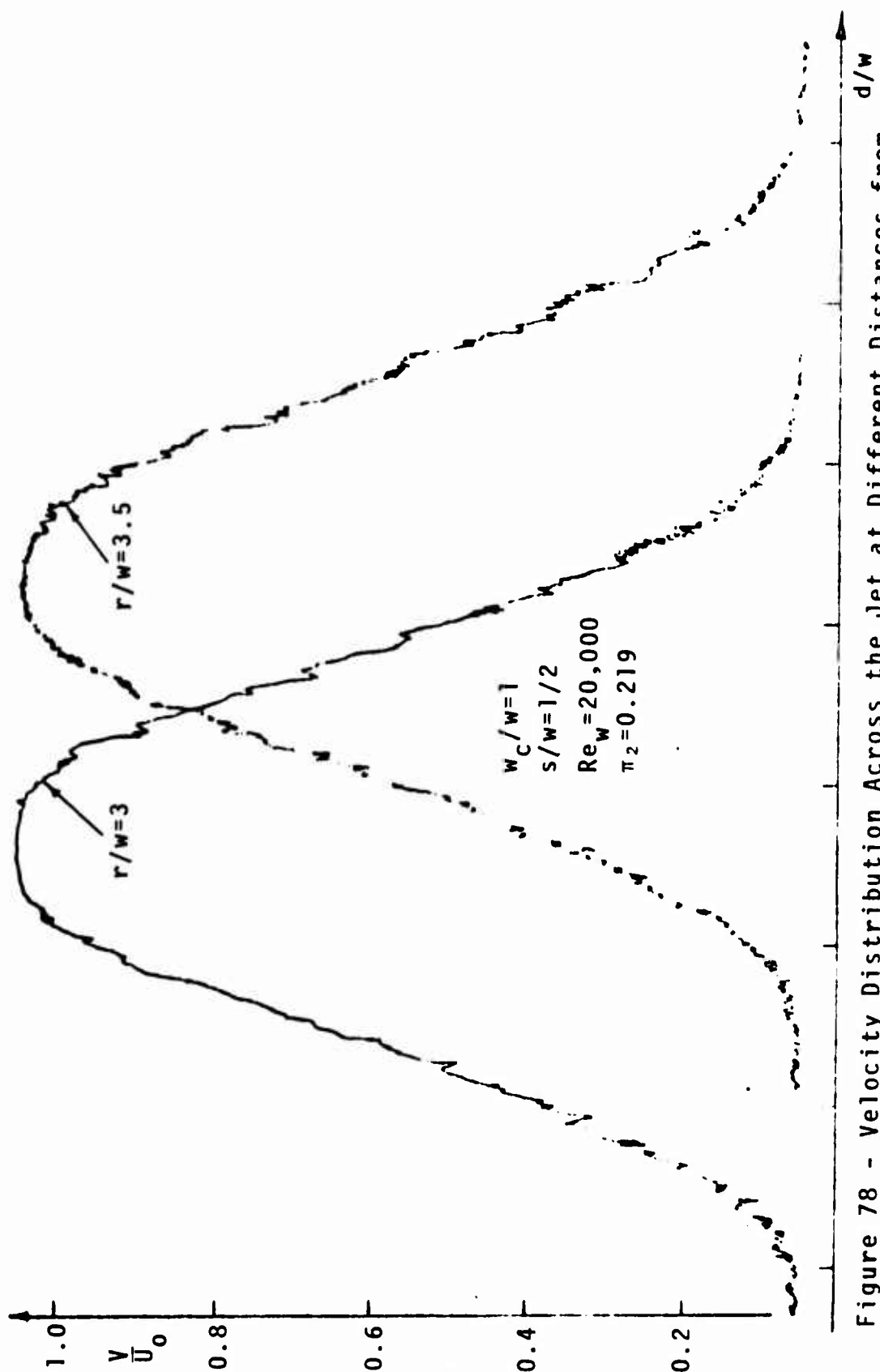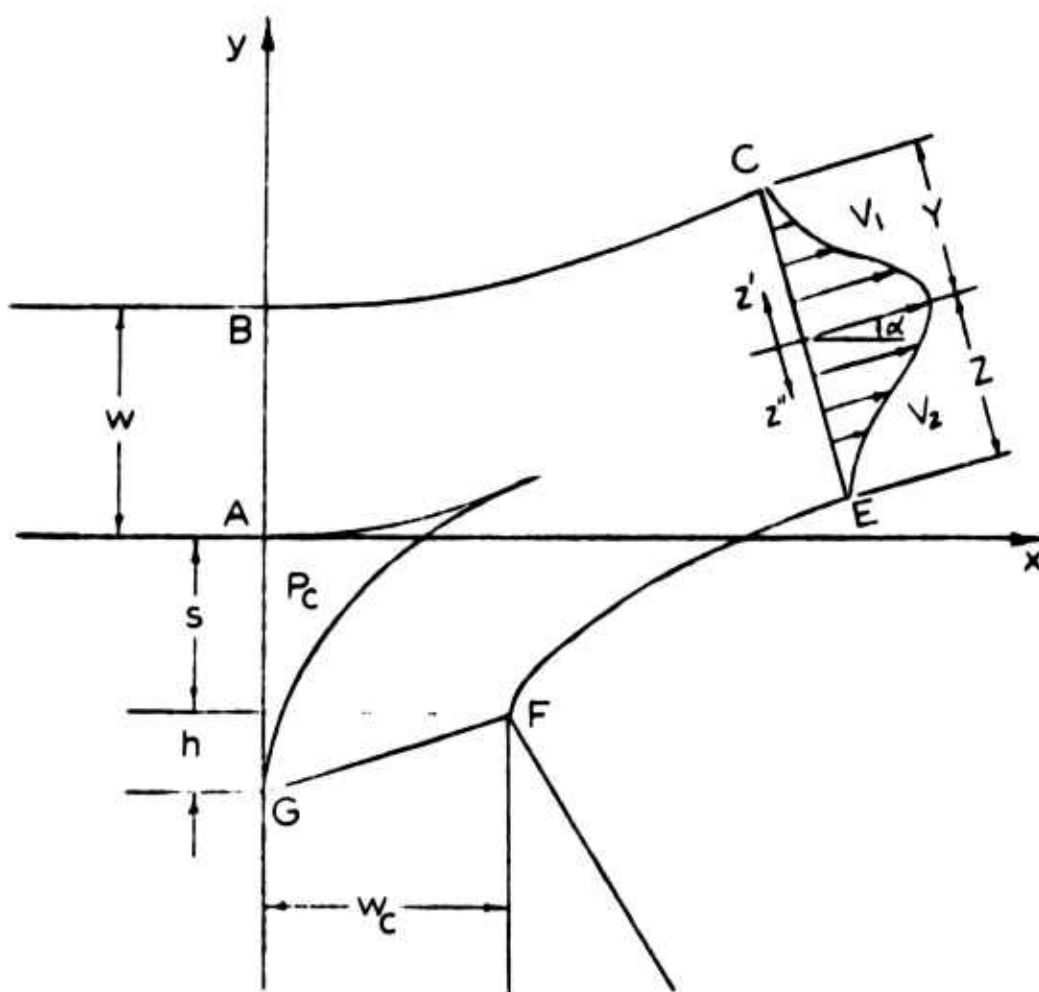
134

Figure 78 - Velocity Distribution Across the Jet at Different Distances from the Pivot Point.

135

Figure 79 - Notation Used in the Ideal Fluid Model.

136

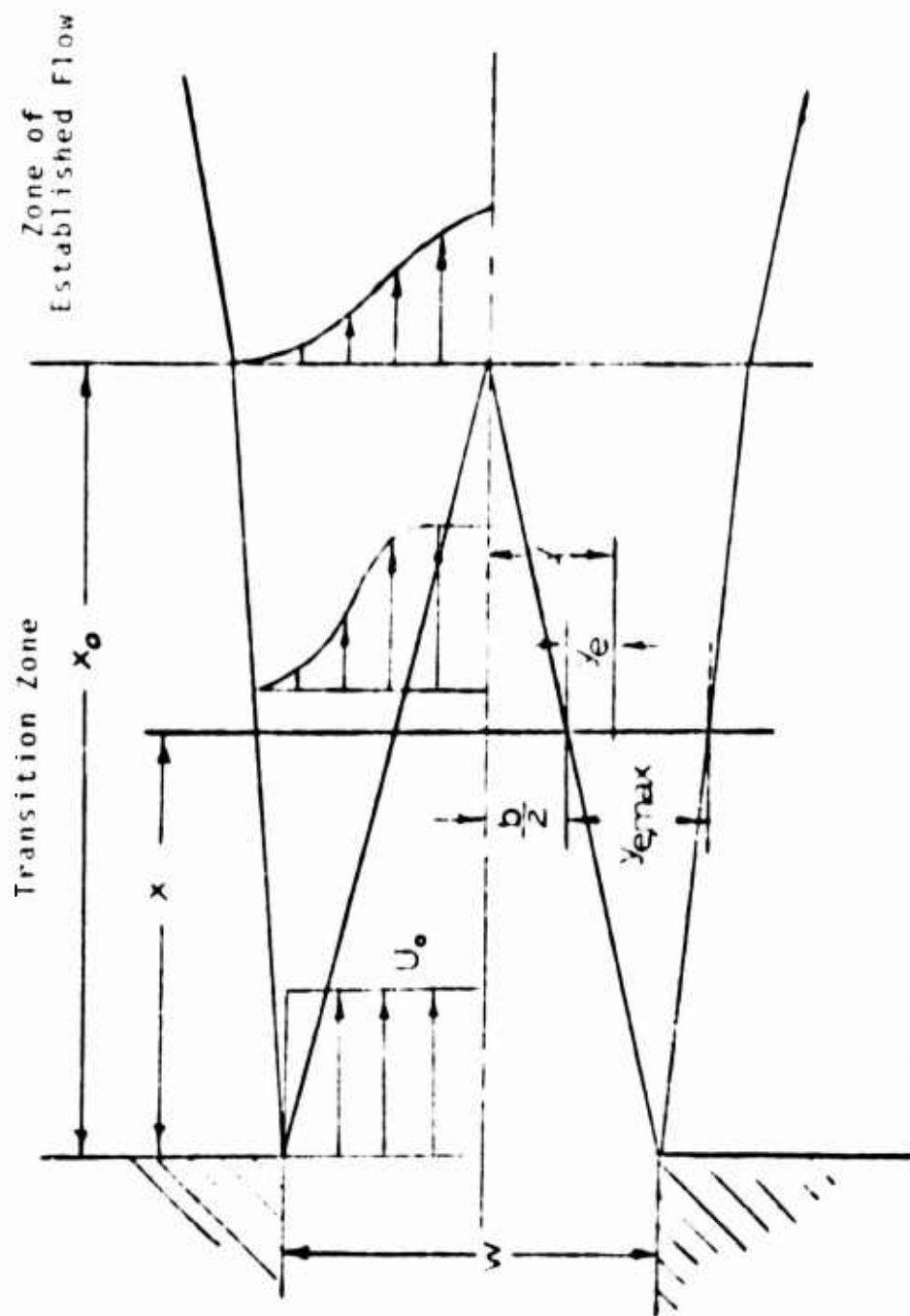Figure 80 - Notation Used in the Real Fluid Model.

137

Figure 81 - Notation Used in the Simson's Profile for a Two-Dimensional Free Jet.
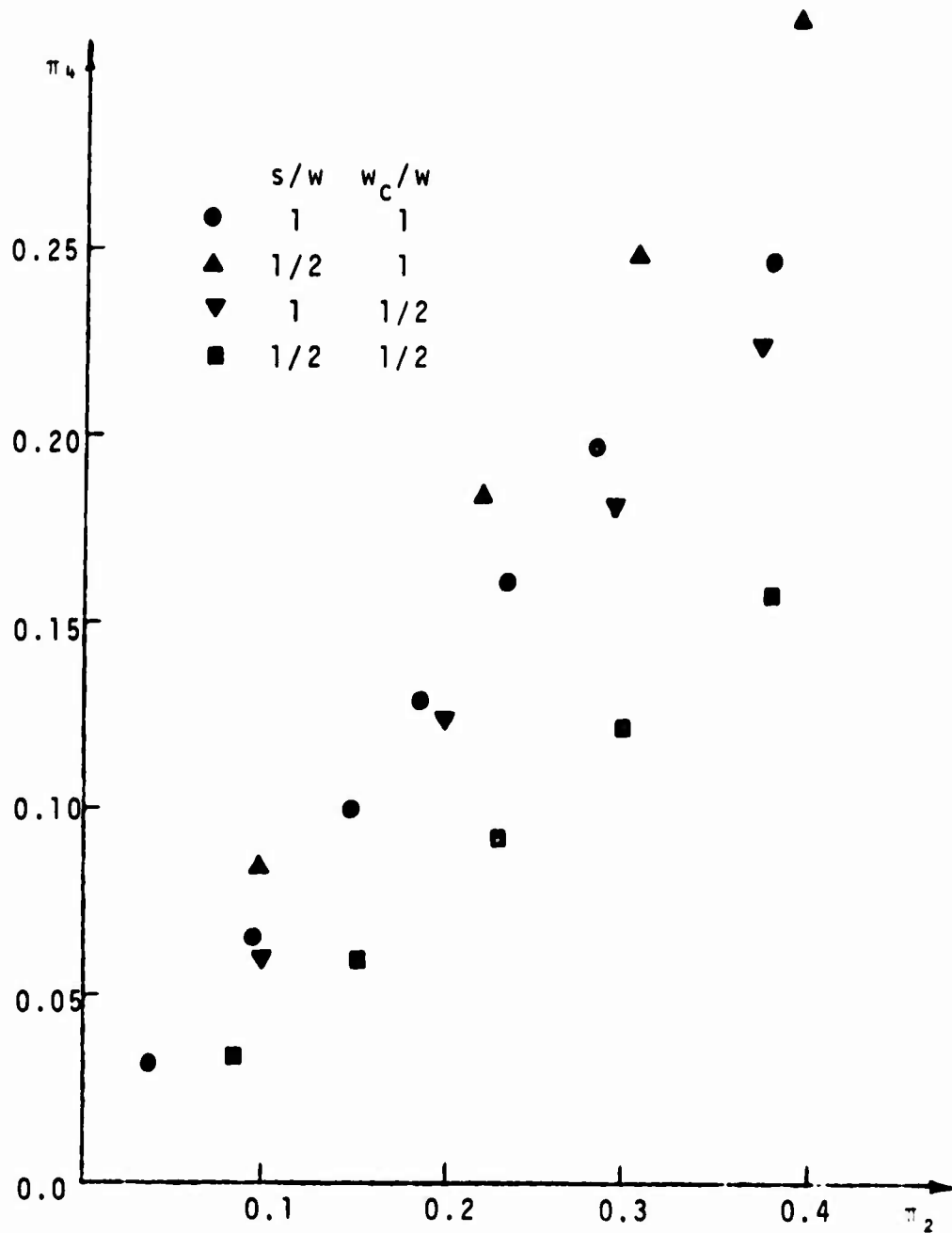
138

Figure 82 - Variation of the Dimensionless Pressure π_4 with the Dimensionless Pressure π_2 for Various Values of Setback and Width of the Control Jet Nozzle.
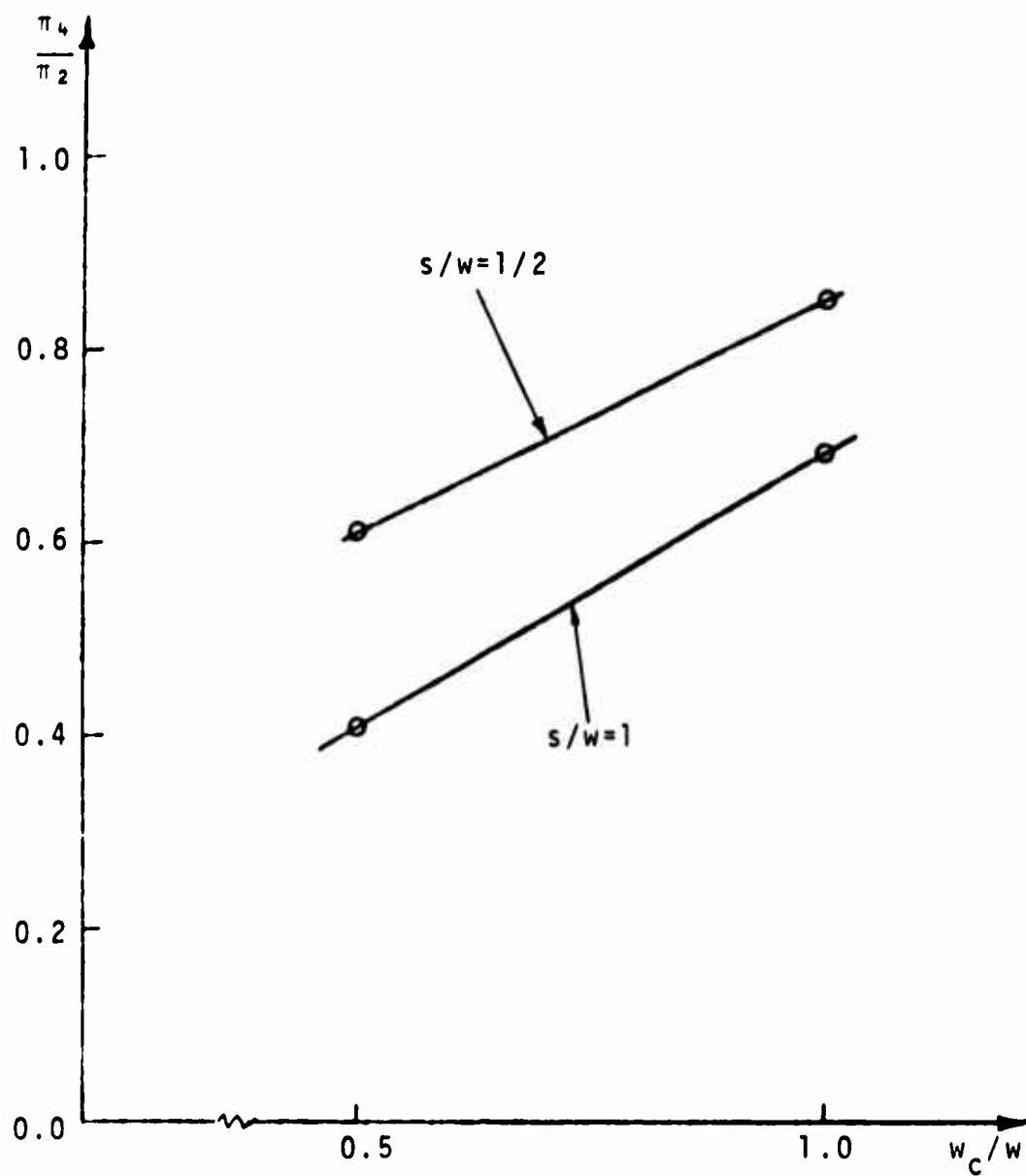
Figure 83 - Variation of the Dimensionless Pressure Ratio π_4/π_2 with the Control Port Width for Different Values of Setback.

140

Figure 84 - Comparison of the Calculated and Measured Angles of Deflection.

141
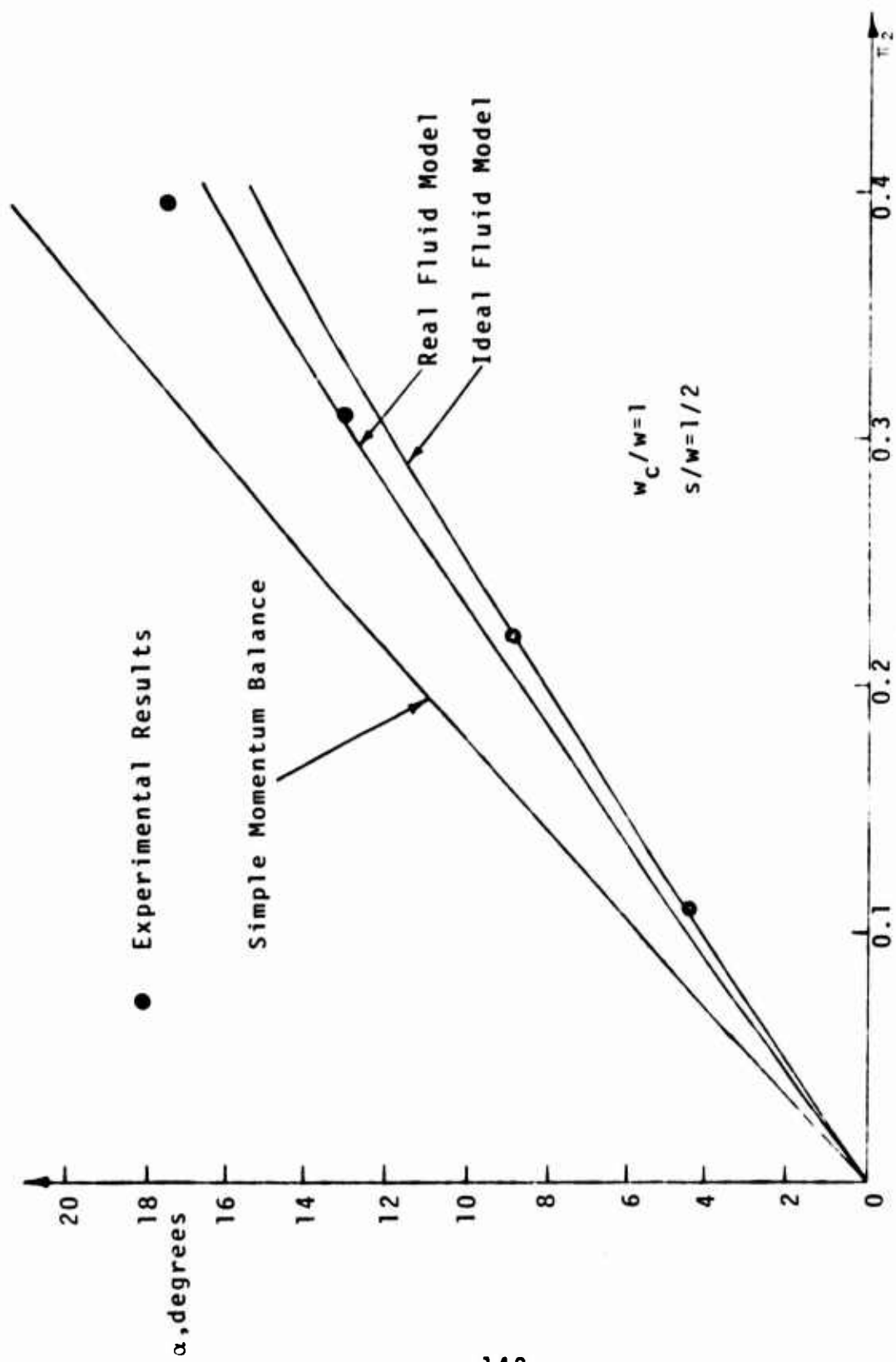
Figure 85 - Comparison of the Calculated and Measured Angles of Deflection.

142

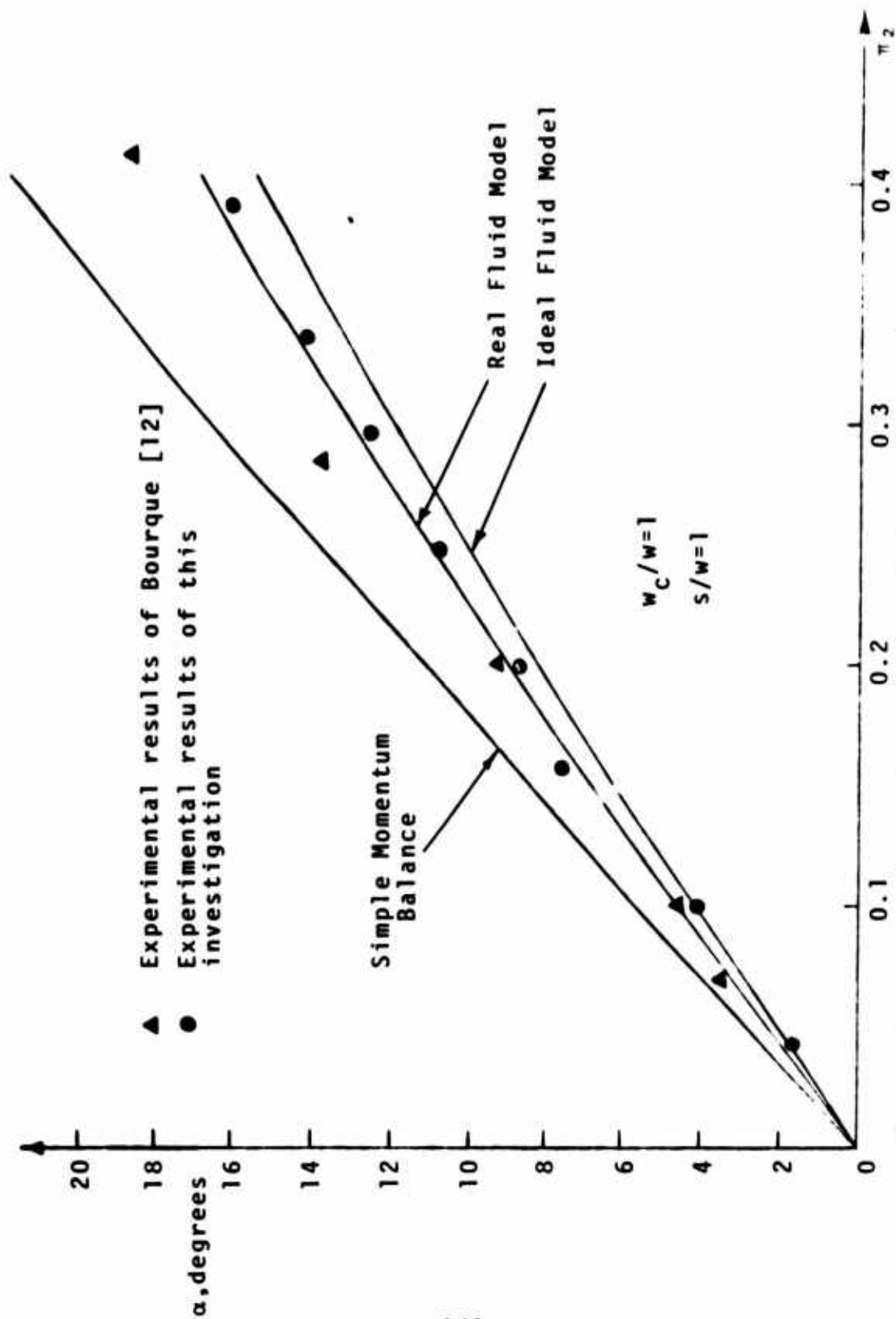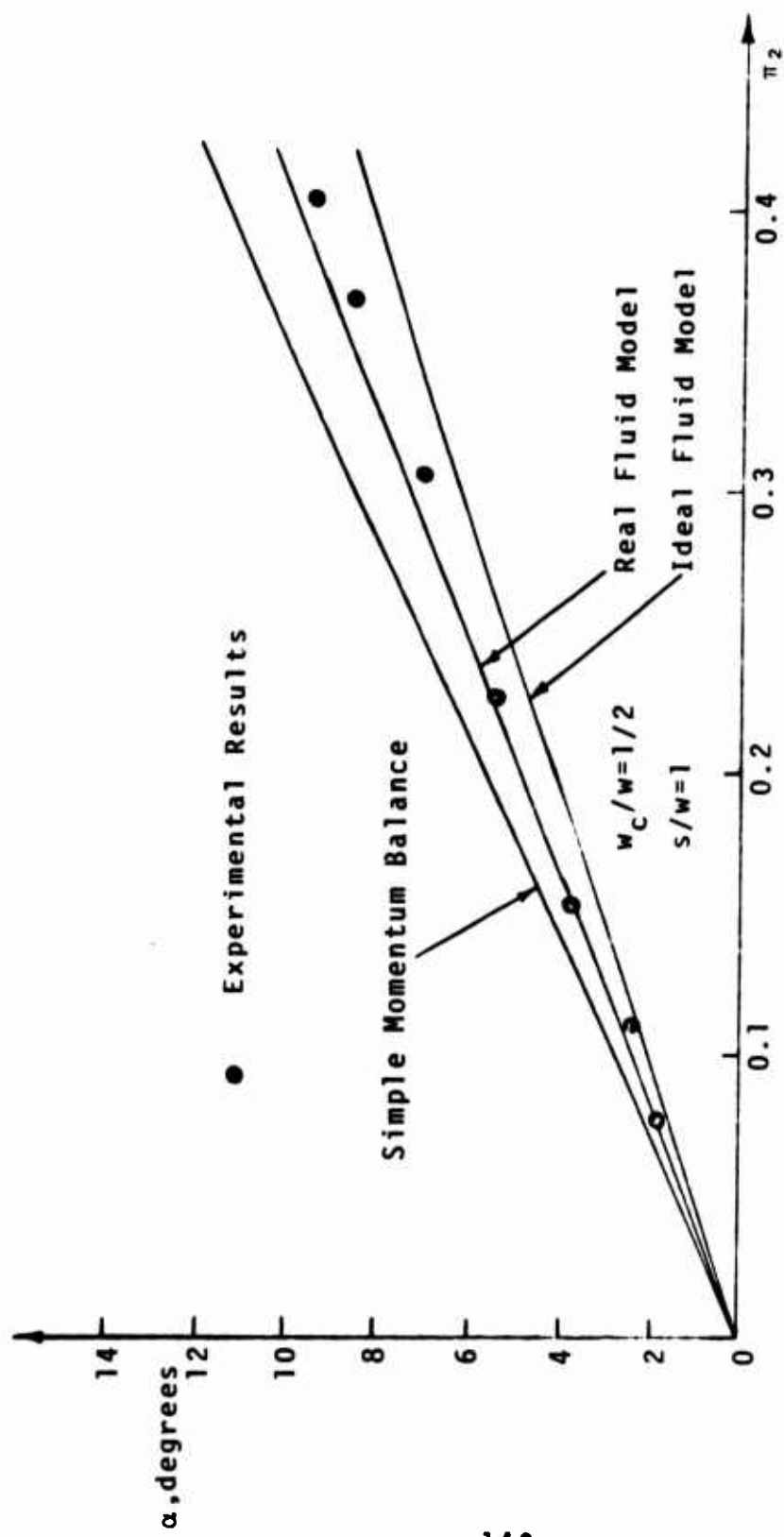Figure 86 - Comparison of the Calculated and Measured Angles of Deflection.

143
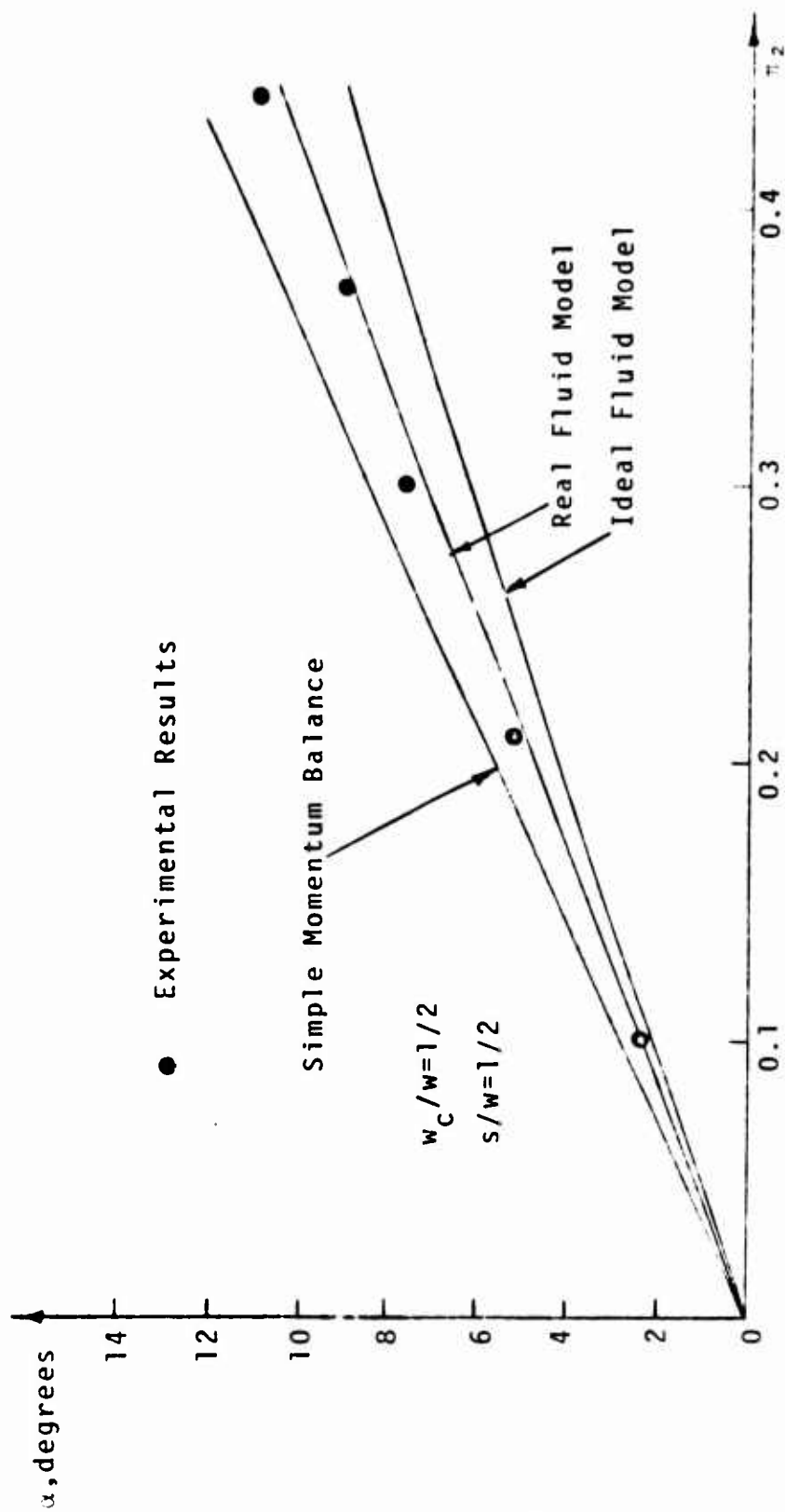
Figure 87 - Comparison of the Calculated and Measured Angles of Deflection.
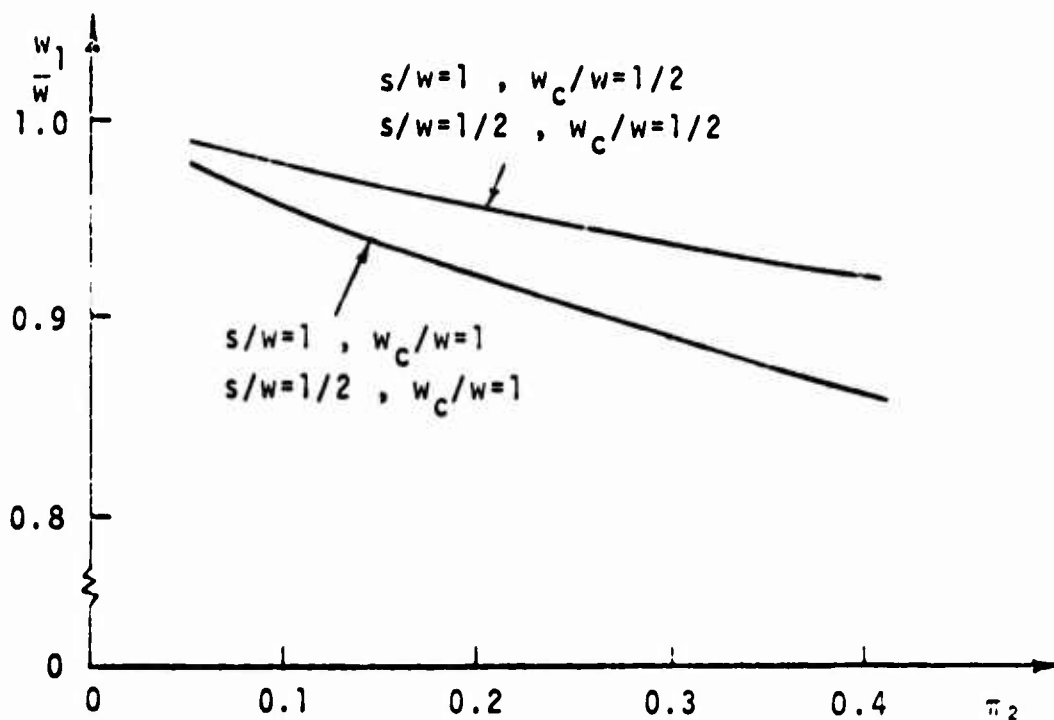
Figure 88 - Calculated Dimensionless Width of
the Power Jet at the Location Where the Pressure
is Uniform Across in the Ideal Fluid Model.
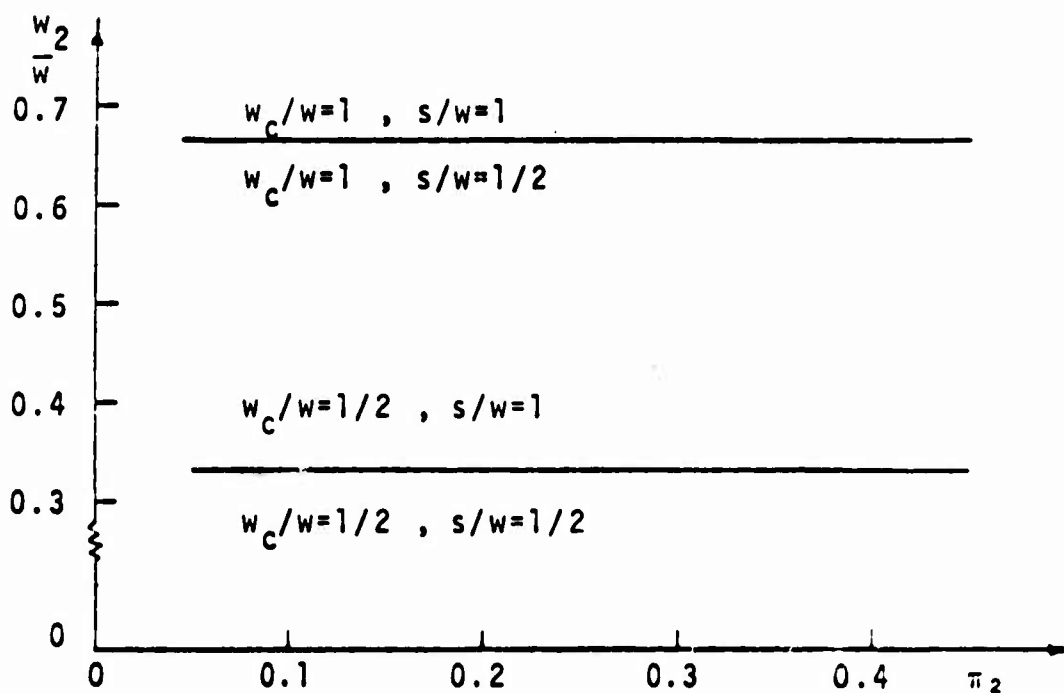
Figure 89 - Calculated Dimensionless Width of
the Control Jet at the Location Where the Pressure
is Uniform Across in the Ideal Fluid Model.

145
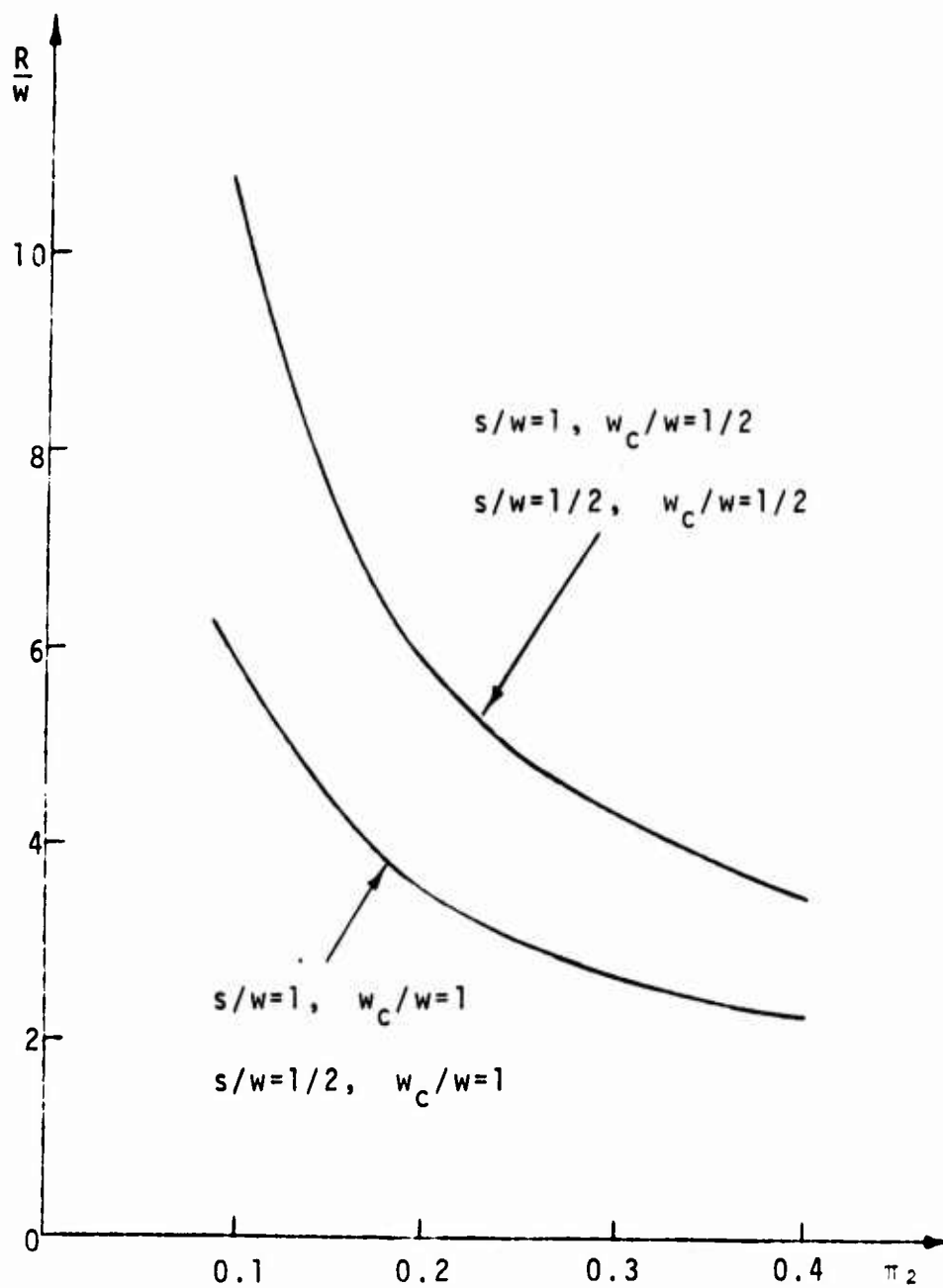
Figure 90 - Calculated Dimensionless Radius of
Curvature of the Power Jet in the Ideal Fluid
Model.

146
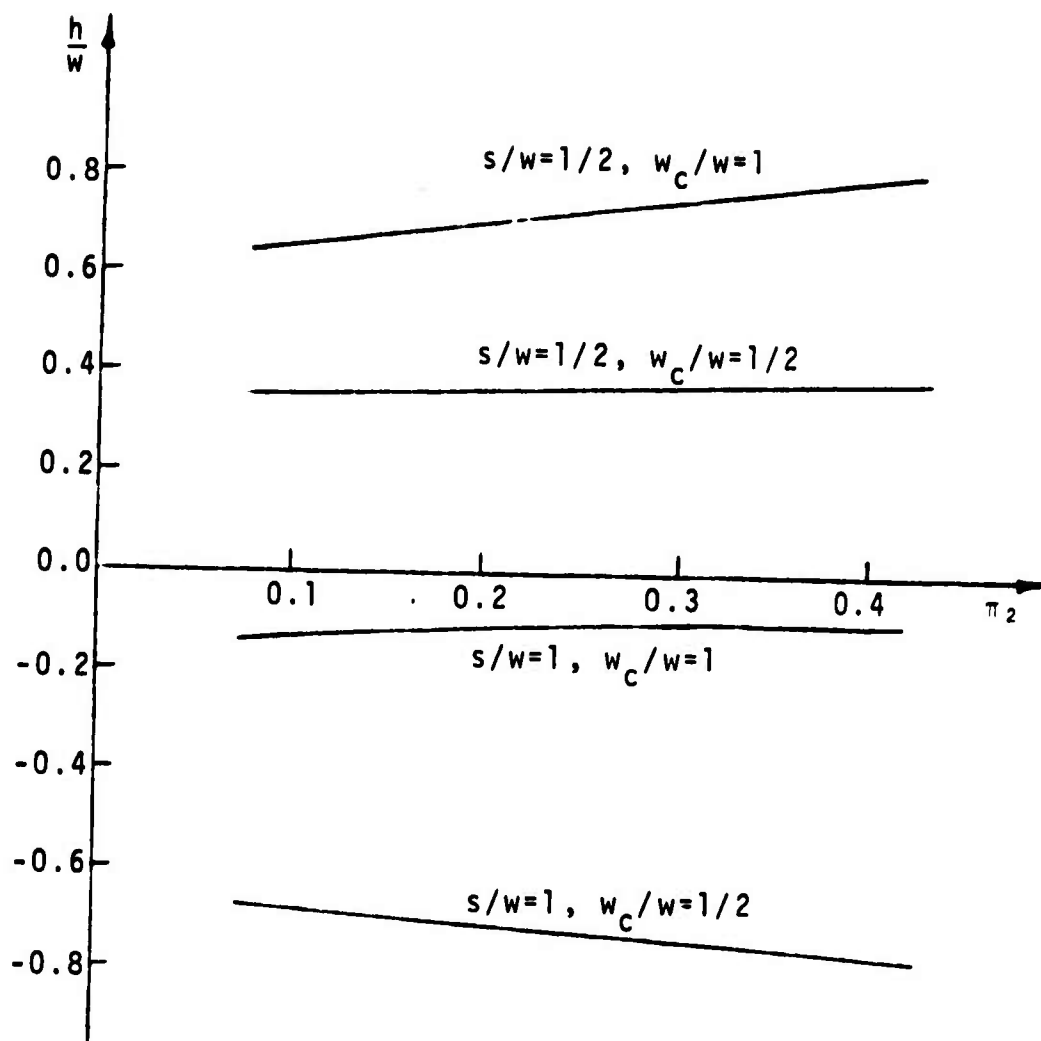
Figure 91 - Calculated Dimensionless Separation Distance of the Control Jet in the Ideal Fluid Model.

147
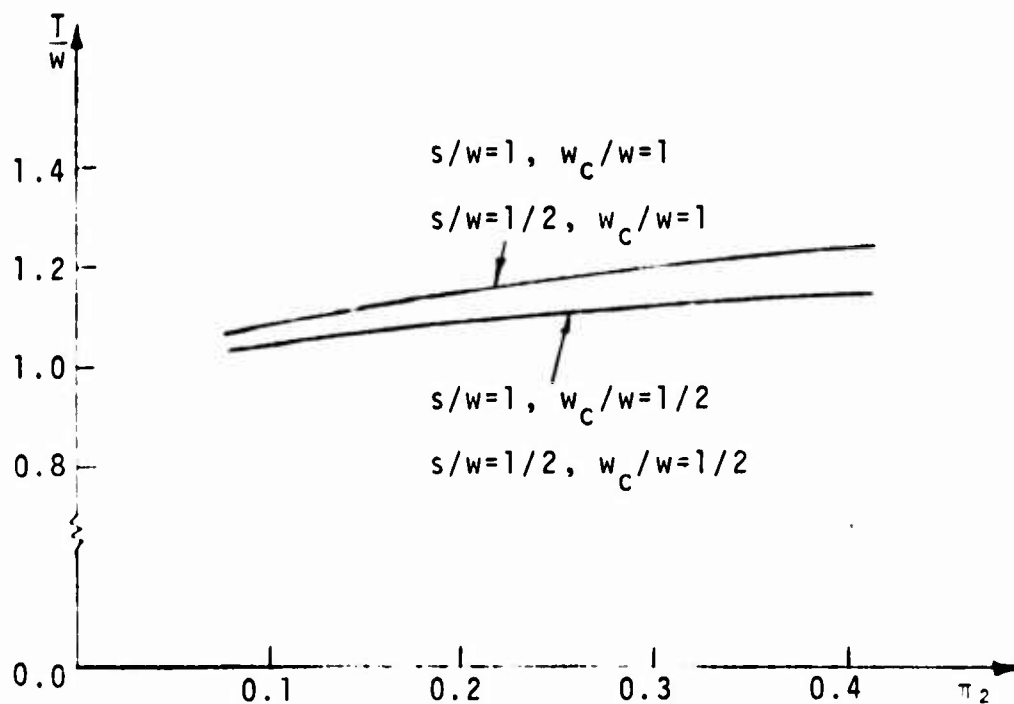
Figure 92 - Calculated Dimensionless
Distance T/w in the Ideal Fluid Model.

148
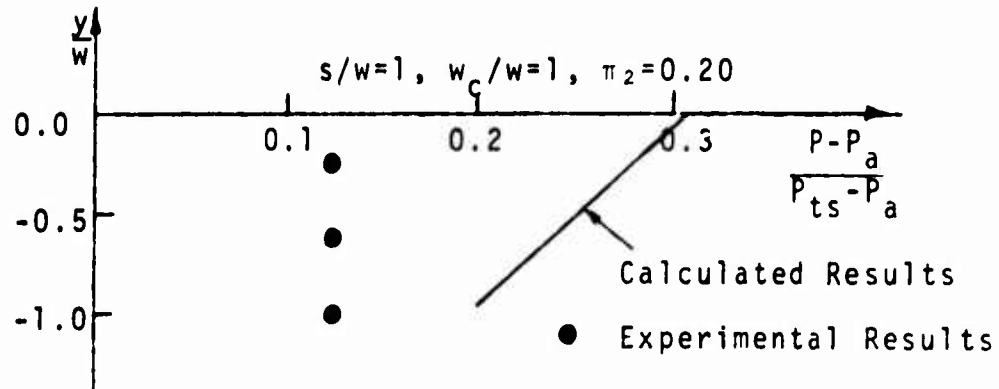
(a)
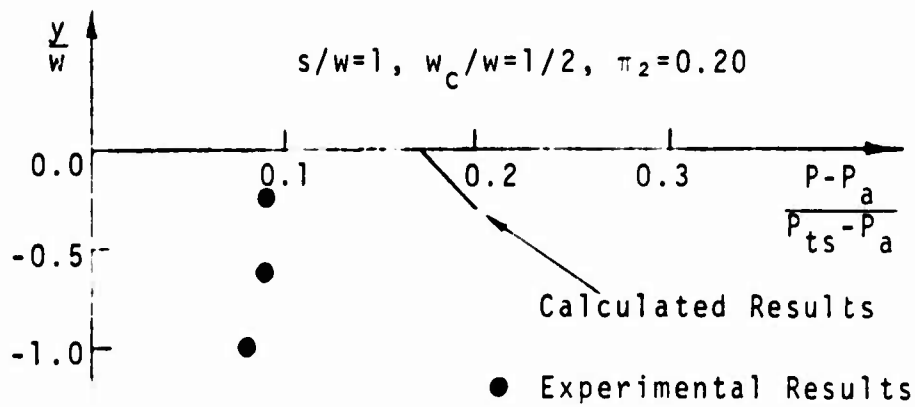
(b)

Figure 93 - Comparison of the Measured Pressure Distribution Along The Setback Wall with That of Calculated from the Ideal Fluid Model.

149
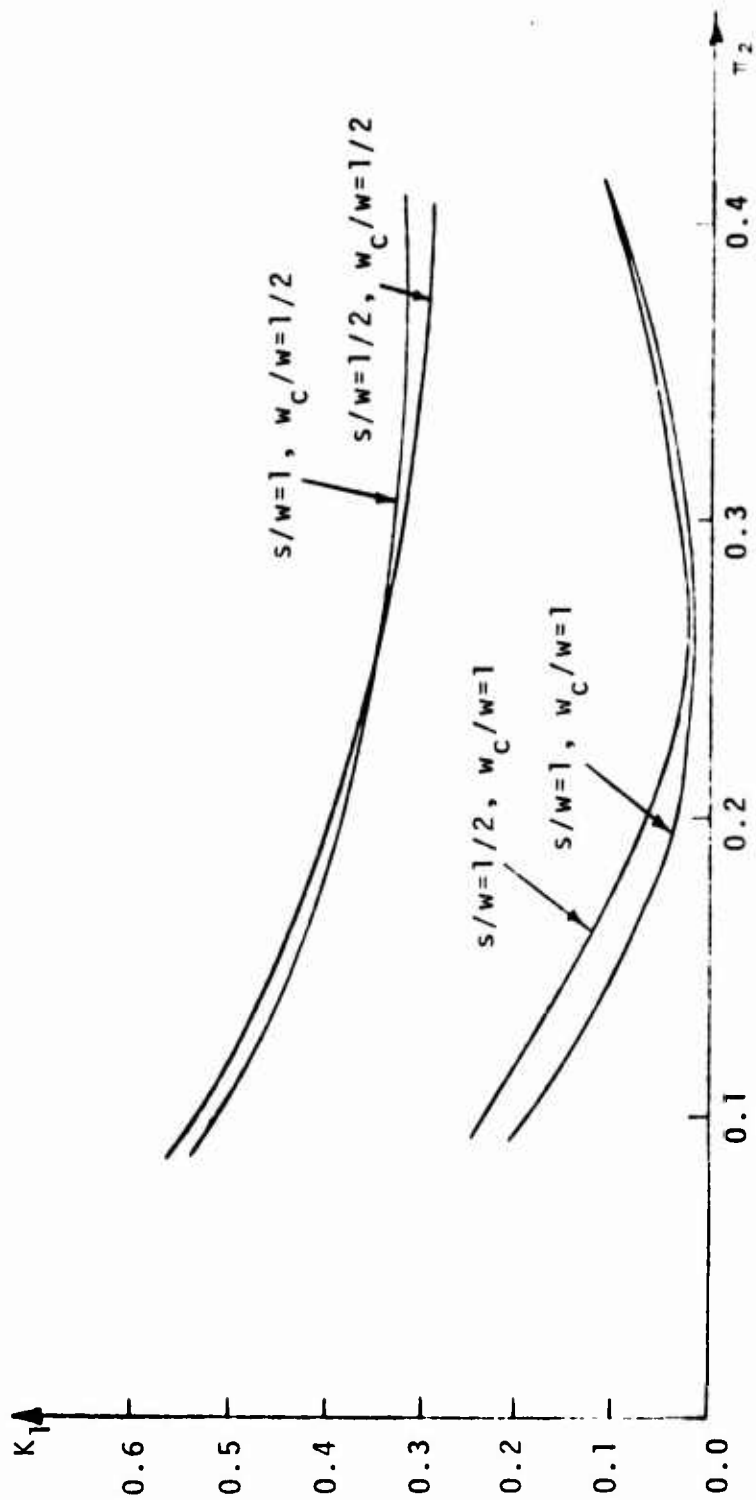
Figure 94 - Calculated Results of the Entrainment Coefficient in the Real Fluid Model.
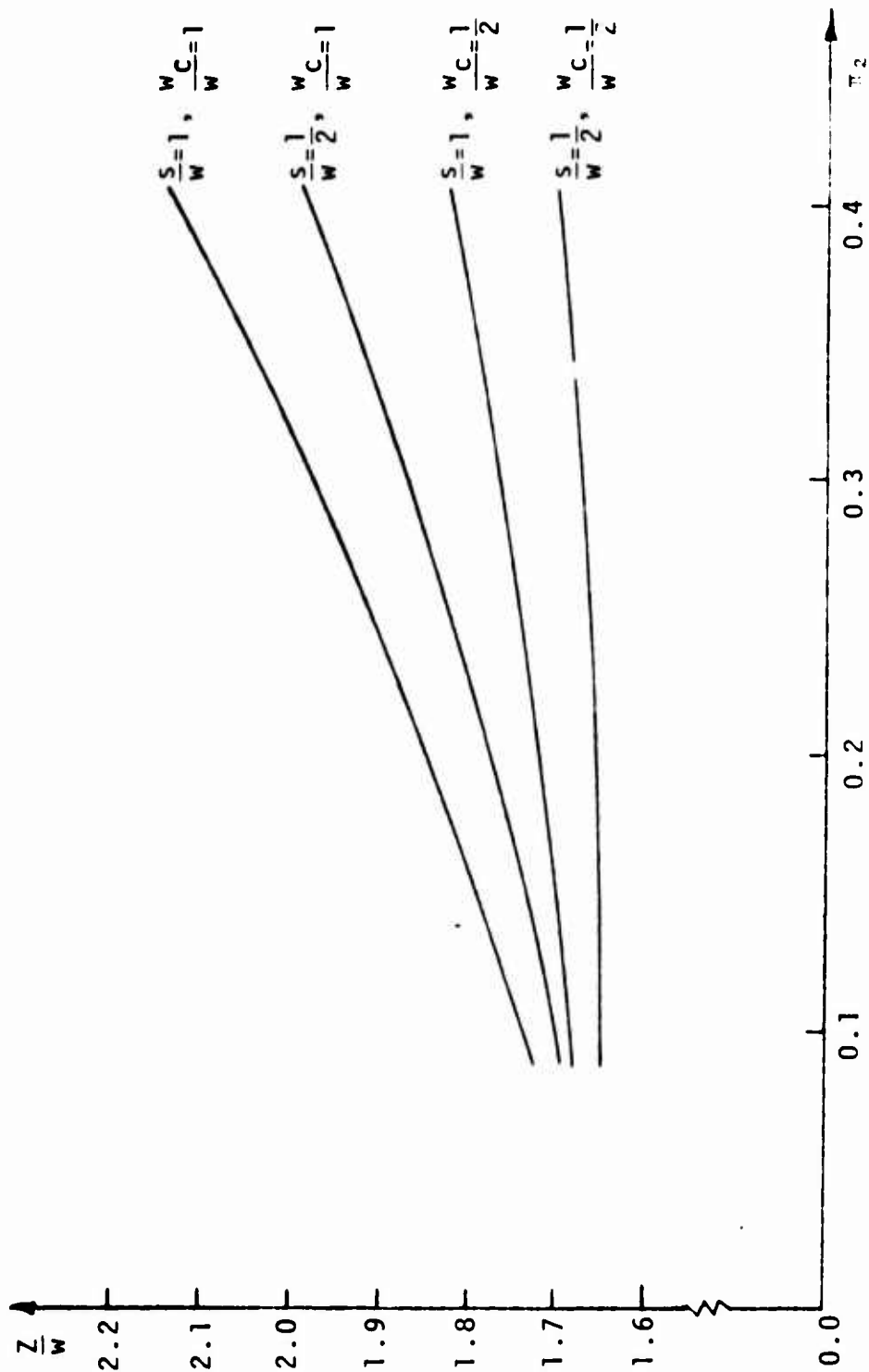
Figure 95 - Calculated Dimensionless Part-Width of the Combined Jet in the Real Fluid Model.
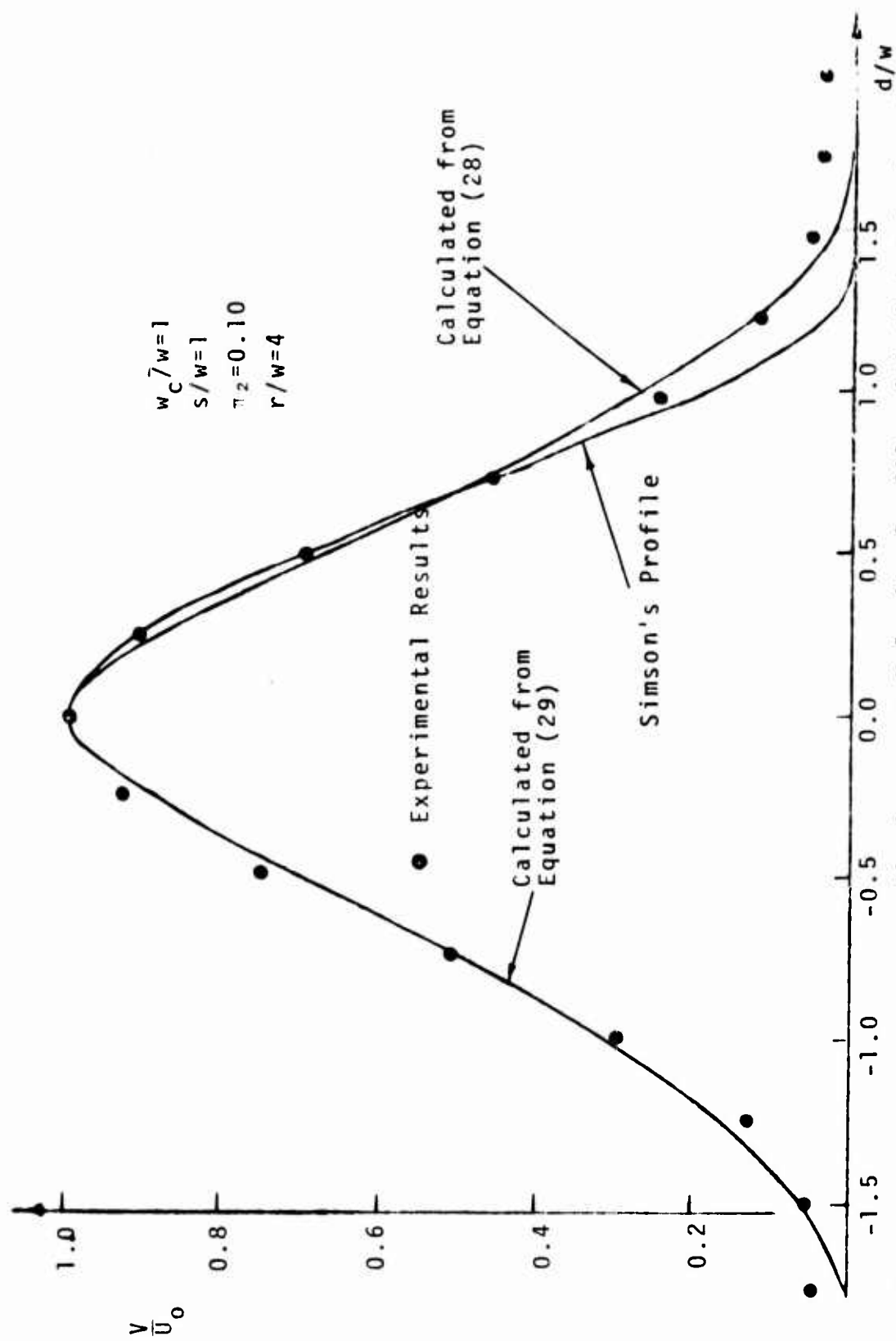
Figure 96 - Comparison of the Measured Velocity Profile with that Calculated from the Real Fluid Model.
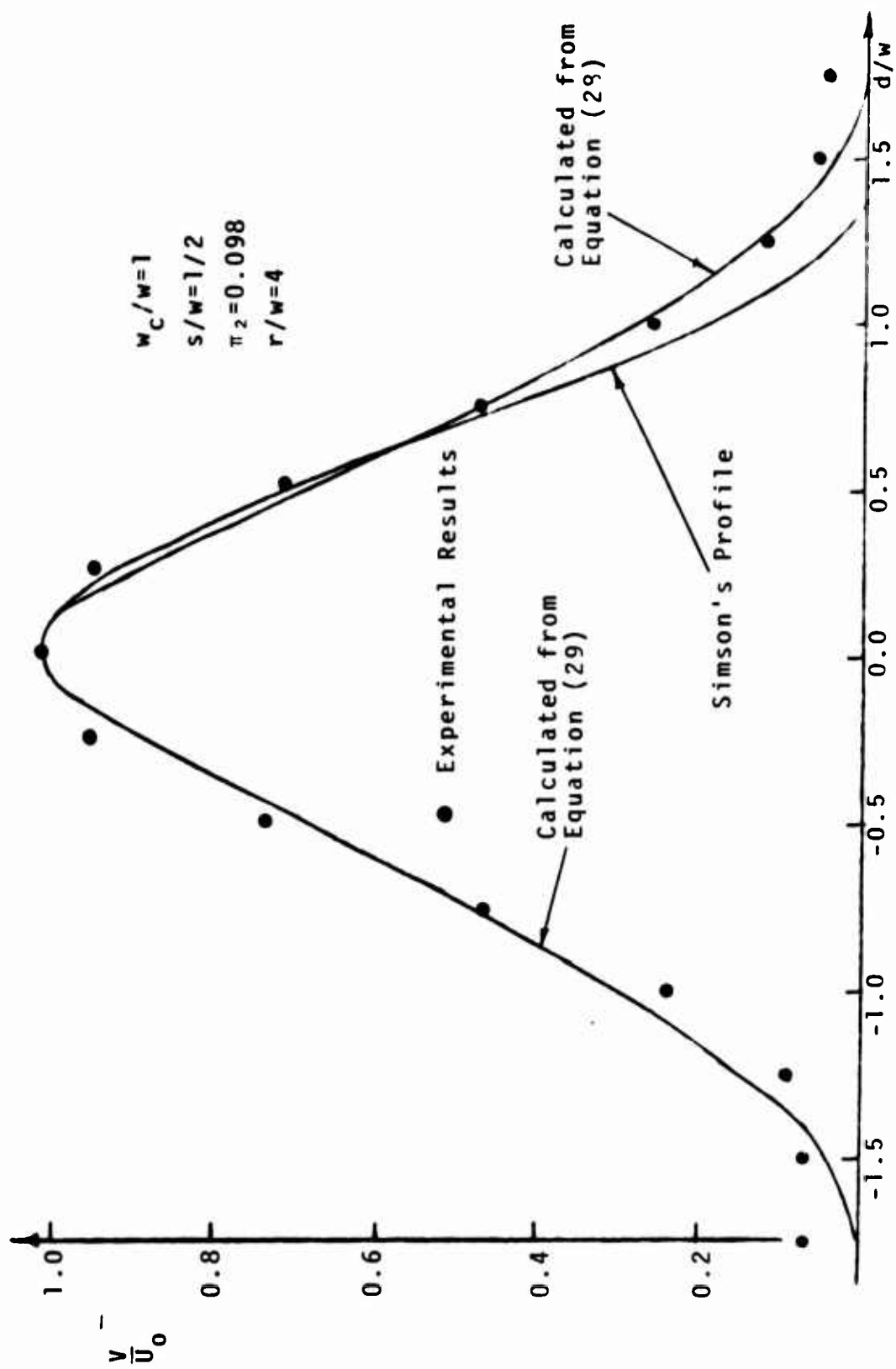
Figure 97 - Comparison of the Measured Velocity Profile with that calculated from the Real Fluid Model.
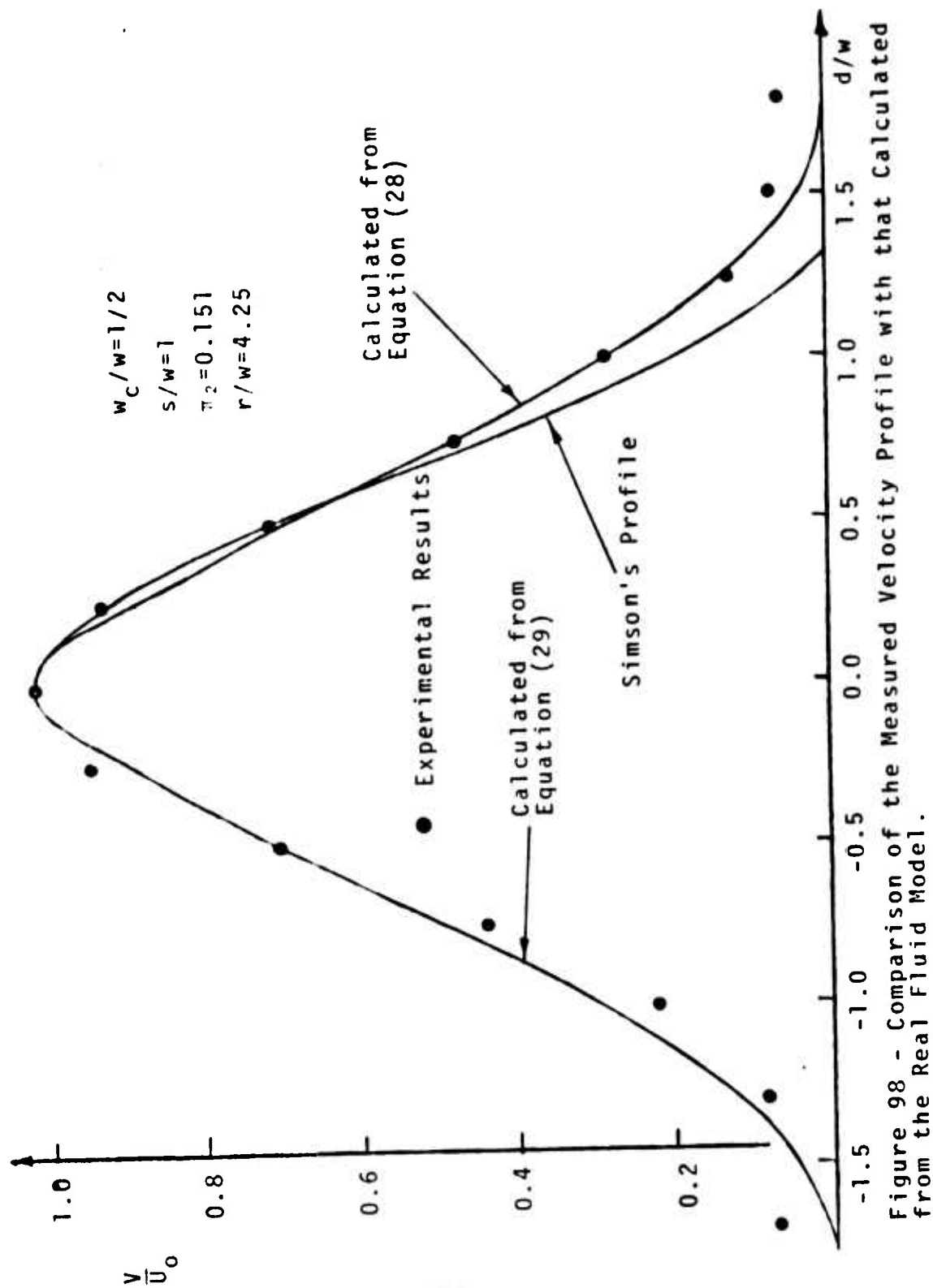
Figure 98 - Comparison of the Measured Velocity Profile with that Calculated from the Real Fluid Model.

154
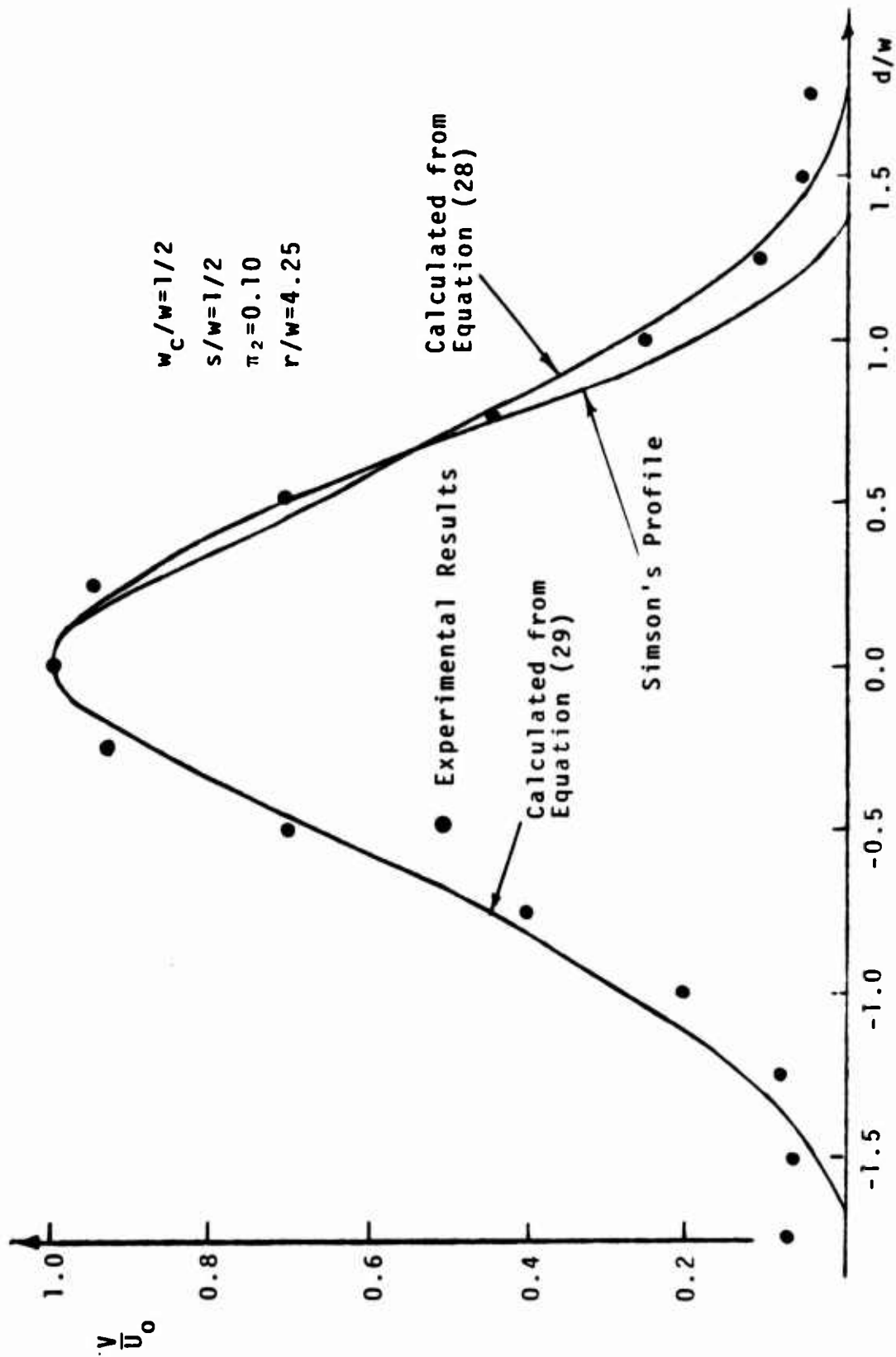
Figure 99 - Comparison of the Measured Velocity Profile with that Calculated from the Real Fluid Model.

155

REFERENCES

[1]   E. M. Dexter, "An Analog Pure Fluid Amplifiers",
       Symposium on Fluid Jet Control Devices, ASME,
       pp. 41-49, November, 1962.

[2]   R. J. Reilly and F. A. Moynihan, "Notes on a Propor-
       tional Fluid Amplifier", Symposium on Fluid Jet
       Control Devices, ASME, pp. 51-58, November, 1962.

[3]   ⁻. A. Moynihan and R. J. Reilly, "Deflection and
       Relative Flow of Three Interacting Jets", Proceedings
       of the Fluid Amplification Symposium, pp. 123-146,
       May, 1964.

[4]   P. C. Chiu and C. P. Man, "An Approximate Analysis
       of Three Two-Dimensional Interaction Jets", ASME
       Paper No. 67-WA/FE-32, Presented at the Winter Annual
       Meeting and Energy Systems Exposition, Pittsburgh,
       Pa., November, 1967.

[5]   J. F. Douglas and R. S. Neve, "Investigation into the
   Behavior of a Jet Interaction Proportional Amplifier",
       Paper C3, Proceedings of the Second Cranfield Fluid-
       ics Conference, Cambridge, England, 1967.

[6]   L. A. Zalmanzon, N. N. Ivanov and M. E. Limonova,
       "Theoretical and Experimental Investigation of
       Fluidic Elements", Paper A4, IFAC Symposium on Fluid-
       ics, November, 1968.

[7]   F. S. Vladimirov, "Collision of Jets Emerging from
       Channels with Parallel Walls", PMM, Vol. 33, No. 1,
       pp. 11-19, 1969.

[8]   N. Gungor, "A Theoretical and Experimental Study of
       the Impingement of Two Subsonic Jets", M.S. Thesis,
       Dept. of Mechanical Engineering, U.S. Naval Postgrad-
       uate School, Monterey, California, June, 1969.

[9]   S. B. Weeks, "A Theoretical and Experimental Inves-
       tigation of Turbulent Jet Interaction", M.S. Thesis,
       Dept. of Mechanical Engineering, U.S. Naval Postgrad-
       uate School, Monterey, California, October, 1969.

[10]   G. L. Hiriart, "A Theoretical and Experimental Study
       of the Three Jet Interaction", M.S. Thesis, Dept. of
       Mechanical Engineering, U.S. Naval Postgraduate
       School, Monterey, California, April, 1970.

[11] T. Sarpkaya, S. B. Weeks and G. L. Hiriart, "A Theoretical and Experimental Investigation of the Interaction of Jets in Beam-Deflection Type Fluidic Elements", Paper A3, Fourth Cranfield Fluidics Conference, Coventry, England, March, 1970.

[12] C. Bourque, "Some Aspects of the Flow Inside Fluidic Elements", Summer Seminars on Fluid Control Systems, Publication No. 1, Dept. of Mechanical Engineering, University of Waterloo, Edited by S. A. Alpay and H. R. Martin, pp. 31-56, 1970.

[13] E. Turken, "Jet Deflection, Noise and Pressure Distribution in Proportional Amplifiers", M.S. Thesis, Dept. of Mechanical Engineering, U.S. Naval Postgraduate School, Monterey, California, September, 1971.

[14] T. Sarpkaya, "Interaction of Semi-Confined Turbulent Jets", Final Report, Dept. of Mechanical Engineering, U.S. Naval Postgraduate School, Monterey, California, August, 1972.

[15] Flow Measurement, Supplement to ASME Power Test Codes, Chapter 4, No. PTC 19-5; 4-1959, The American Society of Mechanical Engineers, 1959.

[16] J. A. Owczarek, D. O. Rockwell and Y. S. Cha, "A Study of Flow from Two Planar Nozzles", Technical Report No. 1, Themis Project: Fluid Amplifiers, Dept. of Mechanical Engineering and Mechanics, Lehigh University, Bethlehem, Pennsylvania, June, 1970.

[17] J. A. Owczarek, D. O. Rockwell and Y. S. Cha, "The Effect of Nozzle Geometry on the Total Pressure Distribution in Wall Jets on a Circular Attachment Wall and on Jet-Wall Edge Interaction", Technical Report No. 2, Themis Project: Fluid Amplifiers, Dept. of Mechanical Engineering and Mechanics, Lehigh University, Bethlehem, Pennsylvania, June, 1970.

[18] J. A. Owczarek and A. N. Siddiqui, "Visualization of Secondary Flows in Planar Nozzles", Technical Report No. 15, Themis Project: Fluid Amplifiers, Dept. of Mechanical Engineering and Mechanics, Lehigh University, Bethlehem, Pennsylvania, May, 1973.

[19] R. D. Trapani, "An Experimental Study of Bounded and Confined Turbulent Jets", Advances in Fluidics, ASME Publication, Edited by F. T. Brown, pp. 1-13, May 1967.

[20]   J. A. Owczarek, "Fundamentals of Gas Dynamics",
        International Textbook Company, June, 1968.

[21]   Lehigh Optimum Parameter Routine, Obtainable from
        Lehigh University Computer Center.

[22]   A. K. Simson, "Gain Characteristics of Subsonic
        Pressure-Controlled, Proportional, Fluid Jet Ampli-
        fiers", Trans. ASME, Journal of Basic Engineering,
        Vol. 88, Series D, No. 3, pp. 295-305, June, 1966.

[23]   D. B. Taulbee and J. M. Robertson, "Turbulent
        Separation Analysis Ahead of a Step", ASME Paper No.
        71-WA/FE-32, Presented at the Winter Annual Meeting,
        Washington, D.C., November, 1971.

APPENDIX A

In the ideal fluid model, there are nine unknowns and eight equations. Therefore an additional equation is needed. Originally an angular momentum equation with respect to point A in Figure A-1 was employed. This equation is given below:

$$\rho \int_0^W V_{AB}^2 y\,dy \;-\; \rho \int_0^{W_1} V_{CD}^2 r_1 \sin(\theta_1 - \alpha)\,dy'$$

$$-\; \rho \int_{-W_2}^0 V_{DE}^2 r_1 \sin(\theta_1 - \alpha)\,dy' \;-\; \rho \int_0^{W_c} V_{GF}^2 x\,dx$$

$$= \; -\int_0^W (P_{AB} - P_a) y\,dy \;+\; \int_0^{W_c} (P_{GF} - P_a) x\,dx$$

$$-\; \int_0^{W_c} (s+h) \frac{h}{W_c} (P_{GF} - P_a)\,dx \;+\; \int_0^{W_c} \left(\frac{h}{W_c}\right)^2 (P_{GF} - P_a) x\,dx$$

$$-\; \int_{-(s+h)}^0 (P_{AG} - P_a) y\,dy \tag{A-1}$$

where

$$r_1 \sin(\theta_1 - \alpha) = -\frac{1}{2} W_1 + \frac{1}{2} w \cos\alpha - x_p \sin\alpha + y' \tag{A-2}$$

Substituting equations (1) through (7) in Section 5.1 and equation (A-2) into equation (A-1) gives

$$1 - 2\left(\frac{1}{2}\,\frac{w_1}{w}\,\cos\alpha - \frac{x_p}{w}\,\frac{w_1}{w}\,\sin\alpha\right) - \frac{\pi_3}{6}\left[1 + \left(\frac{s+h}{w}\right)^2\right]$$

$$= \pi_2\left[-\frac{w_2}{w}\left(\frac{w_1}{w} - \cos\alpha + 2\,\frac{x_p}{w}\,\sin\alpha + \frac{w_2}{w}\right) + \frac{5}{6}\left(\frac{w_c}{w}\right)^2\right.$$

$$\left.- \frac{1}{2}\,\frac{h}{w}\left(\frac{s+h}{w}\right) + \frac{1}{6}\left(\frac{h}{w}\right)^2 + \frac{1}{3}\left(\frac{s+h}{w}\right)^2\right] \qquad (A-3)$$

Equation (A-3) was used as the additional equation in the ideal fluid model. However, when solving the nine simultaneous equations on the computer using the program LOPER, only two sets of solutions (for $w_c/w = 1$, $s/w = 1$ and for $w_c/w = 1$, $s/w = 1/2$) could be obtained. For the cases with $w_c/w = 1/2$, LOPER did not give any solution with an acceptable error. Therefore $x_p/w = 1/2$ rather than equation (A-3) was used in the calculations.

The experimental results described in Section 4.2 show that the value of $x_p/w = 1/2$ was in good agreement with experiments except for the case of $w_c/w = 1/2$ and $s/w = 1$ in which x_p/w has a value lying between 1.5 and 3 depending on the pressure ratio π_2. When these values were used in the calculation, the program LOPER again did not give a solution with an acceptable error. Therefore, $x_p/w = 1/2$ was used for all the calculations.

Another point which should be mentioned is that in the model shown in Figure 79, the coordinate axis r bisects line

CD and makes an angle α with respect to the horizontal axis. The coordinate axis r intersects the centerline of the power jet nozzle at point 0 corresponding to the coordinate of the pivot point x_p. The value of the coordinate x_p may or may not correspond to the value determined experimentally by connecting the points of maximum combined jet velocity at different distances from the pivot point. For small angles of deflection, these values should not differ much.

Figure A-1

161

APPENDIX B

B-1   Simson's profile for a two-dimensional free jet
is given by

$$\frac{V}{V_{\bar{\mathbb{C}}}} = \left[1 - (\frac{y_e}{kx})^M \right]^2 \tag{B-1}$$

with $k = 1.378 \, w/x_o$ and $M = 1.75$. For the definition
of symbols used, see Figure 81.

In the present investigation for a bounded free
jet with power jet nozzle exit aspect ratio of two, the
half-width of the power jet at location x_o is 1.75w
instead of 1.378w. Therefore the following expression
is employed for a bounded free jet with aspect ratio
of two,

$$\frac{V}{V_{\bar{\mathbb{C}}}} = \left[1 - \left(\frac{y_e}{1.75 \, w \frac{x}{x_o}} \right)^M \right]^2 \tag{B-2}$$

At $x = x_o$ $\frac{V}{V_{\bar{\mathbb{C}}}} = \left[1 - (\frac{y}{1.75w})^M \right]^2$ \qquad (B-3)

Equating the momentum of the jet leaving the
nozzle to that of the jet at x_o gives

$$2 \int_0^{1.75w} [V^2]_{x=x_o} \, dy = U_o^2 \, w \tag{B-4}$$

162

Substituting equation (B-3) into equation (B-4) and remembering that $U_0 = V_\xi$ gives

$$2 \int_0^{1.75w} \left[1 - \left(\frac{y}{1.75w}\right)^M \right]^4 dy = w \qquad (B-5)$$

After integration and simplification, equation (B-5) becomes

$$0.7134 - \frac{4}{M+1} + \frac{6}{2M+1} - \frac{4}{3M+1} + \frac{1}{4M+1} = 0 \qquad (B-6)$$

Equation (B-6) then gives M = 1.3616 which is used in the real fluid model in Section 5.2.

B-2   Equation (39) in Section 5.2 is obtained as follows. The velocity profile for a bounded jet of aspect ratio two (equation B-2) is

$$\frac{V}{V_\xi} = \left[1 - \left(\frac{y_e}{1.75 \, w \frac{x}{x_0}}\right)^{1.3615} \right]^2 \qquad (B-2)$$

Referring to Figure 81, in the transition zone, one can write down

$$Q = 2 \int_0^{b/2} U_0 dy + ? \int_0^{y_{e,max}} V dy_e$$

$$= U_0 b + 2U_0 \int_0^{y_{e,max}} \left[1 - \left(\frac{y_e}{1.75 \, w \frac{x}{x_0}}\right)^{1.3615} \right]^2 dy_e \qquad (B-7)$$

163

where $\qquad y_{e,max} = 1.75\, w\, \dfrac{x}{x_0}$ $\qquad\qquad\qquad\qquad$ (B-8)

and $\qquad b = w\left(\dfrac{x_0 - x}{x}\right)$ $\qquad\qquad\qquad\qquad\qquad$ (B-9)

Substituting equations (B-8) and (B-9) into equation (B-7), after integration, equation (B-7) becomes

$$Q = U_0 w\left(1 - \frac{x}{x_0}\right) + 2U_0\left(1.75\, w\, \frac{x}{x_0}\right)\left(1 - \frac{2}{2.3615} + \frac{1}{3.723}\right)$$

$$(B-10)$$

Dividing equation (B-10) by $U_0 w$ gives

$$\frac{Q}{Q_0} = 1 + \left[3.5\left(1 - \frac{2}{2.3615} + \frac{1}{3.723}\right)\right]\frac{x}{x_0}$$

or

$$\frac{Q}{Q_0} = 1 + 0.47588\,\frac{x}{x_0} \qquad\qquad\qquad (B-11)$$

Equation (B-11) is the same as equation (39) in Section 5.2.

164